Polymers with Pendant Ferrocenyl units as Burn Rate Catalyst and Redox Responsive Material

A Thesis Submitted for the degree of

DOCTOR OF PHILOSOPHY

By

Moumita Dhara

School of Chemistry
University of Hyderabad
Hyderabad – 500046
India

July 2021

Dedicated

to

my Family

"Nothing in life is to be feared; it is only to be understood."

Marie curie

Declaration

I hereby declare that the matter embodied in the thesis entitled ***"Polymers with pendant ferrocenyl units as burn rate catalyst and redox responsive material"*** is the result of investigations carried out by me in the School of Chemistry, University of Hyderabad, Hyderabad, India under the supervision of **Prof. Tushar Jana** and it has not been submitted elsewhere for the award of any degree or diploma or membership, etc.

In keeping with the general practice of reporting scientific investigations, due acknowledgments have been made wherever the work described is based on the findings of other investigators. Any omission or error that might have crept in is regretted.

Moumita Dhara

July, 2021

Moumita Dhara

Regd. No. 14CHPH24

Certificate

This is to certify that the work described in this thesis entitled *"Polymers with pendant ferrocenyl units as burn rate catalyst and redox responsive material"* has been carried out by **Moumita Dhara** bearing registration number **14CHPH24** in partial fulfilment of the requirements for award of Doctor of Philosophy in the School of Chemistry is a bona fide work carried out by her under my supervision and guidance and the same has not been submitted elsewhere for any degree. This thesis is free from plagiarism and has not been submitted previously in part or in full tothis or any other University or Institution for the award of any degree or diploma.

Parts of this thesis have been published in the following publications:

1. **M. Dhara**, N. Giri, B. N. Rao, A. K. Patra, P. U. Sastry, M. S. Ingole, T. Jana, ***Euro. Polym. J.***, 2020, *122,* 109380. (Chapter 3)
2. **M. Dhara**, N. Giri, A. Dutta, A. K. Patra, P. U. Sastry, M. S. Ingole, T. Jana, ***Polymer***, 2020, *204,* 122807.(Chapter 4)
3. **M. Dhara**, S. Rudra, N. Mukherjee and T. Jana, ***Polym. Chem.***, 2021, (DOI:10.1039/D1PY00590A. (Chapter 6)

The student has made presentation in the following conferences:

1. 15th international conference on Polymer Science and technology (SPSI MACRO 2018) **(Poster presentation)**
2. 17th Annual In-House Symposium (CHEMFEST 2019) **(Oral presentation)**
3. International conference on Functional Materials (ICFM 2020) **(Oral presentation)**

Further, the student has passed the following courses towards fulfilment of course work:

Sl. No.	Course Code	Course Name	No. of Credits	Grade
1.	CY-801	Research Proposal	3	A
2.	CY-802	Chemistry pedagogy	3	B
3.	CY-805	Instrumental Methods A	3	B
4.	CY-806	Instrumental Methods B	3	A

Kumara Swamy
12/7/2021

Dean
School of Chemistry
University of Hyderabad
Hyderabad-500 046, India

Dean
SCHOOL OF CHEMISTRY
University of Hyderabad
Hyderabad-500 046

Jana 12th July 2021

Prof.Tushar Jana
(Thesis supervisor)

Prof. TUSHAR JANA
School of Chemistry
University of Hyderabad
HYDERABAD-500 046. INDIA.

Preface

The present thesis entitled ***"Polymers with pendant ferrocenyl units as burn rate catalyst and redox responsive material"*** has been divided into eight chapters. ***Chapter 1*** includes a brief introduction about the importance of pendant ferrocenyl polymers together with their systematic evolvement as a side chain by following a variety of well-established polymerization technique since their discovery. Further the utility of ferrocene-based polymers as a burn rate catalyst (BRC) in composite solid propellant (CSP) as well as a well-defined polymer brush *grafted* on the particle surface have been thoroughly discussed in addition with a variety of solution-based morphologies of ferrocene containing polymers. ***Chapter 2*** describes the source of materials, synthetic procedure and methods employed for all the working chapters. ***Chapter 3*** deals with a synthesis and characterization of ferrocenyl polymer *grafted* polybutadiene in presence of an energetic functionality at the backbone as a BRC in CSP as well as their significant improvement in various polyurethane properties owing to the enhancement in segmental compatibility. ***Chapter 4*** demonstrates the structure-property relationship of a ferrocenylsilane tethered polybutadiene polyurethanes with the enhancement in segmental mixing along with the utility of the prepolymers as a BRC in CSP. ***Chapter 5*** illustrates the construction of a smart surface comprises with ferrocenyl polymers *grafted* on the surface of silica nanoparticles *via* surface-initiated RAFT polymerization technique. ***Chapter 6*** outlines a novel pathway to fabricate a nanocomposite of *in-situ* synthesis of aluminium nanoparticle in the cavity of a hollow polymer nanocapsules with ferrocenyl copolymer shell by targeting to utilize as a fuel-cum BRC in CSP. ***Chapter 7*** represents the formation of pendant ferrocenyl polymer based multicompartment morphologies with a switchable pores triggered *via* redox-response. ***Chapter 8*** summarizes the findings of the present investigations with a concluding remark and highlights the most possible directions which can be investigated further based on our outcomes.

Moumita Dhara

July, 2021

Moumita Dhara

Acknowledgements

The entire PhD journey of mine remains a most crucial period of my life. In this period, I have gone through several phases that makes me grow as a much matured and confident person with significant improvement in academic as well as social learnings. It is a genuine pleasure to take this opportunity to express my deep sense of thanks to one and all who were directly or indirectly involved in this successful journey.

Firstly, I express my sincere gratitude to my research supervisor, Prof. Tushar Jana, for giving me the opportunity to work under his guidance in the field of Polymer Chemistry and learn from his expertise; he has always supported and guided me throughout my research period that has bought me this thesis. I feel truly fortunate to have him as a teacher in my academic career who always provide immense work freedom in the lab that has helped me realize my potential and provoked me to think and do things on a broader perspective and grow as a researcher. I am highly thankful for his warm words of appreciation and encouragement for all the effort I have tried to put on to fulfil the research work especially the kind of honest support and freedom he has constantly showers upon a married woman like me its unimaginable and I am deeply indebted to him for this. His all-time kind, generous and positive attitude towards his students makes me inspire to work more efficiently and peacefully in the lab which I feel has a great impact on my research work to do better specially during my struggling period as a PhD student. I cherish those valuable and enjoyable interactions with Sir and other lab mates in each and every group meeting and I must say the way he interacts with each and every student that made me feel as a secured family member of our TJ group. I also want to thank to Madam for her warm welcoming attitude whenever I go to Sir's home and to Babli and Buchan for those enjoyable memories we have spent together whether it was lab party or in their home.

I would like to thank the present and former Dean(s), School of Chemistry, for providing all the facilities and their constant support. I extend my gratitude to all the faculty members of the school, especially thankful to my doctoral committee members, Prof.

Krishnamurthi Muralidharan and Prof. Pradeepta K. Panda for their valuable suggestions, cooperation, and encouragement. I want to extend my sincere gratitude to Prof. S Mahapatra for allowing me to avail his lab facility to carry out the theoretical investigations for my research work.

I sincerely acknowledge Prof. P. U. Sastry from BARC, Mumbai and Prof. S. Ramakrishna from IIT Madras as our research collaborator to study the SAXS and Burn rate measurement, respectively. I also want to thank Mrs. K. S. V. Poorna Chandrika from IIOR, Rajendranagar, Hyderabad for helping me to analyse the iron content of my samples.

The Centre for Nanotechnology, University of Hyderabad is greatly acknowledged for providing the facilities, like TEM and confocal laser microscope. I am thankful to Mr. Pankaj and Durga Prasad for helping me in sample measurements. I want to specially thank to Mr. Sunil in our school who has been very helpful during FESEM measurements. My special thanks to Chaitanya anna, for his kind cooperation to carry out the DVS measurement, Suvobrata, for helping me in learning the BET as well as CV measurement and Tasnim for lifetime imaging study. I also want to thank to Sabari, Ankit, Chandni and Olivia for their kind help in learning and analysing the CV experiment in our school. I thank all the non-teaching staff in School of Chemistry for their support and help specially Durgesh, Turabuddin, Mahinder for NMR data. I also want to thank to Mr. Satish in ACRHEM for helping me to avail the instrumental facility during COVID lockdown.

Financial assistance from DST, India is greatly acknowledged, it is a huge financial support for being a INSPIRE scholar since B.Sc. My special thanks to INSPIRE for providing me the fellowship during my PhD and also for extending six month fellowship during lockdown because of COVID pandemic.

I would like to thank my lab seniors Narasimha anna, Bikash da, Raju anna, Malkappa anna, Suvra di, Bala anna, Rambabu anna, Konda anna, Naidu anna, Mithun da and Amarnath anna for their help and useful discussions. I want to specially thank to Bikash da and Narasimha anna as senior and I really enjoyed the discussions with them which has been always fruitful. I thank my lab mates Harilal, Suchismita, Nilanjan, Anupam, Prasanntha,

Arunava and Somdatta for their valuable interactions. I cherish my friendship with Harilal and Suchismita during my PhD journey. It was a memorable experience to work with Nilanjan specially the valuable discussions we had during my struggling period of work. I want to extend my sincere thanks to Anupam who have always given me the respect as an elder sister and I really enjoyed all those academic and non-academic discussions with you. I am fortunate having junior like Somdatta who helped me a lot with her honest and kind attitude at the end phase of my bench work in the lab. I thank all my lab mates for keeping a friendly atmosphere in the lab.

I cherish the friendship with Vaishnavi, Sujitha and Kranthi during my PhD journey for those enjoyable memories we have spent together. I thank all the research scholar in the school of chemistry who directly or indirectly helped me in this journey.

I enjoyed several events in the campus like Saraswati puja, Diwali. I will cherish those days I spent with Tasnim, Sneha, Sabari, Debika, Sarada and Olivia, especially our hostel 'adda' on several occasion. It will be a nice memory in my PhD life the time we spent together. I value my friendship with Tasnim, I fond of her calmness so much; I thank to Debika for having us delicious food you cooked. I want to thank all of our Bengali seniors and juniors from school of chemistry for having some enjoyable memories especially during the festivals like Saraswati puja and Diwali.

My sincere regards to all the teachers who have come at different stages of my life. I am fortunate enough to have great teachers like CKP sir, DK sir, DG mam during B.Sc and AKS sir, GKK sir, DKM sir during my M.Sc. days. I must mention "Pratul babu's" tution in my school life which indirectly create a pathway for having a good academic career in future. I cherish those school friends like Saheli, Modhumita, Mita, Apu, Dora, Nibedita, which were the golden days of my life. I shared unforgettable memories of college days with friends like Debjani, Juthika, Priya, Sharmisthadi, Madhumita, Riya, Shilpi. I enjoyed a lot in my M.Sc days with a group of people like Priangana, Sangeeta, Jit, Mainak, Sandip. In every phase upto M.Sc I have extremely enjoyed my hostel and mess life with those sweet people like Sagarika, Trishna, Rashmi, Anuradha, Pritha, Arpita, Sweety, Tanushree, Reshmi and many more. I

value my close association with Priangana till date, I have learnt many things from all the discussions we had. I want to thank each one of our "Alumina" member who indirectly always drives me to build a good academic career particularly Ambikesh Kaku.

Finally, I want to convey my heartfelt gratitude to my parents especially to Baba, my father, because of whom I able to come across this far; you inspire me always to do best at every phase of my life. I am lucky enough to have you both in my life, Baba and Maa. I want to thank to Dadu, Dida and Thakuma, my grandparents, for their utmost love and affection towards me which always motivates me to do good in my career. I cherish my close and a very special bonding with my brother (Vai) who is always there for me at any situation and makes me happy. And obviously Kuchivai, another brother, who has always made me feel special at every bit of moment. I value my special bonding with Bittu, Bapan, Mama(s), Mamima(s) for their warm affection and love towards me. I want to thank all those relatives who always appreciate and inspire me to do well in my career. It will be incomplete without the most important person in my life, Nitai, my husband for becoming my strength in every aspect of my life who helps me to learn to lead a peaceful life with full of positivity and morality that actually makes me more happier and I must say this reflects in my research work significantly. I feel our special bonding will help me to do even better in future.

I could not mention all the names but my sincere gratitude to all the people who have been associated with this journey.

Moumita

Contents

CHAPTER 1

Introduction

1.1. Introduction

The present thesis deals with the development including synthesis and characterization of metallopolymers containing ferrocene as a pendant unit and their potential as promising materials for the use in composite solid propellant (CSP) or in redox responsive materials. The main emphsis of this thesis work lies in looking deep insight into various physical properties of pendant ferrocenyl polymers when designed as a polyurethane or else well-controlled polymer chains synthesized *via* living controlled polymerization technique like reversible addition fragmentation chain transfer (RAFT) polymerization.

1.2. Metallopolymer

An extensive variety of fashionable functionalized polymers and novel materials with interesting electrical, physical and magnetic characteristics are discovered by introducing metals into polymeric materials and thereby, a thorough-in-depth analysis on the synthesis and structure-property relationship of these metallopolymers have become a fascinating area of research.[1,2] Metallopolymer comprises of metal centre as a part of its repeat unit located either in polymer main backbone or in side chains. The metal centres connected *via* covalent linkages results generally irreversible or static binding, contrarily noncovalent linkages leads to reversible or dynamic binding. A plenty of strategies for the synthesis of well-defined metallopolymers have been pioneered which are highly compatible with the presence of metal centres like polycondensation, controlled radical polymerization, chain-growth condensation polymerization, ring opening polymerization and so on.[3] In addition to these methodologies, variety of examples are there describing the post-synthesis protocols where polymers can be refashioned by linking metal centres to an already existing backbone or else by connecting metal-containing residues to a polymer chain. Synchronically more efficient and upgraded characterization techniques have been launched that makes the structural analysis of metallopolymers much easier.[4–6] Altogether, a wide range of easily accessible metallopolymer structures have risen the scope to thoroughly study their properties as well as find the suitability in myriad number of sustainable applications. Among all meatllopolymers, ferrocenyl polymer

is known to be widely studied as one of the most promising metallopolymer.

1.3. Ferrocenyl polymers

A breakthrough invention of ferrocene and its detailed structural analysis introduced into an incendiary regeneration of organometallic chemistry. Today even after 70 years, advance utilizations of this outstanding organometallic functionality are still being extensively sought by the researchers. The insertion of ferrocene moiety into polymer matrix has intrigued a massive curiosity owing to the electron donating ability, reversible redox chemistry, steric properties and easy functionalization of this stable fragment.

1.3.1. Ferrocene's basic properties

At first, a process technician spotted the generation of an orange sludge during investigation of the pipes used for the production of cyclopentadiene upon cracking of dicyclopentadiene at Union Carbide in the late 1940s.[7] Later on in 1951, ferrocene was independently recognized by Kealy, Pauson and Miller; it was represented as the compound with two monohapto cyclopentadienyl ligands i.e. $[Fe(\eta^1\text{-}C_5H_5)]_2$.[8,9] The real sandwich structure - $[Fe(\eta^5\text{-}C_5H_5)]_2$ – was uncovered and published in 1952 by Wilkinson, Rosenblum, Whiting, and Woodward[10] in Harvard and by Fischer and Pfab[10] in Munich. It owns a D_{5h} (eclipsed) or D_{5d} (staggered) conformation and a very small rotation energy barrier (as shown in equation 1).

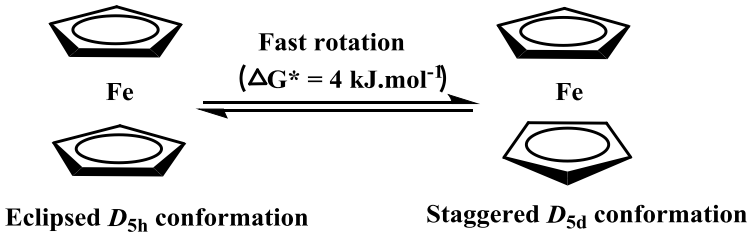

……Equation (1)

Ferrocene (FcH) – the name coined by Woodward and Whitting[10] – consists some exceptional properties as listed below:

i) Highly stable upto 400 °C (m.p. 172.5 °C) with an iron centre having saturated electronic structure like krypton.

ii) Shows very high reactivity just like a superaromatic electrophile.

iii) Mild and reversible oxidation around +0.4 V versus saturated calomel electrode (SCE) (equation 2).

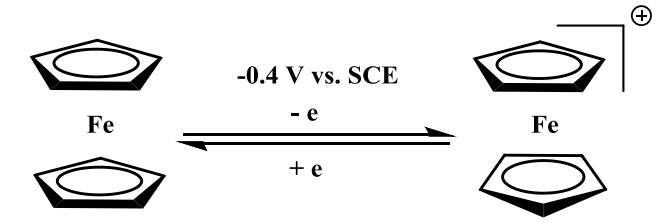

……Equation (2)

In addition to these above mentioned properties, a good solubility in all common organic solvents led to a vast number of ferrocene derivatives and ferrocene containing materials; all these novel synthesis since last 70 years introduced ferrocene as an icon in organometallic chemistry.[11,12]

1.3.2. Ferrocene containing polymers

Mainly, two major category of ferrocene containing polymers are well known: main chain polymers where ferrocene remains as an integral part of the polymer backbone (*Figure 1.1A*) and side-chain ferrocene containing polymers in which the whole ferrocene moiety hanging as pendant group from the main polymer backbone (*Figure 1.1B*). There are other two much less recognized class of ferrocene-containing polymers which are: embedded side-chain polymers where the polymer backbone crosses the same cyclopentadiene ring in one ferrocene unit (*Figure 1.1C*) and unbridged ferrocene containing polymers where polymer backbone connects with the iron centre in a direct line (*Figure 1.1D*).

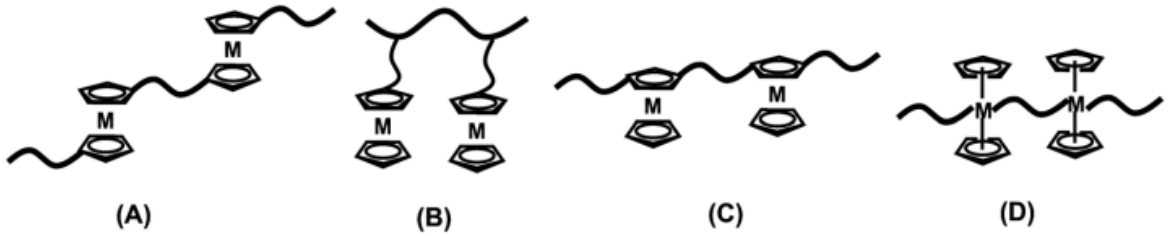

Figure 1.1: *Dfferent categories of ferrocene containing polymers.*[13]

First in 1955, vinylferrocene was subjected to polymerization and resulted a well-defined polymers containing ferrocene as pendant group.[14] Afterwards, it was untill 1980s that there were some reports mentioning the synthesis of acrylate or methacrylate based ferrocenyl polymers using conventional techniques like free radical, cationic and anionic polymerization but most of these polymers were unable to achieve controlled molecular weight distribution also lacking to produce block copolymers types complex materials.[14] In the meantime, Manners et al. introduced well-characterized main-chain polymers of ferrocene with high molecular weights by using anionic ring opening polymerization on ring-tilted ferrocenophanes and this particular area has been developed very rapidly over the last 40 years.[15–17]

Though growth of main-chain ferrocene-containing polymers remains in focus over the years, the side-chain ferrocene-containing polymers have drawn attention only recently. Well-defined side-chain ferrocene-containing polymers and block copolymers have been synthesized *via* living anionic polymerization (LAP)[18], ring-opening metathesis polymerization (ROMP)[18] as well as by controlled/ living radical polymerization (CRP)[19–21] techniques including atom transfer radical polymerization (ATRP)[20], reversible addition fragmentation chain transfer polymerization (RAFT)[19] and nitroxide-mediated polymerization (NMP)[21]. And these are the methodologies that have made a notable advancement due to their potential of synthesizing highly complex functionalized polymers with pre-determined average molecular weight and low dispersities. Owing to the electrochemical reversibility, ease in controlling the redox activity and chemical stability[22–24], ferrocenyl polymers have drawn immense attention of the researchers and have been employed

in variety of applications starting from electrochemical devices[25,26] to actuators,[27] nanoceramics[28] to drug delivery[29,30] and many more.

1.4. Polymers with pendant ferrocene

The focus of this thesis is on the synthesis of the polymers with pendant ferrocene units and studying their intriguing properties in detail along with promising application. Polymers with pendant ferrocene unit carry the distinct properties of ferrocene together with the whole characteristics of the main polymer backbone showcasing the properties like redox activity[31], switchable polarity[32], thermal and oxidative stability [33], moisture resistance[34], biological activity[35] and unusual rheological properties[36]. In these polymers, ferrocene unit may act as a catalyst or chemical-stimulus responsive switch based on designing the materials. One of the beneficial point for designing a pendant ferrocenyl polymer is their ease in synthesis.

1.4.1. Synthesis started from ferrocenyl monomers

A straightforward root of designing the polymers with pendant ferrocene unit is to start the synthesis with the monomers comprising of polymerizable functionality directly connected with the ferrocenyl group. For better understanding some examples of ferrocenyl monomers are mentioned here as a representative (*Figure 1.2*). These monomers can undergo polymerization either *via* radical polymerization or *via* anionic polymerization and can yield polymers with ferrocenyl unit as a pendant group.

1.4.2. Post-synthesis modification with ferrocenyl monomers

Another most possible pathway is to create the polymer backbone first and to connect the ferrocenyl monomers *via* appropriate functionality in a subsequent step. Some of the well-known methodology which are generally employed to carry out these modifications are click reaction[37], thiol-ene reaction[33], hydrosilylation reaction[38], transamination[39], nucleophilic substitution[40], reductive amination[41] and so on.

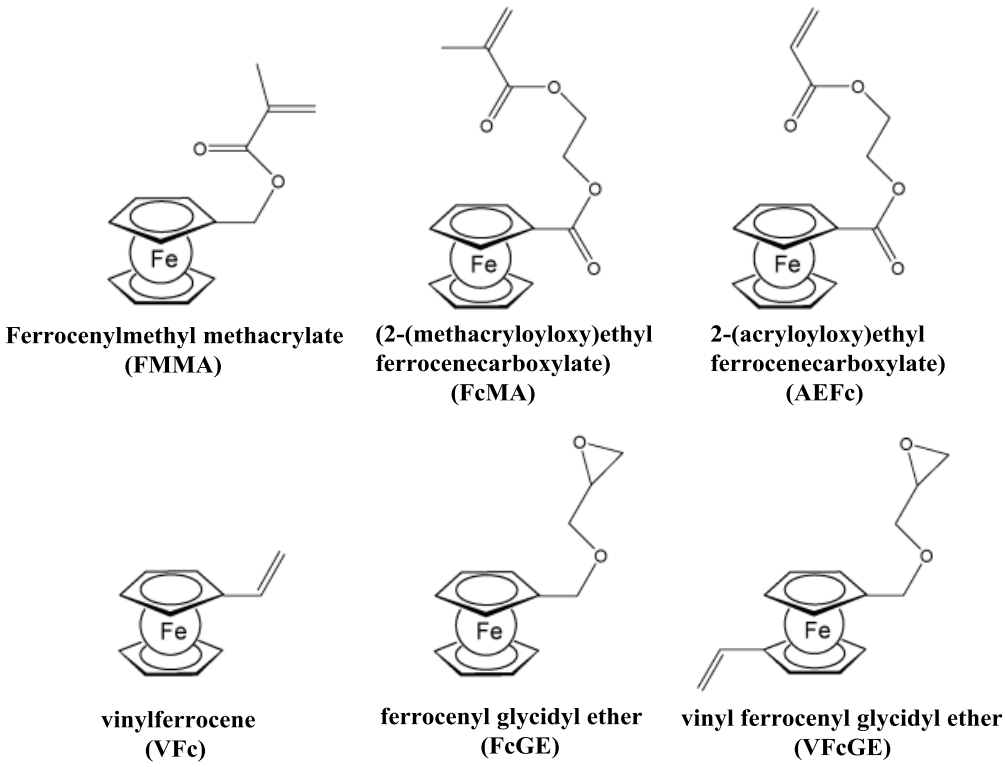

Figure 1.2: *Few typical ferrocenyl monomers.*[34]

In polyurethane application the role of a metallopolymer especially in form of ferrocenyl polymer mostly has been witnessed as a highly useful catalyst. One major part of this thesis work is centred around the synthesis and characterization of a metal based polybutadiene polyurethane. A brief discussion on this is detailed in the following section.

1.5. Metallo polyurethane (PU)

Until such time when metallopolymer field was impeded because of many synthetic hurdles, the cravings for an established methodology to prepare higher molecular weight metallopolymers remains most challenging. During that phase, the conventional polymerization guidelines which were highly suitable for synthesizing organic polymers often led to very low molecular weight metallopolymers as an unwanted by product and these metallopolymers generally were insoluble in nature and poorly characterized. In the mid-1990s,

most of the constraints for synthesizing high molecular weight and soluble metallopolymers were prevailed by a several researchers *via* introducing various novel synthetic procedures those are nicely compatible with the presence of a metal centres.[42] Gradually, metallopolymers with variety of structures became the epicentre of many emerging applications with several exciting properties and interesting characterization tools.[43–46]

Polyurethanes (PUs) are known to be a unique class of materials with immense industrial desirability. The fusion of metallopolymers and polyurethane chemistry introduced a multifunctional strategy towards various applications owing to their low viscosity, liquid crystalline properties and unusual thermal properties.[47] Metals are normally inserted into the PU matrix either *via* coordination[48,49] or by means of ionic bond[50,51], sandwiching the metal within the PU matrix is less explored[52,53]. Since metal-containing isocyanate synthesis is troublesome, generally metal-containing polymeric diols as prepolymer or chain extender are used to synthesis metallopolyurethanes.[36] So, all we need to know is the basic idea of PU synthesis and their related properties and this will assist us to have a overview of metallopolyurethane.

1.5.1. Polyurethanes (PUs) and it's applications

Otto Bayer, "father of polyurethanes" and his team members pioneered polyurethanes at Germany in 1973 by using diols and diisocyanate in addition with a catalyst. The general reaction scheme for synthesizing polyurethanes are mentioned here in *Scheme 1.1*. The basic PU properties mainly relies on the major two raw materials i.e. polyols (which is having more than one hydroxyl group) and diisocyanates.

Scheme 1.1. *General synthetic scheme for polyurethane.*

The core PU-properties are governed by the main features of polyols like molecular weight, viscosity, degree of crosslinking etc. Apart from hydroxyl groups several other functionalities remains part of a polyols such as ether, ester, amides, acrylic and so on. Another major raw material to form PU is isocyanate (R–N=C=O), generally shows very high reactivity because of its low density character of the NCO carbon and thus easily can form urethane without any kind of side-products. An isocyanate can contain several NCO group in a molecule and depending on the presence of isocyanate goup, the materials is named as diisocyanate or polyisocyanate.[54] The reactivity of isocyanate can be easily tuned by varying the "R" group from aliphatic to aromatic. And this isocyanate reactivity plays a pivotal role in PU synthesis *via* regulating the crosslinking region of a PU matrix with the formation of dimers, trimmers and oligomers. Catalyst, an another reagent is well-known to be a part of the PU synthesis; commonly seen in two broad categories i.e. basic amine types and lewis acid types depending on the reaction condition. 1, 4-diazabicyclo [2.2.2] octane (DABCO) and dibutyltin dilaurate (DBTDL) are two majorly used typical amine catalyst and lewis acidic catalyst, respectively.

Since its discovery, PU gradually has become epicentre of wide industrial application in various field owing to its durability, flexibility, abrasion and impact resistance, thermal and mechanical stability. PUs are widely used as adhesives in industries like automotives, aircrafts, textiles, furniture, and electronic applications; in medical industries such as wounds drying, dental reconstructions, tissue engineering, ceramics, engineering plastics and many more.[55,56] The rigid foam PUs are known to be used as insulating materials in roofing purposes, walls, boards etc.[57,58] Now a days, water based PU dispersions are extensively used in coating and painting industries all over the globe because of their certain advantages over solvent based PUs. Our modern society has witnessed a tremendous dependency of PU materials in biomedical applications such as artificial heart valves, vascular devices, aortic valves, tissues replacing, artificial bones, drug delivery applications and many more.[59,60] PU has wide application as a binder in rocket propellant application and some part of this thesis work is devoted in this direction.[36]

1.5.2. PU properties

The urethane linkages present in PU comprise of –N-H and carbonyl –C=O groups between the polyols (*Scheme 1.1*) is mainly responsible for various kind of non-covalent interactions starting from intra to inter chain interactions, van der waals interactions, dipole-dipole interactions to strong hydrogen bonding interactions. These are the key parameters which can govern mechanical strength, thermal properties, chemical stability like core properties of a PU matrix and these properties can be easily tuned as per requirement by incorporating desired functionality in PU backbone. Segmentation is one of the most well-known intriguing properties of a PU matrix that drives to achieve many fascinating characteristics and these are widely studied[61–63]; in fact segmented polyurethanes (SPUs) remain a major choice among many types of PUs. The presence of hard segment (HS) and soft segment (SS) in a PU backbone is the origin of segmentation generally resulting micro phase organization (*Figure 1.3*). This micro phase organization is the commanding force behind majority of the physical properties in case of SPUs and it is mainly regulated by the extent of segmental compatibility between HS and SS.[61]

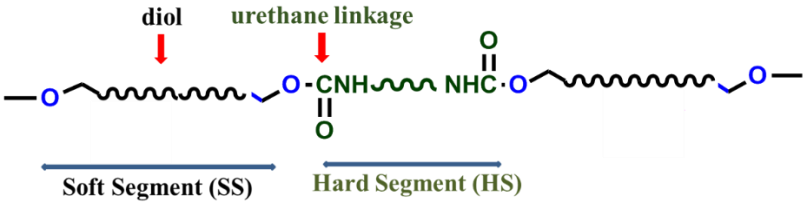

Figure 1.3: *Pictorial diagram of segmented PU structure*

Most of the cases segmentation is synthetically introduced by using low molecular weight diols as chain extender but many reports are there with non-chain extended SPUs where hydrogen bonding is the determining factor for segmentation or we can say as phase separation of HS and SS segments.[62] It has been seen that stronger H-bonding helps in phase mixing which assist significant improvement in various PU properties especially mechanical parameters.[62] Apart from H-bonding Van der Waals interactions also play a key role in phase

segregation within a PU matrix. The Bonart and Clough first introduced two kinds of phase morphology of a PU matrix and these morphologies were analysed in detail by small angle X-ray scattering (SAXS) study which is an important tool to make sure about the presence of segmental phase separation or phase mixing.[62] The PU morphologies vastly can be varied by modulating the processing method, polyols and diisocyanate structures as well as their reactivities for better understanding the structure-property relationships of the PUs.[64,65] Hydroxyl terminated polybutadiene (HTPB) is one of the most studied polyol for PU material where all these above mentioned properties have been explored by several research groups and this is the PU material which is our matter of discussion too.

1.6. HTPB based metallo PU

Hydroxyl terminated polybutadiene (HTPB) is one of a widely used viscous liquid polymer (*Figure 1.4*) and this is very well-recognized due to its excellent physicochemical and mechanical properties like hydrolytic stability, low-temperature flexibility, chemical resistant, adhesives, electrical insulating properties etc.[66] Usually HTPB is synthetically prepared via anionic polymerization rather than free radical polymerization from 1, 3 butadiene by using alcohol as a solvent and H_2O_2 as an initiator.[67] Since past, HTPB is known to be used as a binder in rocket propellant application in all over the world owing to its various specific inherent properties including high loading capacity, longer storage time, sub ambient glass transition temperature (T_g ~ -75 ^oC), excellent flow characteristics, high decomposition temperature >200^oC and superior mechanical properties.[68] From past decades our group have introduced many HTPB based prepolymer after covalently modifying the backbone with various energetic functionality without disturbing the microstructure of HTPB and its inherent properties, as shown in *Figure 1.4, via* terminal functionalization method.[68–71] In addition to that, with the help of a suitable diisocyanate and catalyst, free standing-flexible PU films have been prepared and thoroughly characterized by targeting various applications.[71–75]

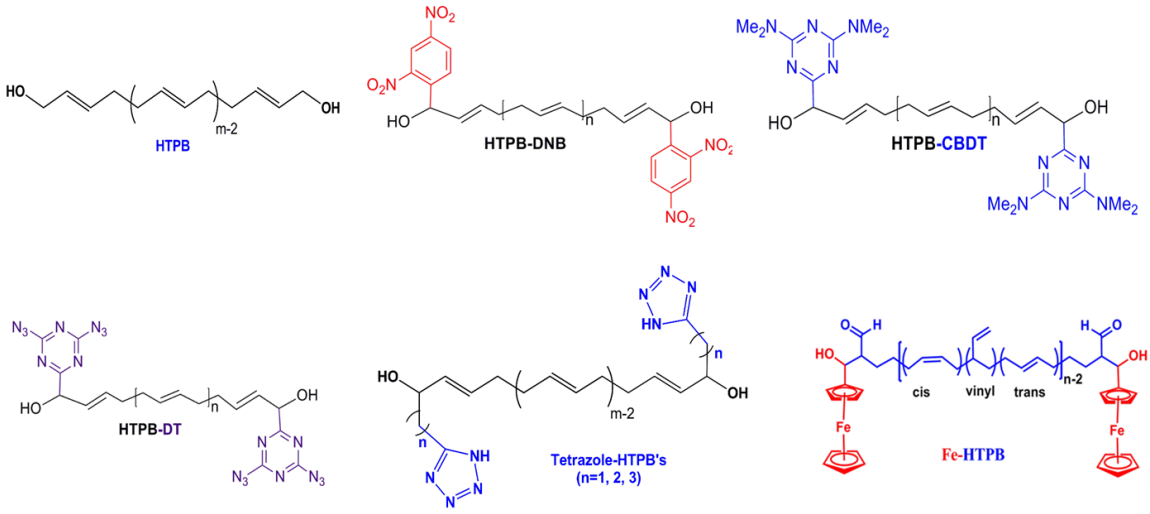

Figure 1.4: *Structural representation of HTPB and its various derivatives.*[68–70,74,76]

Recently, metal-containing functionality has been covalently attached to HTPB backbone as a catalyst and the role of presence of metal has been scrutinized in their PU properties.[36,72,77] Especially, ferrocene based HTPB polymer shows great utility in composite solid propellants (CSPs) for their excellent catalytic effects as burn rate catalyst (BRC) cum binder.

1.6.1. Application in CSP as burn rate catalyst (BRC) cum binder

Propellants are a kind of highly filled polymers comprised of up to 90 wt% of explosives embedded in an elastomeric binder to be used as an energy reservoirs in rocket and missiles.[68] Amidst of a number of physical parameters, a stable high burning rate with low pressure exponent is one of the most determining factor for a highly efficient composite solid propellant (CSP). As we mentioned before, HTPB is known to be extensively used as a propellant binder owing to its outstanding inherent physical properties, still, HTPB, due to its inert nature, cannot fulfil the requirement of a BRC in the propellant formulations. BRC is basically highly effective for varying the burning rate of a propellant under pressure in composite solid propellant (CSP). Generally, a BRC helps to reduce the amount of energy required to initiate the process of converting fuel to hot gases, in turn it lowers the threshold of

activation.[78] For better understanding the process, an energy diagram is outlined here in *Figure 1.5*. Generally, before ignition occurs, it is mandatory to supply energy to the propellant to get conversion of ammonium perchlorate (AP) to gas phase and metal into a liquid phase. The solid line stands for the energy required to carry out the reaction. The igniter supplies this energy to start the burning process and later on the energy released from the burning fuel helps to maintain the process. Presence of BRC initiate the burning process with relatively lesser energy and maintain the further process; dotted line represents the energy diagram in presence of a BRC. It is to be noted that the energy gap between unburnt components to that of the exhaust gases is exactly same with or without a catalyst. So a BRC cannot increase the thrust by itself, rather it can vary the rate at which propellant burns and it is obvious that the increased burn rate of a catalysed propellant is enable to move the higher amount of mass flow through the nozzle results a minor increase in total thrust.

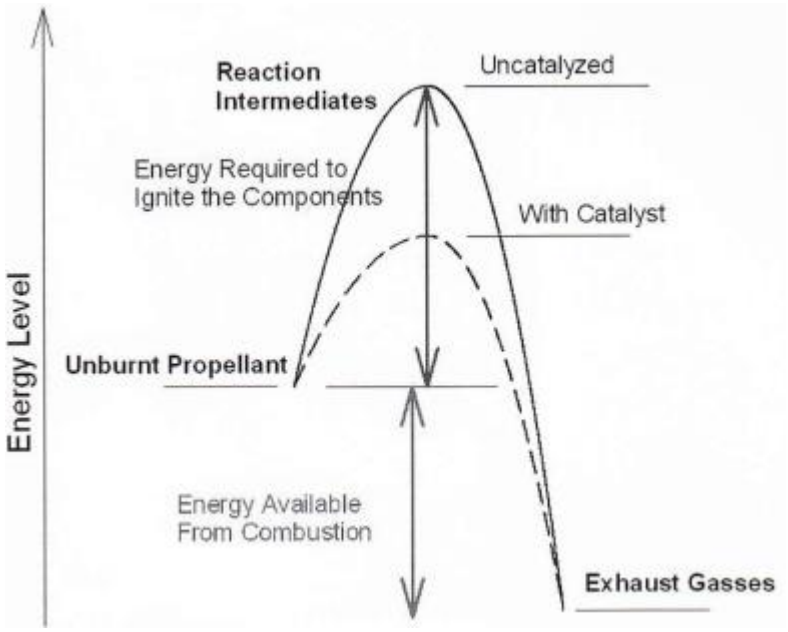

Figure 1.5: *Energy level diagram describing the effect of a BRC.*[78]

Among various kinds of BRCs ferrocene and its derivatives have been drawn much attention owing to their tremendous BR catalytic activity, broad range of BR adjustment and

easy structural modification, though they are associated with migration problems which researchers are trying to overcome in various ways.

1.6.2. Ferrocene based HTPB-PU

There are few ferrocene based BRCs, those are well known to have potential industrial application such as N-butylferrocene, tert-butylferrocene and 2,2′-bis (ethylferrocenyl) propane (catocene) but witnessing migration problems.[79] Researchers are constantly trying to address these issues and there are main two directions researchers have been focusing: one is to synthesize ferrocene-containing polymers and the other one is the modification of the side group of the cyclopentadienyl (Cp) rings. A numerous number of ferrocene containing polymers synthesized either *via* addition polymerization or condensation or else ring opening to living/ controlled polymerization technique and were applied in various field whereas a very few of these polymers has been used as a BRC in composite solid propellants (CSP).[80–82] Apart from ferrocene containing polymers many other ferrocene derivatives has been extensively explored and verified to improve their anti-migration properties. A number of methodology established so far to modify the side groups of a ferrocene derivative such as (1) increase in the carbon chain of the side groups to increase in van der Waals interactions among molecules (2) introduction of polar groups in the moiety to increase the polarity of the ferrocene derivatives (3) introduction of suitable active groups that can react with other substances present in a propellant formulation and help in forming cross-linked networks further (4) incorporation of other inorganic groups to achieve integrated BRCs.[83–85] Generally, in a CSP, a ferrocene containing BRC is physically mixed with polymeric binder HTPB, metal powder, oxidant and along with other additional agents and causes serious unavoidable problems like agglomeration, sublimations. To overcome these issues researchers started functionalizing HTPB backbone by covalently linked with suitable ferrocene derivatives.[86–88] French company SNPE developed Butacene,[89] a derivative of ferrosilicon namely, (4-ferrocenylbutyl)dimethylsilane grafted onto vinylic position of HTPB *via* hydrosilylation reaction and it has been observed that the propellants formulated with butacene exhibit good processibility with higher-energetic performance having extended ranges of burn rates.[90]

Other than butacene some other ferrocene derivatives such as 2-(ferrocenylpropyl) dimethylsilane (FPDS), ferrocene (Fc) have been successfully grafted onto the HTPB backbone;[88,91] polyvinylferrocene-*grafted*-HTPB (PVF-*g*-HTPB) has been synthesized via radical addition reaction by using AIBN as radical initiator at 75 °C [4].[92] But high viscous nature of these ferrocene based HTPB shows several drawbacks such as poor loading capacity, brittleness, and mechanical failure of the final CSPs.[68] So, we can see that binder modified with ferrocene based BRC have certain advantages as well disadvantages. Modification with ferrocene derivatives ensures the binder to act as a BRC, leading to reducing the consumption of BRC in the propellant formulations; contrarily, modifications are proven to hamper some of the original properties of the binders and thus, common BRC are still unable to be substituted by the ferrocene based HTPB binders.

Recently, our group has developed ferrocene-*grafted*-HTPB (Fe-HTPB), a binder cum BRC, without altering the crucial physical properties of pure HTPB and the burn rate of CSP made from Fe-HTPB was found to be enhanced by 125% than the CSP consist of pristine HTPB.[68] In a similar line, our objective is to replace HTPB completely from the propellant formulation with structurally modified HTPB by suitable functionality with unaltered requisite physical properties.

1.7. Ferrocenyl polymers *via* Controlled Radical Polymerization techniques

Current progresses in polymerization methods have conferred plentiful innovative possibilities to design polymer materials with tunable chemistry and composition allied with predetermined molecular weight and narrow dispersity values. As a consequences, well-defined polymers with specific microstructures inclusive of graft, block, gradient type copolymers designing become more facile.[93] The similar kind of efforts has been observed in case of ferrocenyl polymers also. In this context of constructing pendant ferrocenyl polymers as mentioned earlier, that there are several well-established methodology like free radical polymerization (FRP)[94], living anionic polymerization (LAP)[95], ring opening polymerization

(ROP)[96] but still controlled/ living radical polymerization (CRP) is most useful tool so far in this regard.

1.7.1. Controlled/ living radical polymerization (CRP)

Since nearly 50% of commercial polymers are formed by using FRP method, polymer synthesis *via* FRP technique are being employed enormously both in academics and industries.[97] But the higher reactivity of the propagating radicals with bimolecular termination and other side reactions yield higher molecular weight polymers and thus FRP technique is restrained in various application. Now, if we consider about LAP technique, though it is highly successful to deliver the polymers with well-controlled molar mass and distribution this method possesses very high sensitivity to impurities results quick chain termination and thus shows lesser viability than radical processes.[98] In fact, because of overall low yield, complicated operation set up, long duration reaction time related issues ROP technique is also not that much well-favoured polymerization methodology.[99] Consequently there remained an immense desire over the years to develop a novel methodology that should have efficacy to overpower the issues in this line and CRP technique has well-served the purpose. CRP let the researchers to synthesize polymers in a well-defined manner with controlled molar mass and narrow molecular weight distribution having unique architectures and functionalities. Atom transfer radical polymerization (ATRP)[100,101], reversible addition fragmentation chain transfer (RAFT) polymerization[19,102], and nitroxide mediated polymerization (NMP)[21] these are the three most widely used CRP techniques. Because of certain advantages over the other methods RAFT polymerization technique has emerged a most useful tool in recent years for synthesizing simple homopolymers to variety of complex macromolecular motifs like block, graft, multiblock, star, gradient, comb copolymers, hyperbranched, and many more (*Figure.1.6*).[103]

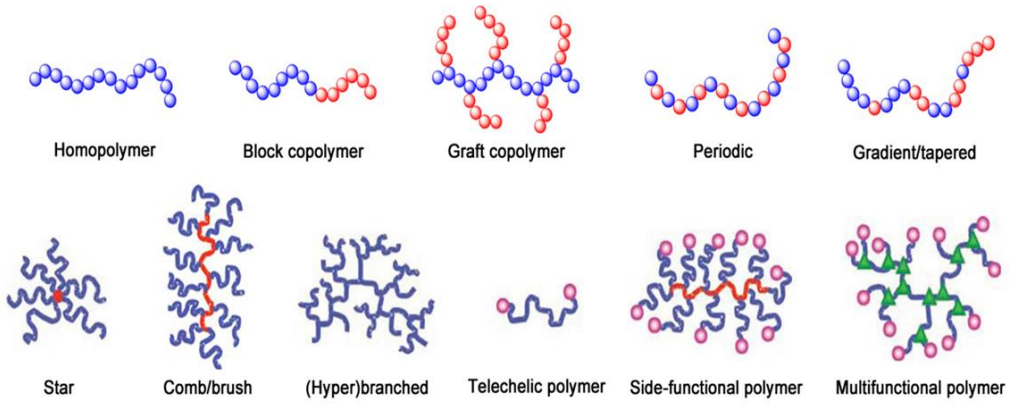

Figure 1.6: *Different macromolecular motifs obtained from RAFT polymerization method.*[103]

1.7.2. Reversible addition fragmentation chain transfer (RAFT) polymerization

The RAFT technique was first introduced at the Commonwealth Scientific and Industrial Research Organization (CSIRO) in 1998 and within a few years it turned out to be a most convenient and versatile methodology for designing living polymers with predetermined molecular weight having low polydispersity. RAFT process is associated with a fast dynamic equilibrium between dormant and active species to offer control in chain length in presence of an external agent known as CTA (chain transfer agent or RAFT agent). *Figure 1.7* represents the general form of CTA which drives the equilibrium between dormant and active species is so strongly towards dormant species that it persists with a lower concentration of propagating radicals and helps to maintain the livingness in the system by diminishing the proportion of unavoidable termination reactions .[13] The CTA which are used to direct RAFT polymerization is based on dithiocarboxylate moiety [-S-C(Z)=S] whereas R group helps to form free radical leaving group R• which must have the ability to reinitiate the polymerization, besides Z group controls the reactivity of C-S double bond and influences the rate of radical addition and fragmentation. A wide variety of CTAs with different R and Z functionality have been synthesized so far and their efficacy has been assessed based on controlling the polymerization process of various compatible vinyl monomers.[104]

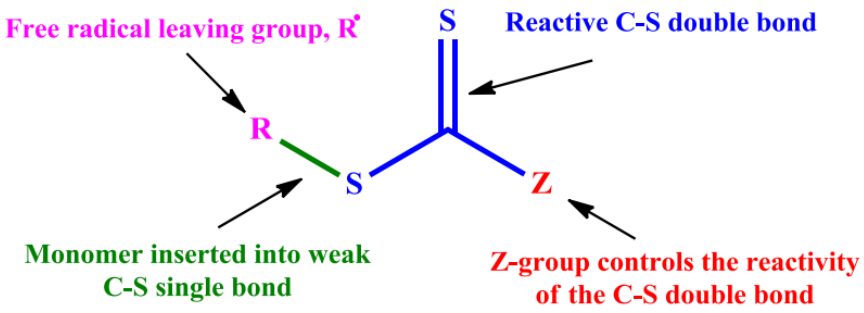

Figure 1.7: *General structure of a chain transfer agent (CTA) used in RAFT method.*

Unlike other conventional free radical polymerization techniques RAFT process is carried out under the similar reaction condition at which a classic free radical process is known to be performed except the addition of an external CTA and thus RAFT process can be conducted in bulk, solutions (aqueous or organic), emulsions, mini-microemulsions and suspensions and also in ionic liquids, even it can be performed at low temperatures.[104] If we see the RAFT mechanism that is presented in *Figure1.8*, a labile intermediate radical **2** is formed which helps to produce a temporarily deactivated dormant polymer species **3** along with a radical R• that involves in reinitiating the polymerization further. It is to be noted that the dithiocarboxylate functionality is present in both initial CTA 1 and dormant polymer chain **3** and hence the species **3** itself can act as a CTA (generally named as macro-CTA) further as shown in *Figure1.8.c.* To maintain the livingness few aspects are very crucial in RAFT process like (1) exchange reaction (*Figure1.8.c.*) should be quicker than the propagation step so that the radical Pn• or Pm• is exchanged rapidly among the growing chains and all chains will have equal probability to add monomer, and therefore all chains will grow at the same rate; (2) to achieve targeted molecular weight with narrow distribution all chains should start growing at the very starting point of the reaction and for that the exchange reaction between CTA **1** and dormant polymer chain **3** should be very fast (*Figure1.8.a.*), here the R group should be a better leaving group rather than being a oligomeric polymer chain; (3) R group should have the higher ability to reinitiate the polymerization otherwise if R• addition to monomer becomes slower than inhibition and retardation may occur that can be end up with broader molecular weight

distribution; (4) the initial concentration of the chains at the beginning of the polymerizations should be equal to that with the initial concentration of CTA so that a constant number of propagating chains are there throughout the reaction; (5) the initiator concentration need to be significantly lower than the CTA concentration to carry on the dithiocarboxylate moiety all along with the propagating polymer chains upto higher monomer conversion.

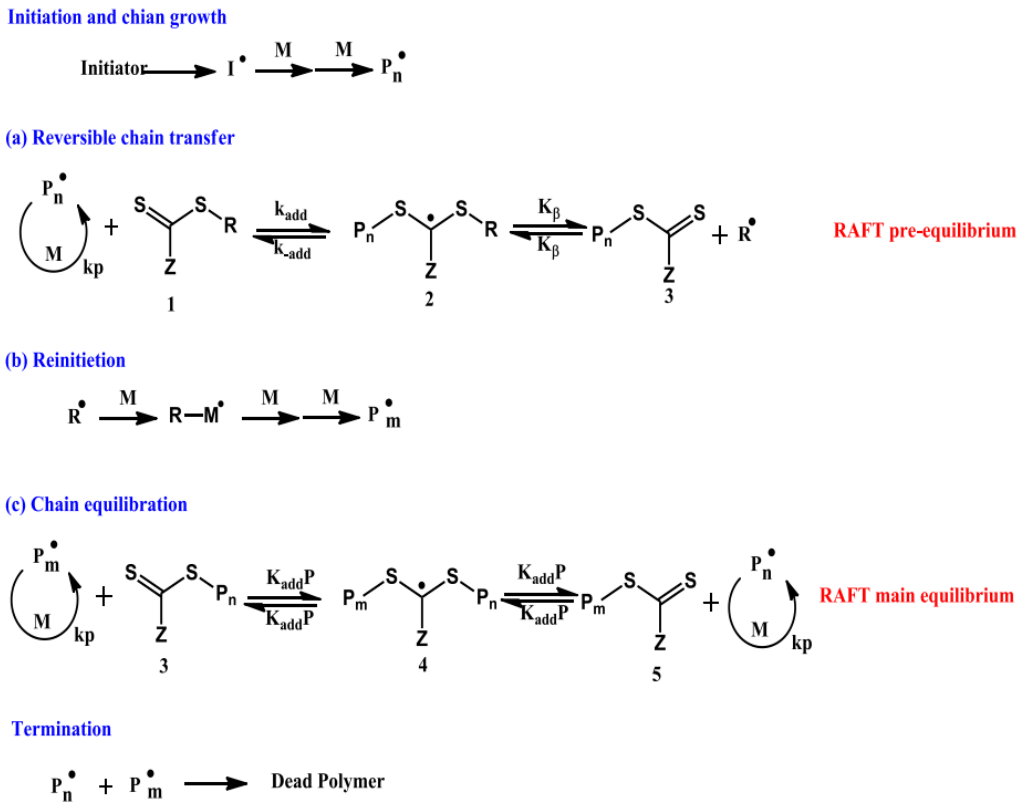

Figure 1.8: *Mechanism of RAFT polymerization method.*[103]

The main advantages of RAFT methodology lies in its versatility towards a wide range of different types of monomers that can be successfully polymerized like styrenic, (meth)acrylates, (meth)acrylamides, vinyl acetates, acrylonitrile, vinyl formamide, vinyl chlorides as well as an array of other vinyl monomers. Normally, more activated CTA is suitable for more activated monomers (MAM) and less activated CTA shows compatibility

towards less activated monomers (LAM). Recently, switchable CTA has been introduced to provide excellent control over both MAMs and LAMs.[105]

1.7.3. RAFT based Ferrocenyl polymers

RAFT polymerization become a very useful technique for synthesizing well-controlled pendant ferrocene containing homo- and copolymers. Earlier for a certain time interval it has been seen that the RAFT method had been specifically applied to a styrene derivative containing both aldehyde and ferrocene moiety[106], with the time being, ferrocene containing acrylates or methacrylates monomer were started being studied *via* RAFT method by selecting a most compatible CTA in every case.[106,107] Bressy et al. mentioned that the length of the alkoxy linker (in between ferrocene and polymerizable functionality) affects the rate of polymerization along with of the corresponding alikyl-ferrocene-methacrylic monomers.[108]

1.8. polyferroecene as redox responsive materials

Ferrocene containing polymers remains the most studied material among redox-responsive polymers with a broad range of applications ranging from biomedicine, batteries, biosensors, actuators, liquid crystals to other related field.[24,109–111] Markus Gallei in his report ascertained the fact that oxidation and reduction of poly(2-(methacryloyloxy)ethyl ferrocenecarboxylate) (PFcMA) chains are remarkably carried out repeatedly without any degradation in the polymer structure and hence these chains were immobilized at the surface.[112] Furthermore, they took their first step to make use of this redox-responsiveness of PFcMA towards a potential application and they employed these polymer chains to study the redox-responsive release of a dye from patchy nanocapsules previously formed in a self-assembly process.[113] End-functionalized polyvinylferrocene (PVFc) grafted on the silica nanoparticle surface has been explored to modulate the catalytic activity of surface attached Grubbs 2nd generation type catalysts for a norbornene monomer by Elbert et al.[114] In an another example, the redox-responsive switching property in terms of surface wettability for surface grafted PFcMA and PVFc polymers have been thoroughly studied where a considerable drop in water contact angle has been noticed for PFcMA and it is highly useful specially in

microfluidic applications.[115] Followingly, mesoporous silica nanoparticles modified with PFcMA chains have been utilized as a redox-responsive polymers to switch the ion-selective permeability *via* nanopores.[116] Therefore, ferrocenyl polymer is one of a versatile member of smart inorganic polymer owing to their redox responsive nature and a diverse range of novel applications make them to construct variety of functional smart materials in addition with many smart surfaces.

1.9. Smart nano surface

Smart materials or intelligent materials are those that can tune their physical properties in response to certain stimuli like temperature, moisture, pH, electric, stress, redox, magnetic field or chemical compounds (*Figure 1.9*).[117] Smart material markets are rapidly growing all over the world day to day and it can be sensed easily while many industries like pharmaceutical and healthcare, defence and aerospace, automotive, consumer electronics are expected to hold the most market share in forecast period. Smart materials might have a broad range of potential application as a self-healing polymers,[118] invisible ink,[119] thermoresponsive hydrogels,[120] switchable surfaces,[121] photoresponsive materials[122] etc., still vast amount of work is in progress for designing new smart materials and surface to enlarge their implementation in useful applications. Silica nanoparticle (SiNP) is one of the extensively used nano surface to be used as a smart surface after designing with suitable smart polymer.

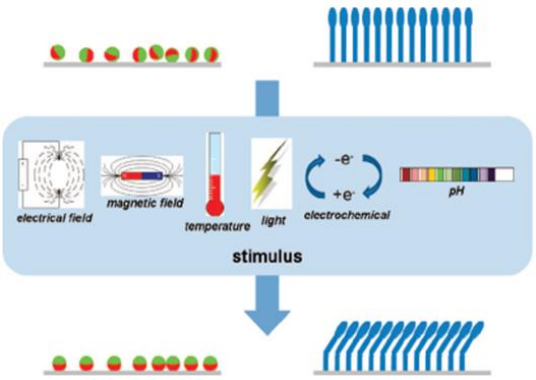

Figure 1.9: *Potential approaches towards designing of a smart material.*[117]

1.9.1. Silica nanoparticle as nano surface

Colloidal silica i.e. silicon dioxide nanoparticles generally are amorphous in nature and spherical in shape. Owing to their ease in synthesis and broad range in variation in size with great control, SiNPs are ascribed to be used extensively as a suitable nano surface in diverse fields. As a nanofiller SiNPs have been used in paint, rubber or in plastic industries; SiNP coated with many organic modifiers is highly useful as stationary chromatography phases, heterogeneous catalysts also in automotive, electronics, appliance, consumer goods, aerospace and sensor industries.[123–126] Irrespective of size, dried silica looks like a white powder; typically in their non-porous form SiNP is known for their utility as absorbent and abrasive whereas in mesoporous form it shows significant application in drug delivery and in nanomedicine. The surface chemistry of SiNP can be easily modified as per requirement by following well-documented surface modification procedure.

1.9.2. Surface functionalization of SiNP

Silica nanoparticle is a fascinating class of material for surface functionalization, it can impart chemical stability, mechanical stability, and biocompatibility to the polymer matrix, more over its surface functionalization techniques are well-established.[127] The fate of the SiNP are strongly influenced by its size as well as surface functionalization as because the surface properties can be considerably changed especially when particles are transferred into a biological system,[128] Normally, polymer matrix properties can be considerably increased by using SiNP as fillers and diminishing of agglomeration of the nanoparticles is a requisite condition to improve polymer nanocomposite properties. Non-grafted bare SiNP usually do not have favourable interactions in the matrix[130] and thus by modifying the nanoparticle surface with polymer chains the agglomeration can be avoided owing to their surface tension arises in between the polymer grafted particle which in turn helps to increase the dispersion of the particles *(Figure 1.10).*

1.9.3. Grafting methods

Polymer chains can be grafted on the surface by means of two ways (i) non-covalent attachment known as physisorption (ii) covalent attachment called as chemisorption. Physisorption has several drawbacks like desorption or weak linkage, here polymers can be

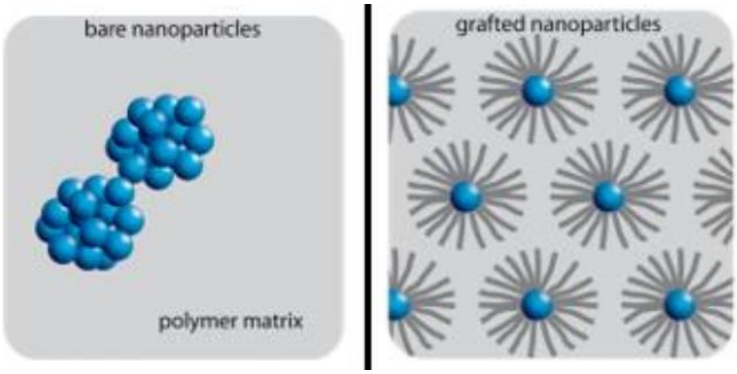

Figure 1.10: *Bare nanoparticles vs. polymer grafted nanoparticles in a polymer matrix.*[129]

detached by thorough washing. Whereas, in chemisorption attachment the polymer chains are covalently bonded with surface and thus very strong in nature and obviously much preferred than the former.[130] There are mainly three strategies for the covalent attachment of the polymer chains: *grafting to*, *grafting from* and *grafting through* (*Figure 1.11*).[130] In '*grafting to'* technique, a previously synthesized polymer is covalently attached with a reactive group end which is already located on the surface by following many well-established reaction method like azide-click[131], thiol-ene[33] and so on. Generally, '*grafting to'* do not results very high grafting density of polymer chains due to steric repulsion between them, with increasing polymer chain length the reaction between the end functionality of chains and the reactive group on the particle surface will be less feasible. One advantage of this technique is the non-grafted impurities can be simply removed by thorough washing and centrifugation. On the other hand, in '*grafting from'* technique, the polymerization is directly initiated from an initiator functionalized particle surface those are previously covalently linked to the surface. This approach is advantageous in terms of achieving nanoparticles with high grafting density of

polymer chains as here steric hindrances are avoided in comparison to previous approach.[132] The other approach i.e, '*grafting through*' strategy can be considered an intermediate approach between the two other techniques discussed above and it is established on performing the solution polymerization in presence of a functionalized surface which can be reactive during polymerization. Typically the vinyl units are attached to the particle surface here to obtain a macromonomer which can further react with the growing chain during polymerization and yield new grafts on the surface, anyhow this particular technique is the least studied among all.[130]

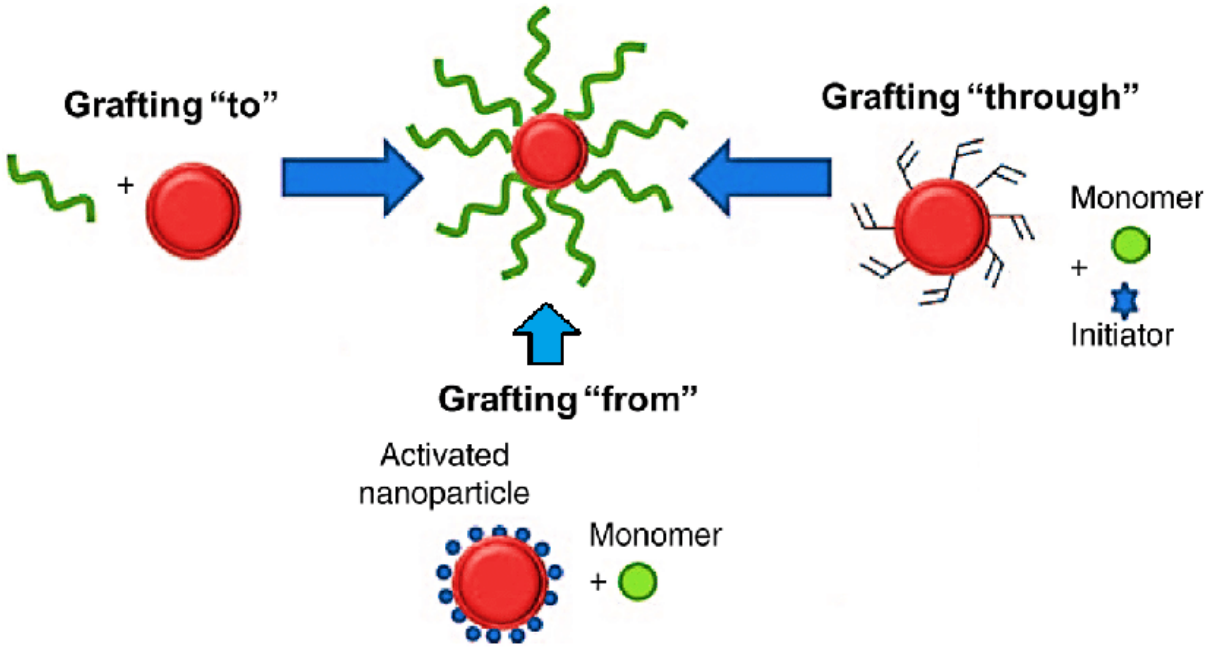

Figure 1.11: *Various technique of polymer attachment on the surface.*[133]

The morphology of the polymer grafted nanoparticles generally relies on grafting density. Higher graft densities basically features with lesser distance between the polymer chains and thus steric hindrance results polymer brush morphology with more extended chain conformations, contrarily, low graft densities allow the polymer chains to stretch back spatially towards the particle surface and attain different conformation like mushroom structure (*Figure 1.12*).[129] Hence, grafting density plays a very crucial role that affects matrix interactions.

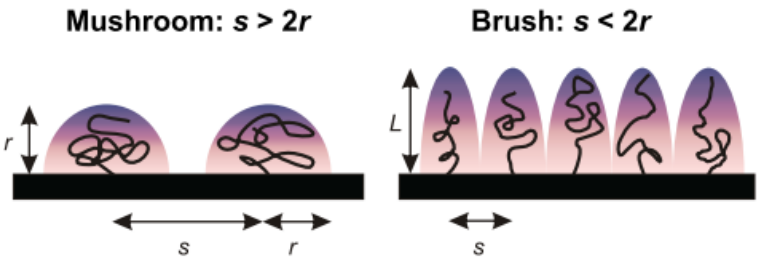

Figure 1.12: *Pictorial representation of mushrooms vs polymer brushes. The mushroom regime occurs when the distance between neighbouring chains (s) is greater than twice the radius of the polymer (r) and the brush regime is noticed when s <2r and the polymer chains are extended away from the surface at a height of L.*[134]

1.9.4. Surface functionalization *via* RAFT method

Surface functionalization *via* RAFT method is carried out by following *grafting from* strategy where the polymer chain growth occurs from the surface by using surface attached chain transfer agent (CTA) and hence it is also known as surface-initiated RAFT (SI-RAFT) polymerization technique. In general, SI-RAFT method have two approaches based on by which end CTA is attached to the surface namely (a) the R-group approach where CTA is attached through the leaving and reinitiating R group and (b) the Z-group approach where CTA is attached *via* the stabilizing Z end and both of these approaches have certain advantages also certain limitations too (*Figure 1.13*).[135]

In R-group approach, the solid support remains part of the leaving R group and the propagating radicals are located at the extreme end of the grafted chain. In this case higher molecular weight of grafted polymer with high grafting density can be achieved although molecular weight distribution can be broader because of possible chain coupling.[136] On the other hand in case with Z-group approach, the surface grafted backbone remains the part of Z-group and the polymeric radical is always propagating in solution before they get attached on to the surface bounded functionality, more similar to "grafting to" technique. Thus, this approaches involve with the linear radical chain formation with functional solid support and

results comparatively monomodal molecular weight distribution with better-defined grafted polymer chains but the grafting density is likely to decrease because of the shielding effect.[137] But the beneficial part of this approach is it involves with the production of true living polymer chains as they can be easily isolated from dead materials formed in the solution just by washing or filtration and results the formation of pure block copolymer synthesis compared to other living radical polymerization systems.

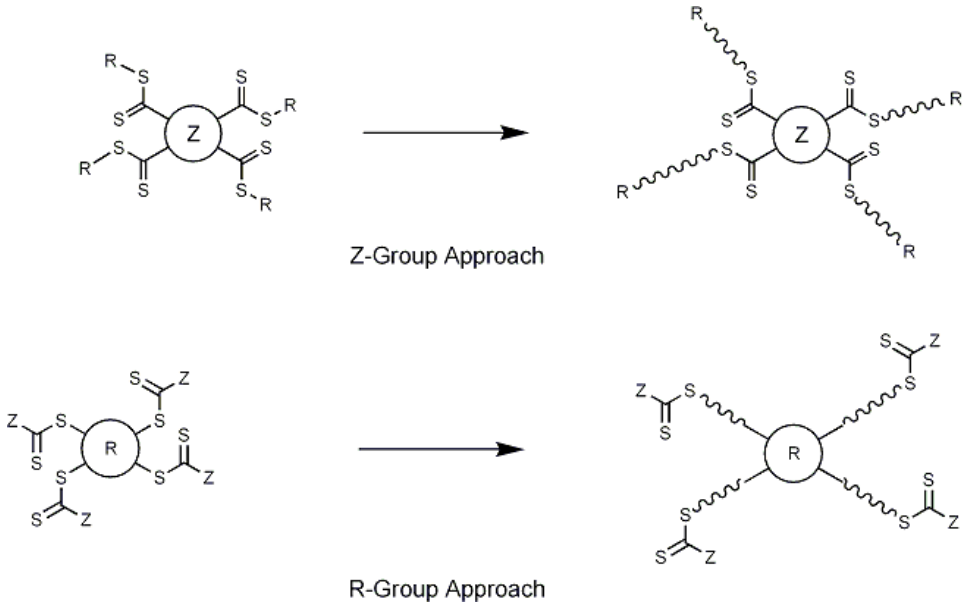

Figure 1.13: *R and Z-group approaches for SI- RAFT polymerization method.*[138]

1.9.5. Polyferrocene as smart polymer

By following any of the above mentioned methodology SiNP surfaces can be nicely functionalized with an appropriate candidate that can make particle surface a smart or intelligent surfaces and polyferrocene will be no doubt a worthy choice to be considered. Multiple pendant ferrocenyl polymer after getting crosslinked with glucose oxidase have shown oxidation activity which imparts electrical potential in presence of glucose, making them smart material as glucose biosensors[139], this is not only limited to glucose but many enzymes or other biomolecules too can be sensed. Polyferrocenylsilanes has been found to

exhibit smart self-assembly and self-disassembly on exposure to electrochemical potential; thin-film of a polystyrene-polyferrocenylsilane is able adsorb and release ferritin with the application of electric potential.[140,141] The various types of topoisomerase enzymes are known to perform a broad range of functions related to the maintenance of DNA topology during DNA replication and transcription and thus they become the targets of a number of antimicrobial and cancer chemotherapeutic agents. Selective targeting of any topoisomerase enzymes especially for cancer treatment is becoming a highly active area of basic and clinical research in recent times.[142] Few ferrocene derivatives have been found to act as a topoisomerase inhibitor and therefore designing a smart nano surface with polyferrocene undoubtedly can be a great interest for cancer-specific drug targeting.[143]

So, polymer functionalized SiNP can have their potential applications as per designing the polymer chains on the surface and now we will focus on the synthesis, properties and various applications of a hollow nano capsules with polymeric shell after removal of the template.

1.10. Hollow polymer nanocapsules (HPN)

Hollow polymer nanocapsules (HPN) are a fascinating class of compounds that are of notable interest for a wide range of application starting from high efficiency targeted therapeutics to ultra-accurate sensing devices.[144] HPNs can be defined as materials that comprised of covalently linked or disassembled polymer materials primarily contain a hollow void and thin polymer shell with an overall size range in nanoscale (1-1000 nm). Owing to the hollow nature of HPN, they feature remarkably high surface areas, are suitable for highly efficient loading and encapsulation and can be designed with diverse structural and functional motifs.

1.10.1. Synthesis of HPN

A number of synthetic protocols are there for synthesizing HPN, among all inorganic nanoparticle templating method is quite popular. Inorganic nanoparticles are a classic model

for constructing a myriad of polymer architectures on the particle surface in a convenient synthesis and processing methodology with tunable size.[145,146] In addition, the core removal is pretty straightforward with a cores like silica or many other metallic nanoparticles and can be easily etched out with hydrofluoric acid, hydrochloric acid or other acidic media. The basics for synthesizing HPNs from inorganic templating begin with a layer-by-layer grafting of polymers on the particle surface as shown in *Figure 1.14*. Moehwald and Kotov who established the ability to create discrete polymeric capsules using this methodology are known as one of the pioneer of this field.[147,148] This wok was further proceeded by Prucker and Rühe in the late 1990s who able to covalently graft polymers to nanoparticle substrate .[149] This work accompanied with the evolvement of controlled radical polymerizations, which naturally fuses these fields in the early 2000s with Pyun, Patten, Benicewicz, and others using ATRP and RAFT process on solid surfaces to grow well defined polymers.[136,150,151] One of the very first example to construct HPN by following inorganic templating was done by Blomberg and his fellow researchers by growing the chains first on particle surface *via* NMP followed by crosslinking the polymer chains and then etching out the core.[152] Simultaneously Kamata et al developed a gold nanoparticle based HPN where they have utilized ATRP as a polymerization technique to grow the polymer chains on the surface.[153] This field has outspread considerably since then, and we can see many significant development in recent times.

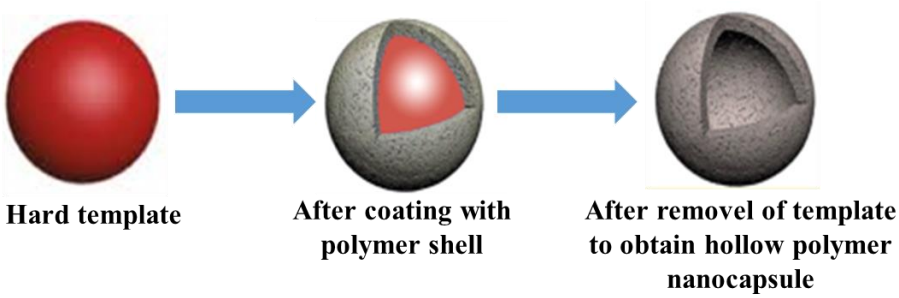

Figure 1.14: *Sketch for the synthesis of a HPN based on inorganic templating method.*[154]

1.10.2. Properties of HPN

HPNs possess a hollow interior and thus it features higher surface area compared to its solid core part. It is important to perceive the HPN properties associated with other materials like metal organic framework (MOF) or covalent organic framework (COF) or else porous materials which helps to acquire a wider perspective of these materials related field for further improvement and research. There are reports that COF and porous materials based HPNs which contains no inorganic component in the main structural unit, surface area are generally lesser than many MOF-based HPNs owing to their higher crystallinity as well as the presence of inorganic block clusters along with smaller organic linkers. It has been normally seen that HPNs hold surface are about ~150 to ~700 m^2/ g while this value ranges from ~1500 to ~2000 m^2/ g for COF based HPNs and it can goes up to even ~10, 000 m^2/ g in case of MOF based HPNs respectively.[155–157] Another significant property associated with a HPN formation is its loading capacity and it is highly crucial especially in drug delivery or energy storage application. Earlier polymeric dendrimers, vesicles were well- known polymeric micellar morphologies that can have a high loading capacity, afterwards with the development of HPNs, their hollow nature become most preferable materials that can deal with regulated higher to lower loading capacity as per requirement.[158–161] Swelling is one another important feature of a HPN and this swelling can be reversible based on the stimuli responsive functionality present in the polymer shell such as temperature, light or solvent conditions; controlled swelling and de-swelling of a HPN is highly favoured in drug delivery also for mechanical modulation in a number of materials.[162,163] Those HPNs that have been synthesized from sacrificial template method generally display an increase in size on chain swelling after removal of the template owing to their relief of tethered chain end.[164]

1.10.3. Application of HPN

HPNs with tunable size, functionality and higher storage capacity are excellent materials for biomedical, drug delivery and biomimetic applications. Owing to their hollow nature they are highly efficient to load with cargo, they can have tremendous opportunity to

create cell mimicking devices, apart from drug delivery these materials are becoming very crucial as storage device in energy and battery applications, these are an ideal candidates for next-generation gas separation membranes.[165–168] Because of highly tailorable surface functionalities, ease of functionalization and high surface area makes HPN a most promising material for catalysis and sensing applications.[169,170]

Redox-active polymer like ferrocenyl polymer based nanocapsules has wide application especially in case of controlled release of different payloads led by redox-chemistry of ferrocene as an external trigger. Apart from this, the various intrinsic properties like catalytic, magnetic, semi-conductive, photo-physical, optoelectronic etc. those are associated with ferrocenyl polymers can be aspired from a HPN comprised of ferrocenyl polymer. The whole thesis work is based on exploring ferrocene based polymers and hence a HPN with ferrocenyl copolymer shell has been designed and developed in **Chapter 6**. In that chapter, after successful HPN synthesis the hollow cavity is further used to encapsulate reactive aluminium nanoparticle inside it. This encapsulation technique helps ferrocenyl copolymer shell to act as a protective shield that can prevent the highly reactive aluminium nanoparticles from being accessed by the outside atmospheric oxygen.

1.10.4. Encapsulation inside the cavity of HPN

Encapsulation is an approach of stabilizing an active compounds in such a way that it is capable of preserving all their basic properties like chemical, physical and biological, besides their releasing process also can be tunes under desired condition.[171] In this technique of encapsulation, either one or mixture of active material is known to be coated with single or combination of materials. Generally the material that is being coated is named as active or core material whereas the other one is shell material also termed as carrier material. The shell can be in the form of either solid, liquid droplets or even gas bubbles and it can encapsulate liquid or gas or else solid inside as a core. After encapsulation the core-shell material can have variety of shapes like sphere, micro/ nanocapsules, multi/ monocore, microbeads, multishell and many more types and it is normally varied based on the application. The encapsulation techniques

can be broadly classified into two main categories, viz. chemical and physical encapsulations. Since past decade the nanoparticles encapsulated with polymeric shell in the order of a few to several tens of nanometers have aroused a significant interest as the integration of nanometer-scale components into the polymer matrix to develope the novel materials with their intrinsic properties including catalytic, optical, mechanical, thermal, magnetic or biological properties along with the unique features of organic polymer matrix like flexibility, durability, ductility, process ability and so on.[171]

Metal nanopowders have a broad range of physical and chemical properties which help themselves to be exploited in a wide variety of applications like a fuels for future energetic material formulations.[172] Owing to their inherent thermodynamic instability, the biggest task for synthesizing such metal nanoparticles is to stabilize kinetically their high surface area towards reactive atmospheric constituents. Encapsulation is a very useful technique to offer such stabilization to the metallic fuel in the form of a polymer nanocomposite that can effectively retain their high energy content as well as other beneficial properties with a good self-life. One of the renowned and simple methodology to passivate and protect reactive metal nanoparticles is to either graft presynthesized polymer chains to the nanoparticle surface or make use of the reactive nanoparticle surface to initiate and further propagate the polymer chains. After HPN formation, encapsulation of this kind reactive metal nanoparticles inside their cavity is yet to be explored and in our **Chapter 6** we have developed a novel method to do so.

1.11. Self-assembly of ferrocenyl polymers

Well-defined functional materials have drawn considerable attention from past decades due to having promising applicability in various field like biomedicine, optoelectronic, energy devices and so on.[173] The self-assembly of block copolymer (BCP) in solution has been remained an efficient tool to fabricate various nanomaterials including spherical, cylindrical or wormlike micelles and vesicles. In specific ferrocene based block copolymer (FcBCP) has been chosen to construct various functional micro/ nanomaterials due to their redox and electro-

chemical properties.[174] Self-assembly of ferrocene containing block copolymers have been found to be a beneficial way to achieve many complex morphology like hollow, sheet or patchy sphere simply by adjusting the concentration of the precursor material. Because of this exclusive proficiency ferrocene based copolymers becomes a unique constituents to form porous matrix with switchable surface triggered *via* redox-responsiveness, besides they may function as a highly efficient long-lasting drug delivery pump that is capable to release drugs upon employing electricity in biomedical application and hence, may be useful to make sure of maximal therapeutic effects.[175,176] In recent years, ferrocenyl polymer based porous multicompartment vesicles are believed to be a smart host to load and release guests

1.11.1. Multicompartment block copolymer micelles

Multicompartment block copolymer micelles (MCBMs) exemplify a notable step towards hierarchical self-assembly with miscellaneous functions and aforethought architectural features on a number of length scale having great possibilities for advanced nanotechnological applications.[177] Generally, an AB diblock copolymer in a selective solvent for A block mainly tend to adopt three classical morphology like spheres, cylinders or bilayers and accordingly developing spherical micelles, worm-like micelles and vesicles, respectively, contrarily the solvophobic B block normally forms a single nanoscale domain. In this scenario, if another solvophobic constituent C is incorporated in the system alike an ABC block terpolymer, then it is highly expected to have even more intricate structure subdivided with B and C core regions. The main aspect of forming MCBMs is the microphase separation within the solvophobic core domains in the micellar system and the discrete subdomains within the core can expedite concomitant storage and therapeutic delivery of a number of incompatible hydrophobic payloads.[177,178] Anyway, if these MCBMs are considered to store cargo with varying chemistry, those phase segregated core domains should have significant difference in their solubility. To design MCBMs, the crucial step is to choose B and C blocks in an ABC triblock copolymers (where A is solvophilic and B, C are the solvophobic blocks) those need to be sufficiently incompatible with each other so that they can readily form distinctly segregated domains. Typically, the balance between interfacial energy and chain conformation of the core

block and solvated corona favour to achieve universal diblock morphologies in a suitable solvent, but a term named "super strong segregation limit" (SSSL) proposed by Semenov, Khokhlov and his fellow researchers plays a dictating role to have many MCBMs.[179] The internal segregation between the two solvophobic blocks considerably uplifts the role of interfacial energy and can drive the system into the SSSL. In case of ABC triblock, the resulting morphology not only depends on the lengths of the three blocks and the difference in interfacial energy between B/ C or B / solvated A but also on the extent of the interfacial energy between C/ solvated A. If this later interfacial energy is too large, C block is expected to be cloistered in the micelle interior while micellar interior will be comprised of B chains if B/ solvated A interfacial energy becomes much larger despite the fact that there must be some B units at the interface of solvated A. Therefore, ABC and BAC triblocks with equal composition should be expected to adopt different morphologies. In this circumstances, linear terpolymers will intend to form core-shell-corona micelles with concentric structure having separate A/ B and B/ C interfaces which will drive to produce a restricted class of MCBMs. On the contrary, ABC if remains as a miktoarm star architecture, restrains the formation of core-shell-corona structures rather the three domains will meet along a curve in space where the competition between the three interfacial energies and the block length can lead to have a peculiarly rich array of MCBMs for a single polymer system. Researchers have developed so far a number of strategies for producing MCBMs and it has been seen that each strategies yields different kind of morphologies based on their spatial restrictions imposed by the triblock copolymer chain architecture as shown in *Figure 1.15*. Zhang and coworkers successfully synthesized porous multicompartment vesicles by employing highly incompatible solvophobic poly(4-vinylbenzyl ferrocenecarboxylate) (PVFC) and poly(benzyl methacrylate) (PBzMA) with a solvophilic poly[2-(dimethylamino) ethyl methacrylate] (PDMAEMA) block *via* RAFT mediated polymerization-induced self-assembly (PISA) process where the pores can be on-off switched triggered through redox responsiveness which is mainly governed by PVFC blocks.[180] As yet ferrocene containing porous MCBMs have been limited to ABC type terpolymers, but we have explored a new strategy to develop ferrocenyl diblock copolymer based porous MCBMs upon

imparting crystallization driven self-assembly (CDSA) technique which is described in **Chapter 7**.

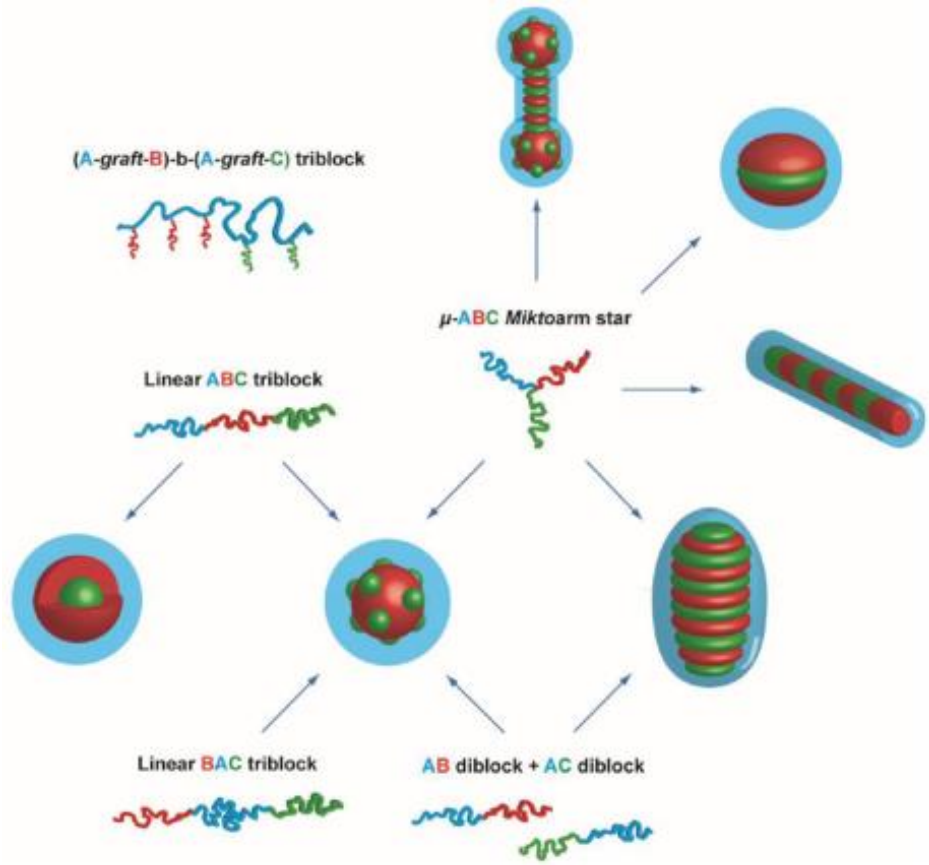

Figure 1.15: *A schematic representation of five principal strategies for producing multicompartment micellar morphology.*[177]

1.11.2. Crystallization driven self-assembly

Usually, block copolymer (BCP) self-assembly is acquired *via* direct dissolution, solvent-switch or else thin film hydration method.[181] In spite of these methods, it is very challenging to regulate the organization of anisotropic structure which are generally associated with multi-step processes, tough to scale up and end up in low concentration BCP solutions. To figure out these issues, crystallization-driven self-assembly (CDSA) has evolved as an

influential alternatives. CDSA employs BCPs having a semi-crystalline core-forming block to produce anisotropic 1D or 2D assemblies with high precision where BCP core crystallization is the driving force for the self-assembly process.[182] Having said that amorphous BCPs generally assembles into spheres, worms, and vesicles, whereas crystalline BCPs will typically evolve as a morphologies with low curvature like 2D platelate lamellae or 1D nano rods those are successfully introduce anisotropy in the system.[183] In the process of CDSA, typically the insoluble block is crystallized by solubilizing the polymer in a chosen solvent to induce crystallization *via* heat-cool process. The consequences of crystallization in the self-assembly of a BCP in solution was first evaluated by Lotz and Keller et al. in their studies of poly (styrene-*b*-ethylene oxide) (PS-*b*-PEO) in PS selective solvents like ethylbenzene and xylene which are poor solvent for crystallisable core PEO in the mid-1960s and has drawn lot of research consideration over the past decade.[184] They achieved thin square-shaped lamellar platelets which was further studied thoroughly by several groups. In 2000, Winnik and Manners et al. inspected a solution self-assembly of ferrocene containing BCPs with a crystallizable core forming polyferrocenyldimethylsilane (PFS) block and successfully achieved either cylindrical micelles or platelet nanoassemblies based on the ratio of crystallizable core to amorphous corona-forming block.[185] It has been seen that in the category of ferrocene containing BCPs, the CDSA study are restricted so far mainly on main-chain based ferrocenyl polymers, one of the suitable reason can be that main-chain ferrocenyl polymer architecture can easily adopt semi-crystallinity than that of a pendant ferrocenyl polymers. But upon imparting heat-cool process as in a CDSA technique how pendant ferrocenyl polymers behave can be a good objective to explore which we have carried out and described in our **Chapter 7**.

1.12. Aims and objectives of the thesis

Generally, ferrocene, a precursor to iron nanoparticles and their numerous derivatives as such have no wide ranging commercial application but have a heap of immensely significant amenities which helps to exploit many anomalous structures (ligand scaffolds, pharmaceutical entities), robustness (precursors to materials, anti-knock formulations) and redox activity (redox standards and various reagents). So, there are enormous possibility to build a pathway

for ferrocene based materials towards commercialization and this inspire me to work on ferrocene based polymer for my thesis. The research demonstrated in this thesis mainly comprises of the synthesis, characterization and application of ferrocene based homopolymers as well as copolymers. In this introductory chapter, initially a brief description of ferrocene based metallopolymers, their history and basic properties have been discussed followed by step by step evolvement of ferrocene containing polymers and then specifically highlighted the various aspects of pendant ferrocenyl polymers as a metallo polyurethane and also as various synthetic polymeric architecture including BCPs using RAFT polymerization. The use of the ferrocenyl polymers in the form of a hollow nanocapsule and redox-responsive smart polymer for the possible applications on BRC or redox active material have been documented. At the end, the basis of various ferrocenyl polymer based complex morphologies has been outlined from different self-assembly technique which opens up several possibilities to play with morphological aspects of pendant ferrocenyl polymers.

In an early work[68] a ferroecene containing HTPB based binder-cum-BRC (Fe-HTPB) has been developed without varying the deciding physical parameters of pristine HTPB by following terminal functionalization methodology established by our group. It has been noticed that ~125% of enhancement in burn rate for Fe-HTPB compared to HTPB with great control over the viscosity build-up as well as significantly improved mechanical properties for Fe-HTPBPU. In an another earlier report based on the polyvinylferrocene (PVF) grafting at the vinylic position of HTPB (PVF-g-HTPB)[92] as a binder-cum-BRC it was mentioned that chemically linked ferrocene in the binder augmented the propellant BR but the related viscosity or mechanical issues were not documented which are one of the main determining physical parameters to make them commercial binder. These facts directed us to study the viscosity and mechanical properties of PVF-g-HTPB materials where we end up with very high viscosity build-up and mechanical failure issues. These failures further motivated us to modify the HTPB backbone with an energetic functionality named 2,4-dinitrochlorobenzene (DNB) at the terminal position that is known to increase the segmental mixing in the PU matrix *via* supramolecular H-bonding[75], followed by PVF grafting at the vinylic position by following

radical pathway. Therefore, in **Chapter 3** we synthesized PVF-*g*-HTPB-DNB in addition with PVF-*g*-HTPB and varied the Fe content by varying different reaction condition to investigate the effect of altered Fe content on various important physical parameters specially viscosity, moreover we investigated in very detail that how presence of DNB at the terminal position regulate viscosity build-up in prepolymer together with the thermal, mechanical properties in PU form.

Among very few ferrocene based commercial product, Butacene, the ferrocenylsilane based HTPB developed by French company SNPE, is well known as a commercial binder-cum-BRC in the rocket propellant formulation. But it is unable to replace HTPB fully from the propellant formulation owing to its viscosity or else mechanical failure issues. Also this is the only ferrocenylsilane linked HTPB which is currently used in CSP, so search for ferrocene containing HTPB based binder-cum-BRC is still continuing with great effort and thus in **Chapter 4** we have explored 2-ferrocenyl(propyl)dimethylsilane grafted HTPB (FPDS-g-HTPB) and compared with FPDS-g-HTPB-DNB like previously carried out in **Chapter 3** to inspect how terminally functionalized DNB can govern the viscosity build-up as well as various physical properties.

Chapter 5 mainly deals with the synthesis and characterization of well-defined ferrocenyl polymer grafted SiNP *via* SI-RAFT technique. Our target is to construct a smart nano surface to be selectively used as a topoisomerase inhibitor for cancer treatment. Hence in **Chapter 5** we have selected 2-(methcryloyloxy)ethyl ferrocenecarboxylate (FcMA) as a monomer and performed SI-RAFT polymerization to graft the polymer chains on the silica nanoparticle surface. The redox-responsiveness of the chains has been verified while the catalytic activity on topoisomerase II is under trial now.

After successful grafting of the ferrocenyl polymer on the silica nanoparticle surface we have proceeded further to make use of the hollow cavity formed after removal of the silica template. **Chapter 6** is based on the polymer nanocomposite synthesis comprising of aluminium nanoparticle and hollow polymer nanocapsule (Al-NP/ HPN) where the Al-NP was

synthesized *in-situ* with a reaction of lithium aluminium hydride and silicon tetrachloride in presence of ferrocenyl copolymer based HPN by targeting a dual functioning framework as a fuel-cum-BRC in CSP.

Generally main-chain based ferrocenyl block copolymers are well known for their various intricate morphologies achieved *via* crystallization driven self-assembly (CDSA) contrarily pendant ferrocenyl polymers are limited to very common micellar morphologies like spherical, vesicle, worms, cylindrical etc. normally obtained by employing conventional solution self-assembly techniques. In our last working chapter, we have explored various complicated porous multicompartment micellar morphologies of pendant ferrocenyl block copolymers after employing the heat-cool process as seen in CDSA technique. On this account **Chapter 7** demonstrates the synthesis and characterization of a number of different chain length of pendant ferrocenyl homopolymers and block copolymers. After successful achievement on forming porous multicompartment micelles predominantly multicompartment vesicles, their morphological tuning based on redox-responsiveness of ferrocenyl block has been thoroughly analysed and it can be hoped to device a smart host that can capable to release multiple payloads together. More detailed discussion of each working chapter has been described in the introductory part of each chapter.

References

[1] I. Manners, *Adv. Organomet. Chem.* **1995**, *37*, 131–165.

[2] I. Kaya, M. Yildirim, *J. Appl. Polym. Sci.* **2008**, *110*, 539–549.

[3] Y. Wang, D. Astruc, A. S. Abd-El-Aziz, *Chem. Soc. Rev.* **2019**, *48*, 558–636.

[4] B. Baytekin, H. T. Baytekin, C. A. Schalley, *Org. Biomol. Chem.* **2006**, *4*, 2825.

[5] M. Raşa, U. S. Schubert, *Soft Matter* **2006**, *2*, 561–572.

[6] Y. Liu, Z. Wang, X. Zhang, *Chem. Soc. Rev.* **2012**, *41*, 5922.

[7] I. Langmuir, *Science* **1921**, *54*, 59–67.

[8] T. J. KEALY, P. L. PAUSON, *Nature* **1951**, *168*, 1039–1040.

[9] S. A. Miller, J. A. Tebboth, J. F. Tremaine, *J. Chem. Soc.* **1952**, 632.

[10] G. Wilkinson, M. Rosenblum, M. C. Whiting, R. B. Woodward, *J. Am. Chem. Soc*. **1952**, *74*, 2125–2126.

[11] M. Rosenblum, *Chemistry of the Iron Group Metallocenes*, *Part 1*, **1965**.

[12] E. S. Philips, *Ferrocenes: Compounds, Properties and Applications*, **2011**.

[13] C. G. Hardy, L. Ren, J. Zhang, C. Tang, *Isr. J. Chem.* **2012**, *52*, 230–245.

[14] R. J. Cremlyn, L. Wu, **1984**, *2115*, 367–368.

[15] D. A. Foucher, B. Z. Tang, I. Manners, *J. Am. Chem. Soc.* **1992**, *114*, 6246–6248.

[16] K. J. Watson, J. Zhu, S. T. Nguyen, C. A. Mirkin, *J. Am. Chem. Soc.* **1999**, *121*, 462–463.

[17] M. Gallei, B. V. K. J. Schmidt, R. Klein, M. Rehahn, *Macromol. Rapid Commun.* **2009**, *30*, 1463–1469.

[18] N. Hadjichristidis, M. Pitsikalis, S. Pispas, H. Iatrou, *Chem. Rev.* **2001**, *101*, 3747–3792.

[19] J. Chiefari, Y. K. Chong, F. Ercole, J. Krstina, J. Jeffery, T. P. T. Le, R. T. A. Mayadunne, G. F. Meijs, C. L. Moad, G. Moad, E. Rizzardo, S. H. Thang, *Macromolecules* **1998**, *31*, 5559–5562.

[20] K. Matyjaszewski, J. Xia, *Chem. Rev.* **2001**, *101*, 2921–2990.

[21] C. J. Hawker, A. W. Bosman, E. Harth, *Chem. Rev.* **2001**, *101*, 3661–3688.

[22] P. Novák, K. Müller, K. S. V. Santhanam, O. Haas, *Chem. Rev.* **1997**, *97*, 207–282.

[23] T. Kawai, C. Iwakura, H. Yoneyama, *Electrochim. Acta* **1989**, *34*, 1357–1361.

[24] R. Gracia, D. Mecerreyes, *Polym. Chem.* **2013**, *4*, 2206-2214.

[25] G. P. Kittlesen, H. S. White, M. S. Wrighton, *J. Am. Chem. Soc.* **1985**, *107*, 7373–7380.

[26] H. Nishihara, M. Noguchi, K. Aramaki, *J. Chem. Soc. Chem. Commun.* **1987**, 628-629.

[27] P. Calvo-Marzal, M. P. Delaney, J. T. Auletta, T. Pan, N. M. Perri, L. M. Weiland, D. H. Waldeck, W. W. Clark, T. Y. Meyer, *ACS Macro Lett.* **2012**, *1*, 204–208.

[28] D. Scheid, G. Cherkashinin, E. Ionescu, M. Gallei, *Langmuir* **2014**, *30*, 1204–1209.

[29] K. Wang, G.-F. Luo, Y. Liu, C. Li, S.-X. Cheng, R.-X. Zhuo, X.-Z. Zhang, *Polym. Chem.* **2012**, *3*, 1084-1090.

[30] M. Li, Z. Tang, H. Sun, J. Ding, W. Song, X. Chen, *Polym. Chem.* **2013**, *4*, 1199–1207.

[31] H. Zhang, L. Peng, Y. Xin, Q. Yan, J. Yuan, *Macromol. Symp.* **2013**, *329*, 66–69.

[32] N. L. Abbott, G. M. Whitesides, *Langmuir* **1994**, *10*, 1493–1497.

[33] I. Martínez-Montero, S. Bruña, A. M. González-Vadillo, I. Cuadrado, *Macromolecules* **2014**, *47*, 1301–1315.

[34] R. Pietschnig, *Chem. Soc. Rev.* **2016**, *45*, 5216–5231.

[35] D. Correia-Ledo, A. A. Arnold, J. Mauzeroll, *J. Am. Chem. Soc.* **2010**, *132*, 15120–

15123.

[36] M. Dhara, N. Giri, B. Narasimha Rao, A. K. Patra, P. U. Sastry, M. S. Ingole, T. Jana, *Eur. Polym. J.* **2020**, *122*, 109380.

[37] L. Q. Xu, D. Wan, H. F. Gong, K.-G. Neoh, E.-T. Kang, G. D. Fu, *Langmuir* **2010**, *26*, 15376–15382.

[38] M. Zamora, S. Bruña, B. Alonso, I. Cuadrado, *Macromolecules* **2011**, *44*, 7994–8007.

[39] T. V. Thang, C. Cougnon, *J. Electroanal. Chem.* **2011**, *657*, 79–83.

[40] S. A. Merchant, M. T. Meredith, T. O. Tran, D. B. Brunski, M. B. Johnson, D. T. Glatzhofer, D. W. Schmidtke, *J. Phys. Chem. C* **2010**, *114*, 11627–11634.

[41] G. V. Dubacheva, A. Van Der Heyden, P. Dumy, O. Kaftan, R. Auzély-Velty, L. Coche-Guerente, P. Labbé, *Langmuir* **2010**, *26*, 13976–13986.

[42] J. C. Eloi, L. Chabanne, G. R. Whittell, I. Manners, *Mater. Today* **2008**, *11*, 28–36.

[43] I. Manners, *Science* **2001**, *294*, 1664–1666.

[44] A. S. Abd-El-Aziz, *Macromol. Rapid Commun.* **2002**, *23*, 995–1031.

[45] B. J. Holliday, T. M. Swager, *Chem. Commun.* **2005**, 23-36.

[46] W.-Y. Wong, *Dalt. Trans.* **2007**, 4495-4510.

[47] B. Lucio, J. L. De La Fuente, M. L. Cerrada, *Macromol. Chem. Phys.* **2015**, *216*, 2048–2060.

[48] G. Georgoussis, A. Kanapitsas, P. Pissis, Y. V. Savelyev, V. Y. Veselov, E. G. Privalko, *Eur. Polym. J.* **2000**, *36*, 1113–1126.

[49] N. Chantarasiri, T. Damrongkosit, W. Jangwong, D. Sridaeng, S. Suebphan, *Eur. Polym. J.* **2004**, *40*, 1867–1874.

[50] R. J. Ayakumar, S. N. Anjundan, *Polym. J.* **2003**, *35*,734–739.

[51] R. Arun Prasath, P. Vijayanand, S. Nanjundan, *Polym. Int.* **2000**, *49*, 1464–1472.

[52] S. C. Tenhaeff, D. R. Tyler, *Organometallics* **1991**, *10*, 1116–1123.

[53] M. E. Wright, C. K. Lowe-Ma, *Inorganica Chim. Acta* **1995**, *232*, 223–226.

[54] A. A. Caraculacu, S. Coseri, *Prog. Polym. Sci.* **2001**, *26*, 799–851.

[55] H. M. Clearfield, D. K. Shaffer, S. L. Vandoren, J. S. Ahearn, *J. Adhes.* **1989**, *29*, 81–102.

[56] Y. Okamoto, P. T. Klemarczyk, *J. Adhes.* **1993**, *40*, 81–91.

[57] A. Demharter, *Cryogenics* **1998**, *38*, 113–117.

[58] A. A. Abdel Hakim, M. Nassar, A. Emam, M. Sultan, *Mater. Chem. Phys.* **2011**, *129*, 301–307.

[59] C. L. Mooney, P. Schwartz, *Text. Res. J.* **1985**, *55*, 449–452.

[60] L. Johnson, J. Samms, *J. Coat. Fabr.* **1997**, *27*, 48–62.

[61] J. T. Koberstein, L. M. Leung, *Macromolecules* **1992**, *25*, 6205–6213.

[62] I. Yilgor, E. Yilgor, *Polym. Rev.* **2007**, *47*, 487–510.

[63] I. Yilgör, E. Yilgör, G. L. Wilkes, *Polymer* **2015**, *58*, A1–A36.

[64] C. H. Y. Chen-Tsai, E. L. Thomas, W. J. MacKnight, N. S. Schneider, *Polymer* **1986**,

27, 659–666.

[65] M. Xu, W. J. MacKnight, C. H. Y. Chen-Tsai, E. L. Thomas, *Polymer* **1987**, *28*, 2183–2189.

[66] Q. Zhou, S. Jie, B.-G. Li, *Polymer* **2015**, *67*, 208–215.

[67] J. Chen, Z. Lu, G. Pan, Y. Qi, J. Yi, H. Bai, *Chinese J. Polym. Sci.* **2010**, *28*, 715–720.

[68] B. N. Rao, K. Malkappa, N. Kumar, T. Jana, *Polymer* **2019**, *163*, 162–170.

[69] R. M. Sankar, T. K. Roy, T. Jana, *Bull. Mater. Sci.* **2011**, *34*, 745–754.

[70] R. M. Sankar, S. Saha, K. S. Meera, T. Jana, *Bull. Mater. Sci.* **2009**, *32*, 507–514.

[71] B. K. Sikder, T. Jana, *ACS Omega* **2018**, *3*, 3004–3013.

[72] B. N. Rao, P. U. Sastry, T. Jana, *Eur. Polym. J.* **2019**, *115*, 201–211.

[73] K. R. Kunduru, B. N. Rao, T. Jana, *Macromol. Symp.* **2018**, *382*, 1–6.

[74] B. N. Rao, P. J. P. Yadav, K. Malkappa, T. Jana, P. U. Sastry, *Polymer* **2015**, *77*, 323–333.

[75] K. Malkappa, T. Jana, *Ind. Eng. Chem. Res.* **2013**, *52*, 12887–12896.

[76] R. M. Shankar, T. K. Roy, T. Jana, *J. Appl. Polym. Sci.* **2009**, *114*, 732–741.

[77] M. Dhara, N. Giri, A. Dutta, A. K. Patra, P. U. Sastry, M. S. Ingole, T. Jana, *Polymer* **2020**, *204*, 122807.

[78] A. Whitmore, *Extreme Rocketry*, **2008**, 40–41.

[79] W. Zhou, L. Wang, H. Yu, R. Tong, Q. Chen, J. Wang, X. Yang, Zain-ul-Abdin, M.

Saleem, *Appl. Organomet. Chem.* **2016**, *30*, 796–805.

[80] J. Kong, T. Schmalz, G. Motz, A. H. E. Müller, *Macromolecules* **2011**, *44*, 1280–1291.

[81] F. Xiao, X. Yu, F. Feng, X. Sun, X. Wu, Y. Luo, *J. Inorg. Organomet. Polym. Mater.* **2013**, *23*, 315–324.

[82] R. Sun, L. Wang, H. Yu, Zain-ul-Abdin, Y. Chen, H. Khalid, N. Abbasi, M. Akram, *J. Inorg. Organomet. Polym. Mater.* **2014**, *24*, 1063–1069.

[83] G. Z. L. Qiu, H. Sheng, *Chem. Propell. Polym. Mater.* **2012**, *10*, 1.

[84] M. Shamsipur, S. M. Pourmortazavi, A. A. M. Beigi, R. Heydari, M. Khatibi, *AAPS PharmSciTech* **2013**, *14*, 287–293.

[85] J. Liu, Z.-L. Liu, J. Cheng, D. Fang, *J. Solid State Chem.* **2013**, *200*, 43–48.

[86] P. J. Swarts, M. Immelman, G. J. Lamprecht, S. E. Greyling, J. C. Swarts, *South African J. Chem.* **1997**, *50*, 208–216.

[87] S. Ahn, Y. S. Song, B. R. Yoo, I. N. Jung, *Organometallics* **2000**, *19*, 2777–2780.

[88] D. Saravanakumar, N. Sengottuvelan, V. Narayanan, M. Kandaswamy, T. L. Varghese, *J. Appl. Polym. Sci.* **2011**, *119*, 2517–2524.

[89] B. H. G. Fonblanc, in *30th AIAA/ASME/SAUASEE Jt. Propuls. Conf. Indianap.*, **1994**, p. 3194.

[90] G. Doriath, *J. Propuls. Power* **1995**, *11*, 870–882.

[91] B.-S. Cho, S.-T. Noh, *J. Appl. Polym. Sci.* **2011**, *121*, 3560–3568.

[92] K. Subramanian, *J. Polym. Sci. Part A Polym. Chem.* **1999**, *37*, 4090–4099.

[93] A. A. Gridnev, S. D. Ittel, *Chem. Rev.* **2001**, *101*, 3611–3660.

[94] J. C. Lai, T. Rounsfell, C. U. Pittman, *J. Polym. Sci. Part A-1 Polym. Chem.* **1971**, *9*, 651–662.

[95] F. S. Arimoto, A. C. Haven, *J. Am. Chem. Soc.* **1955**, *77*, 6295–6297.

[96] Y. Ni, I. Manners, J. B. Sheridan, R. T. Oakley, *J. Chem. Educ.* **1998**, *75*, 766.

[97] K. Matyjaszewski and K., Ed. Matyjaszewski, *ACS Symposium Series: 854; American Chemical Society: Washington, DC,* **2003**, pp. 2–9.

[98] M. Szwarc, M. Levy, R. Milkovich, *J. Am. Chem. Soc.* **1956**, *78*, 2656–2657.

[99] Y. Hu, W. A. Daoud, K. K. L. Cheuk, C. S. K. Lin, *Materials* **2016**, *9*, 133.

[100] J.-S. Wang, K. Matyjaszewski, *J. Am. Chem. Soc.* **1995**, *117*, 5614–5615.

[101] M. Kato, M. Kamigaito, M. Sawamoto, T. Higashimura, *Macromolecules* **1995**, *28*, 1721–1723.

[102] S. Perrier, *Macromolecules* **2017**, *50*, 7433–7447.

[103] G. Moad, Y. K. Chong, A. Postma, E. Rizzardo, S. H. Thang, *Polymer* **2005**, *46*, 8458–8468.

[104] G. Moad, E. Rizzardo, S. H. Thang, *Polymer* **2008**, *49*, 1079–1131.

[105] G. Moad, D. Keddie, C. Guerrero-Sanchez, E. Rizzardo, S. H. Thang, *Macromol. Symp.* **2015**, *350*, 34–42.

[106] Z.-P. Xiao, Z.-H. Cai, H. Liang, J. Lu, *J. Mater. Chem.* **2010**, *20*, 8375.

[107] C. Herfurth, D. Voll, J. Buller, J. Weiss, C. Barner-Kowollik, A. Laschewsky, *J. Polym. Sci. Part A Polym. Chem.* **2012**, *50*, 108–118.

[108] R. W. Nguema Edzang, M. Lejars, H. Brisset, J. M. Raimundo, C. Bressy, *RSC Adv.* **2015**, *5*, 77019–77026.

[109] H. Wang, X. Wang, M. A. Winnik, I. Manners, *J. Am. Chem. Soc.* **2008**, *130*, 12921–12930.

[110] M. F. R. Fouda, M. M. Abd-Elzaher, R. A. Abdelsamaia, A. A. Labib, *Appl. Organomet. Chem.* **2007**, *21*, 613–625.

[111] M. Nakahata, Y. Takashima, H. Yamaguchi, A. Harada, *Nat. Commun.* **2011**, *2*, 511.

[112] M. Gallei, *Macromol. Chem. Phys.* **2014**, *215*, 699–704.

[113] R. H. Staff, M. Gallei, M. Mazurowski, M. Rehahn, R. Berger, K. Landfester, D. Crespy, *ACS Nano* **2012**, *6*, 9042–9049.

[114] J. Elbert, J. Mersini, N. Vilbrandt, C. Lederle, M. Kraska, M. Gallei, B. Stühn, H. Plenio, M. Rehahn, *Macromolecules* **2013**, *46*, 4255–4267.

[115] J. Elbert, M. Gallei, C. Rüttiger, A. Brunsen, H. Didzoleit, B. Stühn, M. Rehahn, *Organometallics* **2013**, *32*, 5873–5878.

[116] J. Elbert, F. Krohm, C. Rüttiger, S. Kienle, H. Didzoleit, B. N. Balzer, T. Hugel, B. Stühn, M. Gallei, A. Brunsen, *Adv. Funct. Mater.* **2014**, *24*, 1591–1601.

[117] M. Yoshida, J. Lahann, *ACS Nano* **2008**, *2*, 1101–1107.

[118] S. R. White, N. R. Sottos, P. H. Geubelle, J. S. Moore, M. R. Kessler, S. R. Sriram, E. N. Brown, S. Viswanathan, *Nature* **2001**, *409*, 794–797.

[119] D. Schurig, J. J. Mock, B. J. Justice, S. A. Cummer, J. B. Pendry, A. F. Starr, D. R. Smith, *Science* **2006**, *314*, 977–980.

[120] J. Yang, M. Yamato, C. Kohno, A. Nishimoto, H. Sekine, F. Fukai, T. Okano, *Biomaterials* **2005**, *26*, 6415–6422.

[121] J. Lahann, R. Langer, *MRS Bull.* **2005**, *30*, 185–188.

[122] A. Lendlein, H. Jiang, O. Jünger, R. Langer, *Nature* **2005**, *434*, 879–882.

[123] Y. Wei, L. Fan, L. Chen, *Fenxi Huaxue* **1997**, *25*, 1046–1047.

[124] J. P. Mathew, M. Srinivasan, *Polym. Int.* **1992**, *29*, 179–184.

[125] C. M. Stafford, A. Y. Fadeev, T. P. Russell, T. J. McCarthy, *Langmuir* **2001**, *17*, 6547–6552.

[126] M. García, W. E. van Zyl, M. G. J. ten Cate, J. W. Stouwdam, H. Verweij, M. S. Pimplapure, G. Weickert, *Ind. Eng. Chem. Res.* **2003**, *42*, 3750–3757.

[127] C. Graf, Q. Gao, I. Schütz, C. N. Noufele, W. Ruan, U. Posselt, E. Korotianskiy, D. Nordmeyer, F. Rancan, S. Hadam, A. Vogt, J. Lademann, V. Haucke, E. Rühl, *Langmuir* **2012**, *28*, 7598–7613.

[128] W. J. Stark, *Angew. Chemie Int. Ed.* **2011**, *50*, 1242–1258.

[129] Al-ali, M. A. *Doctoral dissertation*, **2020**, https://scholarcommons.sc.edu/etd/6088

[130] E. Lizundia, E. Meaurio, J. L. Vilas, *Grafting of Cellulose Nanocrystals, Chapter 3*, **2016**, 61-113.

[131] B. Helms, J. L. Mynar, C. J. Hawker, J. M. J. Fréchet, *J. Am. Chem. Soc.* **2004**, *126*, 15020–15021.

[132] R. Barbey, L. Lavanant, D. Paripovic, N. Schüwer, C. Sugnaux, S. Tugulu, H.-A. Klok, *Chem. Rev.* **2009**, *109*, 5437–5527.

[133] M. Darwish, A. Mohammadi, *Nanotechnology in Environmental Science*, **2018**, 315-350.

[134] N. Backmann, N. Kappeler, T. Braun, F. Huber, H. P. Lang, C. Gerber, R. Y. H. Lim, *Beilstein J. Nanotechnol.* **2010**, *1*, 3–13.

[135] Y. Zhao, S. Perrier, *Macromolecules* **2006**, *39*, 8603–8608.

[136] C. Li, J. Han, C. Y. Ryu, B. C. Benicewicz, *Macromolecules* **2006**, *39*, 3175–3183.

[137] X. Hao, C. Nilsson, M. Jesberger, M. H. Stenzel, E. Malmström, T. P. Davis, E. Östmark, C. Barner-Kowollik, *J. Polym. Sci. Part A Polym. Chem.* **2004**, *42*, 5877–5890.

[138] M. H. Stenzel, T. P. Davis, *J. Polym. Sci. Part A Polym. Chem.* **2002**, *40*, 4498–4512.

[139] H. Deng, W. Shen, Z. Gao, *Sensors Actuators B Chem.* **2012**, *168*, 238–242.

[140] J.-C. Eloi, S. E. W. Jones, V. Poór, M. Okuda, J. Gwyther, W. Schwarzacher, *Adv. Funct. Mater.* **2012**, *22*, 3273–3278.

[141] R. L. N. Hailes, A. M. Oliver, J. Gwyther, G. R. Whittell, I. Manners, *Chem. Soc. Rev.* **2016**, *45*, 5358–5407.

[142] K. E. Hevener, T. A. Verstak, K. E. Lutat, D. L. Riggsbee, J. W. Mooney, *Acta Pharm. Sin. B* **2018**, *8*, 844–861.

[143] Y. N. Vashisht Gopal, D. Jayaraju, A. K. Kondapi, *Arch. Biochem. Biophys.* **2000**, *376*, 229–235.

[144] K. C. Bentz, D. A. Savin, *Polym. Chem.* **2018**, *9*, 2059–2081.

[145] B. Radhakrishnan, R. Ranjan, W. J. Brittain, *Soft Matter* **2006**, *2*, 386-396.

[146] Y. Liu, J. Goebl, Y. Yin, *Chem. Soc. Rev.* **2013**, *42*, 2610–2653.

[147] Y. Lvov, G. Decher, H. Moehwald, *Langmuir* **1993**, *9*, 481–486.

[148] Z. Tang, Y. Wang, P. Podsiadlo, N. A. Kotov, *Adv. Mater.* **2006**, *18*, 3203–3224.

[149] O. Prucker, J. Rühe, *Macromolecules* **1998**, *31*, 602–613.

[150] T. von Werne, T. E. Patten, *J. Am. Chem. Soc.* **1999**, *121*, 7409–7410.

[151] J. Pyun, K. Matyjaszewski, *Chem. Mater.* **2001**, *13*, 3436–3448.

[152] S. Blomberg, S. Ostberg, E. Harth, A. W. Bosman, B. Van Horn, C. J. Hawker, *J. Polym. Sci. Part A Polym. Chem.* **2002**, *40*, 1309–1320.

[153] K. Kamata, Y. Lu, Y. Xia, *J. Am. Chem. Soc.* **2003**, *125*, 2384–2385.

[154] K. Zhong, K. Song, K. Clays, *Nanophotonics* **2018**, *7*, 693–713.

[155] H. Furukawa, K. E. Cordova, M. O'Keeffe, O. M. Yaghi, *Science* **2013**, *341*, 1230444.

[156] N. Huang, P. Wang, D. Jiang, *Nat. Rev. Mater.* **2016**, *1*, 16068.

[157] S. M. Cohen, *J. Am. Chem. Soc.* **2017**, *139*, 2855–2863.

[158] K. M. Huh, S. C. Lee, Y. W. Cho, J. Lee, J. H. Jeong, K. Park, *J. Control. Release* **2005**, *101*, 59–68.

[159] M. Saad, O. B. Garbuzenko, E. Ber, P. Chandna, J. J. Khandare, V. P. Pozharov, T. Minko, *J. Control. Release* **2008**, *130*, 107–114.

[160] U. Bazylińska, A. Lewińska, Ł. Lamch, K. A. Wilk, *Colloids Surfaces A Physicochem.*

Eng. Asp. **2014**, *442*, 42–49.

[161] H.-J. Zhang, J.-H. Wang, Y.-H. Zhang, T.-L. Hu, *J. Polym. Sci. Part A Polym. Chem.* **2017**, *55*, 1329–1337.

[162] D. J. Schmidt, F. Ç. Cebeci, Z. I. Kalcioglu, S. G. Wyman, C. Ortiz, K. J. Van Vliet, P. T. Hammond, *ACS Nano* **2009**, *3*, 2207–2216.

[163] A. Fernández-Nieves, A. Fernández-Barbero, B. Vincent, F. J. de las Nieves, *Macromolecules* **2000**, *33*, 2114–2118.

[164] K. C. Bentz, M. Ejaz, S. Arencibia, N. Sultan, S. M. Grayson, D. A. Savin, *Polym. Chem.* **2017**, *8*, 5129–5138.

[165] F. Caruso, D. Trau, H. Möhwald, R. Renneberg, *Langmuir* **2000**, *16*, 1485–1488.

[166] Y. Gogotsi, *ACS Nano* **2014**, *8*, 5369–5371.

[167] Q. Wei, F. Xiong, S. Tan, L. Huang, E. H. Lan, B. Dunn, L. Mai, *Adv. Mater.* **2017**, *29*, 1602300.

[168] J. Zhang, S.-H. Chai, Z.-A. Qiao, S. M. Mahurin, J. Chen, Y. Fang, S. Wan, K. Nelson, P. Zhang, S. Dai, *Angew. Chemie Int. Ed.* **2015**, *54*, 932–936.

[169] I. M. Henderson, H. A. Quintana, J. A. Martinez, W. F. Paxton, *Chem. Mater.* **2015**, *27*, 4808–4813.

[170] L. Pan, A. Chortos, G. Yu, Y. Wang, S. Isaacson, R. Allen, Y. Shi, R. Dauskardt, Z. Bao, *Nat. Commun.* **2014**, *5*, 3002.

[171] S. H. Sonawane, B. A. Bhanvase, M. Sivakumar, S. B. Potdar, *Current Overview of Encapsulation*, *Chapter 1*, **2020**, 1-8.

[172] W. Zeng, C. O. Nyapete, A. H. H. Benziger, P. A. Jelliss, S. W. Buckner, *Curr. Appl. Polym. Sci.* **2018**, *3*, 3–13.

[173] Z. Deng, H. Yu, L. Wang, X. Zhai, Y. Chen, S. Z. Vatsadze, *J. Organomet. Chem.* **2016**, *821*, 48–53.

[174] G. R. Whittell, I. Manners, *Adv. Mater.* **2007**, *19*, 3439–3468.

[175] K. Zhang, X. Feng, X. Sui, M. A. Hempenius, G. J. Vancso, *Angew. Chemie - Int. Ed.* **2014**, *53*, 13789–13793.

[176] M. Huo, J. Yuan, L. Tao, Y. Wei, *Polym. Chem.* **2014**, *5*, 1519–1528.

[177] A. O. Moughton, M. A. Hillmyer, T. P. Lodge, *Macromolecules* **2012**, *45*, 2–19.

[178] J.-F. Lutz, A. Laschewsky, *Macromol. Chem. Phys.* **2005**, *206*, 813–817.

[179] A. N. Semenov, I. A. Nyrkova, A. R. Khokhlov, *Macromolecules* **1995**, *28*, 7491–7500.

[180] P. Shi, Y. Qu, C. Liu, H. Khan, P. Sun, W. Zhang, *ACS Macro Lett.* **2016**, *5*, 88–93.

[181] A. Blanazs, A. J. Ryan, S. P. Armes, *Macromolecules* **2012**, *45*, 5099–5107.

[182] P. J. Hurst, A. M. Rakowski, J. P. Patterson, *Nat. Commun.* **2020**, *11*, 1–12.

[183] C. E. Boott, J. Gwyther, R. L. Harniman, D. W. Hayward, I. Manners, *Nat. Chem.* **2017**, *9*, 785–792.

[184] B. Lotz, A. J. Kovacs, G. A. Bassett, A. Keller, *Kolloid-Zeitschrift und Zeitschrift für Polym.* **1966**, *209*, 115–128.

[185] J. A. Massey, K. Temple, L. Cao, Y. Rharbi, J. Raez, M. A. Winnik, I. Manners, *J. Am. Chem. Soc.* **2000**, *122*, 11577–11584.

CHAPTER 2

Materials, Synthesis and Methods

This chapter illustrates the source of materials, experimental procedures and all the characterization techniques including the details of the related instruments used in Chapter 3 to 7.

2.1. Materials

The hydroxyl terminated polybutadiene (HTPB) was received as gift sample from Anabond Limited, India was dried at 60^{o} C under vacuum for 1 hour just before use in the reaction. HTPB has the following specification: molecular weight (VPO) ($\overline{M_n}$ = 2300-2900), polydispersity index(GPC) (Đ) is 1.9, viscosity at 30 °C is 5280 cP, and hydroxyl value is 40.08 mg KOH/g. 1-chloro-2,4-dinitrobenzene (DNCB, SRL India), ferrocene (Sigma Aldrich; 98%), aluminum chloride ($AlCl_3$, Merck, India), hexachloroplatinic acid (Sigma Aldrich; 99.9%), sodium hydride (NaH, Merck, India) sodium bi carbonate ($NaHCO_3$, Finar, India), magnesium sulfate ($MgSO_4$, Finar, India) isophoron diisocyanate (IPDI, Sigma Alridch), dibutyltin dilaurate (DBTDL, Sigma Alridch), aluminium chloride hexahydrate (Finar, India) and 3,4-dihydro-2H-pyran (Sigma Aldrich, India) were used without further purification. Also, tetraethylorthosilicate (TEOS, 99%), (3-Aminopropyl) triethoxysilane (APTES, 99%), 3-Mercaptopropionic acid (99%), benzylbromide (98%), 4-dimethylamino pyridine (DMAP) and 1,3-dicyclohexyl carbodiimide (DCC) were purchased from Sigma-Aldrich and used as received without any further purification. Ammonium hydroxide (NH_4OH, 28%), ethyl alcohol (EtOH, 99%), sodium carbonate (Na_2CO_3, 99%), sodium sulphate (Na_2SO_4 99%), cyclohexane (AR grade), ether (AR grade), N-Hydroxysuccinimide (NHS, 99.8%), dry dimethylformamide (DMF, AR grade) and HPLC water were purchased from Finar chemicals Ltd, India. Tetrabutylammonium bromide (98%) was purchased from TCI, India and used as it was. Allyl dimethyl chlorosilane (Sigma Aldrich, India) was distilled before use. 2, 2-azobis-isobutyronitrile (AIBN, Sigma Aldrich) was recrystallized from methanol. 4-vinylbenzyl chloride (90%), propargyl alcohol (99%) and 2-hydroxyethyl methacrylate (99%) were purchased from Sigma-Aldrich and used after purification by distillation. Vinyl ferrocene (VF) and ferrocene mono carboxylic acid (FcCOOH) were purchased from Nanjing Finetech Chemical, China. Tetrabutyl ammonium perchlorate (TBAP) was purchased from Across, India and used as it was. Hydrofluoric acid (HF, 48%) was purchased from Fischer chemicals, India. The solvents dichloromethane (DCM, AR grade), toluene, tetrahydrofuran (THF, AR grade), methanol (MeOH, AR grade), n-hexane, ethyl acetate were purchased from Finar

Limited, India. The solvents were distilled or dried according to standard procedures as per requirement. The high-performance liquid chromatography (HPLC) grade THF and DMF from Merck, India was used for gel permeable chromatography (GPC) experiments.

2.2. Synthesis

2.2.1. Synthesis of pre-polymer and polyurethane

2.2.1.1. Synthesis of HTPB-DNB

2,4-dinitrochlorobenzene (DNB) was attached at the terminal carbons of HTPB backbone by following terminal functionalization methodology established by our group [1] and briefly as follows: 4 g of moisture-free HTPB (0.767 mmol: calculation done as per molecular weight obtained from GPC analysis i.e. $\overline{M_n}$ = 5210) was completely solubilized in 10 mL of dry DCM at room temperature in presence of N_2 atmosphere. After 15 minutes of stirring 0.216 g of NaH (9 mmol) was added together with continuous N_2 gas purging and after another 45 minutes 0.176 g of DNB (0.86 mmol) was added. The reaction mixture was allowed to stir for next 24 hours and after completion it was diluted with excess DCM to filter out the unreacted NaH. The volume of the filtrate was reduced to a certain extent after evaporating the solvent by rotary evaporator and finally the product was purified after subsequent dissolution and precipitation for several times by using hexane as a solvent and methanol as a non-solvent, respectively. The resultant HTPB-DNB was brown in colour and it was further used in polyurethane synthesis step after vacuumed-dried for 12 hours at 60 °C.

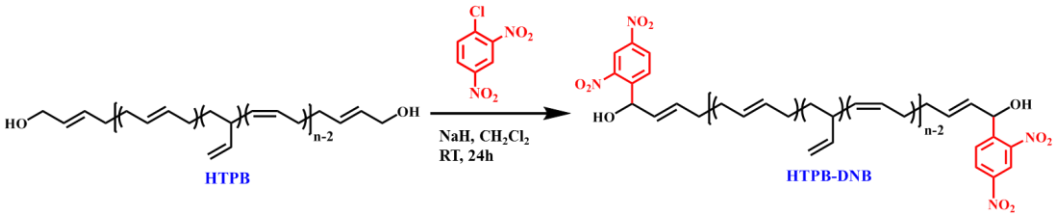

Scheme 2.1: *Synthesis of HTPB-DNB.*

2.2.1.2. Synthesis of HTPB-DNB-PU

The procedure was modified a bit from the reported literature.[2] 3 g of HTPB-DNB (0.536 mmol: calculated based on the $\overline{M_n}$ value which was 5600 obtained from GPC analysis) was dissolved in 20 mL of dry THF at inert atmosphere. After complete dissolution 0.169 g of isophorone diisocyanate (IPDI) (0.759 mmol: calculated from the HTPB-DNB hydroxyl value of 42.5 mg/ KOH and –NCO:-OH was taken as 1:1) was added and allowed to stir for next 30 minutes. After 30 minutes catalytic mount of DBTDL was added as a catalyst and left for stirring for another 3 hours at room temperature in presence of N_2 environment. The time required to complete the reaction was fixed from the disappearance of the isocyanate peak at 2270 cm^{-1} in FT-IR spectroscopy. A brown coloured viscous solution of PU was obtained at the end and it was further transferred into a flat-based petri dish pre-coated with silicone releasing agent and left for curing at 70 °C for next 5 days to get a free-standing flexible film.

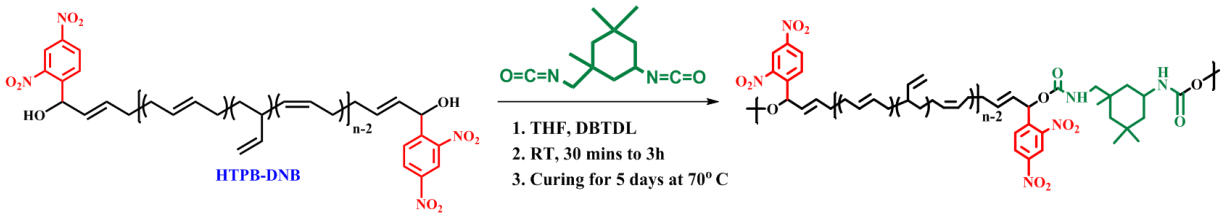

Scheme 2.2: *Synthesis of HTPB-DNB-PU.*

2.2.2. Synthesis of monomers

2.2.2.1. Synthesis of 2-(ferrocenylpropyl) dimethylsilane (FPDS)

The compound was prepared by following the reported literature.[3] At first the alkylation of ferrocene was performed with addition of ferrocene (10.45 g, 56.2 mmol) with allyl dimethyl chlorosilane (1.90 g, 14.1 mmol), and aluminum chloride (0.45 g, 1.41 mmol) in 100 mL of methylene chloride under argon atmosphere and then stirred for 1.5 at 0 °C to create 2-(ferrocenylpropyl)chloro dimethylsilane. The solvent was distilled off by a rotary evaporator. The remaining mixture was dissolved in dried THF and added drop wise to a suspension of lithium aluminum hydride in dried THF, then heated for 1h and hydrolyzed with

water. The organic layer was extracted with diethyl ether, and the extracts were washed with aqueous sodium bicarbonate, dried over anhydrous magnesium sulfate, and then filtered. The solvent was distilled off. ^{1}H-NMR (500MHz): δ 0.06 (6H, $Si(CH_3)_2$), 0.96(1H, $SiCH_aH_b$), 0.99(1H, $SiCH_aH_b$), 2.7(1H CHCp), 3.87-3.9 (1H, SiH), 4-4.4(9H, Cp). Yield: 45%

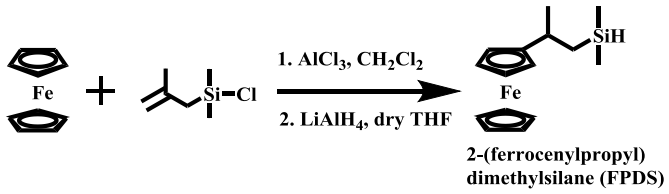

Scheme 2.3: *Synthesis of FPDS*

2.2.2.2. Synthesis of 2-(methacryloyloxy) ethyl ferrocenecarboxylate (FcMA)

The reaction procedure was followed from the published paper.[4] In a two neck round bottom flask, 1g (4.35 mmol) of ferrocene mono carboxylic acid (FCOOH) was added in 15 mL of dry DMF and DCM mixture (1:2) in inert atmosphere. After complete dissolution, catalytic amount of DMAP was added to the stirred solution of FCA at 0° C followed by the addition of 1.345g (6.52mmol) of DCC in three slots. After stirring half an hour the solution of HEMA (0.68g, 5.216mmol) in dry DCM was added drop-wise and stirred for 24 hours. The progress of reaction is monitored by TLC. After completion of reaction, the reaction mixture was extracted from ether with brine solution. This ether layer was collected & passed through anhydrous sodium sulphate. The crude product was obtained by solvent evaporation & dried. Column chromatography (hexane/ethyl acetate) was done to get the pure product.^{1}H NMR (500 MHz, $CDCl_3$): δ 2.00 (dd, 3H), 4.2 (s, 5H), 4.4 (d, 2H), 4.5 (m, 4H), 4.8 (d, 2H), 5.65 (dd, 1H), 6.15 (dd, 1H). HRMS-ESI $[M+H]^+$: calculated for $C_{17}H_{18}FeO_4$: 342.0547, found, 342.0546. Yield: 50%

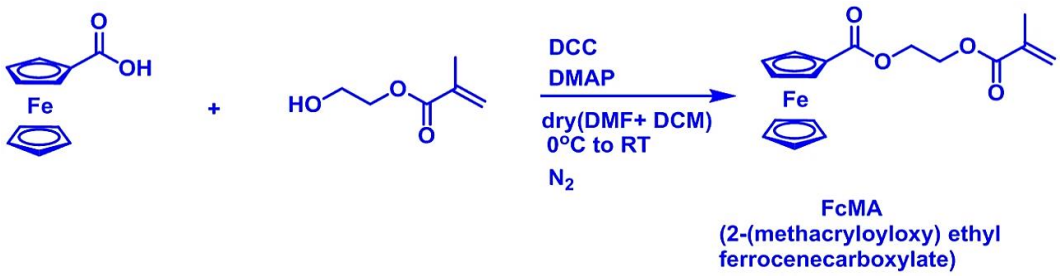

Scheme 2.4: *Synthetic scheme for FcMA.*

2.2.2.3. Synthesis of propargyl 4-vinylbenzyl ether (PVBE)

The experimental method was carried out by following a reported paper.[4] To a solution of propargyl alcohol (0.2 g, 3.56 mmol) in dry THF (5 mL) in inert atmosphere, sodium hydride (0.134 g, 5.56 mmol) was added at 0° C and the mixture was stirred for 15 min. After that, the reaction mixture was allow to come to room temperature and 4-vinylbenzyl chloride (0.544 g, 3.56 mmol) was added followed by the addition of tetrabutylammonium bromide (0.69 g, 2.14 mmol) and after that the reaction was continued to stir at room temperature for next 24 h. After 24h, methanol was added to quench the excess of sodium hydride followed by dichloromethane. The whole mixture was washed with water several times, and the organic phase was dried with Na_2SO4 and concentrated. The residue was purified by column chromatography (hexane/ethyl acetate). ^{1}H NMR (500 MHz, $CDCl_3$): δ 7.5−7.2 (m, 4H), 6.63 (dd, 1H), 5.78 (d, 1H), 5.30 (d, 1H), 4.65 (s, 2H), 4.20 (s, 2H), 2.51 (s, 1H). ^{13}C NMR ($CDCl_3$): δ 137.5, 137.1 (C−Ar), 136.7, 128.6, 126.5, 114.2, 79.8, 74.9, 71.5, 57.2. HRMS (ESI): calcd for: m/z $C_{12}H_{12}ONa$ $[M + Na]^+$, 195.0786; found, 195.0781. Yield: 59%

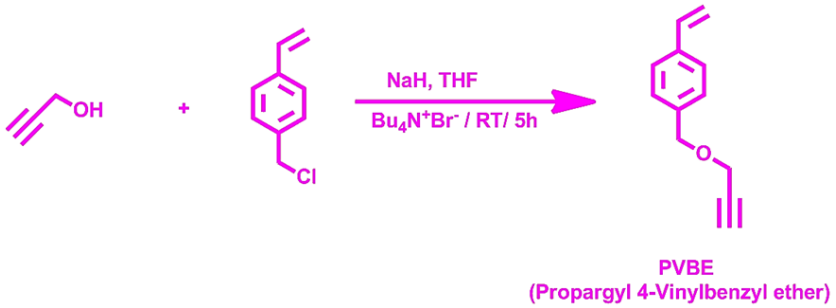

Scheme 2.5: *Synthetic scheme for PVBE.*

2.2.2.4. Synthesis of 1,4-bis(azidomethyl)benzene

The experimental process was carried out after modified the reported procedure.[5] 0.5 g of 1,4-bis(bromomethyl)benzene (1.89 mmol) was added to 10 mL of 0.5 (M) solution of NaN_3 in DMSO and stirred for 24 hours at room temperature in presence of nitrogen environment. Reaction progress was monitored via TLC checking and after completion of the reaction the mixture was quenched with excess water followed by the extraction with DCM. The organic phase was collected and passed through Na_2SO_4 and finally the product was obtained as a colourless liquid after removing the solvent. ^{1}H NMR (500 MHz, $CDCl_3$): δ = 7.37 (s, 4H), 4.38 (s, 4H). ^{13}C NMR ($CDCl_3$): δ = 135.9, 128.9, 54.7. HRMS (ESI): calcd for: m/z $C_8H_8N_6$ $[M + H]^+$, 188.08; found, 188.075. Yield: 53%

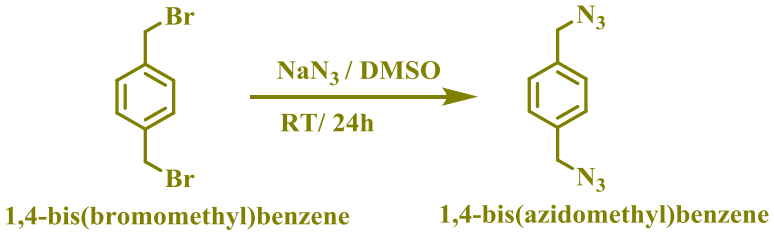

Scheme 2.6: *Synthesis of diazide derivative, 1,4-bis(azidomethyl)benzene.*

2.2.3. Synthesis of chain transfer agent (CTA)

2.2.3.1. Synthesis of 3-benzylsulfanylthiocarbonylsufanyl-propionic acid (BSPA)

The synthesis was done by following the published literature.[6] In a 250 ml RB flask, 3-Mercaptopropionic acid (5 mL, 5.75 mmol) was added to a stirred solution of potassium hydroxide solution (6.5 g, 11.5 mmol) in water (60 mL). Carbon disulfide (7.5 mL) was then added drop wise to the reaction solution which turned into an orange coloured solution. This was further allowed to stir for 5h at room temperature. After that benzylbromide (9.9 g, 5.75 mmol) was added into the reaction mixture and heated for another 12 h at 80 ºC. Then, after cooling down to room temperature, chloroform was added and the reaction mixture was acidified with 1(N) hydrochloric acid until the organic layer became yellow. After that, the water phase was extracted with chloroform several times. The obtained organic phase was dried over anhydrous Na_2SO_4 and solvent was evaporated in rotary evaporator. The product was purified by chromatography with a 3:1 hexane/ethyl acetate mixture as an eluent and separated as a yellow powder. ^{1}H-NMR ($CDCl_3$): 2.84 (t, 2H), 3.62 (t, 2H), 4.61 (s, 2H), 7.27 (m, 5H), 10.1 (b, 1H, OH). 13C-NMR (CDCl3): 30.7, 32.8, 41.4, 127.7, 128.6, 129.1, 134.6, 177.9, 222.5. ESI–MS (m/z) $[M + Na]^+$ calcd for $C_{11}H_{12}O_2S_3Na$: 295.0, Found: 295.0. Yield: 80%.

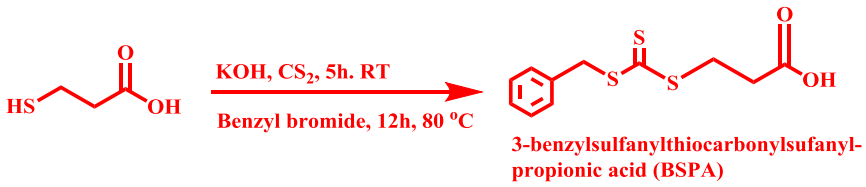

Scheme 2.7: *Synthesis of BSPA.*

2.2.3.2. Synthesis of 4-cyanopentanoic acid dithiobenzoate (CPDB)

The synthesis was performed by following the reported literature.[7] At first, dithiobenzoic acid (DTBA) was prepared with addition of sodium methoxide (30 % solution in methanol, 45 g, 250 mmol), elemental sulphur (8.0 g, 250 mmol), anhydrous methanol (62.5

g) and benzyl chloride (15.75 g, 125 mmol). The reaction mixture was stirred at 67 ºC for 10 h. Next, the reaction mixture was cooled to 7 °C using an ice bath and the organic layer was collected after removing the precipitated salt by filtration followed by solvent evaporation. The residue was dissolved in deionized water (130 mL) and further was acidified with 1.0 N HCl (125 mL) to extract with diethyl ether. Then, deionized water (75 mL) and 1 (N) of NaOH (150 mL) were added to transfer sodium dithiobenzoate to the aqueous phase. Furthermore, the sodium dithiobenzoate solution (87.5 mL) and potassium ferricianide (8.23 g, 25 mmol) were together mixed in deionized water (150 mL) under vigorous stirring and slowly the red colour precipitation started appearing which was filtered further and washed with deionized water until the filtrate become colourless. The deep red solid was properly dried in vacuum at room temperature overnight. After that, the solid residue (dithiobenzoyl disulphide; 2.13 g, 7 mmol) was dissolved in 40 mL of distilled ethyl acetate and 2.92 g of 4,4'-azobis(4-cyanopentanoic acid) (11.5 mmol) was added into it in instalment to perform the radical reaction for 18h at refluxing condition. Finally, a deep pink coloured product was collected after removing the solvent in vacuum and the crude product of 4-cyanopentanoic acid dithiobenzoate (CPDB) was isolated by column chromatography using ethyl acetate hexane (2:3) as eluent. At the end the resultant red oily residue was recrystallized from hexane and ethylacetate (2:3) mixture and a deep pink colour solid (78%) was obtained. ^{1}H-NMR ($CDCl_3$): 7.4 (dd, 1H), 7.41 (dd, 1H), 7.6 (m, 1H), 7.9 (d, 1H), 7.91 (d, 1H), 2.8 (t, 2H), 2.4 (t, 2H), 1.9 (s, 3H). Yield: 80%.

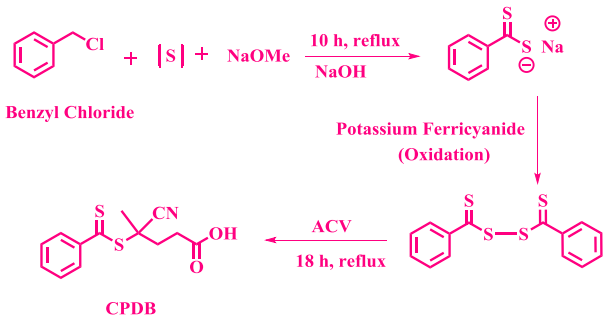

Scheme 2.8: *Synthesis of CPDB.*

2.2.4. Synthesis of CTA anchored silica nanoparticle

The stepwise attachment of CTA on the silica nanoparticle surface was carried out by following the reported method which is mentioned below.[8]

2.2.4.1. Synthesis of silica nanoparticle (SiNP)

Silica Nanoparticles were synthesized by the well-known Stöber process (*Scheme 2.9*). To a 1000 mL round bottomed flask ethanol (400 mL) were added followed by 10 mL of ammonium hydroxide at room temperature. After 10 mintues, HPLC water (10 mL) was added slowly into middle point of the stirring solution. Next, after another 10 minutes, under vigorous stirring, tetraethylorthosilicate (TEOS, 10 mL) was added drop by drop very carefully and the reaction solution was continued to stir at constant rate without any hampering for next 16 hours at room temperature. Just after completion of 16 hours, the formed colloidal solution of silica nanoparticles were collected using centrifugation at 10,000 rpm for 30 min. The particles were redispersed in ethanol and washed with HPLC water (3 times) to wash out the unreacted ammonium hydroxide by centrifugation at 10,000 rpm for 30 min. The pure silica nanoparticles were finally dried at 80 °C for 48 h.

2.2.4.2. Synthesis of amine modified silica nanoparticles (SiNP-NH_2)

The synthesized SiNP (3 g) were nicely dispersed in dry THF (50 mL) by using ultrasonication for 30 min and then 75 µL of (3-Aminopropyl) triethoxysilane (APTES, 0.0003 mol) was added drop wise under constant stirring refluxed for next 16 hours at at 85 ºC. The reaction mixture was then precipitated in hexane and the amine modified SiNP (SiNP-NH_2) were isolated by centrifugation at 7000 rpm for 15 min. The particles were redispersed in THF and centrifuged at 7000 rpm for 15 min; this process was repeated for three times. The obtained amine modified silica nanoparticles (SiNP-NH2) were dried under vacuum at 60 °C for 24 h (*Scheme 2.9*).

2.2.4.3. Synthesis of activated CTA (BSPA-NHS)

BSPA (0.6 g, 2.2 mmol) was dissolved in dry dichloromethane (30 mL) in presence of N2 at 0 °C; catalytic amount of DMAP and 0.664 g of DCC (3.22 mmol) was added and stirred. After 15 minutes of stirring, 0.322 g of N-hydroxysuccinamide (NHS, 2.78 mmol) was added and the stirring was continued for next 16 hours at room temperature nitrogen atmosphere in the dark condition. The volume of the solution was reduced by evaporating to some extent and insoluble product was filtered. The remaining solution was concentrated and was purified by using silica column chromatography in hexane/ethyl acetate using as an eluent. This activated CTA (BSPA) is abbreviated as BSPA-NHS (*Scheme 2.9*).

2.2.4.4. Synthesis of CTA anchored silica nanoparticles (SiNP-BSPA)

SiNP-NH2 (2 g) was nicely dispersed in dry THF (50 mL) in presence of nitrogen atmosphere. Activated BSPA (BSPA-NHS, 0.3 g, 1.1mmol) in 1 mL of dry THF was added drop wise into the solution while stirring, and the reaction mixture was stirred for next 16 h at room temperature in dark condition at inert atmosphere. Finally, the yellow coloured reaction mixture was precipitated from a mixture of cyclohexane and diethyl ether (4:1, 100 mL) and collected by using centrifugation at 3000 rpm for 10 min. This purification cycle was repeated three times and the collected CTA functionalized silica nanoparticles (SiNP-BSPA) was dried under vacuum at room temperature for 24 h. The whole process of SiNP-BSPA synthesis was shown in *Scheme 2.9*.

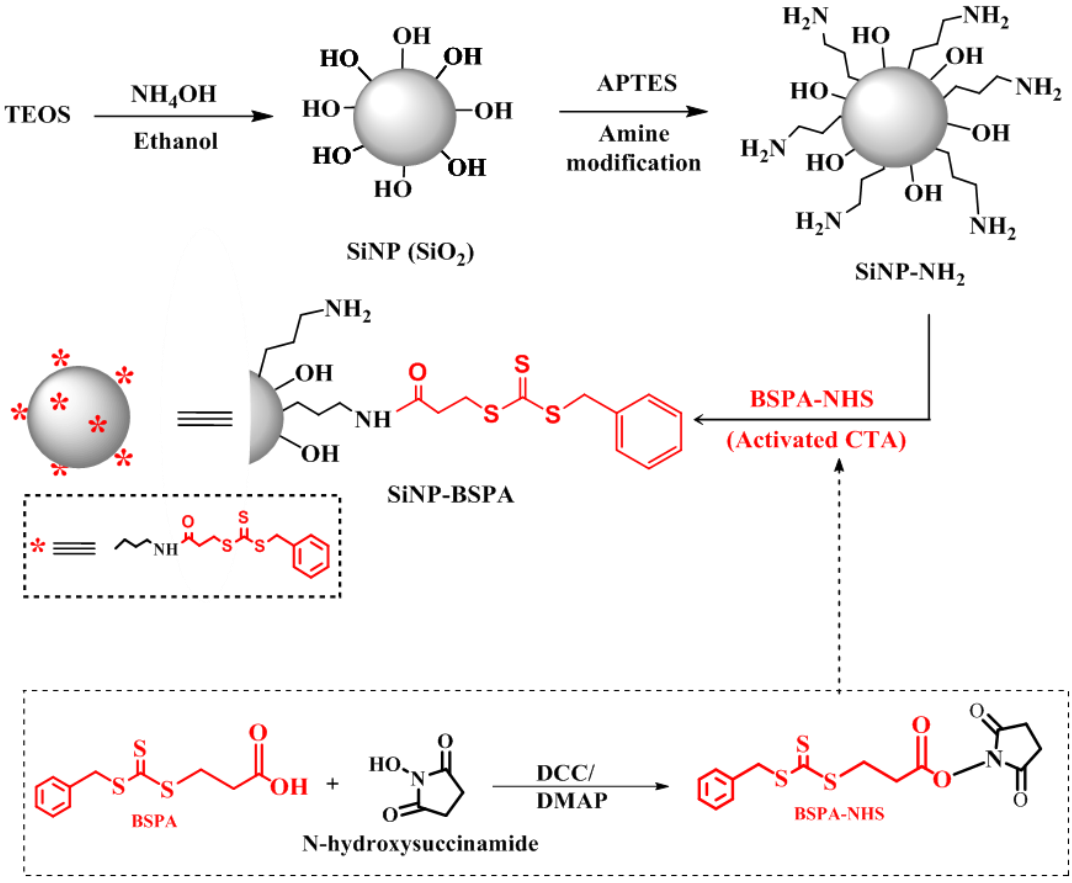

Scheme 2.9: *Synthesis of BSPA anchored SiNP (SiNP-BSPA).*

Similarly CPDB was also anchored on the silica surface to obtain SiNP-CPDB by following exactly similar procedure except using of CPDB as a CTA instead of BSPA in the above experimental procedure.

2.3. Methods

2.3.1. Spectroscopic studies

2.3.1.1. FT-IR study

Attenuated total reflection fourier transform infrared (ATR-FTIR) spectra of all the materials (irrespective of powder and liquid samples) were recorded using a Nicolet iS5 ATR-

FTIR (Thermo scientific, S-3, India) spectrometer in the range of 500 to 4000 cm^{-1} of wavelength with an average of 32 scans at a resolution of 0.5 cm^{-1}.

2.3.1.2. ^{1}H-NMR and ^{13}C-NMR study

The NMR spectra were recorded on Bruker AV 500 and 400 MHz NMR spectrometer by using $CDCl_3$ as a solvent and TMS as internal standard.

2.3.1.3. UV-visible study

Electronic absorption spectra were captured on Jasco V-750 spectrophotometer. The suitable solvents were selected as per solubility of the corresponding material which are mentioned in related chapters.

2.3.2. X-ray studies

2.3.2.1. Wide angle X-ray diffraction (WAXD)

The WAXD patterns of the film or powder materials were collected from an X-ray generator (model Bruker D8 X-ray powder diffractometer) with Cu Kα radiation (λ = 1.54 Å) source at voltage 40 kV and 30 mA current at a scanning rate of 0.6º/minute in the 2θ range of 5º- 85º.

2.3.2.2. Small angle X-ray scattering (SAXS)

The SAXS measurements were carried out using a Rigaku small angle goniometer mounted on rotating anode X-ray generator. Scattered X-ray intensity [I (Q)] was recorded using a scintillation counter with pulse height analyzer by varying the scattering angle 2q where Q is the scattering vector given by 4π.sin (θ)/λ and λ is the wavelength of incident Cu Kα X-rays (λ = 1.54 Å).

2.3.3. Microscopic studies

2.3.3.1. Field emission scanning electron microscope (FESEM)

The morphology of the polymer samples were studied is FESEM, Carl Zeiss Ultra-55 model using EHT detector at 5 kV voltage. The films were fractured after dipping into liquid nitrogen to keep the fracture side morphology intact. The cryo fractured side of the samples was placed vertically in the SEM sample holder and gold coated before imaging in FESEM. Contrarily, powdered samples were dispersed in a suitable solvent and drop casted on a glass plate, dried properly and finally gold coated before imaging.

2.3.3.2. Transmission electron microscope (TEM)

The polymer samples were prepared first, prior to TEM analysis by dispersing in a very diluted solution of suitable solvent followed by drop casting on carbon coated copper (200 mesh) grids and dried and then the images were captured using FEI (Technai Model No. 2083) TEM machine at an accelerating voltage of 200 kV.

2.3.3.3. Confocal laser scanning microscope (CLSM)

The morphology of the dye treated polymer samples were prepared by drop casting the samples on a glass plate, dried and then the images were snapped using Leica model ZEISS LSM 880 confocal laser scanning microscope (CLSM) with an Ar/Ar-Kr laser as the excitation (488 nm) source. The samples were stained with rhodamine dye for imaging which is and mentioned in **Chapter 6**.

2.3.3.4. Fluorescence lifetime imaging microscopic (FLIM)

Dye treated samples were subjected to FLIM study by using PicoQuant Microtime 200 Time-resolved confocal fluorescence microscope. Coumarin has been used as a dye for imaging mentioned in **Chapter 6**.

2.3.4. Thermal analysis

2.3.4.1. Thermogravimetric analysis (TGA)

TGA of all polymer samples were performed using TGA Q500, TA instruments, USA from 30 to 700 ^{0}C with a heating rate of 10 °C/min under constant nitrogen flow.

2.3.4.2. Differential scanning calorimetry (DSC)

Glass transition temperatures (Tg) of the PU films were measured using differential scanning calorimetry (DSC) on Mettler Toledo DSC with heating rate of 5^{o} C/min over a temperature range of -100^{o} C to 50^{o} C under constant nitrogen flow. The DSC instrument was calibrated with indium and zinc before scanning of the samples.

2.3.5. Mechanical properties

2.3.5.1. Universal testing measurement (UTM)

Mechanical properties were carried out using UTM (UTM, 5965-5 kN, Instron) at a constant strain rate of 1mm/min at room temperature. To get the stress-strain relationship for tensile strength measurements the film were cut into dumbbell-shape following ASTM standard D638 (Type IV specimen). The results were averaged from three specimens of each sample.

2.3.5.2. Dynamic mechanical analysis (DMA)

The thermo-mechanical properties of PU films having dimension 18mm x 5mm x 0.4 mm (L x W x T) were carried out using dynamic mechanical analyser (DMA, TA Instrument model Q-800). The samples were annealed at -100^{o} C for 5 min and then scanned from -100^{o} C to 200^{o} C at a heating rate of 3^{o} C/minute. The storage modulus (E'), loss modulus (E'') and tan δ values were measured as a function of temperature at a constant linear frequency of 1 Hz with a preload force of 0.01 N.

2.3.6. Gel permeable chromatography (GPC)

Molecular weights (M. W.) and polydispersity index (PDI) of synthesized polymers were analysed by GPC (Waters 515 HPLC) fitted with Waters 2414 refractive index detector using polystyrene standards at 30 °C at a flow rate of 0.4 mL/min. The solvents chosen as an eluent and were mentioned in each chapter separately. The polymer samples were prepared a day before and kept overnight and filtered 0.5 µm PTFE filter paper before injecting the sample solution.

2.3.7. Dynamic light scattering (DLS) study

The hydrodynamic radius of each particle was measured using a Zetasizer Nano S90 (Malvern Instruments, Germany) operating at 4mW He-Ne laser with 633nm wavelength at

room temperature. The samples were nicely dispersed after sonication for at least half an hour before measurement.

2.3.8. Viscosity measurement

Viscosity measurement of all the samples were carried out in rotoviscometer (Rheolab QC-180, Anton Paar) with the measuring system CC10 at 30^{o} C. Before measuring viscosity to make sure of having no solvent or moisture residue, all the samples were dried under vacuum at 60^{o} C for 4h.

2.3.9. Burn rate measurement

Non-aluminized composite solid propellants (CSPs) were made to study the burn rate from different binder samples with loading of 86% ammonium perchlorate (AP) (coarse and fine AP taken in 1:1 wt ratio) together with IPDI as the curative and 2.3% dioctyl adipate (DOA) as the plasticizer. Burn rate measurement of the prepared CSPs were performed by using a standard Crawford Bomb in conjunction with a pressure transducer. At two different

pressure like 20 and 40 bar analysis was done and in each case of CSP, three specimens were tested to calculate the average burn rate along with their pressure indexe values.

2.3.10. Fe content measurements

Fe content of all the samples were measured in a atomic absorption spectroscopy (AAS, Perkin Elmer Atomic Absorption Spectrometer PinAAcle 900F). All the samples were digested in concentrated nitric acid first with a weighed quantity of sample followed by subsequent heating until the polymers completely decomposed, and mineralized. The mineralized solutions were made up to a known volume and utilized for the AAS analysis.

2.3.11. Hydroxyl value measurement

Hydroxyl value of the HTPB based prepolymer was measured by employing acetylation method that involves the replacement of a hydrogen of hydroxyl group by acetyl group. Briefly the procedure was as follows: Three 250 mL of iodine flasks with glass stopper, one of these for blank determination were taken. 5-8 gm. of HTPB was weight out in to the other two flasks. Then 20 mL of the acetylating agent was pipetted out and placed into all the three flask including the blank flask followed by stirring until the sample was completely dissolved. Next, all three flasks were placed onto a preheated oil bath at 98-100ºC for one hour under reflux. Towards the end of one hour 10 mL of distilled water was added to each flask and continue heating for another fifteen minutes with continuous stirring. Later, the flasks were cooled to room temperature and collected the solution after rinsing the condensers with 2×20 mL water. Finally, the mixture was titrated with 1N sodium hydroxide solution after adding 1mL of phenolphthalein indicator to each flask. The endpoint was noted down when the colour just turns pinkish orange from the original pale yellowish color. The –OH value was calculated by using the following equation.

$$\text{-OH Value} = \frac{\text{Vol. of NaOH for blank titration} - \text{Vol. of NaOH for sample titration}}{\text{Weight of sample}} + \text{Acid value}$$

2.3.12. Cyclic voltammetry (CV) analysis

CV measurements were performed using a Zahner Zanium electrochemical workstation operated with Thales software, by employing a conventional three-electrode system consisting of a Pt working electrode, a Pt wire auxiliary electrode and a Ag wire as reference electrode. CV experiments were carried out after complete dissolution of the equal concentration of the polymer solution in a 10 mL of suitable dry solvent in presence of 0.1 (M) of electrolyte TBAP.

2.3.13. Dynamic vapour sorption (DVS) analysis

DVS analysis were carried out by using a Q5000SA vapor sorption analyzer (TA Instruments, Delaware, and USA) at 40 °C. The experiment was carried out with completely dried powdered samples.

2.3.14. Brunauer–Emmett–Teller (BET) measurement

All the powdered polymer samples after grinding properly were used to conduct BET experiments which was carried out in Autosorb iQ (Quantachrome, ADIQC000-4) using nitrogen as adsorbing gas. Before performing the analysis the samples were subjected to outgas for 12 hours at 60 °C to activate the pores.

References

[1] R. M. Shankar, T. K. Roy, T. Jana, *J. Appl. Polym. Sci.* **2009**, *114*, 732–741.

[2] K. Malkappa, T. Jana, *Ind. Eng. Chem. Res.* **2013**, *52*, 12887–12896.

[3] S. Ahn, Y. S. Song, B. R. Yoo, I. N. Jung, *Organometallics* **2000**, *19*, 2777–2780.

[4] J. Zhang, L. Ren, C. G. Hardy, C. Tang, *Macromolecules* **2012**, *45*, 6857–6863.

[5] E. G. Doyagüez, J. Rodríguez-Hernández, G. Corrales, A. Fernández-Mayoralas, A. Gallardo, *Macromolecules* **2012**, *45*, 7676–7683.

[6] M. H. Stenzel, T. P. Davis, *J. Polym. Sci. Part A Polym. Chem.* **2002**, *40*, 4498–4512.

[7] C. Li, J. Han, C. Y. Ryu, B. C. Benicewicz, *Macromolecules* **2006**, *39*, 3175–3183.

[8] S. N. R. Kutcherlapati, R. Koyilapu, U. M. R. Boddu, D. Datta, R. S. Perali, M. J. Swamy, T. Jana, *Macromolecules* **2017**, *50*, 7309–7320.

CHAPTER 3

Effect of segmental compatibility imposed over metal based polybutadiene polyurethane

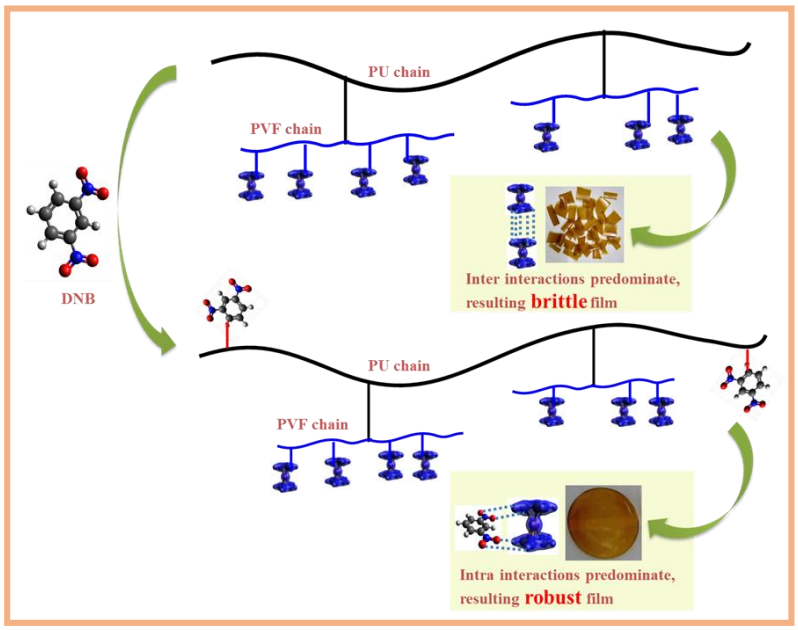

This chapter illustrates the synthesis and characterization of ferrocenyl polymer based polybutadiene polyurethane and investigates the effect of positioning a suitable functionality at the soft segment of polyurethane on various physical properties that enables to enhance the segmental mixing between hard segment and soft segment.

3.1. Introduction

The global consumption of polyurethane (PU) based materials is growing rapidly for the use in various applications like surface coatings, high performance elastomers, bio-materials, synthetic fibers, automotive suspension bushing, aerospace and so on.[1-3] Recently, metal based PU is the subject of extensive research because of the unique properties owing to the presence of metal in the polymer chain. Significant numbers of reports are now available with complete description of synthesis, properties and applications.[4-7] Ferrocene functionalized metallo-polyol has been used in order to increase burning rate (BR) of composite solid propellant (CSP).[8-9] However, sublimation while processing, migration and phase separation by crystallization during storage and sensitivity toward aerial oxidation are the main drawbacks of ferrocene based catalysts to be used in CSP.[8-10] To overcome these problems, several attempts have been made for covalent linking of ferrocene derivatives such as vinyl ferrocene, ferrocenyl silane, acetyl ferrocene etc. onto the polymeric binder such as hydroxyl terminated polybutadiene (HTPB).[11-13] However, the high viscosity build-up of these ferrocene linked HTPB on storage causes several hurdles such as poor loading, brittleness and mechanical failures of the resulting CSP.[14], [15] All the modifications of HTPB reported so far are relied on the grafting of ferrocene derivatives at the pendant vinyl position which alters the microstructure (relative ratio of cis, trans and vinyl content) of HTPB and hence causes the change in the physical properties of HTPB and thus the CSP made from it.[16-19] Therefore, it is a challenge to attach ferrocene derivatives to the HTPB backbone by keeping intact the various physical properties almost similar like parent HTPB.

Ferrocenyl groups are known to impart stiffness on the flexible polybutadiene backbone and thus very poor flexibility of the resulting materials was observed with increased Fe content.[11], [12] Though many groups had figured out how to improve the mechanical strength (yield strain) of HTPB based PU films[17], [20-23] but no efforts were found in literature to improve the flexibility of HTPB based PU films with high Fe content. Very recently, our group has been successful in controlling the viscosity of ferrocene grafted HTPB with improved mechanical properties.[24], [25] But further improvement in Fe loading is needed with good control on viscosity and higher mechanical strength of PUs for the use in CSP.

Earlier our group have also explored the influence of terminal functionalization of HTPB on the structure-property (particularly on the mechanical property) relationship of HTPB-PUs using both hydrogen bonding and non-hydrogen bonding functional moieties without altering the inherent properties of parent HTPB.[26-29] We have shown that the nitro functionality containing molecules such as dinitrobenzene (DNB) when attached to terminal position of HTPB is responsible for segmental mixing through hydrogen bonding interactions which in turn improves both tensile strength and elongation of PUs simultaneously.[26] Water dispersible PU (WDPU) developed from HTPB-DNB also displayed superior properties like hydrophobicity, mechanical strength, antibacterial activity etc.[31, 32]

These observations, as noted above, motivated us to investigate the effect of enhanced segmental mixing on various physical properties of ferrocenyl based HTPB-DNB-PU owing to the presence of DNB and grafted PVF in the HTPB. Hence in this article, we have modified HTPB by attaching DNB functionality at the terminal position followed by the grafting of poly (vinyl ferrocene) (PVF) at the pendant vinyl bond of HTPB. We expect to get control over viscosity build-up as well as increase in the flexibility of resulting PU films which might happen due to the preponderance of intra-polymer chain interactions between DNB and PVF chains over inter chain interactions throughout the polymer matrix. Very few literature also reported the electrochemistry studies of ferrocenyl based burn rate catalyst.[33, 34] To the best of our prior knowledge this work is going to be the first report on the investigation of the redox property of ferrocenyl polymer attached with HTPB matrix. Overall, poly (vinyl ferrocene) grafted HTPB-DNB (PVF-*g*-HTPB-DNB) with a combination of potential energetic material DNB which is capable to impart some energy to inert HTPB and PVF which can enhance the burn rate property, can be an unique potential binder for rocket propellant in near future.

3.2. Experimental Section

3.2.1. Synthesis of poly (vinyl ferrocene) grafted HTPB-DNB (PVF-*g*-HTPB-DNB)

DNB groups were attached to HTPB terminal position by following terminal functionalization methodology[30] as developed by us earlier. Then vinyl ferrocene (VF) was grafted as PVF chain at the pendant vinyl position of HTPB-DNB by following a clue from the

reported literature[35] and modified it substantially. Briefly the procedure was as follows: 3 g (0.536 mmol: calculated based on the molecular weight obtained from GPC analysis) of vacuum dried HTPB-DNB was dissolved in 10 ml of dry toluene in a two neck round bottom flask. 0.051 g (0.268 mmol) of VF was added to this solution in the presence of nitrogen atmosphere. 0.039 g (0.268 mmol) of AIBN was added to the stirring solution and placed in a preheated oil bath at 75º C under nitrogen atmosphere. The reaction conditions were varied in terms of equivalents of VF with respect to HTPB-DNB and reaction time as detailed in *Table 1*. The PVF grafted HTPB-DNB (PVF-*g*-HTPB-DNB) was precipitated by methanol from the reaction mixture. Then the resulting product was re-dissolved in hexane and precipitated repeatedly using methanol until it was completely free from VF and AIBN. Finally, the obtained product was dried under vacuum at 60º C for 6 hours to remove the last traces of solvent. The brown colored viscous liquid grafted polymer was stored in a closed flask for further use.

3.2.2. Synthesis of polyurethane (PU) from PVF-*g*-HTPB-DNB

In a two neck round bottom flask, 3 g (0.516 mmol: calculated based on the molecular weight obtained from GPC analysis) of prepolymer was dissolved in 30 mL of anhydrous THF under nitrogen atmosphere. After stirring for 15 minutes, 0.49 g (2.2 mmol: based on equivalents calculated from hydroxyl value of prepolymer) of isophorone diisocyanate (IPDI) was added and stirred at room temperature for 30 minutes under continuous nitrogen flow. We kept the –NCO to –OH ratio as 1:1 for all the PU systems. The hydroxyl value of prepolymer was measured to calculate the moles of –OH present in the prepolymer samples. After 30 minutes, catalytic amount of DBTDL was added as a catalyst and the whole reaction mixture was stirred for another 3 hours at room temperature under nitrogen atmosphere. The progress of the reaction was monitored by FT-IR spectroscopic analysis where disappearance of the isocyanate peak at 2270 cm^{-1} was observed after PU formation. The brown colored viscous polymer solution was then transferred into a clean flat based petri dish pre-coated with silicone releasing agent and the reaction (curing) was continued at 70º C for 5 days to obtain a free standing PU film.

All details of materials source and the various characterization techniques are described in the **Chapter 2**.

3.3. Results and Discussion

3.3.1. Synthesis of PVF-*g*-HTPB-DNB

The synthesis of PVF-*g*-HTPB-DNB was carried out via the free radical reaction pathway with radical initiator AIBN as shown in *Scheme 3.1*. At first HTPB-DNB was synthesized by covalently attaching DNB at the terminal carbon of HTPB polymer backbone by using terminal functionalization technique which is already established by our group.[30], [36], [37] Then free radical grafting of VF was performed onto the pendant vinyl bond of HTPB-DNB backbone as discussed in the experimental section. The mechanism of free radical grafting proceeds in such a way that VF is attached as a growing PVF chains onto HTPB-DNB. We have altered the VF equivalents and the reaction time to tune the viscosities of resulting prepolymer and also to vary the net Fe content in the product. Several parameters such as molecular weight, polydispersity (Đ), viscosities, Fe content and hydroxyl values of the products were measured and listed in *Table 3.1*. All the changes in various physical parameters due to successful grafting of ferrocene functionality onto butadiene backbone are seen. For example, with increased reaction time as well as increased monomer equivalence, both iron content and viscosity of the product increases. The increase in molecular weight is observed along with gradual decrease in hydroxyl value but up to a certain extent. All the parameters show reverse trend beyond 6 equivalent of VF. Ferrocenyl polymer known to cause higher crosslinking in HTPB polymer matrix[4] and as expected higher viscosity build-up during storage was observed with higher amount of iron content in the sample.[3], [11], [38] In order to optimize the viscosity build-up on storage, we have varied the reaction time up to a certain extent with gradual increase in monomer equivalence (*Table 3.1*). It is important to note that the change in the viscosity values on storage as shown in *Table 3.1* measured after two months of storage. All the PVF-*g*-HTPB-DNB (abbreviated as FHD) samples shows an increase in viscosity on storage but still within the measurable limit and samples remain fluidic. But in

case of PVF-*g*-HTPB (FH) sample (entry 2 in *Table 3.1*) becomes sticky solid for which viscosity could not be measured. The reason for this will be discussed in the following section.

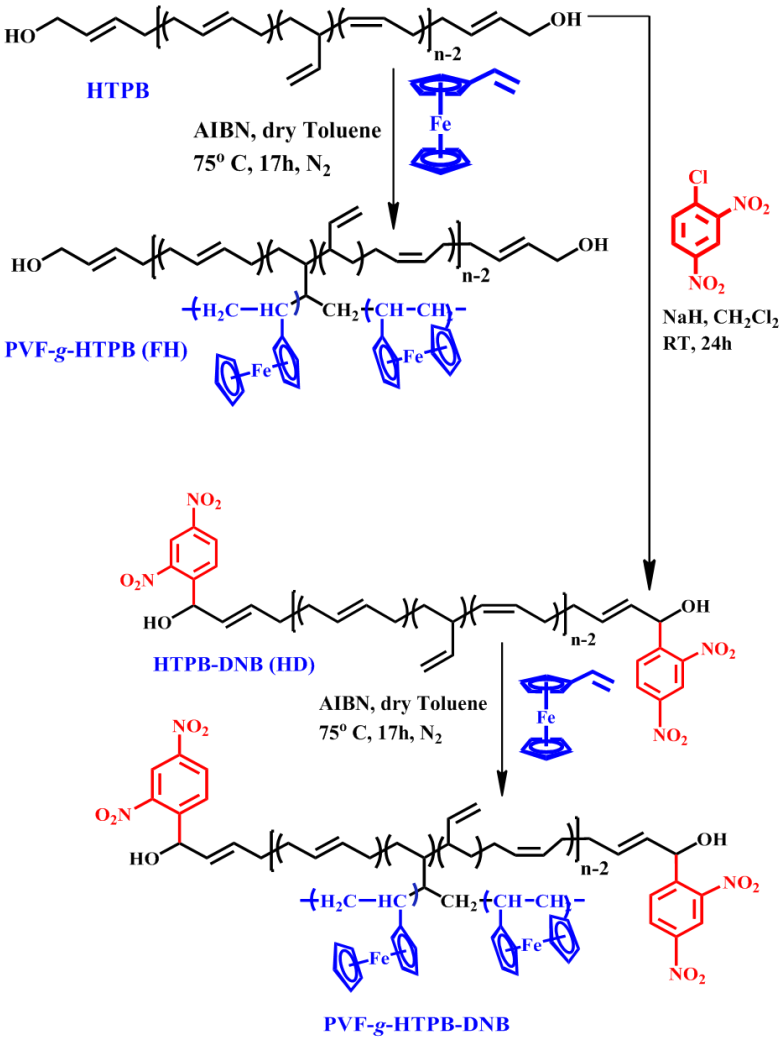

Scheme 3.1: *Synthesis of HTPB-DNB, poly (vinyl ferrocene)-grafted-HTPB (abbreviated as PVF-g-HTPB), poly (vinyl ferrocene)-grafted-HTPB-DNB (abbreviated as PVF-g-HTPB-DNB). To make the representation easier HTPB-DNB, PVF-g-HTPB, and PVF-g-HTPB-DNB have been abbreviated as HD, FH and FHD, respectively for the remaining part of this articles.*

Table 3.1: *Variation in reaction conditions and various physical parameters of the all PVF-g-HTPB-DNB (FHD) samples including HTPB-DNB (HD, first entry) and PVF-g-HTPB (FH, 2nd entry).*

Sample identity	Reaction time (hrs)	[VF] (equivalent)	$\overline{M_n}$[a]	Đ[a]	Viscosity (cp) at 30°C[b]	Viscosity (cp) at 30°C[c]	Hydroxyl value (mg KOH/g)[d]	Fe content (Wt %)[e]
HD	24	--	5600	2.53	5600	5669	42.5	0.0
FH	17	0.5	6190	2.67	5809	sticky	27.56	0.83
FHD1	4	0.5	5811	2.16	6670	7880	41.78	0.52
FHD2	4	1.5	6332	2.22	5696	10662	36.33	0.92
FHD3	4	3	8530	1.87	7841	12892	18.37	2.2
FHD4	4	6	5749	2.6	9883	10640	23.58	0.88
FHD5	6	0.5	5818	2.55	5100	9620	37.09	0.65
FHD6	6	1.5	6795	2.21	6346	9447	37.42	1.0
FHD7	6	3	6440	2.25	6622	10913	29.52	1.1
FHD8	6	6	5699	2.45	8292	8957	40.52	0.87
FHD9	17	0.5	6290	2.69	5308	8332	37.9	0.91
FHD10	17	1.5	8143	1.76	7020	12501	23.05	1.9
FHD11	17	3	7395	2.0	8287	11530	22.33	1.4
FHD12	17	6	6291	2.8	10989	13953	23.62	1.2

[a] Number average molecular weight ($\overline{M_n}$) and dispersity (Đ) are obtained from GPC analysis. All the GPC chromatograms are shown in *Appendix I-Figure 3.1*. [b] Measured immediately after preparation. [c] Measured after two months. [d] Measured by following acetylation method, which involves the replacement of a hydrogen of hydroxyl group by acetyl group. [e] Obtained from atomic absorption spectroscopic (AAS) analysis.

Pristine HTPB-DNB (HD), PVF-*g*-HTPB (FH) and few selected PVF-*g*-HTPB-DNB (FHD)

samples have been used to make PUs with IPDI using DBTDL as catalyst. All together five PU films were prepared in anhydrous THF solvent followed by curing for 5 days at 70º C keeping the stoichiometric ratio between -NCO/-OH constant and equal to 1:1. The reaction scheme for the PU synthesis is represented in *Scheme 3.2*.

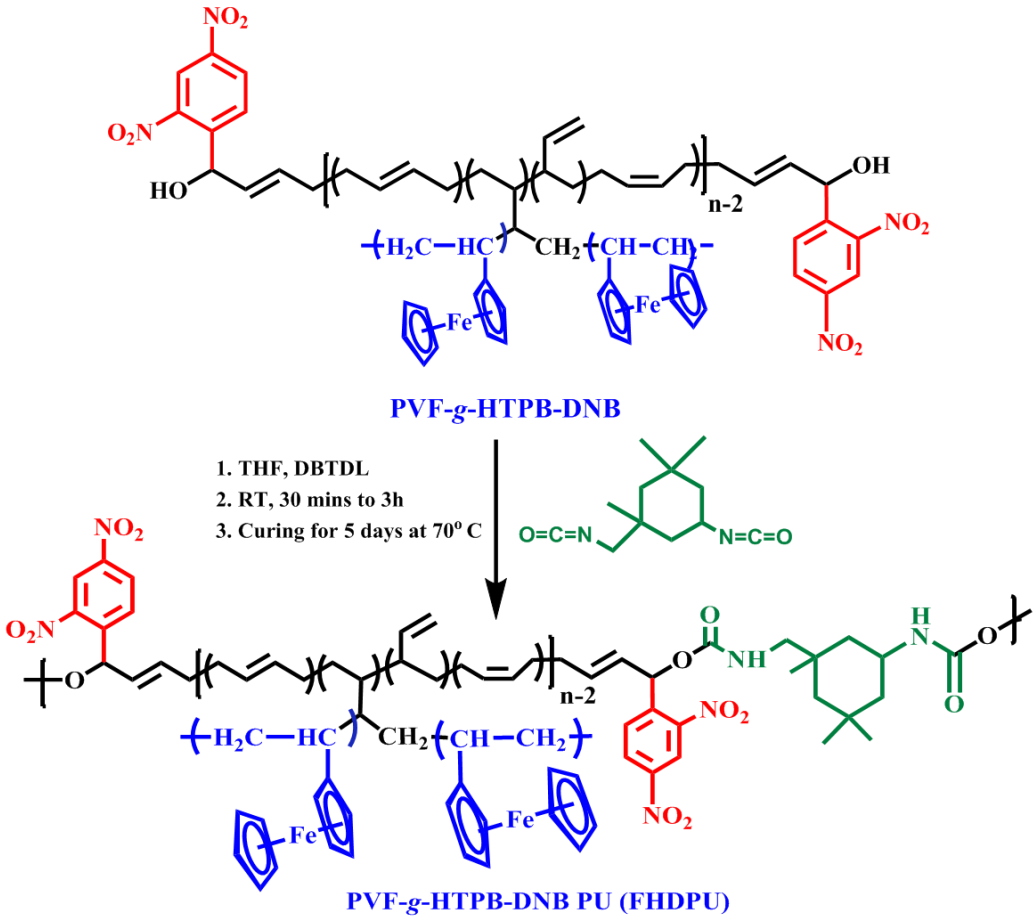

Scheme 3.2: *Synthesis of PVF-g-HTPB-DNB (FHD) based polyurethanes (PU). These samples are abbreviated as FHDPU(XX) where XX indicate the Wt.% of Fe in the FHD samples.*

3.3.2. Spectroscopic study

The FTIR spectra of HTPB-DNB (HD) and PVF-*g*-HTPB-DNB (FHD) samples are presented in *Figure 3.1*. The characteristic peaks for HD appeared at 969 cm^{-1}, 887 cm^{-1} and

753 cm^{-1} [*Figure 3.1(A)*] which correspond to 1, 4- trans, 1,2-vinyl and 1,4-cis microstructure of polybutadiene backbone, respectively.[30] After grafting the PVF chains, the 1,2 vinyl peak intensity at 887 cm^{-1} gradually decreases while a prominent shift has been observed for the peak at 753 cm^{-1} (1,4 cis) to 699 cm^{-1} with huge decrease in peak intensity. It is clear from [*Figure 3.1(A)*] data that grafting of VF has occurred at the pendant vinyl bond which also mainly affects the cis-microstructure of the DNB modified polybutadiene backbone. Another characteristic peak of HD appears at 1349 cm^{-1} which corresponds to asymmetric stretching of $–NO_2$ of DNB moiety[30] displays peak broadening and shifting to 1324 cm^{-1} indicating the involvement of $–NO_2$ in interactions with grafted PVF. For higher reaction time, most probably because of higher Fe content in the sample FHD9 (0.91) [*Figure 3.1(A)*] and due to even more interactions the characteristic peak at NO_2 becomes broader and weaker. This interaction between PVF and NO_2 of DNB also affects the OH stretching frequency of FHD which shifts towards higher frequency (3396 to 3412 cm^{-1}) [*Appendix I-Figure 3.2(A)*] attributing to the fact that grafted PVF decreases the extent of hydrogen-bonding between $–NO_2$ and –OH by increasing the interactions between PVF chain with $–NO_2$. However, we did not see the similar observations in case of FH sample (data is not shown here) where DNB is not present. These results together indicate that this increased interaction between NO_2 and PVF helps in reducing a substantial increase in viscosity built up in case of FHD. But no such interaction happens in the absence of NO_2 in case of FH which helps to build up very high viscosity on storage and it becomes solid like sticky mass as shown in *Table 3.1*. A more detailed discussion on these interactions will be discussed in the forthcoming section.

After curing with IPDI, the characteristic peak of –OH at 3396-3412 cm^{-1} completely disappeared and two new bands appeared in principle vibrational region i.e. at 3324-3341 cm^{-1} for amine (-NH-) stretching [*Appendix I-Figure 3.2(B)*] and at 1720 cm^{-1} for carbonyl peak of the urethane segment *Figure 3.2(B)*. The peak at 1639 cm^{-1} corresponds to the carbonyl frequency of those which are involved in hydrogen-bonding within the PU matrix and 1085 cm^{-1} correspond to C-O-C stretching band for the linkage between –OH and –NCO to form urethane bond.[38], [53] A shift for the amide III and amide II band at 1256 cm^{-1} and 1559 cm^{-1} of HTPB-DNB towards higher wavelength upholds the fact that the hydrogen-bonding between

DNB and urethane amide linkage in PU matrix gets disturbed by grafted PVF chain.[38] And the gradual broadness of the characteristic symmetric and asymmetric stretching frequency of $–NO_2$ at 1452 cm^{-1} and 1306 cm^{-1} ascertains the gradual increased interaction of $–NO_2$ with grafted PVF chain.[26]

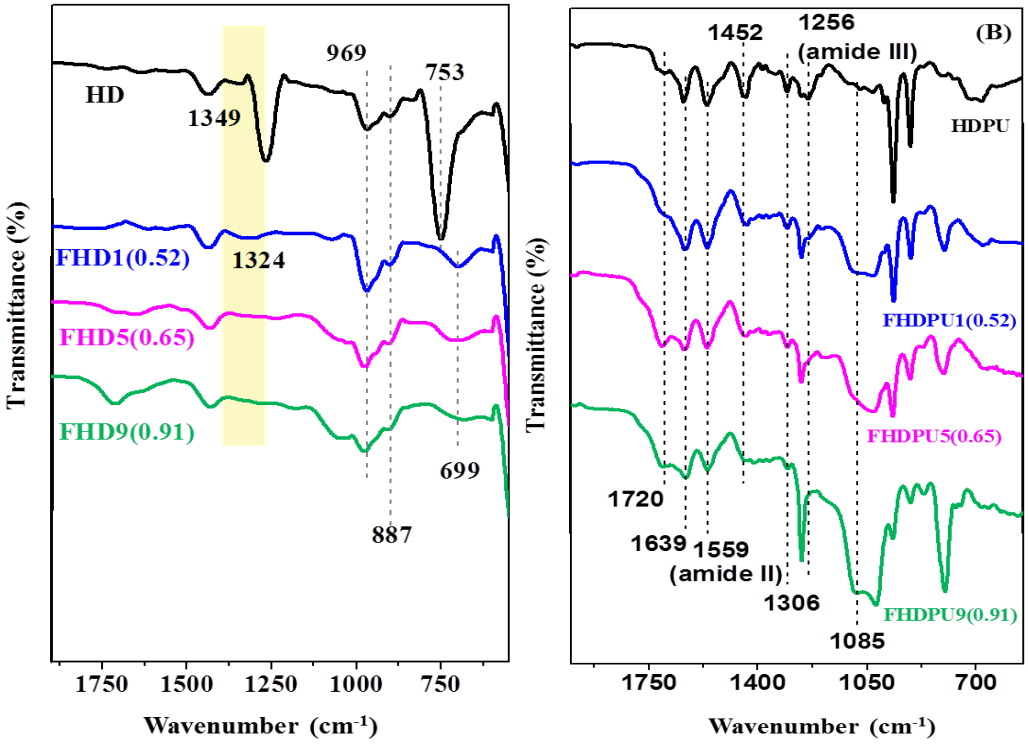

Figure 3.1: *FTIR spectra of (A) HTPB-DNB (HD) and PVF-g-HTPB-DNBs (FHD), (B) HTPB-DNB-PU (HDPU) and PVF-g-HTPB-DNB-PUs (FHDPU). Sample names are indicated in the figure. Amount of Fe content in the sample is mentioned in the parenthesis after the sample name.*

^{1}H and ^{13}C NMR spectra of HD and FHD along with VF in $CDCl_3$ are shown in *Figure 3.2*. ^{1}H NMR spectrum of HD shows resonance peaks at ~7.78, ~8.37 and ~8.75 ppm correspond to aromatic region of DNB moiety which is clearly present in FHD also. Signals appear at ~4-4.4 ppm in case of VF are assigned to the cyclopentadiene ring protons of VF. However, HD also shows the peaks in the similar region. From *Figure 3.2(A)*, it is clearly visible that due to

presence of both ferrocene and DNB, the peak intensity at ~4-4.4 ppm increases prominently in case of FHD with stronger intensities than HD. The other chemical shift regions of HD at δ = 2-2.1, 3.4-4.2 and 4.9-5.6 are exactly similar with parent HTPB[26],[30] which mainly correspond to the cis, trans-1,4-unit and vinyl-1,2-unit protons. Some of these peaks are not shown here for better representation. Similarly, ^{13}C NMR further confirms the structure of the FHD. As shown in *Figure 3.2(B)*, the resonance peak of ferrocene in case of FHD appears at~ 69 ppm which is matching with the resonance peak of ferrocene carbon of VF. Representative peaks for DNB appears at 133.8 and 141 ppm which also present in FHD sample implying the confirmation of grafting of PVF onto HTPB-DNB polymer backbone.

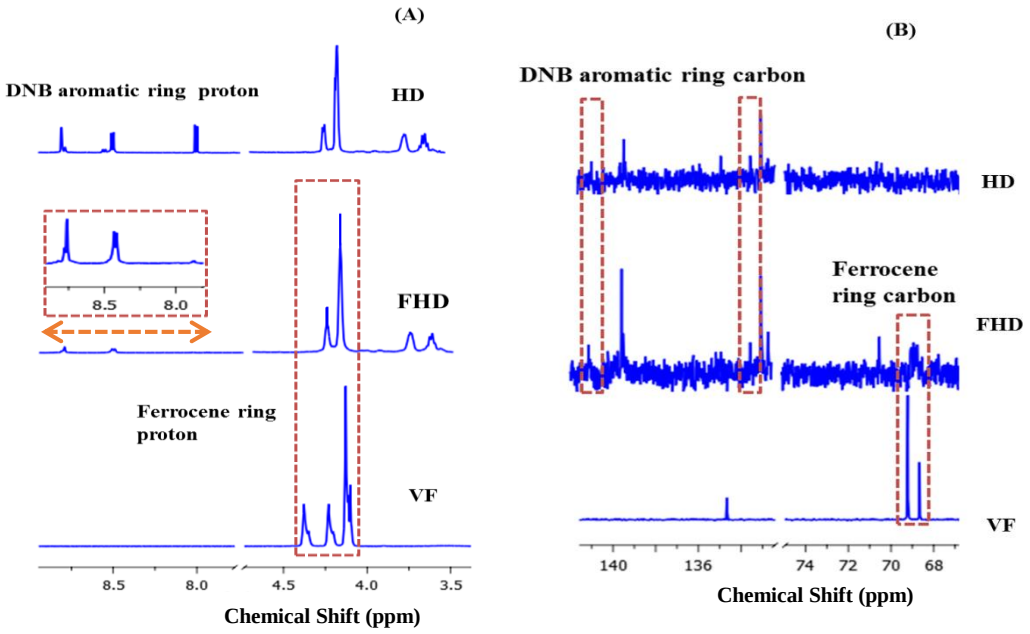

Figure 3.2: *(A) ^{1}H-NMR and (B) ^{13}C-NMR spectra of HD, FHD and VF. NMR spectra were recorded using $CDCl_3$ as a solvent.*

3.3.3. Theoretical study

To understand the origin of the interactions between cyclopentadiene and NO_2 functionality, as evident from IR and NMR studies, we carried out theoretical calculation using density function theory (DFT). Theoretical evaluation using DFT has been performed on two important moieties of polymer chain and these are 2, 4-dinitrobenzene (DNB) and ferrocene, to understand their function in the polybutadiene chain. The physical parameters obtained through DFT calculations using Gaussian package (GAUSSIAN-09) of these two units are shown in the *Table 3.2*. Ferrocene has approximately zero dipole moment (0.0004 Debye, Table 2) and high polarizability of 33 $Bohr^3$ which is obtained from DFT calculation. Because of this high polarizability, ferrocene molecule can easily interact with another ferrocene unit through instantaneous induced dipole interactions (London dispersion force). This dispersion force energy can be calculated using the equation.

$$E_L = -\frac{3I\alpha^2}{4r^6}$$

Where, I is ionization energy, r is intermolecular distance between two ferrocene unit which is considered as 0.3 nm and α is polarizability of ferrocene molecule. Dispersion energy of interaction obtained from the above equation for ferrocene is found to be 17 kJ/ mol per pair. Because of this type of strong interactions, ferrocene has strong inter interactions with other ferrocene unit throughout the polymer matrix and results very high viscosity in case of PVF-*g*-HTPB (FH) sample. The most profound aspect is that these non-covalent interactions between the ferrocene units are quite higher even almost equivalent to hydrogen bonding interactions.

However, once DNB comes into the frame of FH as in FHD, owing to the high electron affinity (201 kJ/mol) and high dipole moment (4.39 Debye) of DNB (*Table 3.2*), DNB instantaneously interacts with highly polarizable ferrocene unit available within the same polymer chain (*Figure 3.3*) and indirectly reduces the extent of London dispersion force among ferrocene moieties for further inter interactions. This fact is also supported by the lower ionization value of ferrocene unit (698 kJ/mol, *Table 3.2*). Because of lower ionization value

ferrocene moiety can easily interact with DNB through its electron cloud as graphically shown in *Figure 3.3*. There will be possibility of both intra and inter interactions throughout the polymer matrix but intra will be dominated as soon as DNB grafted onto the FH backbone (as it is in FHD sample) and will help to minimize the inter polymer chain crosslinking. So, this theoretical calculation clearly certifies that dominance of intra over inter interactions in presence of DNB molecule in the FHD polymer matrix perhaps helps in controlling the viscosity increase. But in absence of DNB as in case of FH, the viscosity increases because of strong inter-chain interactions. In the following section, we will see how this interaction helps in modulating electrochemical properties of FHD.

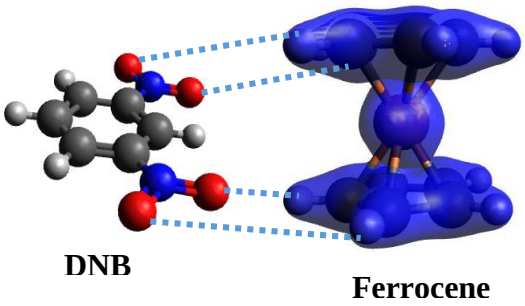

Figure 3.3: *Graphical view of interactions between DNB and ferrocene ring.*

Table 3.2: *Physical parameters obtained from DFT calculation*

Molecule of interest	**Type of calculation**	**Basis set**	**Electron affinity (kJ/mol)**	**Ionization energy (kJ/mol)**	**Dipole moment (Debye)**
DNB	B3LYP/ DFT	aug-ccpvdz	201	986	4.39
Ferrocene	B3LYP/ DFT	Fe : LANL2DZ C, H: 631+G*	-16	698	0.0004

3.3.4. Electrochemical study

Cyclic voltammetric (CV) waves showing both oxidation and reduction peaks were recorded for monomer (VF), FH and FHD samples with different Fe content in CH_2Cl_2 solution. *Figure 3.4* depicts the current-voltage scan of samples obtained at 20 mV/s scan rate.

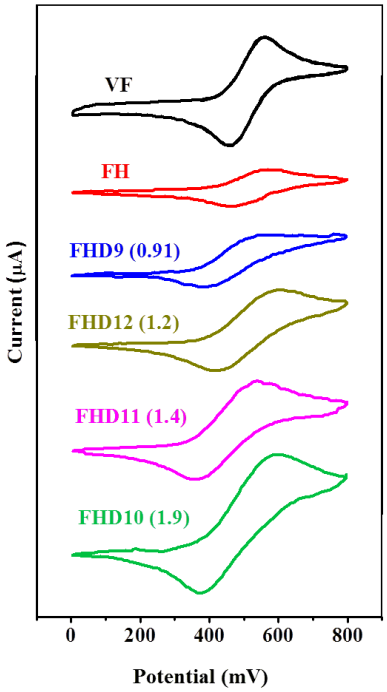

Figure 3.4: *Cyclic voltagramms of PVF-g-HTPB-DNB (FHD) samples along with vinyl ferrocene (VF) and PVF-g-HTPB (FH) in CH_2Cl_2 solution. Fe content in the samples is indicated in the parenthesis after sample name. CV were recorded by scanning 800 mV to -200 mV with scan rate of 20 mV/s. 10 mg/ml polymer concentration was used, however for VF 1 mg/ml concentration was used. 10 mmol/L tetrabutylammonium perchlorate was used as supporting electrolyte in N_2 atmosphere. Pt electrode was used as working electrode and Ag wire was used as reference electrode.*

The cyclic voltagramms show oxidation peaks at 537 mV to 597 mV and reduction peaks at 358 mV to 455 mV. Various electrochemical parameter extracted from the CV waves (*Figure 3.4*) are presented in *Table 3.3* for better clarity. Both anodic current (I_{pa}) and cathodic current

(I_{pc}) values are increasing with increasing Fe content in the FHD samples (*Table 3.3*), this observation is consistent with the increase of number of electroactive ferrocene groups per polymer molecule. The difference between anodic and cathodic peak potential (ΔE_p) of FHD samples found to be significantly higher than VF and FH, and increasing with increasing Fe content in FHD samples. This attributes the slow electron transfer process compared to an ideal Nearstian system[39-42] owing to the strong interactions between cyclopentadiene rings and DNB as discussed in earlier sections. *Table 3.3* data also clearly shows that the anodic (oxidation) potential (E_{pa}) values are increasing with Fe content in the FHD indicating that the oxidation becoming more difficult in presence of higher ferrocene content in the backbone of polymer chain. This is because of the fact that the electron cloud of cyclopentadiene is getting pulled by DNB molecules as discussed from our DFT study making the Fe^{+2} of ferrocene relatively electron deficient and hence higher E_{pa} is obtained. Similarly, we observed the reverse results decreasing cathodic (reduction) potential (E_{pc}) as Fe content increase.

Table 3.3: *Electrochemical parameters of the PVF-g-HTPB-DNB (FHD) in CH_2Cl_2 soultion.*

Sample Identity (% of Fe)	**E_{pa} (mV)**	**E_{pc} (mV)**	**$E_{1/2}$ (mV) [a]**	**ΔE_p (mV)**	**I_{pa} (µA)**	**I_{pc} (µA)**
VF	556 (1.41)	455 (0.47)	505.5 (0.62)	101 (1.7)	2.8×10^{-1}	1.05×10^{-1}
FH	564 (4.64)	449 (5.66)	506.5 (4.77)	115 (4.02)	1.23×10^{-1}	-1.01×10^{-2}
FHD9(0.91)	542 (8.01)	373(8.52)	457.5 (8.25)	169 (0.94)	2.99×10^{-1}	1.50×10^{-1}
FHD12(1.2)	597 (0.94)	410 (1.63)	503.5 (2.35)	187 (2.82)	3.84×10^{-1}	9.19×10^{-2}
FHD11(1.4)	537 (2.62)	358 (1.63)	447.5 (0.85)	179 (4.03)	3.83×10^{-1}	9.86×10^{-2}
FHD10(1.9)	594 (3.77)	371 (0.94)	482.5 (1.23)	223 (0.94)	6.86×10^{-1}	1.34×10^{-1}

Note: All the values are averages of at least three independent measurements. Standard deviations are shown in the parentheses after the data. [a] $E_{1/2}$ values are obtained from the E_{pa} and E_{pc} by averaging their values.

3.3.5. Mechanical properties of polyurethane obtained from FHD

To investigate the influence of DNB, ferrocene and their interactions in the mechanical properties of PVF grafted HTPB-DNB based PUs (FHDPU), few selected FHD samples were converted into PU films and stress-strain profiles were obtained (*Figure 3.5*). Various parameters such as tensile strength (σ_b), % elongation at break (ε_b), Young's modulus (E) and toughness were obtained from *Figure 3.5* are listed in *Table 3.4*. The effective cross linking density (N) was also estimated and tabulated. *Figure 3.5* and *Table 3.4* data show clearly that elongation at break (ε_b) increased remarkably from FHPU to FHDPU in which DNB is present. This observation can be explained using our DFT calculation results as discussed earlier. The presence of DNB which has very high electron affinity (193 kJ/mol) helps to minimize the inter polymer chain crosslinking through intra interactions of highly polarizable ferrocene unit. These strong intra interactions between DNB and ferrocene help to diminish the effective crosslinking density (*Table 3.4*) in the resulting PU matrix and help to obtain more flexible film rather than rigid and hard film. In addition, DNB helps in increasing segmental mixing through extra supramolecular hydrogen bonding between the soft segment (SS) chain end and urethane linkages at the hard segment (HS) region as demonstrated by us earlier.[26] But in case of FHPU, no segmental mixing expected in between polar urethane groups and non-polar PVF chain, rather high rigidity observed throughout the polymer matrix. This fact is attributed to strong intermolecular attraction of hard-to-hard segments as well as higher degree of crosslinking of PVF attached SS chain[4] Thus the FHPU displays much higher effective crosslinking density to very high Young's modulus (*Table 3.4*). But the moment DNB causes segmental mixing through supramolecular hydrogen bonding with urethane groups, crosslinking density also increases at the HS area compared to FHPU. This helps to increase the inter polymer chain distance and reduce the tendency of crosslinking in the polymer matrix which occurs through inter interaction between the grafted PVF. This effect allows the SS to be more flexible to achieve better elongation. *Table 3.4* indicates that with the increase in Fe%, tensile strength and elongation at break of FHDPU increases. As Fe% increases, the intra polymer interactions started dominating over the inter interactions and hence flexibility of SS

chain increases. However, at higher Fe% such as in case of FHDPU (2.2), we observed reverse trend, may be due to inter interactions are dominating after a certain amount of Fe content.

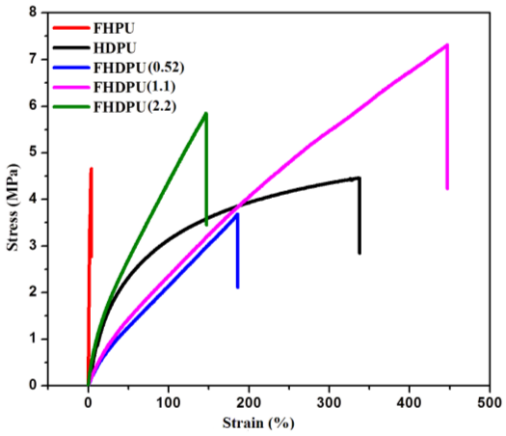

Figure 3.5: *Stress-strain plots of PVF-g-HTPB-PU (FHPU), HTPB-DNB-PU (HDPU) and PVF-g-HTPB-DNB-PUs [FHDPUs (0.52-2.2)]. Fe content in the sample is given in the parenthesis after the samples name.*

Table 3.4: *Various parameters obtained from tensile study of PVF-g-HTPB-DNB PUs (FHDPU).*

Samples	Tensile strength (σ_b, MPa)	Elongation at break (ε_b, %)	Toughness (MPa) [a]	Young Modulus (E, MPa) [b]	Effective cross linking (N, m^{-3}) [c]
FHPU	4.626	3.974	12.07	1.89	1.52×10^{20}
HDPU	4.44	338.68	1152.53	0.076	6.11×10^{18}
FHDPU(0.52)	3.63	184.9	372.59	0.038	3.06×10^{18}
FHDPU(1.1)	7.285	446.03	1877.84	0.034	2.73×10^{18}
FHDPU(2.2)	5.82	146.88	501.05	0.114	9.1×10^{18}

[a] calculated by integrating the area under stress-strain plot. [b] calculated from the slope of the linear portion of the stress-strain plot. [c] estimated according to equation N = E / (3RT), where E is the Young's modulus, R the gas constant (8.314 $J.mol^{-1}.K^{-1}$) and T the absolute temperature in Kelvin.

3.3.6. Thermal analysis of the modified PUs

The thermal degradation of most of the samples displays two distinct regions of weight loss (*Figure 3.6*) which is a common feature of this type of PU based on HTPB.[26-28] In the first stage degradation of HDPU started at around~247 °C and reached up to~340 °C with near about 14% weight loss due to the decomposition of urethane linkage in the HS domain, while this range is shifted to lower temperature by~20° C, i.e. 224° C to 319° C for ferrocene modified samples which illustrates the catalytic effect of ferrocene moieties on the thermal decomposition of the hard domains [(*Figure 3.6(A)]*. Although the NCO/OH remains constant for all of the samples, different amount of HS degradation has been observed, most likely for some chain scissions in the SSs simultaneously occurred along with depolycondensation of the urethane linkages at this first degradation stages.[43] The second degradation stage i.e. the major decomposition region for all the HTPB-based PUs started decomposing at~415° C up to~483° C with more than 80% weight loss for HDPU while for organometallic PUs (FHPU and FHDPUs) it is starting at lower temperature, i.e., 367° C to 483° C due to catalytic effect of ferrocene. This second stage mainly is associated with the degradation of polybutadiene segments. Finally, derivative weight% plots i.e. DTG curves [(*Figure 3.6(B)*]. explicitly indicate that due to the presence of ferrocene all the FHDPUs and FHPU started decomposing much earlier than parent HDPU especially at the major degradation region. Another aspect also can be analyzed particularly from the DTG curves [(*Figure 3.6(B)*] i.e., all the char residues after complete decomposition are more for organometallic based PUs rather than HDPU which is an indirect proof of grafting ferrocene moiety onto the polymer matrix.

The degradation pattern obtained from TGA and DTG measurements are in well agreement with the heat change profile obtained from DSC analysis under nitrogen atmosphere [*Figure 3.7(A)*]. The DSC thermograms of FHDPUs show an exothermic peak between 127-145º C while FHPU displays exothermic peak at 135º C [*Figure 3.7(A)*]. The presence of ferrocene and DNB in the system causes significant changes in DSC profiles. DSC exotherm as obtained is most possibly corresponds to the positive energy balance of endothermic depolymerisation, exothermic cyclization and oxidative crosslinking processes.[35], [43]

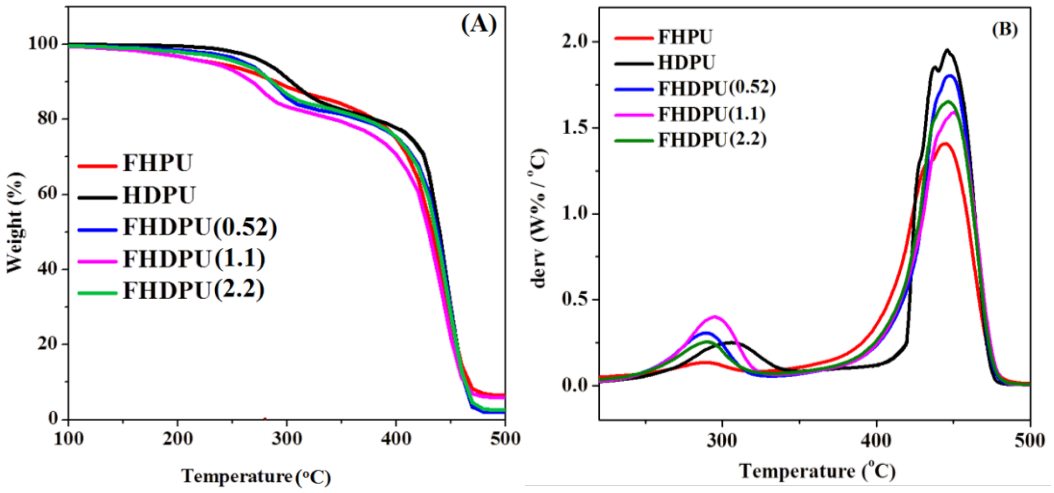

Figure 3.6: *(A) TGA and (B) DTG curve of FHPU, HDPU and FHDPUs(0.52-2.2).*

But for HDPU, the exothermic peak appears at about 275° C only. So it is clear from the data that both DNB and ferrocene has significant influence on the appearance of exothermic peak of FHDPU system. The DSC evaluations have been further studied to see the phase segregation between HS and SS domains [*Figure 3.7(B)*]. Glass transition temperature of SS domain ($T_{g\text{-}SS}$) of all the PUs has been found to be varied from -77 to -66° C [*Figure 3.7(B), Table 3.5*]. As expected in absence of DNB, FHPU displayed the highest T_g value at -66.46° C (*Table 3.5*). For FHDPUs, the observed T_g differences of the resulting polyurethanes can be explained in terms of Fe content variation. FHDPU(0.52), which contains least Fe amount, showed the highest T_g among all the FHDPU which is quite obvious because of highest segmental mixing for the lowest amount of Fe in presence of DNB.[44] For higher chain length intra and inter polymer chain interactions playing the key factor to have different T_g value. Among all, FHDPU(1.1) showed the lowest T_g which again because of the preponderance of intra interaction between DNB and PVF chain over inter polymer crosslinking resulting an increase in the mobility of polymer chain soft segments. For further higher Fe content than FHDPU(1.1), again inter polymer interaction is prevailing than the intra, because of which FHDPU(2.2) possess higher T_g value than FHDPU(1.1) [*Figure 3.7(B)*]. From DSC thermogram the hard

segment T_g ($T_{g\text{-}HS}$) cannot be obtained very clearly and hence we carried out dynamical mechanical analysis (DMA) to find out $T_{g\text{-}HS}$.

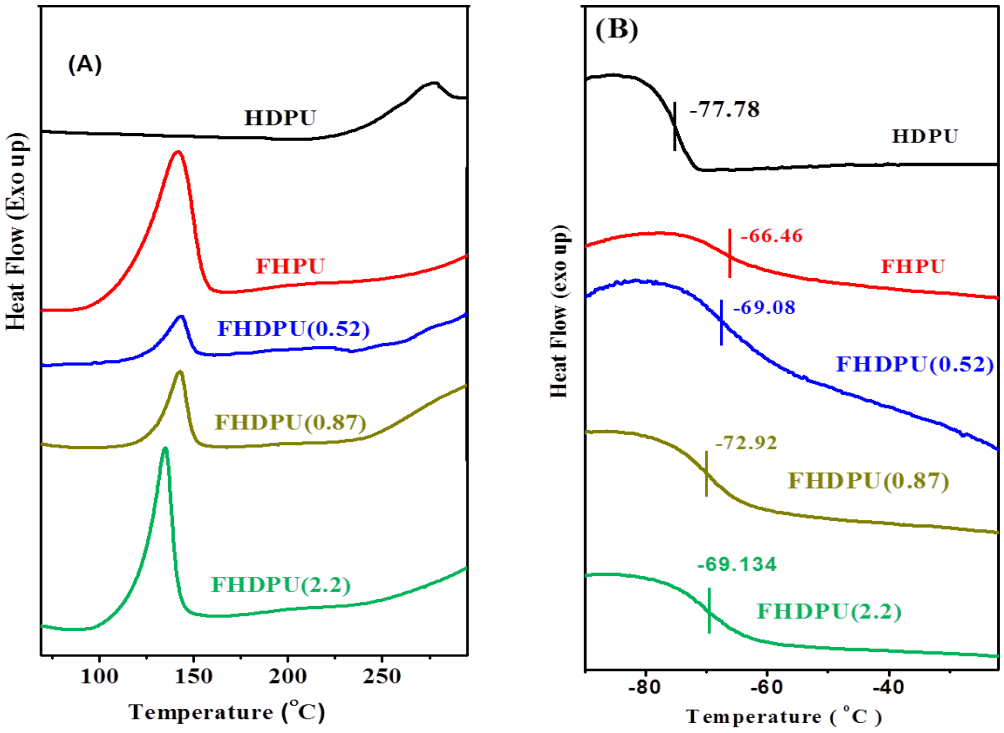

Figure 3.7: *DSC thermograms of FHPU, HDPU and FHDPUs of their indicated Fe %; in the temperature range: (A) 25º C to 370º C (B) -100º C to 25º C.*

The dependence of tanδ over temperature has been analyzed thoroughly in DMA investigation [*Figure 3.8(A)*]. In maximum cases, two different glass transition regions was observed: the first transition reflects the polymer chain motions of the soft-segment (SS) domain and the second transition corresponds to the motions within hard-segment (HS) units caused by the presence of ferrocenyl groups.[4], [45] *Figure 3.8(B)* and *Table 3.5* data clearly demonstrate that absence of DNB causes too much stiffness in FHPU film, showing high modulus in the DMA study while the presence of DNB makes FHDPU much more flexible. This result is in agreem6nt with stress-strain plots as discussed in earlier section shows usual trend like earlier report.[26] The soft segment T_g ($T_{g\text{-}SS}$) for HDPU and FHDPUs vary from -58.5º C to -45.5º C and hard segment T_g ($T_{g\text{-}HS}$) which originates due to the existence segmental

Table 3.5: *Glass transition temperature and modulus values of all the PUs from DSC and DMA.*

PU samples	$T_{g\text{-}SS}$ (°C) from DSC	$T_{g\text{-}SS}$ (°C) from tanδ	$T_{g\text{-}HS}$ (°C) from tanδ	Storage modulus, E' (MPa)
HDPU	-77.78	-58.5	121	1168
FHPU	-66.46	-42.9	70.68	1025
FHDPU(0.52)	-69.08	-57.8	138	531
FHDPU(1.1)	-73.96	-57.5	141	3501
FHDPU(2.2)	-69.13	-45.54	17.73	2416

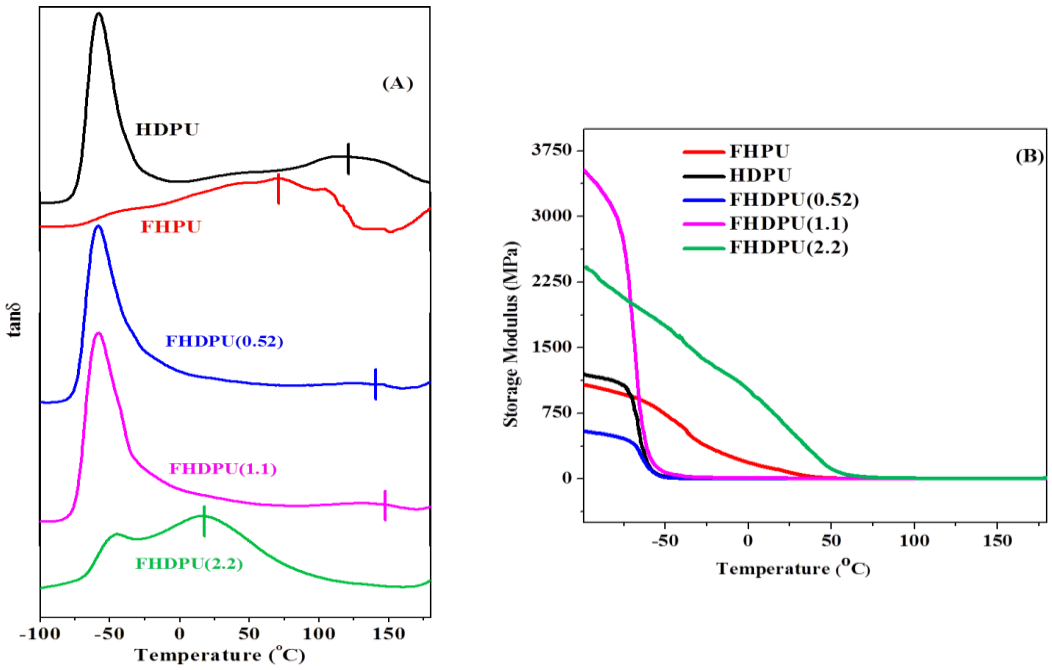

Figure 3.8: *(A) tanδ vs temperature (B) Storage modulus vs temperature plots of FHPU, HDPU and FHDPUs of their indicated Fe content. Plots in case of tanδ vs temperature are shifted vertically for better clarification.*

mixing is also obtained from tanδ vs temperature plots and listed in *Table 3.5*. The FHDPU (2.2) shows relatively lower $T_{g\text{-}HS}$ may be due to very high degree of segmental mixing. DSC and DMA data (*Figure 3.7, 3.8* and *Table 3.5*) clearly indicated that both SS and HS T_g alters as Fe content in the FHDPU changes, attributing significant effect of interactions between cyclopentadienyl ring of ferrocene and NO_2 group of DNB.

3.3.7. X-ray studies:

The structure of samples was explored by investigating WAXD and SAXS techniques. For WAXD analysis, the X-ray patterns of PU samples are compared with bare HTPB-PU for better understanding of difference in the structure in presence of ferrocene functionality along with DNB. HTPB-PU shows a major broad peak at 2θ = 19.3º and a minor peak at 42º reflecting the amorphous nature of the general polybutadiene based polyurethanes.[28] HDPU exhibits the presence of crystalline peaks at 2θ = 13.89º, 16.68º and 25.11º (*Appendix I-Figure 3.3*) which is in well agreement with reported in literature[26] as all other PUs show almost identical diffraction pattern like HDPU exhibiting crystalline peaks at 2θ = 13.89º, 16.68º, 25.11º and broad amorphous peaks at 19.3º and 42º. The crystalline peaks vary only in intensity, may be due to strong interactions between HS and SS through intra as well as inter polymer chain crosslinking. Among FHDPUs, the differences in crystalline peak intensity clearly indicate that varying amount of Fe percentage makes difference in polymer interaction pattern.

Small angle X-ray (SAXS) measurements were carried out on all samples of HDPU, FHPU and FHDPU. *Figure 3.9 and 3.10* shows typical SAXS profiles displayed on log-log scale for HDPU and FHDPU (0.52), respectively. For other samples, the shape of curves is similar to anyone of these two. The SAXS profiles of HDPU, FHDPU (1.1) and FHDPU (2.2) show linear variation in low-Q, high-Q regions and a broad hump in the middle-Q region as shown in *Figure 3.9*. The linear behavior indicates power-law ($Q^{-\alpha}$) variation of intensity I(Q) where the value of the exponent (α) indicates structural morphology of scatterers. If the linear variation spans over more than a decade of Q, a non-integer value of α suggests fractal nature;

mass fractals of dimension D_m (= α) if α < 3 and a surface fractal with rough surface if 3 < α < 4.[46]

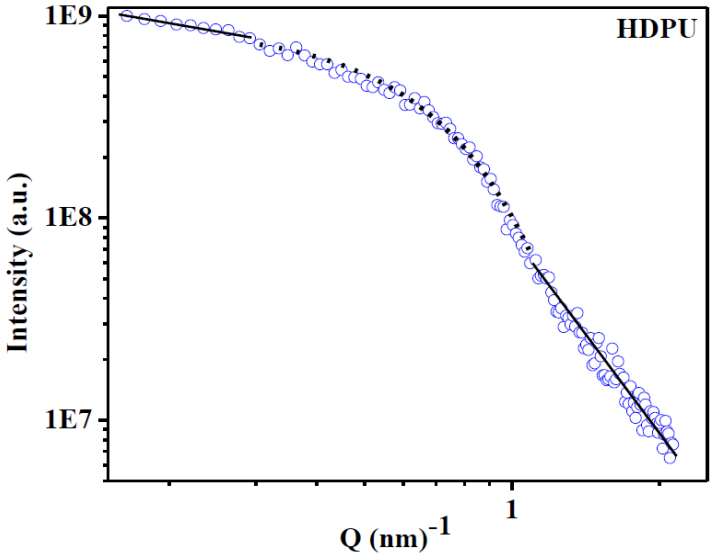

Figure 3.9: *Small angle X-ray scattering profile of HDPU. Solid line is representation of power-law. Dashed line is fit to the data.*

For scattering from smooth surface α will be 4, following Porod's law. Extensive structural studies[25], [28], [47], [48] showed that PU undergoes micro-phase segregation to hard and soft segments during preparation. If the hard segment domains are spatially correlated, a peak will be visible in the SAXS data. Thus, broad maximum in the mid-Q region suggests correlation between the positions of domains existing in the polymer matrix. The data in this region is fitted well to the Gunier equation.[49, 50]

$$I = I_0 e^{-R_g^2 \frac{q^2}{3}}$$

where R_g is the radius of gyration of the domains. The radius of the domains is found to vary between 2.7-3.3 nm. The average distance (d) between domains can be found from the peak position (Q_m) and is in the range 8-10 nm with minimum value for FHDPU (1.4). The slope of

SAXS data in the High-Q region varies between 2.8-2.9, suggesting that domains are made of compact, highly dense mass with fractal morphology. The low-Q region has limited number of data points; hence details on the structure cannot be obtained, although the slope value in the range 1.1-1.3 indicates the presence of loosely bound polymer aggregates. It is known[51], [52] that the hard segment domains self-organize to form aggregates of μm size due to inter molecular hydrogen bonding. Thus, it is possible that SAXS profiles at low-Q region arise from aggregation of HS formed during the preparation of samples. Since the upper Q-limit of the mass fractal is well below the Q-range of study, the average size of the aggregates cannot be obtained from SAXS data, though it will be > 40 nm. On the hand for the samples FHPU, FHDPU (0.52), the SAXS profiles vary lineally with change of slope at a Q as showed in *Figure 3.10.*

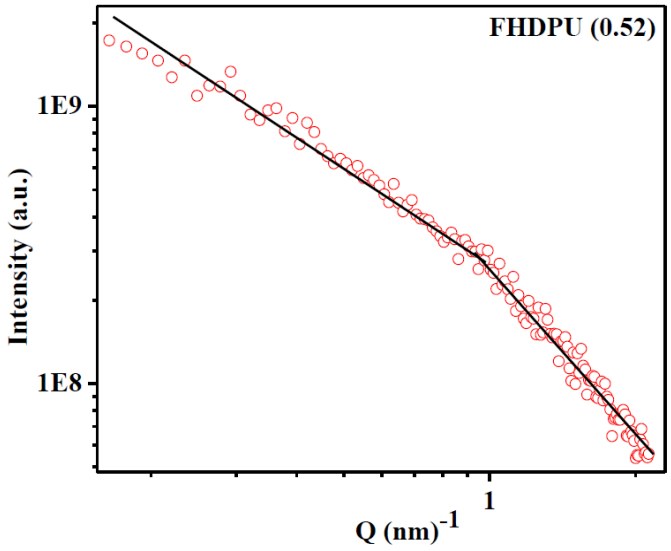

Figure 3.10: *SAXS profile of samples FHDPU (0.52). Solid lines are representation of power-law.*

The power-law exponent in the low-Q region varies between 1.1-1.3 suggesting that the samples consist loose compact polymer rich regions or aggregates of HS domains with mass fractal structure. In the high-Q region, representing the structure on smaller length scale, the slope of the line varies between 1.7-2.3. This indicates the presence of smaller dense crystallites

or HS domains. From the crossover point of two lines, the average radius of the domains is found to be in the range 3.6-4.1 nm. Comparing the two set of samples, two prominent differences can be noticed. The domains formed in *Figure 3.10* are not spatially correlated, less compact and marginally larger whereas in *Figure 3.9*, they are correlated and highly compact.

3.3.8. Morphological study

The formation of HSD as confirmed by SAXS study also appears in morphology when the cross-section of the cryo-fractured PU films studied by FESEM analysis (*Figure 3.11*). The fibrous-assembly morphology which are crossed and entangled with each other has been observed for HDPU (not shown here) which is well accord with our earlier report.[36] In other cases, we can clearly see that the phase segregated polymer rich regions with compact mass fractal appear like solid elliptic sphere (shown by the dotted red line in the images). This again may be attributed to preponderance of DNB to PVF intra interaction over inter polymer chain interactions. Another aspect also can be observed in terms of packing nature, except for FHPU all other ferrocene modified PU has got nice well-ordered packing pattern, this may be because of presence of DNB. Ferrocene containing polymer in presence of DNB gets packed in a particular manner giving nice layered kind morphology which is totally absent for FHPU. And as expected with increase in Fe content segregated domain size also increases.

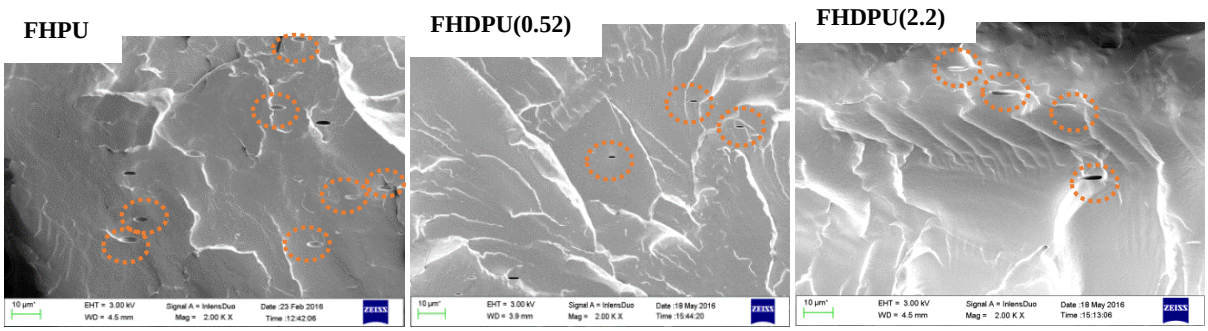

Figure 3.11: *FESEM images of the cross-section of cryo-fractured PU films: FHPU, FHDPU(0.52) and FHDPU(2.2).*

3.3.9. Composite solid propellants (CSPs) studies

Burn rate data of HTPB, HTPB-DNB and one of the representative sample FHD2 have been tabulated in *Table 3.6*. It shows that burn rate has been increased upto~18% on PVF grafting than HD and~12% than that of pristine HTPB. Though this increment is not that much significant than our previous report but from the pressure index value we can conclude that the CSPs made from FHD(0.92) as well as HD are quite stable and confirms the less sensitivity of the CSPs.[24] Compared to previous report this study reveals that apart from Fe wt % there must have some other issues which may responsible for higher burn rate. Overall this result clearly suggests that PVF has been successfully grafted onto the HTPB-DNB binder backbone.

Table 3.6: *Burn rate and pressure index of CSPs made from HTPB, HTPB-DNB and HTPB-DNB-g-PVF binders.*

CSP	Binder Used	Fe (wt%) in Binder	Burn rate 40 bar (mm/s)	Burn rate 70 bar (mm/s)	Pressure index
P1	HTPB	0.00	10.64	14.36	0.53
P2	HD	0.00	10.08	13.95	0.58
P3	FHD2	0.92	11.95	14.44	0.33

3.4. Conclusion

A series of poly (vinyl ferrocene) grafted dinitrobenzene containing polybutadiene (PVF-*g*-HTPB-DNB) have been prepared successfully and all their physical properties have been characterized and correlated with PVF-*g*-HTPB as well as bare HTPB-DNB. In every case, we have been able to incorporate good amount of Fe with good control in viscosity having high storage capacity and hence can be claimed to be a potential burn rate modifier binder for composite solid propellant. The reversible redox property of grafted PVF over HTPB polymer

matrix has been thoroughly analyzed which may explore a new direction of this polymer. Further, we have made polyurethane samples by using PVF-*g*-HTPB-DNB as soft segments and IPDI as hard segments with constant NCO/OH ratio. In comparison with PVF-*g*-HTPB-PU, all the PVF-*g*-HTPB-DNB-PUs displayed an outstanding elasticity, attributed to inclusion of DNB into the polymer matrix. DNB caused a supramolecular hydrogen bonding with HS at the SS chain end. That helped to increase the inter polymer chain distance and thus SS flexibility increases. Based on DSC and DMA study, PVF-*g*-HTPB-DNB-PUs possessed lower glass transition temperature than of PVF-*g*-HTPB-PU. WAXD and SAXS analysis indicated the presence of small dense aggregates or crystallites which appeared because of phase segregation. This phase segregation in PU film had been further confirmed by the appearance of round to ellipsoid shaped hard segment domains in FESEM. Based on the burn rate data as well as other characterization data, PVF-*g*-HTPB-DNB-PUs expected to be used as binder cum burn rate catalyst in composite solid propellant.

Appendix I

GPC profiles of all the samples, FT-IR of the few selected samples and WXD pattern of the PUs are included in the Appendix I (page no. 236-238).

References

[1] D. Randall, S. Lee, The Polyurethanes Book; John Wiley & Sons, London, **2003**.

[2] C. Prisacariu, Springer-Verlag, Wien, New York, **2011**.

[3] B. Lucio, J. L. D. L. Fuente, *Polymer* **2018**, *140*, 290-303.

[4] B. Lucio, J. L. D. L. Fuente, L. M. Cerrada, *Macromol. Chem. Phys.* **2015,** *216*, 2048−2060.

[5] G. R. Whittell, I. Manners, *Adv. Mater.* **2007**, *19*, 3439-3468.

[6] J. C. Eloi, L. Chabanne, G. R. Whittell, I. Manners, *Mater. Today* **2008,** *11*, 28-36.

[7] A. S. A. E. Aziz, E. A. Strohm, *Polymer* **2012**, *53*, 4879-49211.

[8] R. Tong, Y. Zhao, L. Wang, H. Yu, F. Ren, M. Saleem, W. A. Amer, *J. Organomet. Chem.* **2014**, *755*, 16–32.

[9] J. Gao, L. Wang, H Yu, A. Xiao, W. Ding, *Propellants Explos. Protech.* **2011,** *36*, 404-409.

[10] W. Zhou, L. Wang, H. Yu, R. Tong, Q. Chen, J. Wang, X. Yang, Z. Abdin, M. Saleem, *Appl. Organometal. Chem.* **2016,** *30*, 796–805.

[11] K. Subramanian, K. S. Sastri, *J. Appl. Polym. Sci.* **2003,** *90*, 2813–2823.

[12] A. Unver, N. Dilsiz, M. Volkan, G. Akovalı, *J. Appl. Polym. Sci.* **2005,** *96*, 1654–1661.

[13] B. S. Cho, S. T. Noh, *J. Appl. Polym. Sci.* **2011,** *121*, 3560–3568.

[14] K. Fujimura, A. Miyake, *Sci. Technol. Energetic Mater.* **2010,** *71*, 65–69.

[15] G.M. Gore, A.N. Nazare, C. N. Divekar, S. K. Hait, S.N. Asthana, *J. Energetic Mater.* **2004,** *22*, 151–169.

[16] Q. Zhou, S. Jie, B.G. Li, *Ind. Eng. Chem. Res.* **2014,** *53*, 17884–17893.

[17] Z. Cao, Q. Zhou, S. Jie, B.G. Li, *Ind. Eng. Chem. Res.* **2016,** *55*, 1582–1589.

[18] Q. Zhou, B.G. Li, S. Jie, N. Zheng, *Catal. Sci. Technol.* **2014**, *4*, 773–779.

[19] Q. Zhou, S. Jie, B.G. Li, *Polymer* **2015,** *67*, 208–215.

[20] J. P. Santerre, J. L. Brash, *Ind. Eng. Chem. Res.* **1997,** *36*, 1352-1359.

[21] S. Sarkar, B. Adhikari, *Eur. Polym. J.* **2001,** *37*, 1391-1401.

[22] S. L. Huang, P. H. Chang, M. H. Tsai, H. C. Chang, *Sep. Purif. Technol.* **2007,** *56*, 63–70.

[23] M. Amrollahi, G. M. M. Sadeghi, Y. Kashcooli, *Mater. Design.* **2011**, *32*, 3933–3941.

[24] B. N. Rao, K. Malkappa, N. Kumar, T. Jana, *Polymer* **2019,** *163*, 162–170.

[25] B. N. Rao, P. U. Sastry, T. Jana, *Euro. Polym. J.* **2019**, *115*, 201-211.

[26] K. Malkappa, T. Jana, *Ind. Eng. Chem. Res.* **2013,** *52*, 12887−12896.

[27] B. K. Sikder, T. Jana, *ACS Omega* **2018**, *3*, 3004−3013.

[28] B. N. Rao, P. J. P. Yadav, K. Malkappa, T. Jana, P. U. Sastry, *Polymer* **2015**, *77*, 323-333.

[29] K. R. Kunduru, B. N. Rao, T. Jana, *Macromol. Symp.* **2018**, *382*, 1800090 (1-6).

[30] R. M. Shankar, T. K. Roy, T. Jana, *J. Appl. Polym. Sci.* **2009,** *114*, 732−741.

[31] K. Malkappa, B.N. Rao, T. Jana, *Polymer* **2016**, *99*, 404–416.

[32] K. Malkappa, T. Jana, Hydrophobic, *Ind. Eng. Chem. Res.* **2015**, *54*, 7423-7435.

[33] F. Xiao, X. Sun, X. Wu, J. Zhao, Y. Luo, *J. Organomet. Chem.* **2012**, *713*, 96-103.

[34] Z. Cheng, G. Zhang, X. Fan, F. Bi, F. Zhao, W. Zhang, Z. Gao, *Inorganica Chimica Acta* **2014**, *421*, 191–199.

[35] K. Subramanian, *J. Polym. Sci. A.* **1999**, *37*, 4090–4099.

[36] R. M. Shankar, S. Saha, K. S. Meera, T. Jana, *Bull. Mater. Sci.* **2009,** *32*, 507−514.

[37] R. M. Sankar, T. K. Roy, T. Jana, *Bull. Mater. Sci.* **2011,** *34*, 745−754.

[38] B. Lucio, J. L. D. L. Fuente, *Eur. Polym. J.* **2014**, *50*, 117–126.

[39] Y. Tang, X. Zeng, *J Electrochem Soc.* **2008**, *155*, F82-F90.

[40] A. L. Crumbliss, D. Cooke, J. Castillio, P. W. Neilson, *Inorg. Chem.* **1993**, *32*, 6088-6094.

[41] D.C. Kraiter, P. W. Neilson, C. Zhang, A. L. Crumbliss, *Macromolecules* **2012**, *45*, 3658-3668.

[42] B. M. Upton, R. M. Gipson, S. Duhovic, B. R. Lydon, N. M. Matsumoto, H. D. Maynard, P. L. Diaconescu, *Inorg. Chem. Front.* **2014**, *1*, 271-277.

[43] B. Lucio, J. L. D. L. Fuente, *Polym. Degrad. Stab.* **2017**, *136*, 39-47.

[44] S. Alibeik, A. S. Rizkalla, K. Mequanint, *Eur. Polym. J.* **2007**, *43*, 1415−1427.

[45] T. Seyidoglu, M. A. Bohn, *Propellants Explos. Pyrotech.* **2017**, *42*, 1–13.

[46] P.W. Schmidt, *J. Appl. Cryst.* **1991**, *24*, 414- 435.

[47] S. L. Chang, T. L. Yu, C. C. Huang, W. C. Chen, K. Linliu, T. L. Lin, *Polymer* **1998**, *39*, 3479-3489.

[48] J. T. Koberstein, A. F. Galambos, L. M. Leung, *Macromolecules* **1992**, *25*, 6195-6204.

[49] A. Guinier, G. Fournet, Wiley, New York, **1955**.

[50] O. Glatter, O. Kratky, London, **1982**.

[51] M. Song, H. S. Xia, K. J. Yao, D. J. Hourston, *Euro. Poly. J.* **2005**, *41*, 259-266.

[52] A. Aneja, G.L. Wilkess, *Polymer* **2003**, *44*, 7221-7228.

[53] J. Bandekar, S. Klima, *J. Mol. Struct.* **1991**, *263*, 45-57.

CHAPTER 4

Enhancing segmental compatibility and tuning the structure–property relationship in ferrocenylsilane tethered polyurethane

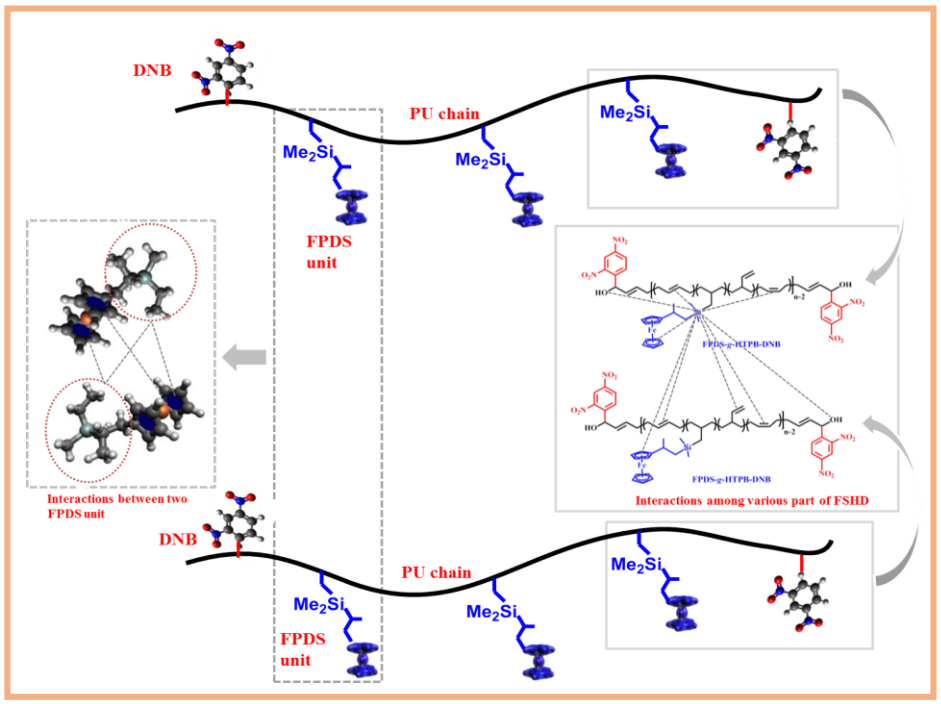

This chapter describes the effect of enhancing segmental mixing by incorporating a suitable functionality at the soft segment in a polyferrocenyl silane based polybutadiene polyurethane, besides all the synthesis and characterization of polymers has been thoroughly mentioned.

4.1. Introduction

During the past decade there has been immense attention on metallopolymers owing to their considerable potential in material science. The presence of a metal atom in a polymer chain offers many unique properties that differ significantly from those of conventional organic polymers.[1, 2] The ferrocenylsilane, a compound consisting of ferrocene and organosilane units, when introduced either in the main chain or side chain of a polymer then the resulting metallopolymer finds several applications in the field of aerospace, automobiles, ceramics, magnetic memory materials, photoconductive devices, electro-catalytic oxidation and even in medical science.[3-8] In particular, ferrocenylsilane based derivatives are often used as burn rate catalyst (BRC) for aerospace application.[8] The burn rate (BR) of the solid propellant is a vital parameter which predominantly influences the composite solid propellants (CSPs) internal ballistic behavior and it has been already well known that the incorporation of ferrocene derivative has been a promising avenue for effectively increasing the BR of CSPs.[8-11] In order to avoid undesired problems like aggregation, sublimation etc.; many attempts have been made to introduce ferrocene based derivatives into the propellant binder.[8-16] Among various binders of this kind developed so far - Butacene (product of SNPE, France), which is (ferrocenyl-4-butyl) dimethylsilane grafted HTPB, is found to be the most effective in the composite propellant because of its high-energetic performances, excellent burning rate catalytic activities and improved anti-migration properties.[17, 18] However, Butacene is unable to replace HTPB as a binder completely; instead it is usually mixed with HTPB as a BRC up to 50 wt %.[18] So, enormous efforts are being pursued by the researchers to acquire a compatible binder cum BRC that can serve as an effective and complete replacement of HTPB.

There are several ways to incorporate ferrocene onto the binder backbone[8,9,11], hydrosilylation is one of them where Si-H reacts with pendant double bond of butadiene backbone in presence of Pt catalyst.[15, 17, 19] Several reports have studied extensively various aspects of ferrocene grafted of HTPB and its PUs[18, 20-22], however the main cause behind the increasing viscosity for ferrocenylsilane based polybutadiene is yet to be ascertained. These findings can help to get into the insight of origin of various important properties starting from thermal, viscoelastic, rheological, mechanical to morphological characteristics of the desired

CSPs composition made with ferrocenylsilane based PU. And, this is required, because, these are the processing parameters well known to understand the thermodynamic compatibility for film formation by mixing polymers.[23, 24]

Our group has explored the influence of terminal functionalization without altering the inherent properties of pristine HTPB.[25-33] It has been demonstrated that viscosity remains constant even after long time storage. Nitrogen rich derivative 2, 4-dinitrobenzene (DNB) was found to be responsible for significant improvement in mechanical properties of PU of HTPB which is attributed to the extra cross-linking through hydrogen bonding occurred between soft segment (SS) and hard segment (HS).[28] DNB even induced many fascinating properties for water dispersible polyurethane (WDPU) nanocomposite synthesized from HTPB-DNB.[34,35] Following the similar methodology recently our group successfully synthesized ferrocene grafted HTPB with improved burn rate with no alternation in microstructure of HTPB which in turn helped in retaining physical properties of pristine HTPB, particularly viscosity and loading capacity.[32] Very recently, we have successfully grafted poly(vinyl ferrocene) (PVF) radically at the pendant vinyl double bond of HTPB-DNB backbone and illustrated that how terminal functionalization able to control viscosity build up rate even for very higher Fe percentage.[36] Presence of DNB makes PVF-*g*-HTPB-DNB-PU films more elastomeric by increasing HS-SS segmental mixing. These studies propelled us to introduce the same nitrogen rich derivative, DNB, to investigate the structure-property relationship for ferrocenylsilane based polybutadiene polymers. In this article, DNB has been incorporated onto the HTPB backbone following the similar functionalization methodology.[25,28,36] Further, 2-(ferrocenylpropyl) dimethylsilane (FPDS) was synthesized and then grafted onto the HTPB-DNB chain through hydrosilylation reaction. The electrochemistry of ferrocenylsilane grafted polymers has also been analyzed by cyclic voltammetry study. The amount of both Fe and Si grafted onto the polymer matrix has been measured by AAS and further investigated to find out their role in various physical properties. Theoretical study also carried out to see the effect of various interactions arises from Si center. PU membranes having different degree of grafted FPDS have been prepared and the effect of enhanced segmental compatibility on various polyurethane properties has been studied. Due to limited availability of ferrocenyl grafted

HTPB in the open market, this work is a successful attempt to explore the possibility of using a ferrocenylsilane based polybutadiene polymer as binder cum BRC in composite propellant.

4.2. Experimental Section

Details of the source of materials are documented in **Chapter 2**. The complete synthetic process of FPDS-*g*-HTPB-DNB was carried out in four steps: first step was the synthesis of HTPB-DNB, second step was the protection of terminal hydroxyl group, FPDS grafting on protected HTPB-DNB was conducted in third step and in the final step (fourth step) protection was removed from the FPDS-*g*-HTPB-DNB. All these steps are discussed briefly in the following sections:

4.2.1. Synthesis of FPDS-*g*-HTPB-DNB [2-(ferrocenylpropyl) dimethylsilane *grafted* HTPB-DNB]

HTPB-DNB was synthesized from HTPB by following our reported method[25, 28] and the synthetic procedure is mentioned in **Chapter 2**. In the second step, 3 g of vacuum dried HTPB-DNB (0.536 mmol, calculated based on the molecular weight obtained from GPC analysis) was dissolved in 10 mL of anhydrous THF in a two neck round bottom flask fitted with a reflux condenser followed by the addition of aluminum chloride hexahydrate (0.275 g,1.138 mmol) at room temperature. After that 0.191 g of 3, 4-dihydro-2H-pyran (DHP, 2.276 mmol) was added drop wise into the stirred solution and refluxed at 60 ºC for 24 hours. The amount of DHP taken based on equivalents calculated from the hydroxyl value of HTPB-DNB. After completion, the reaction mixture was diluted with THF and the product was precipitated by methanol. The obtained polymer was re-dissolved in THF and precipitated again by methanol until the product was free from unreacted aluminum chloride hexahydrate and 3,4-dihydro-2H-pyran. The protected HTPB-DNB polymer was dried in vacuum at 60 ºC for 24 hours.

In the third step, a mixture of 2 g of protected HTPB-DNB (0.346 mmol, calculated based on the molecular weight obtained from GPC analysis) and 0.071 g (0.173 mmol) of hexachloroplatinic acid in 10 mL of dry toluene was stirred at 60 ºC under nitrogen atmosphere.

After 1 hour previously prepared FPDS (0.496g; 1.73 mmol) (synthesis of FPDS was mentioned in **Chapter 2**)[37] was taken in dry toluene and this solution was added drop wise. The reaction mixture was refluxed for another 16h at 80 ºC. The grafted polymer was collected by consecutives precipitation and dissolution process by methanol and hexane until the product was becoming free from excess FPDS. Finally the grafted polymer was dried in vacuum at 60 ºC for 6 hours.

In the final step, mixture of FPDS grafted protected HTPB-DNB (1.5 g, 0.241 mmol, calculated based on the molecular weight obtained from GPC analysis) and aluminum chloride hexahydrate (0.058g, 0.241 mmol) were refluxed in excess methanol at 60 ºC for 24 hours to remove the protection. FPDS-*g*-HTPB-DNB was purified using methanol precipitation process. The reaction mixture was filtered to wash out the excess aluminum chloride hexahydrate. The polymer was re-dissolved in hexane and precipitated again in methanol repeatedly to remove excess FPDS completely. The final grafted polymer was dried in vacuum at 60 ºC for 6 hours. The very deep brown colored grafted polymer (FPDS-*g*-HTPB-DNB) thus further used as a final pre-polymer to form polyurethane.

FPDS was also *grafted* to HTPB following the similar grafting methodology (using last three steps) as discussed above in case of HTPB-DNB. The complete reaction sequence is presented in *Scheme 4.1*.

4.2.2. Synthesis of polyurethane (PU) from FPDS-*g*-HTPB-DNB

In a two neck round bottom flask 3 g of prepolymer (0.373 mmol, calculated based on the molecular weight obtained from GPC analysis) was dissolved in 10 mL of anhydrous THF under nitrogen atmosphere. After stirring 15 minutes, 0.378 g of isophorone diisocyanate (IPDI, 1.7 mmol) (taken based on equivalents calculated from hydroxyl value of prepolymer) was added and stirred at room temperature for 30 minutes under continuous nitrogen flow. After 30 minutes, DBTDL was added as a catalyst and the whole reaction mixture was stirred for 3 hours under nitrogen atmosphere. The progress of the reaction was monitored by FT-IR spectroscopic analysis where disappearance of the isocyanate peak at 2270 cm^{-1} was observed after PU formation. The brown coloured viscous polymer solution was then transferred into a

clean flat based petri dish pre-coated with silicone releasing agent and cured at 70 ºC for 5 days to obtain a free standing PU film.

A similar procedure was also used to make PU from FPDS-*g*-HTPB. The complete reaction process for making PU is given in *Scheme 4.2*. All details of the various characterization techniques are described in the **Chapter 2**.

4.3. Results and Discussion

4.3.1. Synthesis of 2-(ferrocenylpropyl) dimethylsilane *grafted* HTPB-DNB (FPDS-*g*-HTPB-DNB) and polyurethane of FPDS-*g*-HTPB-DNB

Dinitrobenzene (DNB) functionalized hydroxyl terminated polybutadiene (HTPB-DNB) were prepared via terminal functionalization technique following our reported procedures.[25, 28] Further FPDS was synthesized and grafted at the pendant vinyl double bond of HTPB-DNB backbone through hydrosilylation reaction in presence of Pt catalyst *via* a protection-un-protection sequence. The complete reaction process is presented in *Scheme 4.1*. All the physical characteristics of FPDS-*g*-HTPB-DNB (FSHD) are listed in *Table 4.1* along with the characteristics data of HTPB-DNB (HD) and FPDS-g-HTPB (FSH). Recently, we have demonstrated that viscosity (fluidity) of ferrocene modified HTPB with high Fe content can be controlled effectively by introducing DNB at the terminal position of HTPB. This was achieved because of strong interaction between DNB and the ferrocene molecule. We have extended our this idea by introducing DNB to get control over viscosity for ferrocene and silicon based polybutadiene polymers in this work. But the presence of high bonding agent like Si restricted the flow characteristic considerably.[38] With high monomer equivalence (content of FPDS), Fe content gradually increases with gradual decrease in hydroxyl value (*Table 4.1*). The increased molecular weight obtained by GPC analysis confirms the successful attachment of FPDS onto the HTPB and HTPB-DNB matrix (*Table 4.1*). All the FPDS-*g*-HTPB and FPDS-*g*-HTPB-DNB polymers have similar molecular weight distribution. Both Fe and Si content of the synthesized polymers were estimated spectrophotometrically by AAS method and found to increase with increasing FPDS equivalence (*Table 4.1*).

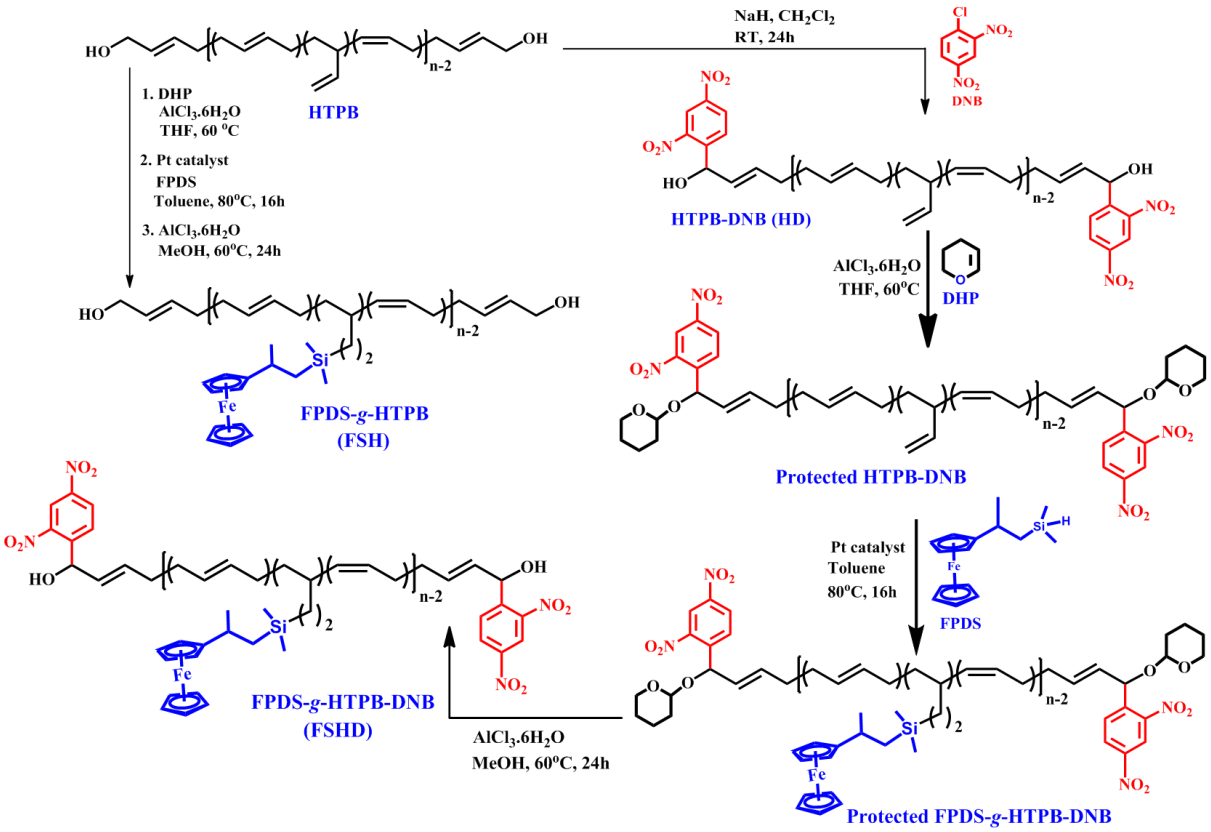

Scheme 4.1: *Synthesis of HTPB-DNB, 2-(ferrocenylpropyl) dimethylsilane-grafted-HTPB (abbreviated as FPDS-g-HTPB), 2-(ferrocenylpropyl) dimethylsilane-grafted-HTPB-DNB (abbreviated as FPDS-g-HTPB-DNB). To make the representation easier HTPB-DNB, FPDS -g-HTPB, and FPDS-g-HTPB-DNB have been abbreviated further as HD, FSH and FSHD, respectively.*

After DNB modification even with lesser Fe content, all this FPDS based samples becoming more viscous compared to PVF-*g*-HTPB-DNB (FHD) in our recently published work.[36] In order to understand this observation, further a solubility test in toluene has been performed to prove that Si acts as a good bonding center in the polybutadiene polymer.[38]

Table 4.1: *Variation in reaction conditions and various physical parameters of the all FPDS-g- HTPB-DNB (FSHD) samples including HTPB-DNB (HD, first entry) and FPDS-g-HTPB (FSH, 2nd entry).*

Sample identity		$\overline{M_n}$ [a]	Đ [a]	Viscosity (cp) at 30°C	Viscosity (cp) at 30°C	Hydroxyl value (mg KOH/g)	Fe content (wt. %)	Si content (wt. %)
HD	--	5600	2.53	5600	5669	40.8	0.0	0.0
FSH	5	8005	1.88	9130	Sticky	39.2	0.23	1.6×10^{-3}
FSHD1	1	8015	1.93	7190	Sticky	38.96	0.26	1.8×10^{-3}
FSHD5	5	8035	1.77	9235	Sticky	31.74	0.83	1.8×10^{-3}
FSHD10	10	9182	1.68	11587	Sticky	19.51	1.3	2.5×10^{-3}

[a] Number average molecular weight ($\overline{M_n}$) and dispersity (Đ) are obtained from GPC analysis. All the GPC chromatograms are shown in *Appendix II- Figure 4.1*. [b] Measured immediately after preparation. [c] Measured after two months. [d] Measured by following acetylation method, which involves the replacement of a hydrogen of hydroxyl group by acetyl group. [e] Obtained from atomic absorption spectroscopic (AAS) analysis. [#] Amount of FPDS added for carrying out grafting process.

Toluene has been chosen as solvent to investigate the interaction between Si and double bond of HTPB which is suspected as the prime reason for more cross-linking for Fe and Si containing HTPB. The solubility results of the synthesized FSHD polymer, which contains both Fe and Si, are compared with HD and our earlier reported[36] FHD polymer (contain only Fe) in *Table 4.2*. The data show that the presence of Si improves the solubility of FSHD polymer compared to FHD. Only a small difference in the solubility observed between HD and FHD which contains only Fe in the chain. These observations are suggesting that the presence of Si in case of FSHD makes it quite different than FHD even though amount of Fe present in both the cases

are quite similar. Si can interact strongly with terminal hydroxyl functionality of HTPB as well as with -NO_2 group of DNB and Fe center of ferrocene- all these interaction makes the FSHD is quite different than the HD, FSH and FHD. In the later section, we have probed all these interaction theoretically using DFT calculation.

Table 4.2: *Solubility of HD, FHD and FSHD in toluene. Solubility duration is the time after which amount of samples dissolved (wt.%) as shown in the table was measured. FHD sample is from our previous work [36] which contains 1 wt. (%) Fe. FSHD10 contains 1.3 wt. % Fe.*

Solubility duration (min)	**HD (wt. %)**	**FHD (wt. %)**	**FSHD10 (wt. %)**
3	1.98	2.13	2.98
5	1.93	2.23	3.10
10	1.68	2.43	3.10

Further the synthesis of FPDS based polybutadiene PUs were carried out in anhydrous THF with IPDI in presence of DBTDL catalyst by keeping the –NCO / -OH constant and equal to 1:1 at inert atmosphere (*Scheme 2.2*). Finally, PU films were prepared after curing for 5 days at 70 ºC. In order to compare various properties we have also made PU from HD and FSH samples following the similar procedure and these are named as HDPU and FSHPU, respectively.

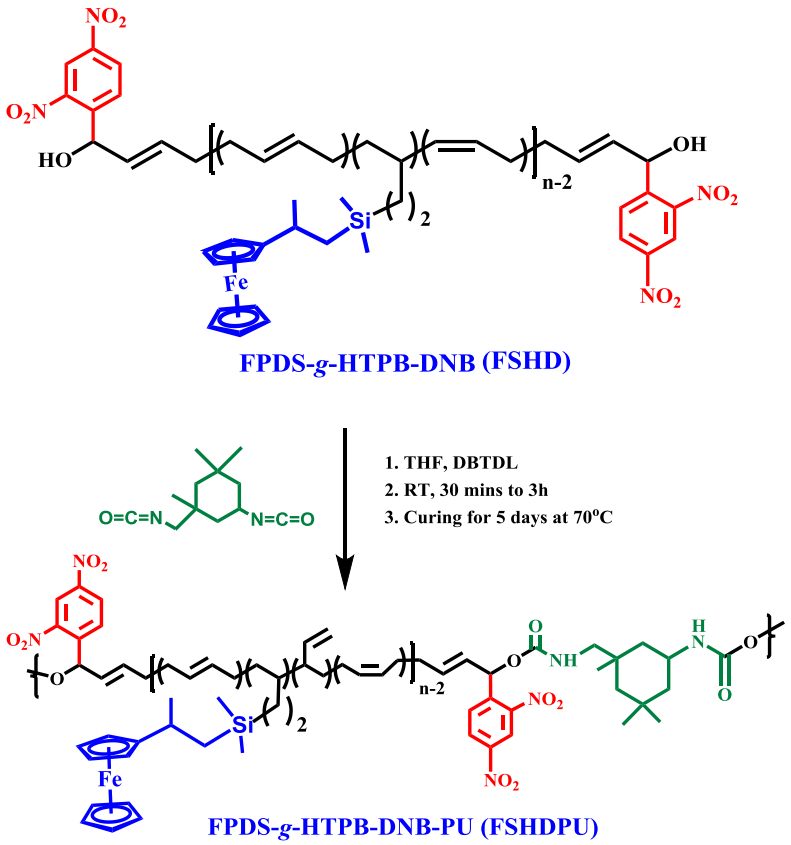

Scheme 4.2: *Synthesis of FPDS-g-HTPB-DNB (FSHD) based polyurethanes (PU). These samples are abbreviated as FSHDPU(XX) where XX indicate the wt.% of Fe in the FSHD samples.*

4.3.2. Spectroscopic study

The FTIR spectra of HTPB-DNB (HD) and FPDS-*g*-HTPB-DNB (FSHD) along with FPDS are presented in *Figure 4.1(A)*. The characteristic peaks at 887 cm^{-1} and 753 cm^{-1} correspond to 1,2-vinyl and 1,4-cis microstructure of polybutadiene backbone in HD sample. After modification with FPDS, the peak intensity at 887 cm^{-1} gradually decreases and only when Fe and Si amount is more a prominent shift has been observed for the peak at 753 cm^{-1} to 707 cm^{-1}. The characteristic Si-H peak in FPDS at 2115 cm^{-1} disappeared indicating the successful grafting of FPDS onto the HTPB backbone. Another characteristic peak of HD appears at 1349 cm^{-1} which corresponds to asymmetric stretching of $–NO_2$ of DNB moiety[28],

[36] is gradually shifted to lower wavelength with decrease in intensity supports the fact that –NO_2 is in interaction with the grafted ferrocene ring of FPDS, similarly like our previous report.[36] Because of strong H-bonding with –NO_2, the free hydroxyl group for HTPB-DNB appears at 3396 cm^{-1} which is well accord with earlier report.[28] With higher degree of grafted FPDS, the –OH peak gradually increases from 3415 cm^{-1} to 3439 cm^{-1} [*Appendix II- Figure 4.2(A)*] in FSHD attributes to the fact that grafted FPDS helps to decrease the extent of H-bonding between –NO_2 and –OH by increasing the interaction between FPDS and –NO_2 and this interaction mainly involved ferrocene unit not Si centre which was shown theoretically in the later section.

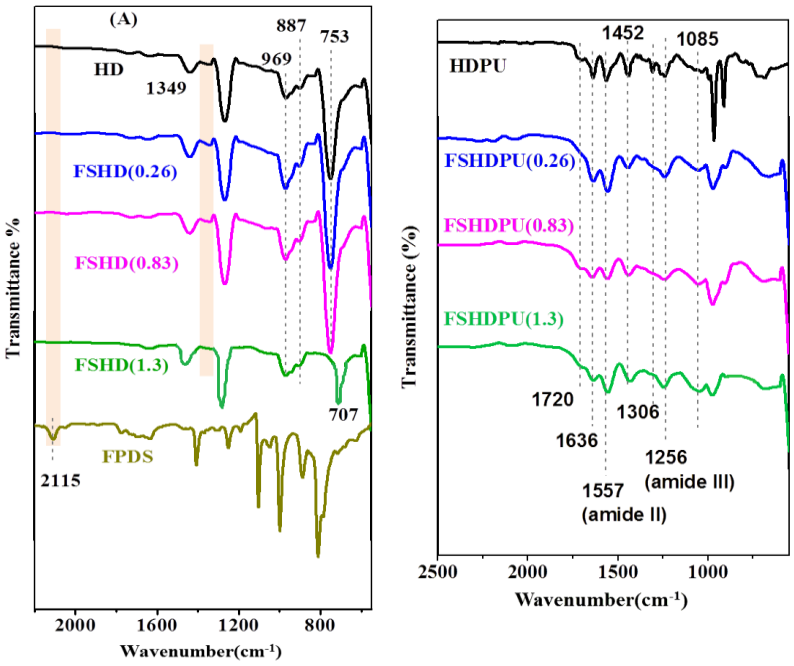

Figure 4.1: *FTIR spectra of (A) HTPB-DNB (HD), FPDS-g-HTPB-DNBs (FSHD) and FPDS (B) HTPB-DNB-PU (HDPU) and PVF-g-HTPB-DNB-PUs (FHDPUs). Sample names are indicated in the figure. Amount of Fe content in the sample is mentioned in the parenthesis after the sample name.*

In *Figure 4.1(B),* the complete disappearance of isocyanate peak at 2270 cm^{-1} confirmed the completion of PU reaction. After curing with IPDI, the characteristic peaks for –OH at 3396

cm^{-1} completely disappears and two new bands appear in two principle vibrational region i.e. at 3335-3352 cm^{-1} for amine (-NH-) stretching [*Appendix II- Figure 4.2(B)*] and at 1720 cm^{-1} for carbonyl peak of the urethane segment [*Figure 4.1(B)*]. The peak at 1636 cm^{-1} corresponds to the carbonyl frequency those are involved in H-bonding within the PU matrix. Negligible shift for the amide III band at 1256 cm^{-1} of HD towards higher wavelength upholds the fact that the H-bonding between DNB and urethane amide linkage in PU matrix gets disturbed by grafted FPDS chain. And the gradual broadening of the characteristic symmetric and asymmetric stretching frequency of $–NO_2$ at 1452 cm^{-1} and 1306 cm^{-1} ascertains the gradual increased interaction of $–NO_2$ with grafted FPDS chain.

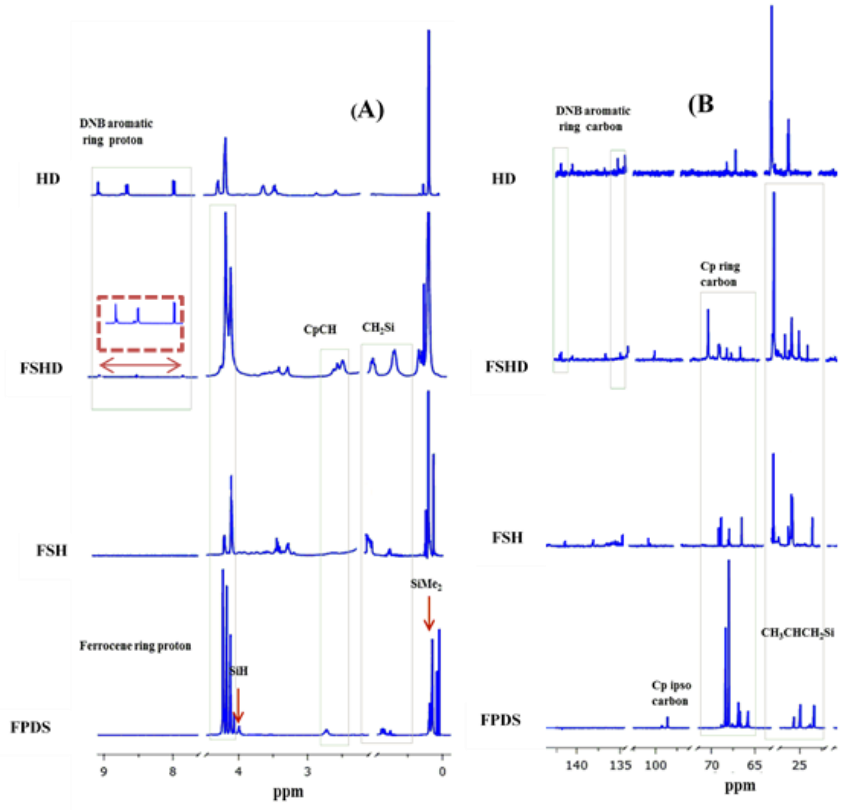

Figure 4.2: *^{1}H-NMR* ***(A)*** *^{13}C-NMR* ***(B)*** *spectra of FPDS modified HTPB.*

Both ^{1}H NMR and ^{13}C-NMR spectra (*Figure 4.2*) were recorded to confirm the structure of the FPDS modified HTPB. Majority of the peaks appeared in these spectra

correspond to the peaks of HTPB. The signals at ~7.78, ~8.37 and ~8.75 ppm in case of HD indicate the presence of DNB moiety which also can be noted in FSHD spectrum. In case of FPDS, Si-H shows multiplates at 3.87-3.9 ppm while 0.06, 0.96, 0.99 and 2.7 ppm are assigned to SiMe2, Si-CH2 and CH(Cp), respectively. The cyclopentadienyl (cp) ring protons for FSH and FSHD appear at 4-4.4 ppm with increased intensity which is exactly matching with FPDS. In the modified polymer the presence of $SiMe_2$ at 0.06 ppm can be clearly observed. ^{13}C NMR also gives the structural confirmation of the modified HTPB polymers. The peaks at 133.8 and 141 ppm in FSHD refer to the aromatic carbons of DNB moiety which is quite similar with HTPB-DNB. Peaks at 67-69 ppm clearly indicate the presence of ferrocenyl carbon exactly identical with FPDS cyclopentadiene ring carbon. The peaks at 23.7, 28.8 and 29.5 ppm appear in FPDS for the carbon signal of $MeCHCH_2Si$ which are also present in both FSH and FSHD. In FPDS, the peak at 98 ppm corresponds to Cp-ipso carbon signal which can be seen in both FSH and FSHD.

4.3.3. Theoretical study

Theoretical study using density function theory (DFT) has been carried out to investigate how the presence of Si and ferrocene functionality affects various physical properties of FSH and FSHD polymers. Very recently, we have proposed theoretically that DNB functionality by interacting with Π electron of cyclopentadiene ring of ferrocene helps to weaken the extent of London dispersion interactions between two ferrocene units which indirectly controls the viscosity of PVF-g-HTPB-DNB prepolymer.[36] Now the main interest here in this article is the presence of Si center along with ferrocene and DNB functionality in the HTPB chain. Theoretical calculation using DFT has been performed on two important moieties of polymer chain and these are CH3CH2Si(Me2)CH(Me)CH3 (these are portion of FPDS) and ferrocene in order to understand their function in the HTPB chain. The physical parameters obtained through DFT calculations using Gaussian package (GAUSSIAN-09) are shown in *Table 4.3 and 4.4*. We have reported the polarizability value of ferrocene is 33 $Bohr^3$ in our previous report[36] and therefore being a highly polarizable group, ferrocene can interact with $CH_3CH_2Si(Me_2)CH(Me)CH_3$ unit as well as other ferrocene unit. The London dispersion

force energy (E_L), which are tabulated in *Table 3.3*, arising from these interactions are calculated using the equation, $E_L = -3I\alpha^2/4r^6$ where I is the ionization energy, r is the intermolecular distance between two ferrocene unit which is considered as 0.3 nm and α is polarizability of ferrocene and $CH_3CH_2Si(Me_2)CH(Me)CH_3$ unit. Though the ferrocene-ferrocene interactions are most effective but from the dispersion energy value (*Table 3.3*) it is clear that $CH_3CH_2Si(Me_2)CH(Me)CH_3$ unit also has a major role in the non-covalent interactions and this arises only because of the presence of Si center in the chain.

Table 4.3: *London dispersion force energy among various possible interacting sites of FSHD. Data obtained from DFT calculation.*

Possible interacting units	**London dispersion force energy (kJ/mol)**
$CH_3CH_2Si(Me_2)CH(Me)CH_3$ - $CH_3CH_2Si(Me_2)CH(Me)CH_3$	−1.6
Ferrocene - Ferrocene	−17.1
$CH_3CH_2Si(Me_2)CH(Me)CH_3$ - Ferrocene	−5.2

The various energy values of HOMO-LUMO interactions between Si and other part of the polymer chain have been calculated by using DFT calculation and summarized in *Table 4.4*. LUMO of Si will interact with the HOMO of other functionality. From the HOMO-LUMO energy value it is clear that Si can strongly interact with ferrocene also with trans/cis double bond present in the butadiene backbone as well as with the terminal –OH functionality of polymer chain. The possibility of interaction of Si with DNB is quite less as the HOMO-LUMO energy gap between DNB (HOMO) and Si (LUMO) is much larger than all other HOMO-LUMO gaps (*Table 4.4*). *Figure 4.3* shows a graphical representation of various interactions among two FPDS units [*Figure 4.3(A)*] and the interactions of Si with other functionalities in

the HTPB chain [*Figure 4.3(B*)] in case of FSHD samples. It is clearly visible from this representation the absence of any kind of interaction between Si and DNB in the FSHD chain as the HOMO (DNB) – LUMO (Si) gap is very significant (*Table 4.4*).

Table 4.4: *HOMO and LUMO energies obtained from DFT calculation for various molecules of interest. (B3LYP/DFT calculation is used in all the cases).*

Molecule of interest	**Basis set**	**HOMO energy (a.u.)**	**LUMO energy (a.u.)**
Si	6-31+G(d,P)	−0.161	−0.130
Ferrocene	Fe : LANL2DZ C, H: 631+G*	−0.202	−0.014
DNB	aug-ccpvdz	−0.320	−0.131
CH_3OH	6-31+G(d,P)	−0.282	0.0004
Trans-butene	6-31+G(d,P)	−0.244	0.014
Cis-butene	6-31+G(d,P)	−0.243	0.009

In our recent report we mentioned how electron affinity of DNB predominates the intra-interactions of ferrocene and DNB by reducing the inter-interactions of ferrocene-ferrocene unit.[36] But in the present scenario, presence of Si causes various types of non-covalent interactions with different part of the polymer chain and these interactions make the DNB effect over the ferrocene functionality quite insignificant. This is the reason we cannot see much control over viscosity increment even in presence of DNB unlike our previous report.

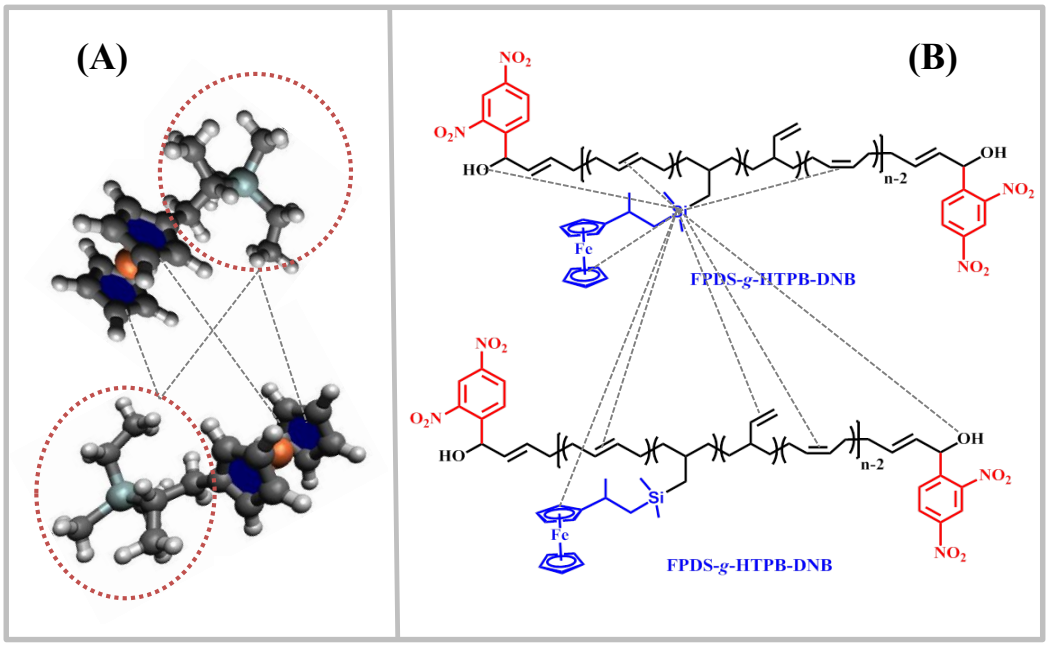

Figure 4.3: *Graphical view of various kinds of interactions (A) among various parts of FPDS units and (B) between Si and other functionalities of FSHD chain. Interactions are shown by dotted black lines. Dotted red circles are used to show the portion of FPDS which contains Si center. Note the absence of interaction between Si and DNB part of the FSHD chain.*

4.3.4. Electrochemical study

Figure 4.4 represents the cyclic voltammetric (CV) waves of the FSH and FSHD samples with different Fe content in CH_2Cl_2 solution. The cyclic voltagramms waves show that the oxidation peak (E_{pa}) of FSHD varies between 610 mV to 428 mV and reduction peak (E_{pc}) of those samples ranges between 567 mV to 310 mV (*Table 4.5*). It is to be noted that the values of both E_{pa} and E_{pc} changes with the change in Fe content in the FSHD sample. E_{pa} and E_{pc} of FSH appears at 611 mV and 578 mV, respectively (first entry in the *Table 4.5*). The various electrochemical parameters including E_{pa} and E_{pc} values extracted from the CV waves (*Figure 4.4*) are also tabulated in *Table 4.5*. A gradual increase in both anodic current (I_{pa}) and cathodic current (I_{pc}) values observed with increasing Fe content in the FSH and FSHD samples (*Table*

4.5) which is consistent with the increase of number of electroactive ferrocene groups per polymer molecule.

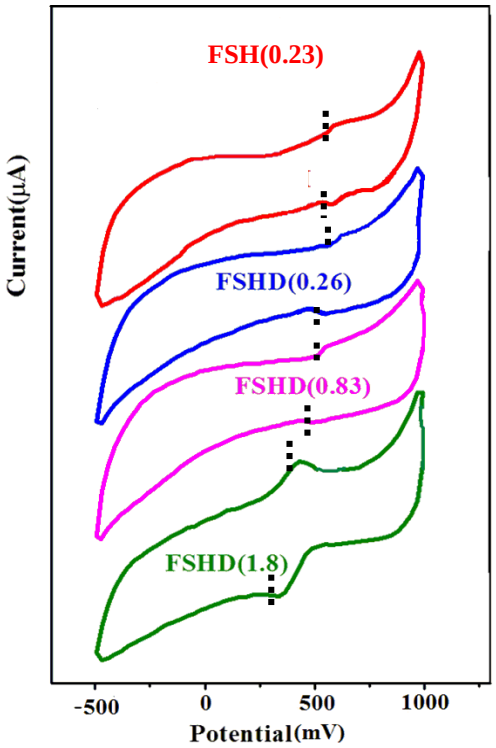

Figure 4.4: *Cyclic voltagramms of FPDS-g-HTPB-DNB (FSHD) samples along with FPDS-g-HTPB (FSH) in CH_2Cl_2 solution. Fe content in the samples is indicated in the parenthesis after sample name. CVs were recorded by scanning 1.5 V to - 0.8V with scan rate of 0.02 V/sec. 10 mg/mL polymer concentration was used. 10 mmol/L tetrabutylammonium perchlorate was used as supporting electrolyte in N_2 atmosphere. Pt electrode was used as working electrode and Ag wire was used as reference electrode. Dotted vertical lines are used to identify the peak positions in the CV waves.*

The difference between anodic and cathodic peak potential (ΔE_p) of FSHD samples found to be significantly higher than FSH, and increasing with increasing Fe content in FSHD samples (*Table 4.5*). This is because of the delayed electron transfer process compared to an ideal Nearstian system[39-42] because of the strong interactions between Si center with

cyclopentadienyl rings and as well as with various groups of HTPB chains as discussed in earlier sections. It is also noticeable that $E_{1/2}$ value decreases as Fe content increases in FSHD and this is because of the fact that the electron cloud of cyclopentadiene is getting pulled by various interactions with Si center as discussed from DFT study which makes reduction-oxidation of Fe more difficult.

Table 4.5: *Electrochemical parameters of the FPDS-g-HTPB-DNB (FSHD) and FSH in CH_2Cl_2 solution. All the values are averages of at least three independent measurements. Standard deviations are shown in the parentheses after the data.* [a] *$E_{1/2}$ values are obtained from the E_{pa} and E_{pc} by averaging their values.*

Sample Identity (% of Fe)	E_{pa} (mV)	E_{pc} (mV)	$E_{1/2}$ (mV) [a]	ΔE_p (mV)	I_{pa} (µA)	I_{pc} (µA)
FSH(0.23)	611 (0.24)	578 (0.33)	595 (0.28)	33 (0.21)	2.7×10^{-8}	1.59×10^{-8}
FSHD(0.26)	610 (1.31)	567(0.74)	589 (0.47)	43 (1.96)	4.98×10^{-8}	2.27×10^{-8}
FSHD(0.83)	566 (1.41)	469 (0.21)	518 (0.61)	97 (1.6)	5.17×10^{-8}	3.00×10^{-8}
FSHD(1.3)	428 (0.14)	310 (0.41)	369 (0.22)	118 (0.43)	1.00×10^{-7}	1.10×10^{-7}

4.3.5. Mechanical properties of polyurethanes (PUs) obtained from FSHD

Tensile properties of the membranes were measured by universal testing machine and the stress-strain curves (*Figure 4.5*) are analyzed in details. All the mechanical stability related parameters like tensile strength (σ_b), % elongation (ε_b) and Young's modulus (E) were tabulated in *Table 4.6*. A simple comparison of FSHPU profile to others (*Figure 4.5***)** clearly indicates that the rigidity of the PU is greatly affected by terminal functionalization of HTPB. We have discussed in great detail in our earlier reports - how terminal functionalization at the end of polybutadiene chain helps to increase both σ_b and ε_b simultaneously by increasing segmental

mixing between hard segment (HS) and soft segment (SS),[28-31, 33, 36] *Figure 4.5* clearly shows that FSHDPU becomes much more flexible and elastomeric after modification with DNB by terminal functionalization at the SS chain end while in FSHPU (which do not have DNB) displays very poor elongation. The presence of FPDS at the soft segment (SS) domain of FSHPU causes very high crosslinking by intermolecular interaction through Si and double bond of polybutadiene backbone which is also earlier reported by Kishore et al.[38] But the presence of DNB in case of FHSDPU helps to increase the elongation at break remarkably exactly like our recently reported work.[36] The extra supramolecular H-bonding between DNB and urethane linkage at the terminal end of soft segment (SS) domain helps to increase the mobility of FPDS containing SS polymer chain which makes the membrane to be more elastomeric. FSHDPU(0.83) shows maximum elongation among the series which can be ascribed to the significant correlation between intra and inter polymer chain interactions.[36] Further increase in Fe%, effective crosslinking density is increasing through inter-chain crosslinking process resulting higher tensile strength with lower elongation at break.

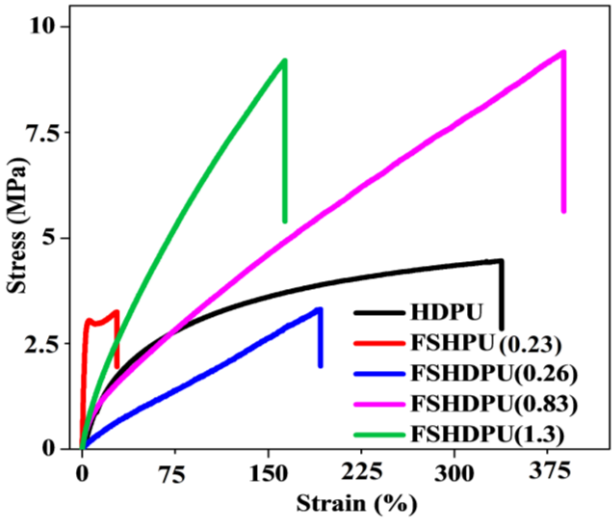

Figure 4.5: *Stress-strain plots of FSHPU, HDPU and FSHDPUs. Fe content (in wt %) in the sample is given in the parenthesis after the samples name.*

Table 4.6: *Various mechanical parameters obtained from tensile studies of PUs*

Samples	Tensile strength (σ_b, MPa)	Elongation at break (ε_b, %)	Toughness (MPa)[a]	Young Modulus (E, MPa)[b]	Effective cross linking (N, m^{-3})[c]
FSHPU(0.23)	3.25	27.9	81.43	1.02	8.2×10^{19}
HDPU	4.45	336.9	1050.53	0.08	6.1×10^{18}
FSHDPU(0.26)	3.22	191.8	333.66	0.03	1.8×10^{18}
FSHDPU(0.83)	9.41	388.3	2093.98	0.09	7.2×10^{18}
FSHDPU(1.3)	9.22	163.8	875.73	0.11	8.7×10^{18}

[a] calculated by integrating the area under stress-strain plot. [b] calculated from the slope of the linear portion of the stress-strain plot. [c] estimated [36] according to equation N = E / (3RT), where E is the Young's modulus, R the gas constant (8.314 $J.mol^{-1}.K^{-1}$) and T the absolute temperature in Kelvin.

4.3.6. Thermal analysis of the PUs

TGA and DTG analysis were conducted in nitrogen atmosphere from 25 ºC to 500 ºC with a heating rate 10 ºC/ min and data are presented in *Figure 4.6*. All the PUs obtained from FSH and FSHD prepolymers display less thermal stability than HDPU mainly because of the catalytic effect of ferrocene moiety. All the PUs show mainly two stage thermal degradation-quite similar to those of HTPB-based polyurethane.[15, 28, 33, 36] In the first stage, PUs started to decompose at around 247 ºC and reached upto 380 ºC with nearly 14% weight loss. This first stage mainly caused by the degradation of urethane linkages in PU materials. The final and major degradation stage occurred from 415 ºC to 483 ºC with more than 80% weight loss where the decomposition rate is much faster than the former and this stage degradation is associated with the degradation of SS of polybutadiene segments. For both the stages, ferrocene modified PUs started degrading bit earlier because of the catalytic effect of the ferrocene which can be clearly observed from DTG curve [*Figure 6.6(B)*]. The char residue amount is even more than our previously reported PVF-g-HTPB-DNB where only Fe was present as metal residue.[36]

This is an indirect proof of presence of Si along with Fe as a metal residue for FPDS based PUs. Despite the NCO/OH ratio is constant, HS decomposition rate is different because of the concomitant chain scission of some SS part along with the depolycondensation of HS domain.[36, 43] This can be esteemed from the higher degree of decomposition of PU having lesser amounts of Fe and Si and thus FSHDPU(0.26) degrades at higher extent compared to others.

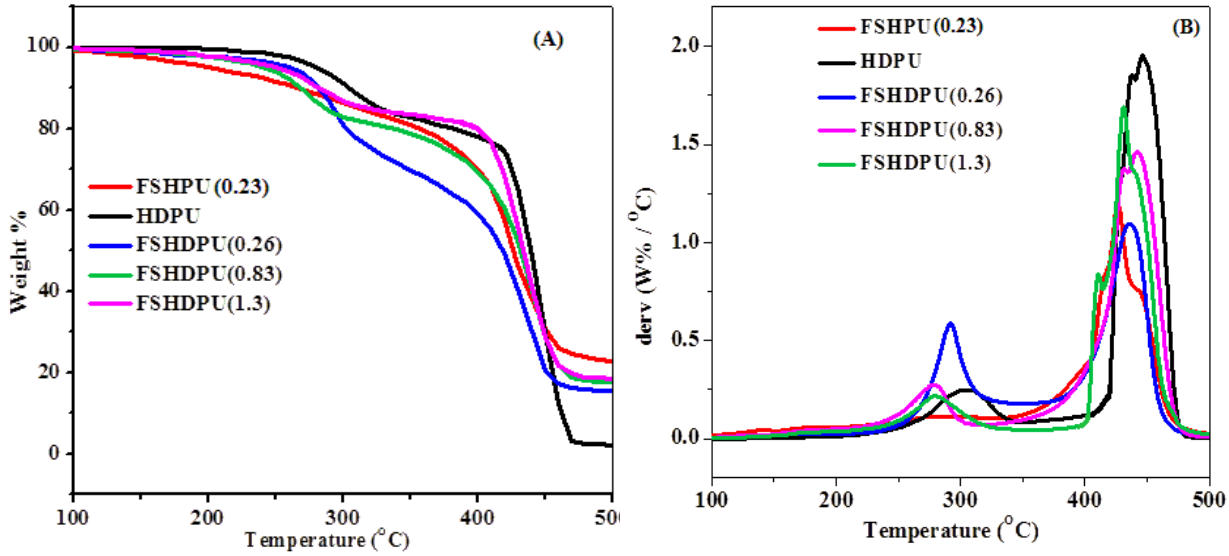

Figure 4.6: *(A) TGA and (B) DTG curves of HDPU, FSHPU and FSHDPUs.*

DMA analysis for a wide range of temperature (-100 ºC to 200 ºC) shows how the elastomeric PUs changes from glassy to rubbery state with the gradual increase of temperature. The storage modulus (E'), loss modulus (E") and tanδ plots against temperature are shown in *Figure 4.7* and the parameters obtained from DMA data are summarized in *Table 4.7*. The results clearly shows that E' of the FSHDPU samples is higher than both FSHPU and HDPU attributing that all the FSHDPUs are more resilient and have better mechanical properties which is in well agreement with tensile data shown in *Figure 4.5* and *Table 4.6*. From E" and tanδ plots, it is clear that presence of DNB helps to have much lower glass transition temperature (T_g) for FSHDPUs than FSHPUs.

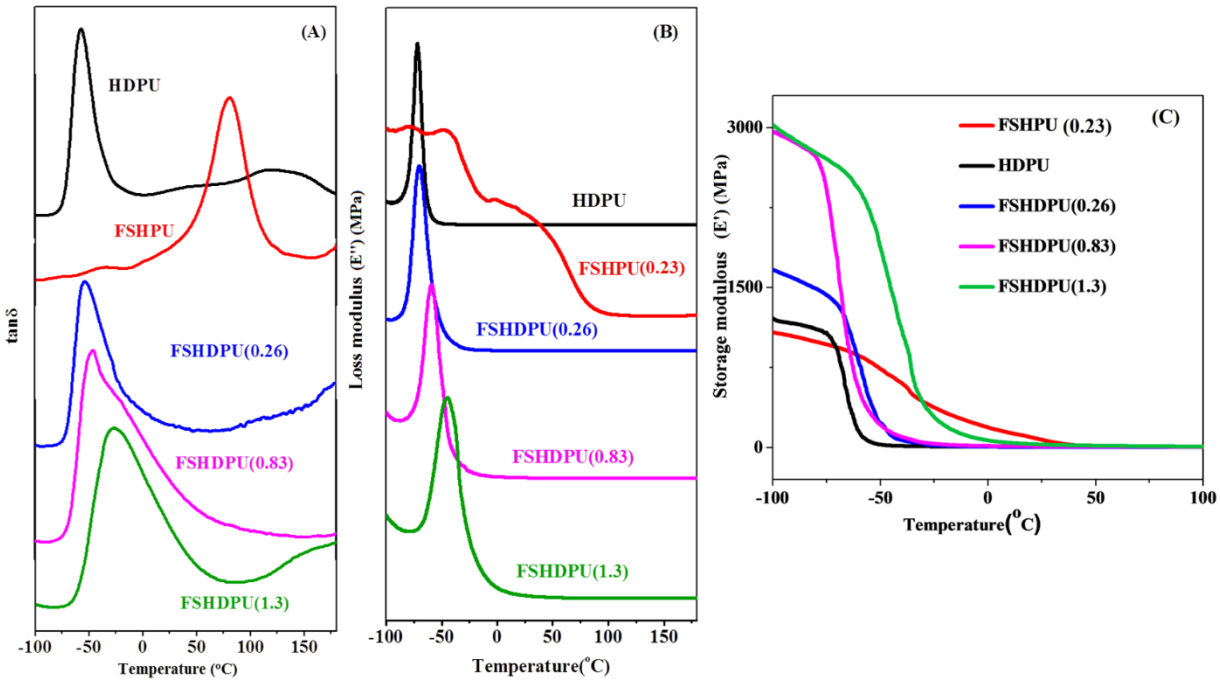

Figure 4.7: *Temperature dependent plots of (A) tanδ (B) Loss modulus and (C) Storage modulus vs of FSHPU, HDPU and FSHDPUs. Plots in case of tanδ vs temperature and loss modulus vs temperature are shifted vertically for better clarification.*

To reconfirm the T_g value and elastic nature of the FPDS based PUs, DSC analysis was further carried out (*Figure 4.8*) and as expected FSHPU displays the highest T_g at –55.29 ºC while the presence of DNB makes FSHDPUs much more elastic and varies the T_g from -74.34 ºC to -62.25 ºC depending on the Fe content. FSHDPU(1.3) possess the highest T_g among all attributing more crosslinking for high Fe and Si containing sample. DSC experiment was further extended to analyze the heat change profile beyond 25 ºC up to 370 ºC. The thermal transitions obtained under inert gas exhibits quite similar profile with the DTG analysis shown in *Figure 6.6(B)*. In this thermogram, the first exotherm is observed between 150 ºC to 250 ºC followed by the second endothermic peak approximately at 350 ºC. This first peak corresponds to the energy released due to cross-linking and cyclisation reactions of the polybutadiene backbone over the chain scission during degradation of polymer.[43] The second endothermic peaks are mainly due to energy absorption by the PUs with subsequent rapid chain scission as

well as cyclisation in the SSs.[43, 44] Like DTG curve, the exothermic peaks for ferrocene based PUs appeared much earlier than HDPU (appear at~270 ºC) because of the catalytic activity of the organometallic compounds.

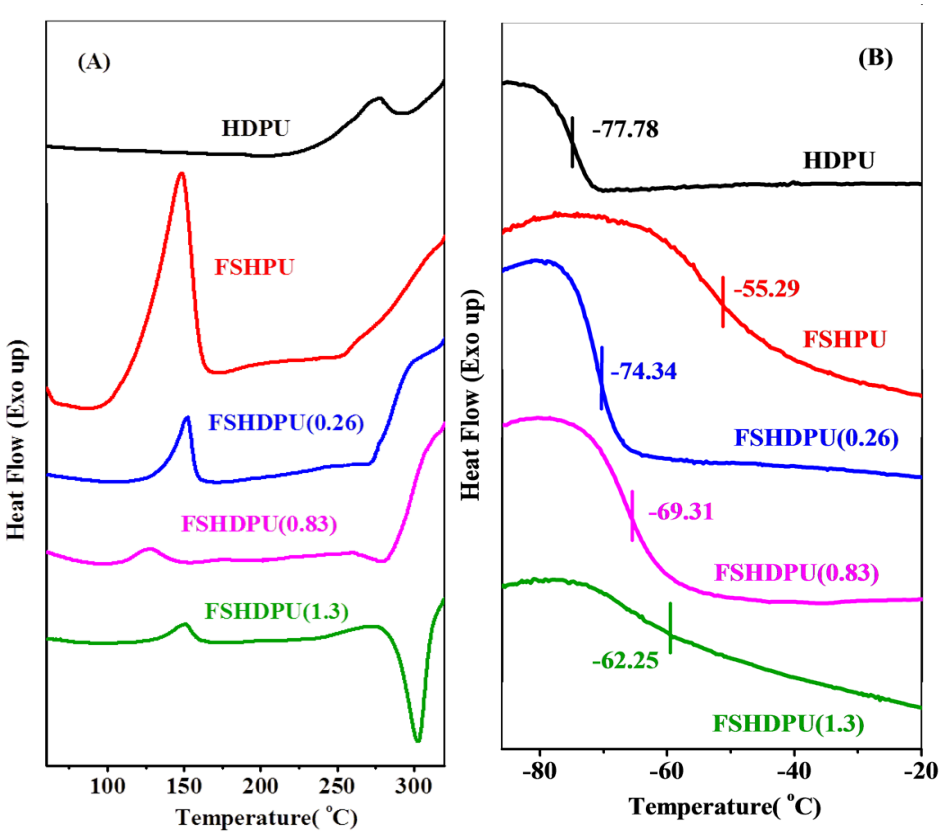

Figure 4.8: *DSC thermograms of HDPU, FSHPU and FSHDPUs in the temperature range: (A) 25 ºC to 370 ºC (B) -100 ºC to 25 ºC.*

Table 4.7: *Glass transition temperature (T_g) and modulus values of all the PUs obtained from DSC and DMA study. The T_g values are written as T_{ssg} because these T_g values are for soft segment (SS) T_g of PUs.*

PU samples	T_{SSg}(°C) from DSC	T_{SSg} (°C) from tanδ	T_{SSg} (°C) from Loss Modulus, E"	Storage modulus,E' (MPa)
HDPU	- 77.8	- 58.5	- 72.1	1168
FSHPU(0.23)	- 55.3	- 30.2	- 42.9	1055
FSHDPU(0.26)	- 74.3	- 60.7	- 69.4	1673
FSHDPU(0.83)	- 69.3	- 47.9	- 59.9	2981
FSHDPU(1.3)	- 62.3	- 28.4	- 45.3	3008

4.3.7. X-ray studies

Appendix II-Figure 4.3 shows the diffraction pattern of all PUs which looks alike to each other. HDPU shows the crystalline peaks at 13.89º, 16.68º, 25.11º and broad amorphous peaks at 19.3º and 42º, quite analogous to previously reported literature.[28] Si and ferrocene based organometallic derivative causes even more crosslinking to the polymer matrix in case of FSHPU and FSHDPU which show more intense crystalline peak at 16.68º. Even though all other peaks are exactly matching with parent HDPU, the intensity of the crystalline peaks at 13.89º and 16.68º varies with increased amount of Fe and Si content. These are arising due to strong interactions between HS and SS through intra as well as inter polymer chain interactions. The similar peak position in all the PUs suggests that they possess identical packing pattern but as their intensity varies hence it may be concluded that their extent of packing pattern may be quite different.

Small angle X-ray (SAXS) measurements were carried out on all samples of FSHDPU including HDPU and FSHPU(0.23) samples. Representative SAXS profiles on log-log scale

for FSHDPU(1.3), FSHPU(0.23) are shown in *Figure 4.9*. A linear variation is observed with change of slope at a Q in the SAXS profile of FSHDPU(1.3). The power-law exponent is found to be 1.2 in the low-Q region which attributes the presence of aggregated hard segment (HS) domains with mass fractal structure. The slope of the line in the high-Q region of *Figure 4.9(A)* is found to be 1.84 which indicates the presence of dense hard segment domains of size about 5.1 nm within the polymer matrix. The SAXS profiles of FSHDPU(0.26) and FSHDPU(0.83) are quite similar to HDPU[36] suggesting that the structure of the samples remain same with the presence of silicon and ferrocene units. The radii of HS domains are 3.73 nm, 4.6 nm with average distances of about 10 nm, 14 nm for FSHDPU(0.26) and FSHDPU(0.83), respectively. Thus, domains are larger as compared to HDPU with gradual increase of size as well as distance with increase in the Fe content from 0.26 to 0.83.[36] The slope of SAXS data for FSHDPU(0.26) and FSHDPU(0.83) in the high-Q region is 2.6, 2.7 suggesting that domains possess mass fractal morphology with nearly same compactness as in HDPU. It can be noticed that with increasing content of Fe from 0.83 to 1.3 in the samples, the spatial correlation among domains in FSHDPU is lost and hence they are randomly distributed in the polymer matrix.

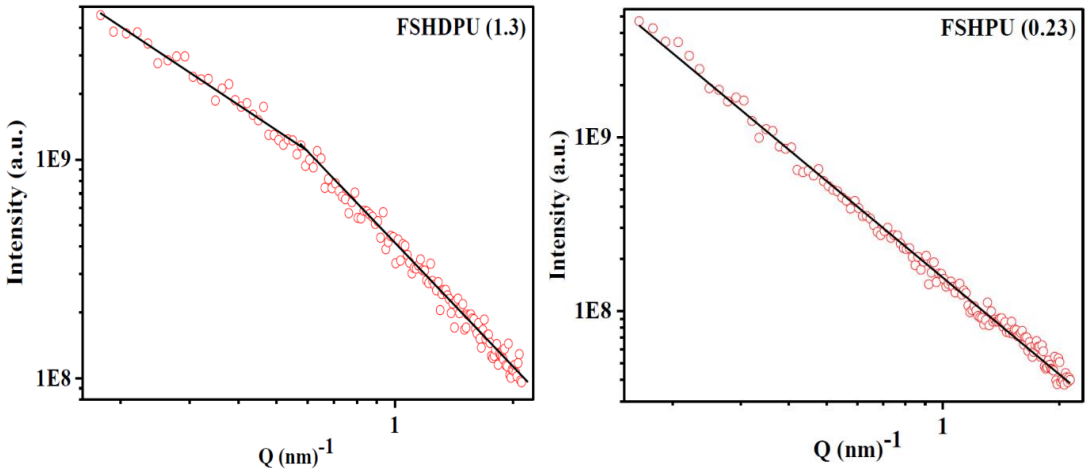

Figure 4.9: *SAXS profile of (A) FSHDPU (1.3) and (B) FSHPU (0.23). Solid lines are representation of power-law.*

In case of FSHPU(0.23), the SAXS profile varies linearly in the entire Q-range with slope (power-law exponent) of 1.85 [*Figure 6.9(B*)**]**. Thus, the sample consists mass fractal aggregates of fractal dimension of 1.85. These clusters may be of polymer solid coexisting within dilute solution or polymer-poor regions formed due to phase separation. Since the line extends up to lowest Q of measurement, the size of the aggregate cannot be estimated though it will be > 35 nm. Combining the structural features of PUs in this study as well as our earlier work[36] it may be noted that the samples exhibit one of the three type of microstructure: a) larger aggregation of HS domains as well as spatially correlated domains -Type I as in HDPU[36] b) larger aggregation of HS domains and uncorrelated or randomly arranged domains -Type II as in *Figure 4.9(A)* and c) only larger domains - Type III as in *Figure 4.9(B).* Thus the SAXS study clearly indicates the influence of Fe and Si contents in the PU on their microstructural behaviors which in turn influences various physical properties.

4.3.8. Morphological study

Cross-section of the cryo-fractured PU films was studied through FESEM analysis (*Figure 4.10*). Small ellipsoid shaped domains are observed in case of PUs obtained from FSH and FSHD. These are hard segment domain (HSD) as discussed in the SAXS analysis in the previous section. Earlier, we have observed that the presence of DNB in HTPB chain enables to get fibrous-assembly type morphology due to strong supramolecular H-bonding between HS and SS region [28] but because of high appetency towards crosslinking owing to the presence of ferrocene as well as Si [38], [45 - 47] in the chain, FPDS modified polybutadiene PUs exhibit phase segregated polymer rich crystallites even in presence of DNB (*Figure 4.10*). It also may be noted that some kind of layer type morphology constituting of fibrils along with ellipsoid domain for HSD is observed in the morphology particularly in case of FSHDPU where DNB is present. These observations suggest the coexistence of segmental mixing between soft and hard segments, which resulted fibrillary type morphology, and also phase separation between the segments as manifested by the formation of HSD.

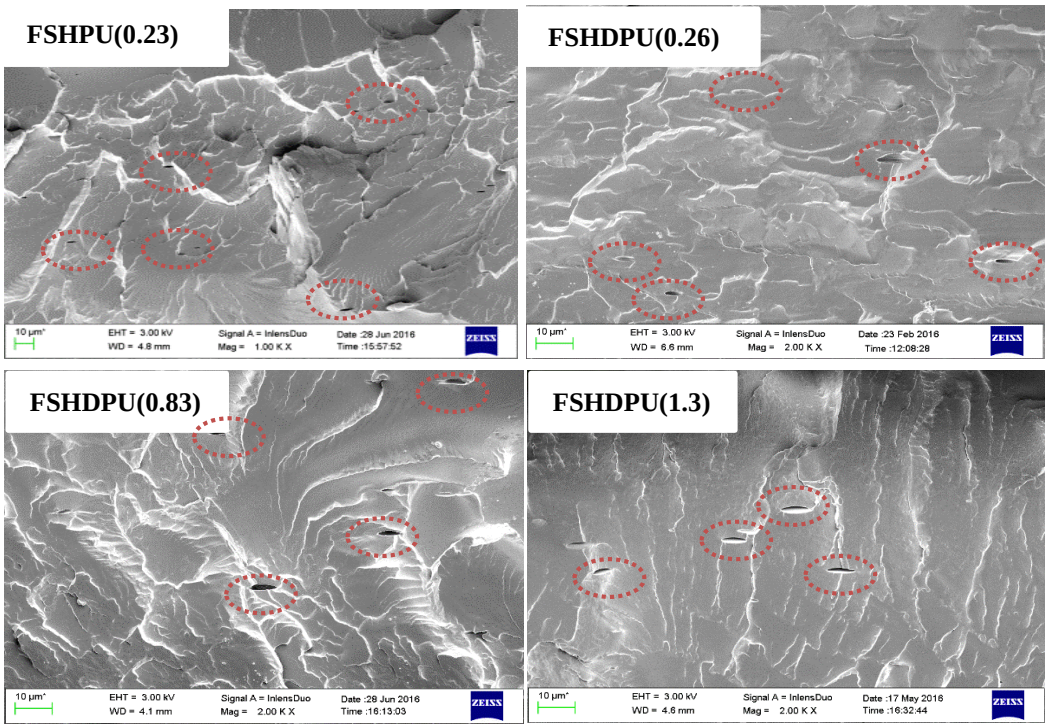

Figure 4.10: *FESEM images of the cross-section of cryo-fractured films of FSHPU, FSHDPUs at their indicate composition. Ellipsoid shaped domains are shown using dotted red circles.*

4.3.9. Composite solid propellants (CSPs) of modified HTPB

Burn rate measurements of CSPs made from HTPB, HTPB-DNB (HD), FSH and one of the representative sample FSHD have been carried out by using a standard Crawford bomb in conjunction with a pressure transducer and the results are tabulated in *Table 6.8*. The detailed experimental procedure for making CSP is described in the supplementary materials. The burn rate measured from FSHD1, which contain 0.26% (wt. %) Fe, is found to be ~10% higher than the pristine HD while it is only ~6% higher for FSH than the pristine HTPB. It confirms that the CSP made from DNB modified FPDS *grafted* HTPB binder gives better burn rate result. The pressure index value of all the composite are within the acceptable range and hence we can conclude that the CSP made from all the modified binders are quite stable. However, it is

also to be noted that the pressure index of FSHD sample is lower than FSH in fact it is significantly lower than others indicating best stable CSP in this case.

Table 4.8: *Burn rate and pressure index of CSPs made from HTPB, HTPB-DNB (HD), HTPB-g-FPDS (FSH) and HTPB-DNB-g-FPDS (FSHD) binders.*

CSP	Binder Used	Fe (Wt%) in Binder	Burn rate 40 bar (mm/s)	Pressure index
P1	HTPB	0.00	10.64	0.53
P2	FSH	0.23	11.25	0.497
P3	HD	0.0	10.08	0.58
P4	FSHD1	0.26	11.05	0.389

4.4. CONCLUSION

We have successfully synthesized Fe and Si containing HTPB binder system in order to prepare composite solid propellant binder with high burn rate. FPDS has been grafted to DNB tethered HTPB (HTPB-DNB) to produce FPDS-*g*-HTPB-DNB prepolymer. The degree of grafting of FPDS in the prepolymer backbone has been varied to see the effect on the viscosity of the resulting prepolymer. Solubility test in toluene suggested that presence of active Si bonding centre causes more crosslinking inside the polymer matrix which may be the prime reason for very high viscosity of this modified prepolymer. Electrochemistry study indirectly proved the successful grafting of FPDS over polybutadiene polymer backbone. Theoretical study revealed that presence of Si makes various kind of interaction within the different parts of the polymer chain which overshadowed the interaction of DNB with ferrocene. This interactions resulted higher viscosity but the presence of DNB helped to improve much better mechanical properties and elastic behavior for the PU films. SAXS and morphology study confirmed the co-existence of segmental mixing and phase separated

morphology in case of FPDS modified HTPB-PUS. Burn rate measurement confirmed the fact that both FPDS-*g*-HTPB and FPDS-*g*-HTPB-DNB can be used as a burn rate cum binder in CSPs. Finally we can conclude that the synthesized polymers are expected to replace the HTPB in the composite propellant formulation by improving the burn rates and mechanical properties of CSPs.

Appendix II

GPC profiles of all the samples, FT-IR of the few selected samples and WXD pattern of the PUs are included in Appendix II (page no. 239-241).

References

[1] G. R. Whittell, M. D. Hager, U. S. Schubert, I. Manners, *Nat. Mater.* **2011**, *10*, 176-188.

[2] I. Manners, *J. Polym. Sci., Polym. Chem.* **2002,** *40*, 179-191.

[3] A. Dumitru, A. Morozan, C. Mirea, D. Mihaiescu, C. Panaiotu, V. Ciupina, I. Stamatin, *Compos Sci Technol.* **2005**, *65*, 713-717.

[4] R. L. N. Hailes, A. M. Oliver, J. Gwyther, G. R. Whittell, I. Manners, *Chem. Soc. Rev.* **2016**, *45*, 5358-5407.

[5] V. Bellas, M. Rehahn, *Angew. Chem. Int. Ed.* **2007**, *46*, 5082-5104.

[6] G. Singha, A. Arorab, P. Kalraa, I. K. Maurya, C. E. Ruizc, M. A. Estebanc, S. Sinha, K. Goyal, R. Sehgal, *Bioorg. Med. Chem.* **2019**, *27*, 188-195.

[7] K. Rahimpour, R. Teimuri-Mofrad, *Polymer* **2020**, *192*, 122310.

[8] R. Tong, Y. Zhao, L. Wang, H. Yu, F. Ren, M. Saleem, W. A. Amer, *J. Organomet. Chem.* **2014**, *755*, 16-32.

[9] M. Usman, L. Wang, H. Yu, F. Haq, M. Haroon, R. S. Ullah, A. Khan, S. Fahad, A. Nazir, T. Elshaarani, *J. Organomet. Chem.* **2018**, *872*, 40-53.

[10] J. Gao, L. Wang, H. Yu, A. Xiao, W. Ding, *Propellants Explos. Protech.* **2011**, *36*, 404-409.

[11] W. Zhou, L. Wang, H. Yu, R. Tong, Q. Chen, J. Wang, X. Yang, Z. Abdin, M. Saleem, *Appl. Organometal. Chem.* **2016,** *30*, 796-805.

[12] K. Subramanian, *J. Polym. Sci. A.* **1999**, *37*, 4090-4099.

[13] K. Subramanian, K. S. Sastri, *J. Appl. Polym. Sci.* **2003**, *90*, 2813-2823.

[14] A. Unver, N. Dilsiz, M. Volkan, G. Akovalı, *J. Appl. Polym. Sci.* **2005**, *96*, 1654-1661.

[15] B.S. Cho, S.T. Noh, *J. Appl. Polym. Sci.* **2011**, *121*, 3560-3568.

[16] D. Saravanakumar, N. Sengottuvelan, V. Narayanan, M. Kandaswamy, T. L. Varghese, *J. Appl. Polym. Sci.* **2011**, *119*, 2517-2524.

[17] K. Ghosh , S. Behera , A. Kumar , D. G. Padale , D. G. Deshpande , A. Kumar , M. Gupta, *Cent. Eur. J. Energ. Mater.* **2014**, *11*, 323.

[18] R. Kurva, G. Gupta, K. I. Dhabbe, L. S. Jawale, P. S. Kulkarni, M. Maurya, *Propellants Explos. Pyrotech.* **2017**, *42*, 401-409.

[19] K. Rahimpour, R. Teimuri-Mofrad, H. Abbasi, M. Parchehbaf, S. Abedinpour, S. Soleimani, *Polym. Plast. Technol. Mater.* **2019**, *58*, 2056-2065.

[20] B. Lucio, J.L. de la Fuente, *Eur. Polym. J.* **2014,** *50*, 117-126.

[21] B.Lucio, J.L. de la Fuente, *React. Funct. Polym*. **2016,** *107*, 60-68.

[22] B. Lucio, J. L. de la Fuente**,** *Polymer* **2018**, *140*, 290-303.

[23] D. Rana, H. L. Kim, H. Kwag, J. Rhee, K. Cho, T. Woo, B. H. Lee, S. Choe, *J. Appl. Polym. Sci.* **2000,** *76*, 1950-1964.

[24] D. Rana, H. L. Kim, H. Kwag, S. Choe, *Polymer* **2000,** *41*, 7067-7082.

[25] R. M. Shankar, T. K. Roy, T. Jana, *J. Appl. Polym. Sci.* **2009**, *114*, 732-741.

[26] R. M. Shankar, S. Saha, K. S. Meera, T. Jana, *Bull. Mater. Sci.* **2009**, *32*, 507-514.

[27] R. M. Sankar, T. K. Roy, T. Jana, *Bull. Mater. Sci.* **2011**, *34*, 745-754.

[28] K. Malkappa, T. Jana, *Ind. Eng. Chem. Res.* **2013**, *52*, 12887-12896.

[29] B. N. Rao, P. J. P. Yadav, K. Malkappa, T. Jana, P.U. Sastry, *Polymer* **2015,** *77*, 323-333.

[30] B. K. Sikder, T. Jana, *ACS Omega* **2018**, *3*, 3004-3013.

[31] K. R. Kunduru, B. N. Rao, T. Jana, *Macromol. Symp.* **2018**, *382*, 1800090.

[32] B. N. Rao, K. Malkappa, N. Kumar, T. Jana, *Polymer* **2019**, *163*, 162-170.

[33] B. N. Rao, P. U. Sastry, T. Jana, *Eur. Polym. J.* **2019**, *115*, 201-211.

[34] K. Malkappa, B.N. Rao, T. Jana, *Polymer* **2016**, *99*, 404-416.

[35] K. Malkappa, T. Jana, Hydrophobic, *Ind. Eng. Chem. Res.* **2015,** *54*, 7423-7435.

[36] M. Dhara, N. Giri, B. N. Rao, A. K. Patra, P. U. Sastry, M. S. Ingole, T. Jana, *Eur. Polym. J.* **2020**, *122*, 109380.

[37] S. Ahn, Y. S. Song, B. R. Yoo, I. N. Jung, *Organometallics* **2000**, *19*, 2777-2780.

[38] K. Kishore, P. Rajalingam, *J Polym. Sci. C Polym. Lett.* **1986**, *24*, 471-476.

[39] Y. Tang, X. Zeng, *J Electrochem Soc.* **2008**, *155*, F82-F90.

[40] A. L. Crumbliss, D. Cooke, J. Castillio, P. W. Neilson, *Inorg. Chem.* **1993**, *32*, 6088-6094.

[41] D.C. Kraiter, P. W. Neilson, C. Zhang, A. L. Crumbliss, *Macromolecules* **2012**, *45*, 3658-3668.

[42] B. M. Upton, R. M. Gipson, S. Duhovic, B. R. Lydon, N. M. Matsumoto, H. D. Maynard, P. L. Diaconescu, *Inorg. Chem. Front.* **2014**, *1*, 271-277.

[43] B. Lucio, J.L. de la Fuente, *Polym. Degrad. Stab.* **2017**, *136*, 39-47.

[44] T. Gupta, B. Adhikari, *Thermochim. Acta*, **2003**, *402*, 169-181.

[45] T. Seyidoglu, M. A. Bohn, *Propellants Explos. Pyrotech.* **2017,** *42*, 1-13.

[46] B. Lucio, J. L.de la Fuente, M. L. Cerrada, *Macromol. Chem. Phys.* **2015**, *216*, 2048-2060.

[47] K. Kishore, S. Prema, K. lyanar, L. P. Pandureng, *Fuel* **1994**, *73*, 1583-93.

CHAPTER 5

Ferroceneyl polymer grafted smart nano surface *via* surface initiated RAFT polymerization

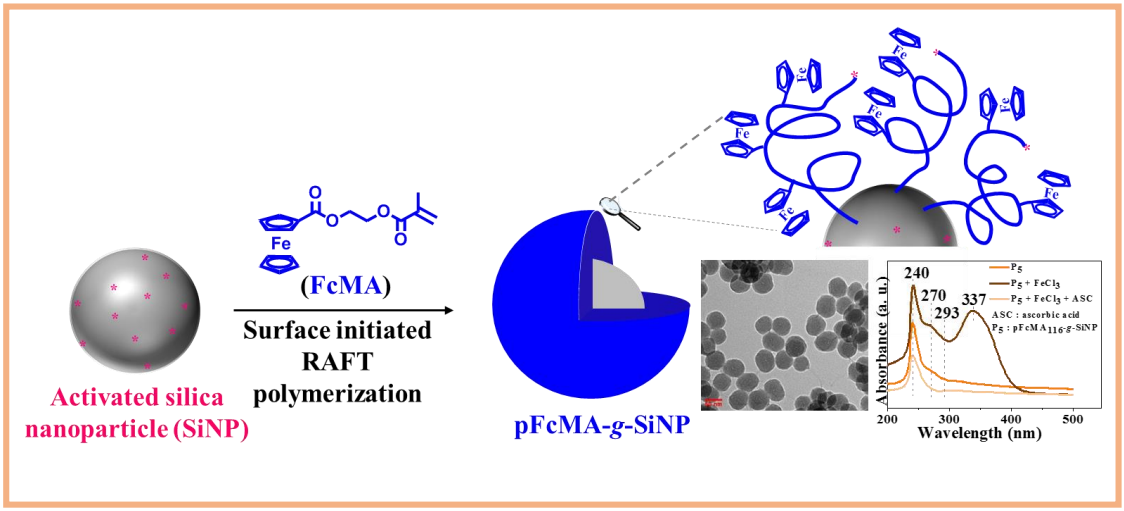

This chapter demonstrates the designing of a smart nano surface by grafting redox responsive ferrocenyl polymer on the silica nanoparticle surface via surface initiated reversible addition fragmentation chain transfer (SI-RAFT) polymerization technique.

5.1. Introduction

3D polymer brushes are a type of hybrids consisting of polymer chains densely tethered on a spherical or cylindrical (three dimensional, 3D) solid templates *via* a stable covalent or non-covalent bond linkages. The tethered polymer chains shall become responsible for the newly developed matrix inclusive of many significant properties such as corrosion protection, colloidal stability, adhesive behaviour, stimuli-responsiveness, lubrication and friction properties etc.[1] Designing of polymer brushes has been found to be a beneficial strategy to achieve the desired polymeric layer in a well-controlled manner. Immobilized stimuli-responsive polymer brushes, knows as smart surfaces, has been fascinated by enormous applications,[2–5] but the number of literature studying redox-responsiveness polymers are not many as compared to the reports comprises of various other classical stimuli.

Ferrocene/ ferrocenium polymeric system is an interesting redox-active couple and very well-known due to their wide-ranging applications as smart surface materials, semiconductor materials, phase separation materials, catalysts, redox-responsive drug-carriers, biosensors and magnetic ceramic precursors.[2,6–8] Smart polymer surface which is a very active and exciting field in functional materials in recent years, can be achieved *via* engineering the particle surfaces and making use of the stimuli-responsiveness of surface-grafted polymer chains.[9–13] Xu *et. al.* demonstrated an efficient approach to prepare novel block copolymer *grafted* carbon nanotube containing ferrocene groups as side chain and exhibited good electrochemical responses to detect the trace amount of melamine and trichlorfon residues in the food and fruits.[6] Lillethorup *et al* developed a dual functional polymer brushes comprising of ferrocene and nitro-benzene groups on glassy carbon and used as a versatile chemical platform in the construction of double functionalized films with a high electrochemical activity.[14] Among the ferrocene monomers those can be polymerized by anionic or reversible-deactivation radical polymerizations, ferrocenyl methacrylates appeared to be most promising candidates.[2,15,16] Redox-responsive behavior of poly(2-(methacryloyloxy)ethyl ferrocenecarboxylate) (pFcMA) tethered on cross-linked polystyrene particles *via* surface-initiated-atom transfer radical polymerization (SI-ATRP) and studied by scattering and electrochemical measurements. Also

the switchable surface wettability for immobilized polyvinylferrocene (PVFc) and pFcMA on silica wafers were investigated by Rehahn *et al*.[2,15] Recently, Gallei *et al* demonstrated one-pot methodology for the synthesis of metallopolymer-containing core-shell particles and fabricated as novel redox-responsive porous opal films.[16] Based on these literatures, pFcMA is found to be an interesting polymer chain to be investigated here as a polymer brush to construct a smart surface for biological studies for example as a topoisomerase inhibitor for cancer-specific drug targeting.

RAFT polymerization technique *via* grafting from approach among various living/ controlled polymerization methods, is one of the most versatile pathway employed so far to construct polymer brushes over a surface and achieve an excellent control over the composition, architecture, and length of tethered polymer chains.[1,17–20] In this work, silica nanoparticle (SiNP) is chosen as surface owing to its high chemical, thermal and colloidal stabilities. In addition, often SiNP is used in various field specially in biomedical applications due to their biocompatibility, low toxicity, low density, capacity for encapsulation and easy synthesis.[12,21–23] Our group has designed several hybrid materials composed of various kinds of polymer coated silica nanoparticles and explored their use in variety of applications starting from carbohydrate based therapeutics to enhancement of physical properties of polybenzimidazole based proton conducting membrane (PEM) for the use in in high temperature PEM fuel cell.[24–26] Very recently, we have fabricated ferrocenyl polymer coated hollow nanocapsules by using silica nanoparticle as sacrificial template and Al-NP is encapsulated to device a dual functional framework to be used in composite solid propellant.[27] This work is discussed in **Chapter 6** in the thesis. Herein, in this report we have constructed redox-responsive metallo-polymer brush on the silica nanoparticle surface *via* SI-RAFT polymerization technique by using (2-(methacryloyloxy)ethyl ferrocenecarboxylate (FcMA) as a monomer. The polymers are characterized by NMR, IR, GPC and CV techniques. The grafting amount of the polymer chains is confirmed by thermogravimetric analysis (TGA). The core-shell morphology of the poly(2-(methacryloyloxy)ethyl ferrocenecarboxylate) grafted silica nanoparticle (pFcMA-*g*-SiNP) is ascertained by FESEM and TEM, the change in

hydrodynamic radius with increase in polymer chain length is studied by using DLS measurement. Finally, the redox-responsiveness is studied by using UV-visible spectroscopy. Thus, we envision our version of designing pFcMA containing smart surface to be used as a probe to investigate the catalytic activity of topoisomerase II in DNA replication and recombination.

5.2. Experimental procedure

All the details about materials used in this chapter are discussed in **Chapter 2** including the synthesis of monomer, 2-(methacryloyloxy)ethyl ferrocenecarboxylate (FcMA); chain transfer agent, CPDB and silica template (SiNP-CPDB). Also characterization technique details including spectroscopic analysis by using UV-Vis, FT-IR and NMR, thermal analysis by TGA, electrochemical study by CV, molecular weight measurements by GPC, particles size analysis by DLS, FESEM and TEM are described thoroughly in **Chapter 2**.

Polymer chains were grafted over the silica nanoparticle (SiNP) surface via surface-initiated (SI-RAFT) polymerization. To perform the RAFT polymerizations on the particle surface, 4-cyanopentanoic acid dithiobenzoate (CPDB) was selected as chain transfer agent (CTA) and 2-(methacryloyloxy)ethyl ferrocenecarboxylate (FcMA) was selected as a ferrocene containing monomer.

5.2.1. Grafting of pFcMA chains using RAFT polymerization on SiNP surface

In a typical experiment, 274 mg (0.8 mmol) of FcMA, 3.83 mg (13.7 µmol) of CPDB, 200 mg of CPDB anchored SiNP particle (which is equivalent to 3.83 mg of CPDB attached to SiNP) and 1.12 mg (6.85 µmol) of AIBN were dissolved in 1.5 mL of dry DMF in a Schlenk tube. Then reaction mixture was degassed by three cycles of freeze–pump–thaw technique. The molar ratio of reagent were [SiNP-CPDB]: [free CPDB]: [AIBN] = 1:1:0.25. After cooled down to room temperature, the whole reaction mixture was placed in a preheated oil bath and stirred for next 12 hour at 90 ^{o}C. After completion of the reaction, the polymer (pFcMA) coated particles were purified by centrifugation at 2000 rpm for 15 minutes with the addition of ether

as non-solvent. Finally, the obtained pFcMA grafted SiNP (pFcMA-g-SiNP) particles were collected and kept in vacuum oven for drying at room temperature for 24 hrs. In order to alter the pFcMA chain length onto the particle surface, exactly similar methodology was followed but by the addition of varying amount of FcMA in the reaction feed.

5.2.2. HF treatment to cleave pFcMA chain from SiNP particle surface

In a 15 mL of Teflon vial, 50 mg of pFcMA-*g*-SiNP was dispersed in 4 mL of DCM and DMF mixture (3:1) followed by the addition of catalytic amount of phase transfer catalyst tetrabutylammonium bromide. After 15 minutes of stirring 1.5 mL of 48% HF was added and continued for another 6 hours at room temperature. After 6 hours the polymer solution was extracted with saturated sodium bicarbonate solution and precipitated with ether. Finally, the cleaved polymer was collected and dried under vacuum for 24 hours at room temperature.

5.3. Results and discussion

5.3.1. Synthesis of Silica nanoparticle functionalized with RAFT agent

Silica nanoparticles (SiNP) is chosen as template as it can be easily synthesized by Stöber process and the size can be controlled just by varying the concentrations of the ingredients like water and ammonia in the reaction mixture.[28] In this work, the size of the used SiNP is 45 ± 3 nm as obtained from FESEM and TEM presented in *Figure 5.1*. As outlined in *Scheme 5.1*, the SiNP surface is functionalized by refluxing with commercially available amine terminated silylating agent, (3-aminopropyl)triethoxysilane (APTES). Calculated amount of APTES was added to achieve a desired loading of amine functionalized SiNP (SiNP-NH_2) so that the chain transfer agent (CTA) loading can be further varied accordingly. The diameter of amine is 45 ± 3 nm functionalized particles which is similar to bare SiNP as obtained from FESEM and TEM (*Figure 5.1*) whereas hydrodynamic diameter (R_h) of SiNP-NH_2 is found to be 65 nm (obtained from DLS study [*Figure 5.2(A)*]. Generally, surface modification based on surface-initiated (SI) '*grafting from*' approach is a very popular method to carry out the RAFT-mediated polymerization over SiNP surface. In this process, the particle surface is designed

with an active initiation site followed by polymerization and thus, the functionality, density and polymer thickness can be well controlled on the surface.[29] Here, we chose to immobilize the chain transfer agent (CTA) on the particle surface to perform the SI-RAFT process by using conventional R group approach where the CTA is grafted to the surface *via* the leaving and reinitiating R end.[24–26,30]

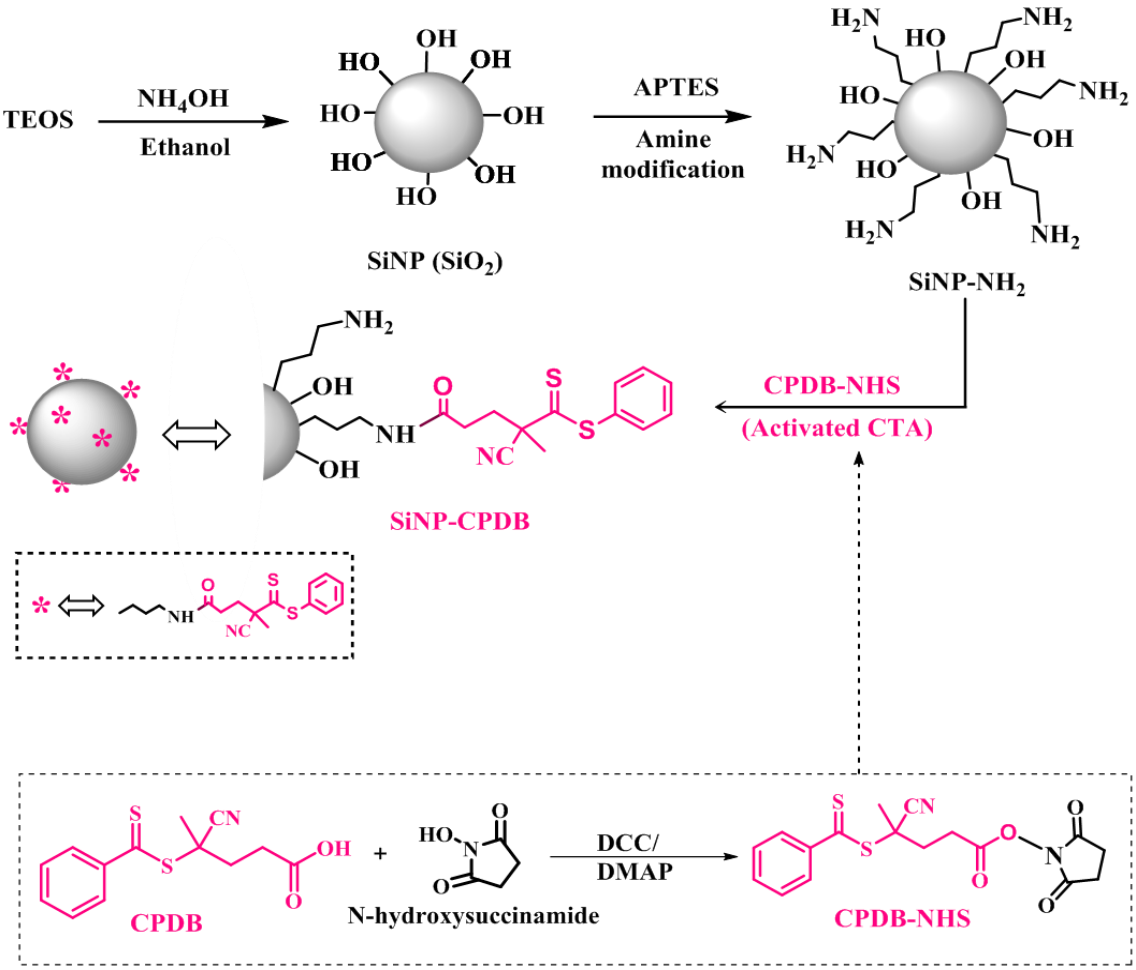

Scheme 5.1: *Attachment of CPDB on the surface of silica nanoparticles.*

We chose this method because R group approach is well known to achieve higher molecular weight and higher grafting density of the grafted polymer chain than Z group approach where CTA is tethered to the surface *via* stabilizing Z end.[24,30] Accordingly, in our

present work to anchor the CTA onto SiNP-NH_2 surface, first the CTA need to be activated with its R group end. It is very well known that the dithiobenzoate-based CTA are suitable for the monomer like methacrylates, acrylates, styrenes, etc.,[31,32] to achieve polymers with predictable molecular weight as well as narrow polydispersities.

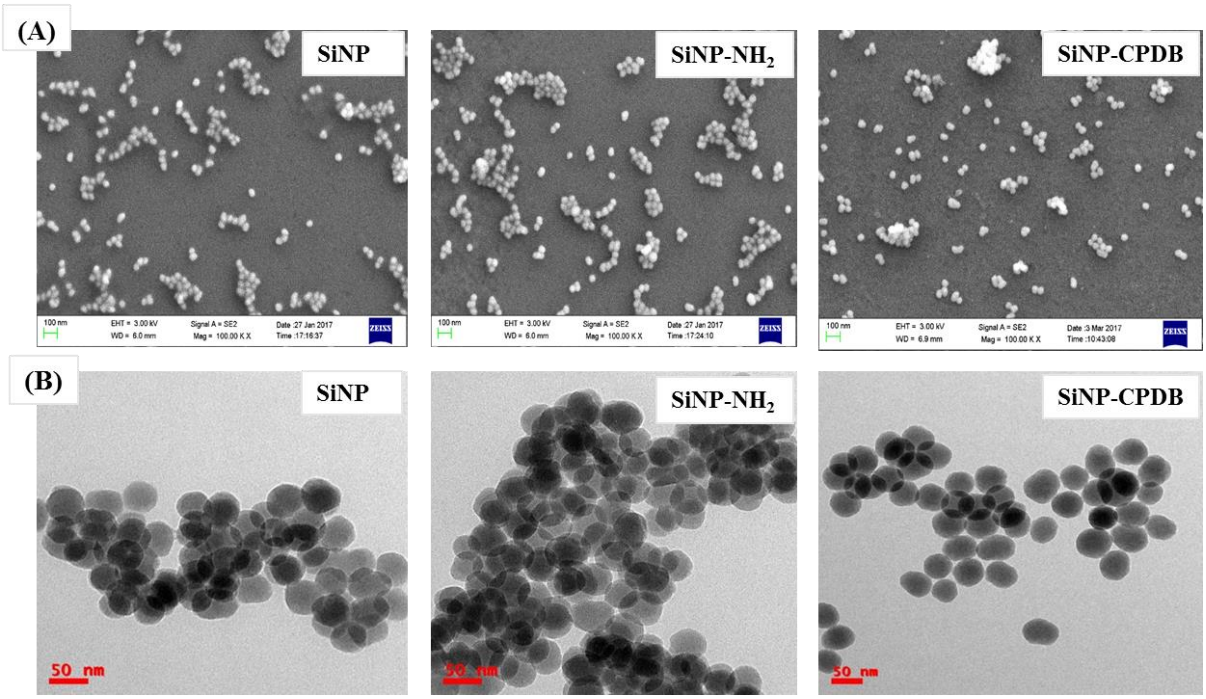

Figure 5.1*: FESEM (A, upper row) and TEM (B, lower row) images of SiNP, SiNP-NH_2 and SiNP-CPDB. Particle size were measured using microscope image software. The sizes reported in the text are average of at least three measurements.*

Based on these literatures, CPDB (4-cyanopentanoic acid dithiobenzoate) is chosen as CTA to polymerize FcMA monomer and it is activated by reacting with N-hydroxysuccinamide (NHS) which is named as CPDB-NHS. Though the carboxylic end of the CPDB is prone to react with surface attached amino group, but the reactivity of the activated CPDB end is sufficiently high to consume the free amino groups of the particle surface. The CPDB anchored SiNP is obtained by the continuous addition of SiNP-NH_2 solution into the stirred solution of CPDB-NHS solution. The final product was subjected to centrifuge and

purified by repeated washing with cyclohexane/ diethyl ether (4:1) solutions until the supernatant layers become colorless. The CPDB attachment onto SiNP surface was confirmed structurally by FT-IR spectroscopy [*Figure 5.2(B)*] which shows the bands at 1635 cm^{-1} correspond to C=O and 1565 cm^{-1} for the N-H stretching of amide bond. The absorption band at 2268 cm^{-1} is the characteristic peak for -CN functionality present in CPDB; the peaks at 2940, 1446 and 1080 cm^{-1} attributed to the C-H vibrations of CPDB and SiNP, respectively. Furthermore, the amount of CPDB attached onto SiNP surface was calculated from TGA results [*Figure 5.2(C)*] and found to be equal to 19.15 mg/g which is equivalent to (the grafting density) 0.82 no of chain / nm^2 of CPDB on the surface of SiNP. The diameter of SiNP-CPDB is 45 ± 3 (*Figure 5.1*), obtained from the morphological (FESEM and TEM) study and as per DLS study it is 59 nm [*Figure 5.2(A)*]. Therefore, it is clear from the above results that though size of the SiNP particle upon modification do not changes (in all the cases SiNP, SiNP-NH_2 and SiNP-CPDB size is around 45 nm as obtained from FESEM and TEM results shown in *Figure 5.1*) much in the solid state but the size shows a significant increase in solvated state – bare SiNP is around 58 nm whereas SiNP-NH_2 and SiNP-CPDB are around 68 and 59 nm respectively. This also indirectly proves the modification of SiNP surface by organic modifier which swells when dispersed in organic solvent resulting increase in particles size as observed in DLS plots [*Figure 5.2(A)*].

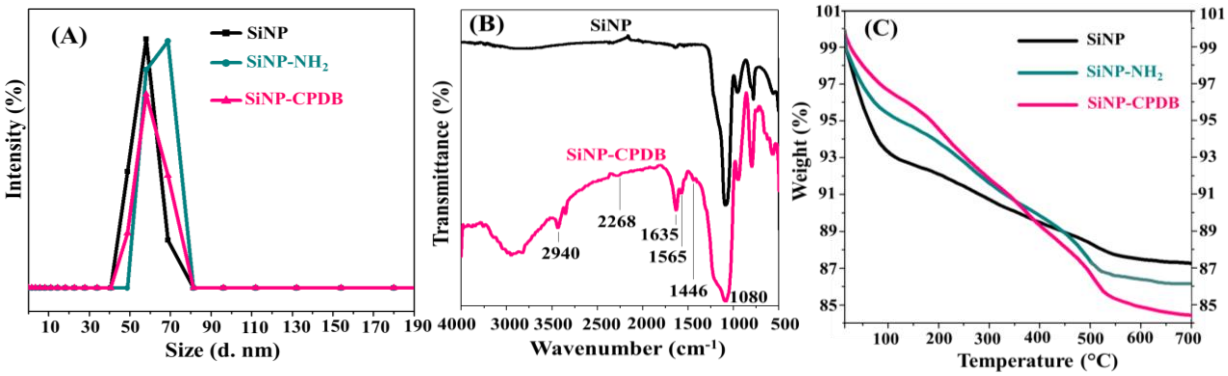

***Figure 5.2**: (A) DLS plots (B) FT-IR spectra and (C) TGA plots of SiNP, SiNP-NH_2 and SiNP-CPDB. DLS measurement was carried out by dispersing the particles in ethanol.*

5.3.2. Growth of pFcMA Chains on the SiNP Surface

SI-RAFT polymerization over the SiNP surface was carried out by employing FcMA as a monomer, SiNP-CPDB as a CTA and AIBN as an initiator in presence of equal amount of free CPDB as with the loaded amount on surface (*Scheme 5.2*). The free CPDB was added in the polymerization system in order to control the polymerization on the particle surface by allowing efficient exchange reaction between graft and free polymers.[24] FcMA monomer was synthesized first by following the reported literature[33] and the procedure is described in the **Chapter 2**. The polymerization was performed in dry DMF at 90 ºC for 12 hours with the final molar ratio as [SiNP-CPDB] : [Free CPDB] : [AIBN] = 1:1:0.25 and this ratio is kept constant for the other sets of the reaction while varying the amount of FcMA to achieve different chain length of pFcMA on the particle surface. Five different chain length of pFcMA, namely P_1, P_2, P_3, P_4 and P_5 were synthesized and all the physical characteristic data are summarized in *Table 5.1* where P_6 is the polymer without any silica core.

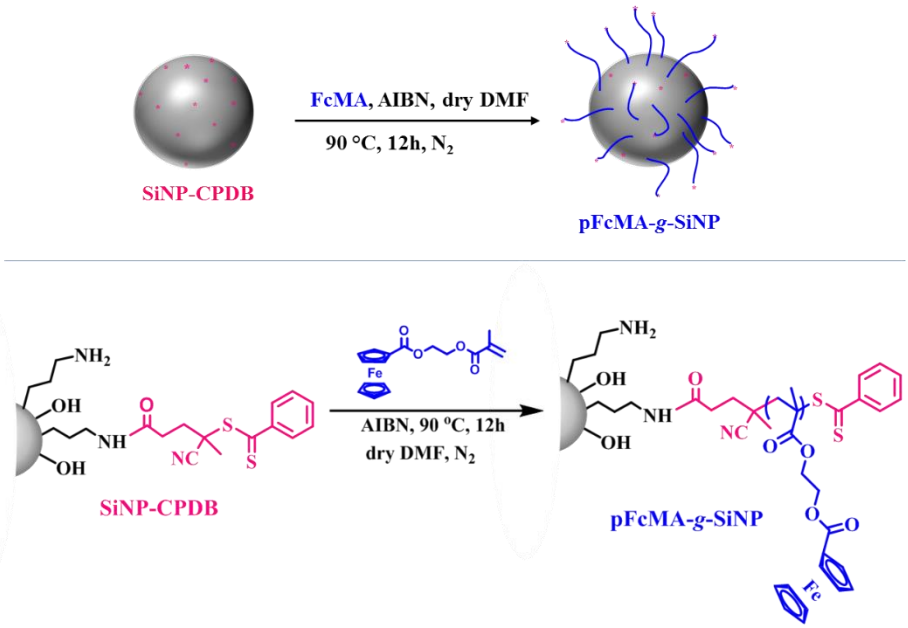

Scheme 5.2: *Polymerization of FcMA on the surface of SiNP-CPDB to prepare pFcMA-g-SiNP. Upper panel is a pictorial representation and lower panel shows the chemical structure of the pFcMA-g-SiNP.*

5.3.3. Spectroscopic proof for the grafting of pFcMA on SiNP

The appearance of new absorption peak at 1655 cm^{-1} which is due to FcMA ester carbonyl peak, and 1485 cm^{-1} and 1391 cm^{-1}, which are for Cp ring of FcMA along with SiNP-CPDB characteristic peaks of pFcMA-*g*-SiNP sample confirm the successful grafting of pFcMA on the SiNP surface (*Figure 5.3*).

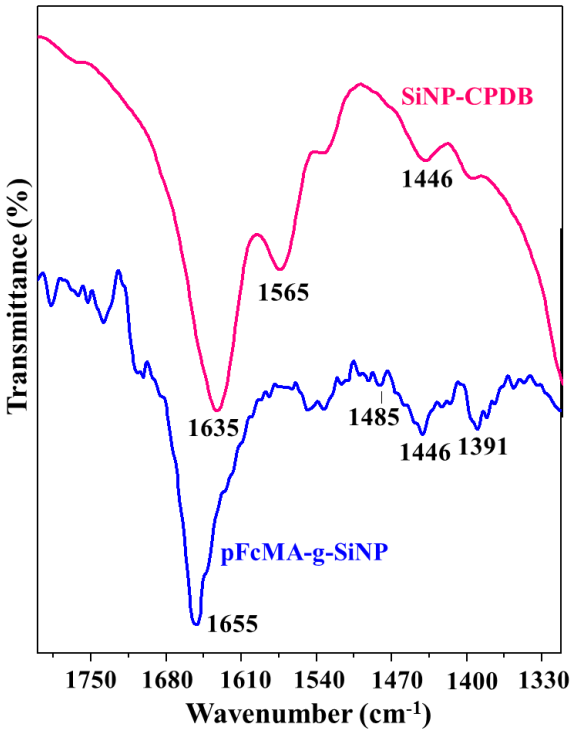

Figure 5.3: *FT-IR spectra of SiNP-CPDB and pFcMA-g-SiNP*

The polymer structure further confirmed by ^{1}H and ^{13}C NMR spectroscopy (*Figure 5.4*). In order to perform NMR study, the polymer chains were cleaved from the surface by HF treatment as discussed in **Chapter 2**. The resonance peak at 4.15 to 4.85 ppm [*Figure 5.4(A)*] correspond to Cp ring protons and also the CH_2 proton peaks of HEMA backbone merged in this region. The disappearance of the proton peaks related to the double bond of FcMA indicates about the successful polymerization. After polymerization, the CH_3 and CH_2 protons of the repeat unit show the resonance peak at 1.0 and 1.4; apart from these, some extra small

peaks appeared from 0.8 to 2.2 ppm attributed to peaks originated from different stereochemistry of methacrylate type monomers which are difficult to assign separately. End group CH_3 proton peak appeared at 1.1 ppm and the rest of the peaks like CH_2 and phenyl ring protons are indicated by the peaks at 2.3 ppm and 7.3 to 8.2 ppm, respectively as shown in *Figure 5.4(A)*. Furthermore, ^{13}C-NMR spectra also confirmed the polymer structure presented in *Figure 5.4(B)*. All the peak positions for both ^{1}H and ^{13}C-NMR are assigned with the pFcMA structure and shown in the *Figure 5.4*.

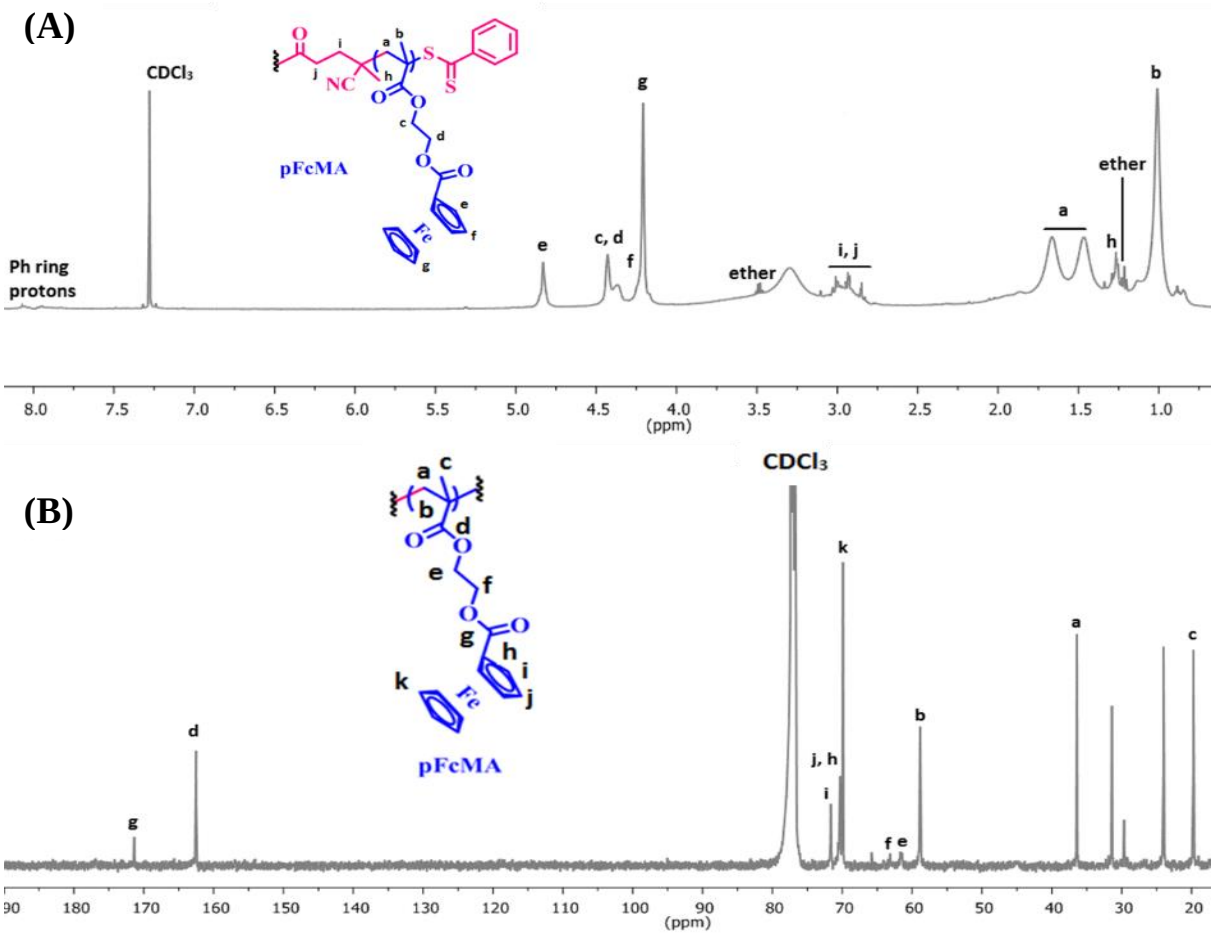

Figure 5.4: (A) *^{1}H-NMR spectra of pFcMA and* ***(B)*** *^{13}C-NMR spectra of pFcMA. The spectra were taken by dissolving the pFcMA (which was cleaved from the SiNP surface by HF treatment) in $CDCl_3$*

5.3.4. Molecular weight of the grafted pFcMA

To measure the molecular weight of the grafted polymer, GPC analysis was carried out with the polymers after cleaved out from the particle surface by HF treatment. The GPC plots are shown in *Figure 5.5*. The parameters obtained from GPC analysis such as number average molecular weight ($\overline{M_n}$), polydispersity value (Đ) and degree of polymerizations (DP) are summarized in the *Table 5.1*. The narrow PDI values (<1.4) revealed the fact that polymerization has taken place successfully with very well controlled manner over the particle surface as expected from RAFT technique. Another point to be noted from *Table 5.1* is that, polydispersity value of P_1 to P_5 (pFcMA *grafted* silica sample) is much lower than P_6 (the homopolymer of pFcMA without silica core; the Đ value of P_6 is 1.71). This is quite expected in case of surface modification. It is also to be noted from *Figure 5.5* that the GPC curves are much sharper in all the cases of P_1 to P_5 in comparison to P_6. In particular a closer look of P_5 and P_6 plots and Đ values (both of these polymer have almost similar $\overline{M_n}$ value, see *Table 5.1*) clearly indicate that less polydispersed chains are obtained in case of P_5.

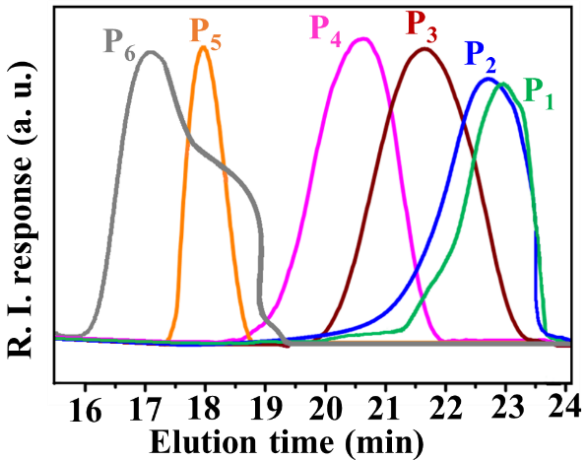

Figure 5.5: *GPC plots of polymers after cleaved out from the particle surface. GPC was carried out by dissolving 1.8 mg/mL polymer in DMF/ LiBr. GPC was calibrated using polystyrene standards.*

The molecular weight of the samples are also measured from the peak integration of ^{1}H-NMR data. All the NMR data with peak integrations are shown in *Figure 5.6*. Both GPC and *Table 5.1* data clearly show that molecular weight alter as the concentration of FcMA changes in the polymerization feed. Also the achieved $\overline{M_n}$ both from GPC and NMR data have similar trend with the targeted molecular weight. The small difference between GPC and NMR data is expected and always observed as reported vastly in the literature.

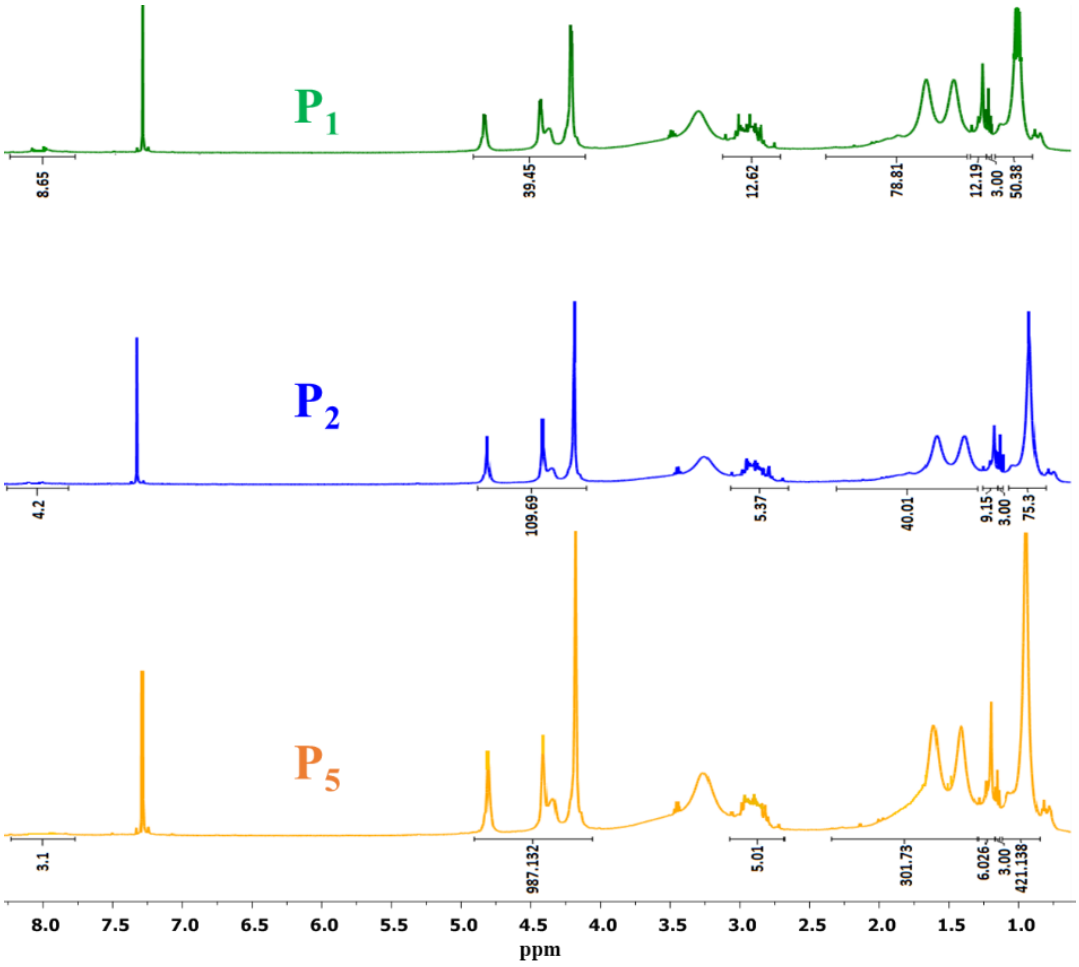

Figure 5.6: *^{1}H-NMR spectra of polymers with peak integration*

Table 5.1: *Various parameters obtained from GPC, TGA analysis for different chain length of polymers grafted over SiNP surface.*

Polymer Sample[a]	$\overline{M_n}$ targeted[c] (g/mol)	$\overline{M_n}$ achieved[c] (g/mol)	Đ[d]	$\overline{M_n}$ from ^{1}H-NMR[e] (g/mol)	Amount of polymer grafted over surface[f] (mg/g)	Grafting density (chains/nm^2) [g]	D/ Rg[h]
SiNP-CPDB	--	--	--	--	22.5	0.82	--
pFcMA$_8$-*g*-SiNP (P$_1$)	3,000	3,010	1.17	1,143	25.8	0.103	2.21
pFcMA$_{13}$-*g*-SiNP (P$_2$)	5,000	4,800	1.21	2,737	48.3	0.12	1.61
pFcMA$_{28}$-*g*-SiNP (P$_3$)	10,000	9,800	1.3	--	68.4	0.084	1.3
pFcMA$_{40}$-*g*-SiNP (P$_4$)	20,000	14,000	1.26	--	92.2	0.079	1.13
pFcMA$_{99}$-*g*-SiNP (P$_5$)	40,000	34,200	1.12	27,715	128.5	0.045	0.88
pFcMA$_{111}$ (P$_6$)[b]	40,000	38,172	1.71	28,812	--	--	--

[a] Degree of polymerization (DP) obtained from GPC analysis and the DP values are indicated in the subscript of the polymer chain. [b] pFcMA synthesized via solution RAFT polymerization without silica core. [c] $\overline{M_n}$ and [d] dispersity (Đ) are obtained from GPC analysis. [e] $(\overline{M_n})$ calculated based on the integration value obtained from ^{1}H-NMR spectra by following end group analysis method. [f, g] Estimated from TGA analysis. [h]D represents the distance between the grafted polymer chains which is calculated from the equation $D = \sigma^{-1/2}$ where σ is the grafting density; R_g refers the radius of gyration determined by $R_g = 0.5\ N^{0.5}$, where N is no of repeat unit i.e. DP values.

5.3.5. Quantification of surface-grafted pFcMA by TGA analysis

The amount of grafted pFcMA can be determined *via* TGA analysis, a useful method to quantify the surface attached polymers. Polymer grafted particles were subjected to TGA analysis and the resulting thermograms of P$_1$ to P$_5$ (*Figure 5.7*) are compared with SiNP-CPDB

and P_6 (the homopolymer of pFcMA without silica core). All the thermograms started decomposing at ~120 °C and degraded partly till ~680 °C, while as expected, the pure pFcMA (without silica core, P_6) degraded almost completely compared P_1 to P_5 at around ~470 °C and after complete combustion, the left over mass content was about 25%, which could be assigned to metal residue.[15] This attributes the increased stability of grafted polymer because of SiNP particle.

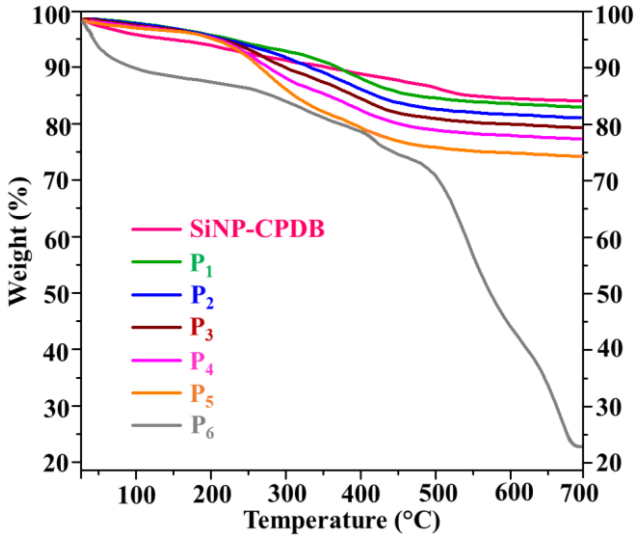

Figure 5.7: *TGA plots of polymer grafted particles and compared with SiNP-CPDB and pFcMA without silica core.*

The amount of grafted pFcMA over the silica surface is calculated and tabulated in the *Table 5.1*. It can be clearly seen that, with increase in chain length of pFcMA from P_1 to P_5, the grafted amount also increases which show a nice correlation with the molecular weight data mentioned earlier. The grafting density for P_1 to P_5 is also calculated and listed in *Table 5.1* by considering the SiNP density as 2.65 g/cm^3. This data reveals that the grafting density decreases significantly with increasing chain lengths. This attributes that all the CTA activated site do not participates in the polymerization when the chains are bigger. This may be due to steric hindrance between the long polymer chains which disable all the CTA sites to get involved in the growing polymer chain.[15] The average distance between the neighbouring polymer chains

is denoted as D and can be calculated for $D = \sigma^{-1/2}$ where σ is the grafting density. The ratio of D to the radius of gyration (D/R_g) values are < 2 (*Table 5.1*) for P_2 to P_5 suggesting the brush morphology of the polymer chains on the particle surface while chains are in mushroom conformation in case of P_1 with D/R_g value > 2.[34] It is also to be noted that D/R_g value decreases significantly with increasing chain length indicating the change in the morphology from mushroom to brush morphology from P_1 to P_2 - P_5.

5.3.6. Scattering studies of polymer grafted particles

The dynamic light scattering of polymer grafted particles (DLS) analysis was conducted in two different solvent namely ethanol and THF, these solvents of different polarity are chosen so that the effect of solvent polarity on the grafted pFcMA chains can be studied. The polymer grafted particle (P_1 to P_5) and SiNP-CPDB are dispersed in these solvent at a concentration 1mg/ mL and each dispersion was sonicated for 1 hours prior to measurements. The hydrodynamic radius of the particles in the swollen state in a particular solvent is denoted by R_h and the shell thickness due to polymer chains swelling symbolized as brush length (l_b) which is the difference in the hydrodynamic radius of the polymer grafted particle and bare silica particle. The DLS plots of all the samples in both solvents are shown in *Figure 5.8*. *Table 5.2* lists the value of R_h and l_b and dispersity of all the samples studied here.

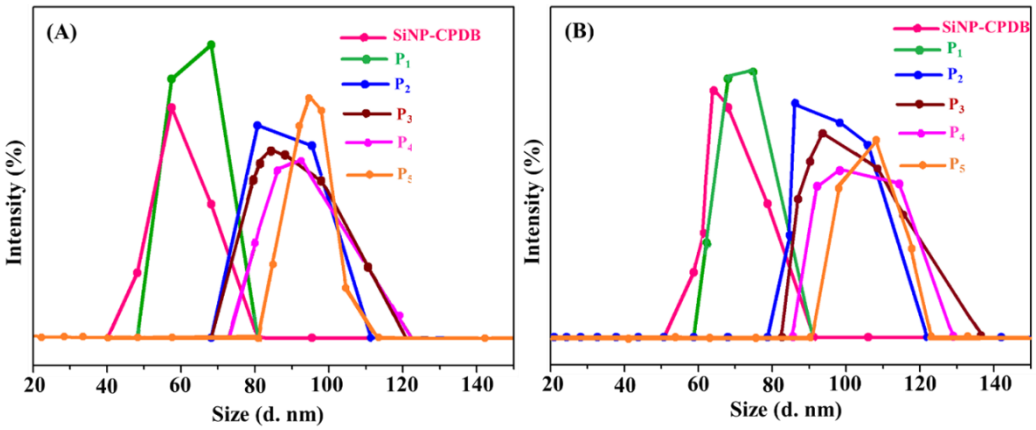

Figure 5.8: *DLS plots of SiNP-CPDB and polymer grafted particles in two solvents of different polarity;* ***(A)*** *ethanol and* ***(B)*** *THF.*

A clearer picture emerges when both R_h and l_b values in two solvents are plotted together as shown in *Figure 5.9*. Two facts to be noted from *Figure 5.9* and *Table 5.2* data: increase in R_h and l_b values with increasing chain length which is obvious as size of the polymer chain increases and more importantly, it is necessary to note that both R_h and l_b values for all the grafted sample are larger in less polar THF than relatively high polar ethanol solvent. This second observation is simple due to the hydrophobic nature of pFcMA chains which allows more swelling of pFcMA-g-SiNP in THF than ethanol resulting higher R_h and l_b. This also attributes the better solubility of the grafted chain in THF than ethanol.

Table 5.2: *Various parameters obtained from DLS analysis for different chain length of polymers grafted over SiNP surface.*

Sample Identity	**Size (TEM) nm[a]**	**Size (FESEM) nm[a]**	**DLS size in (nm)**			
			Ethanol[b]		**THF[c]**	
			R_h	l_b	R_h	l_b
SiNP-CPDB	45±3	47±3	59	--	61	--
pFcMA$_8$-*g*-SiNP (P$_1$)	46±3	48±3	72	13	77	16
pFcMA$_{13}$-*g*-SiNP (P$_2$)	49±3	54±3	82	23	89	28
pFcMA$_{28}$-*g*-SiNP (P$_3$)	56±3	60±3	86	27	95	34
pFcMA$_{40}$-*g*-SiNP (P$_4$)	61±3	65±3	94	35	103	42
pFcMA$_{99}$-*g*-SiNP (P$_5$)	70±3	71±3	100	41	111	50

[a] Measured from the TEM and FESEM software and the data shown here is the average of at least six measurements, [b] DLS size measured by dispersing the samples in ethanol and [c] THF and in both cases the hydrodynamic radius (R_h) and brush length (l_b) are determined.

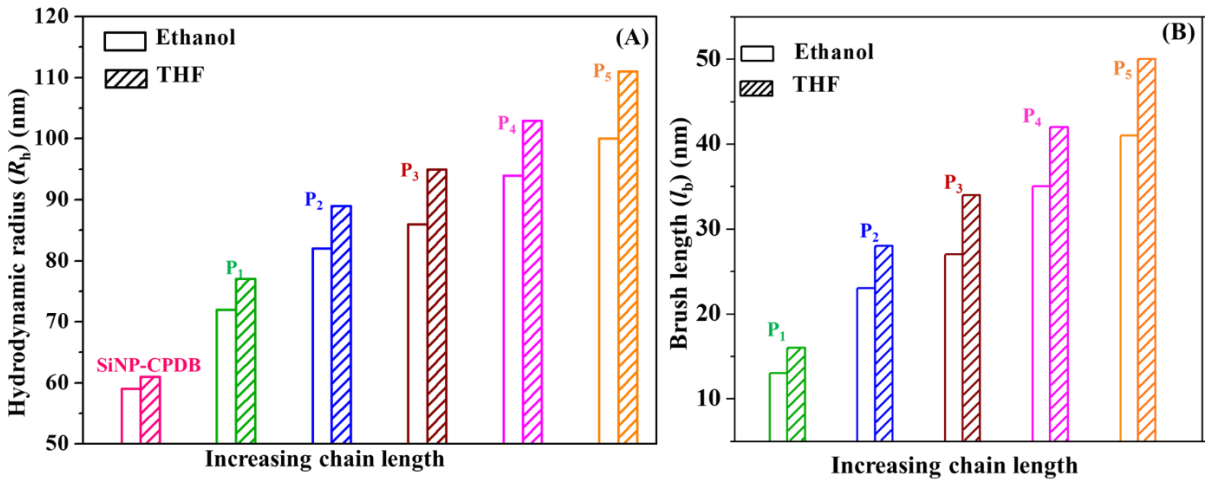

Figure 5.9: *Comparison of the (A) hydrodynamic radius and (B) brush length of polymer grafted particles along with SiNP-CPDB in two solvents (ethanol and THF) of different polarity.*

5.3.7. Morphological study of the polymer *grafted* silica particles

Both the TEM and FESEM images shown in *Figure 5.10* clearly show that the shape of the particle remains spherical as it was in case of SiNP even after polymer grafting. However, there are noticeable changes in morphological features. For example TEM images of synthesized particles (P_1 to P_5) clearly shows the polymer layer on the silica core compared to pristine SiNP-CPDB (*Figure 5.10, Top panel*). It is also noticed that with increase in polymer chain length the particles gradually display more core-shell morphology from P_1 to P_5 with increasing particle size as noted in *Table 5.2*. The particles diameter were calculated from both TEM and FESEM image and mentioned in *Table 5.2*. The data between two images are matches well. FESEM images also follow the similar trend (*Table 5.2*) and show nice spherical morphology (*Figure 5.10, lower panel*) which reconfirms the fact of the successful formation of pFcMA layer on silica surface. However, it is to be noted that the particle size measured from microscopic images are quite smaller than the size obtained from DLS study as the size measured in former method is the size of the dry particles whereas size of DLS is the size of particles swelled in solvent. This again reconfirms the grafting of polymer chain. Another observation must be noted from the morphology study is the agglomerated nature of the

morphology with increased chain length. Both TEM and FESEM images of P_4 and P_5 sample particularly display aggregated morphology of the particles attributing the presence of inter chain and interparticle attraction when the chain length of grafted polymer is sufficiently long.

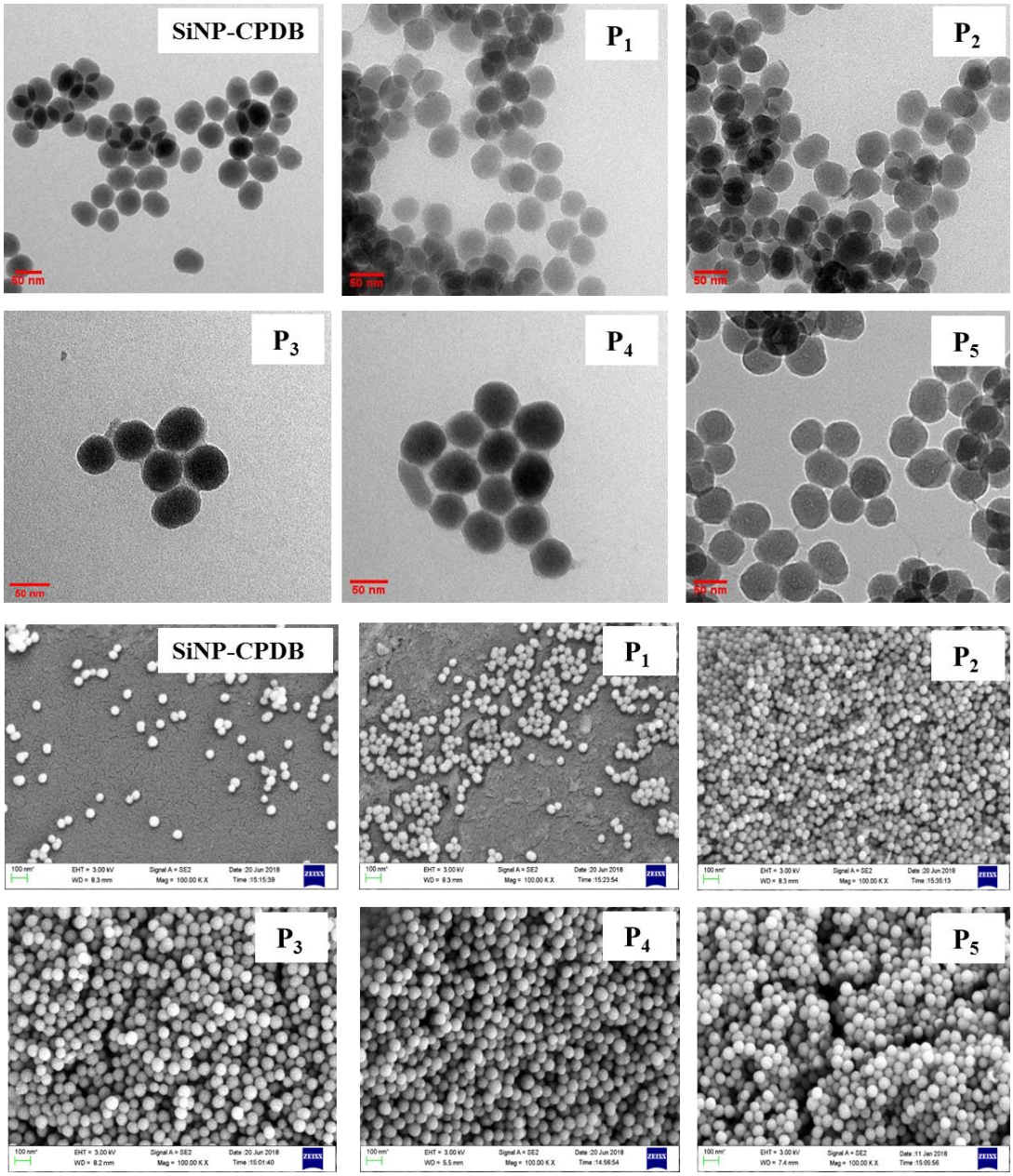

***Figure 5.10**: TEM (top two panels) FESEM (lower two panels) images of SiNP-CPDB and pFcMA-g-SiNP (P_1 to P_5)*

5.3.8. Redox properties of pFcMA *grafted* silica particles

To study the redox behavior of pFcMA *grafted* silica particles, the polymer chains after being cleaved from the particle surface were subjected to cyclic voltammetry (CV) measurement. CV analysis helped to realize the reversibility of oxidation/ reduction cycles of the pFcMA shell which will be a deciding factor for the use as a redox-responsive material. The analysis was conducted by using Pt as working electrode in presence of 100 mM of tetrabutyl ammonium perchlorate solution in dry DMF at ambient temperature. The concentration of each polymer solutions were kept constant at 1mg/ mL. The cyclic voltammogram of polymer P_1 to P_5 displayed reversible oxidation/ reduction peak potential (*Figure 5.11*).

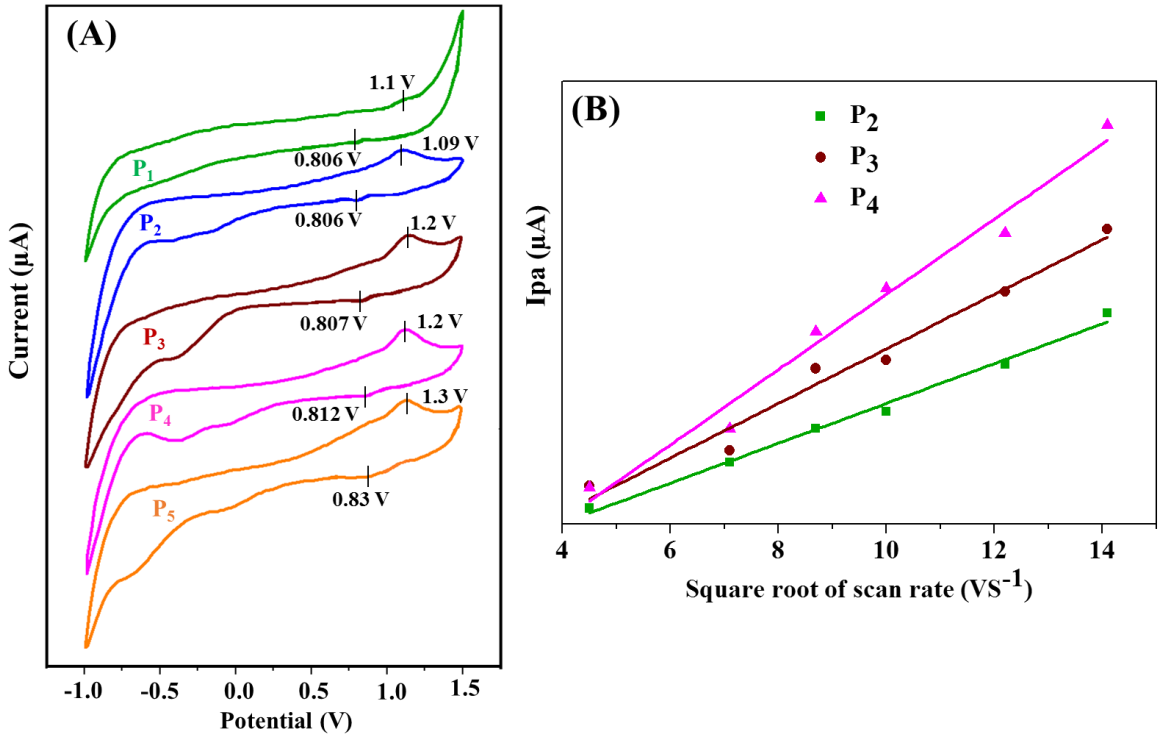

Figure 5.11*: (A) CV diagram of pFcMA chains which were grafted over silica surface. (B) Anodic peak current vs. square root of scan rate of the redox process of the three representative ferrocenyl polymers grafted over particles. CV data were recorded after cleaving the samples from particle surface.*

The anodic peak (oxidation) potential varies from 1.09 V to 1.3 V and the cathodic peak (reduction) potential alters between 0.806 to 0.83 V. It is seen that the both oxidation and reduction peak shifted a little towards higher value with the increase in polymer chain length [*Figure 5.11(A)*]. This fact indicated a little delay in oxidation process which might have been happened by the increment in bulkiness for higher chain length. The scan rate dependency study shown in [*Figure 5.11(B)*] attributes to the point that ferrocene involves as a freely diffusing redox species in the redox process in polymer dispersed solution and follows Randles-Sevcik equation. The increasing slope values of *Figure 5.11(B)* link with increasing chain length indicate the impact of pFcMA chain on the redox behaviour and this may be linked to the gradual increase in bulk concentration of the analytes from P_2 to P_3 to P_4, respectively. All the parameters extracted from CV study are presented in *Table 5.3*.

Table 5.3: *Various parameters obtained from CV analysis for different chain length of polymers grafted over SiNP surface.*

Polymer Sample	**E_{pa} (V)**	**E_{pc} (V)**	**ΔE_p (V)**	**$E_{1/2}$[a] (V)**	**I_{pa} (µA)**	**I_{pc} (µA)**
$pFcMA_8$-*g*-SiNP (P_1)	1.1	0.806	0.294	0.953	0.52	0.0377
$pFcMA_{13}$-*g*-SiNP (P_2)	1.09	0.806	0.284	0.948	1.145	0.213
$pFcMA_{28}$-*g*-SiNP (P_3)	1.2	0.807	0.393	1.003	1.601	0.306
$pFcMA_{40}$-*g*-SiNP (P_4)	1.2	0.812	0.388	1.006	2.165	0.628
$pFcMA_{99}$-*g*-SiNP (P_5)	1.3	0.83	0.47	1.065	1.733	0.431

[a] $E_{1/2}$ values were determined as the average values of E_{pa} and E_{pc}.

The various data obtained from CV studies which are shown in *Table 5.3* reveal many

Interesting aspects which need to be noted. In addition to increasing both E_{pa} and E_{pc} with increasing chain length (P_1 to P_5), it is observed that ΔE_p (difference between cathodic and anodic peak potential) values also increases indicating higher delay between oxidation and reduction process which mean slow electron transfer process compared to an ideal Nernstian process. This may be due to increasing interchain interactions when the chain is long. Similarly, $E_{1/2}$ values also increases with increasing chain length. Both I_{pa} and I_{pc} increases with chain length indicates the availability of increasing number of electro active sites in the chain from P_1 to P_4. In case of P_5 it has been seen that both the peak current value decreases from P_4 and this may be due to the fact that in P_5 overlapping of the polymer chains in their brush conformation is very prominent and hence it is affecting the diffusion of the electro active ferrocene moiety which in turn hampers the redox reaction a bit resulting with a comparatively lower peak current value.[35]

5.3.9. Redox responsiveness of pFcMA *grafted* silica particles

The redox responsiveness of the pFcMA polymer chains were examined by using UV-visible spectroscopic study. All the experiments were carried out with polymer *grafted* silica particles after dispersed in THF. Two representative samples P_3 and P_5 are studied here along with control sample P_6 and SiNP-CPDB (*Figure 5.12*). Similar results are obtained for all other samples. The transition peak appear at 240, 270 and 293 nm in P_3, P_5 and P_6 among which first one is a sharp peak and later two peaks appear as shoulder. It is to be noted that in case of P_6, these shoulder are bit more prominent and shifted a little to 263 and 307 instead of 270 and 293, respectively as in P_3 and P_5. These are may be due to the fact that later two samples are polymer grafted SiNP whereas the former (P_6) is the homopolymer and hence, the solubility in solvent may differ resulting such observation. The peaks at 240 and 270 nm are ascribed to the π - π^* of Cp ring and d – d transitions of Fe^{+2} to Cp ring whereas 293 nm peak originated from the phenyl ring and thio carbonyl based transitions that is also present in SiNP-CPDB [*Figure 5.12(A)*]. We treated P_3 and P_5 dispersion by adding oxidizing agent like ferric chloride into the dispersion and this treatment resulted the appearance of a characteristic strong transition peak at 337 nm [*Figure 5.12(B) and 5.12(C)*] which is because of the formation of the

ferrocenium ion from ferrocene due to oxidation by added $FeCl_3$. Logically, the peak at 240 and 270 nm should have disappeared after oxidation which are assigned for the transitions in ferrocene moeity of pFcMA backbone, but the reappearance of these peaks with even higher intensity confirmed the simultaneous reduction of ferric chloride to ferrous chloride and also indirectly tells us that the 240 and 270 nm peaks are actually correspond to the transition of Cp ring and Fe^{2+} to Cp unit. Further, the redox reversibility was tested by adding L-ascorbic acid (ASC) into the oxidized polymer solution and it is observed that 337 nm disappears and the original transition peaks in case of both P_3 and P_5 appears again [*Figure 5.12(B) and 5.12(C)*]. All these results prove that our polymer grafted SiNP particles are redox responsive.

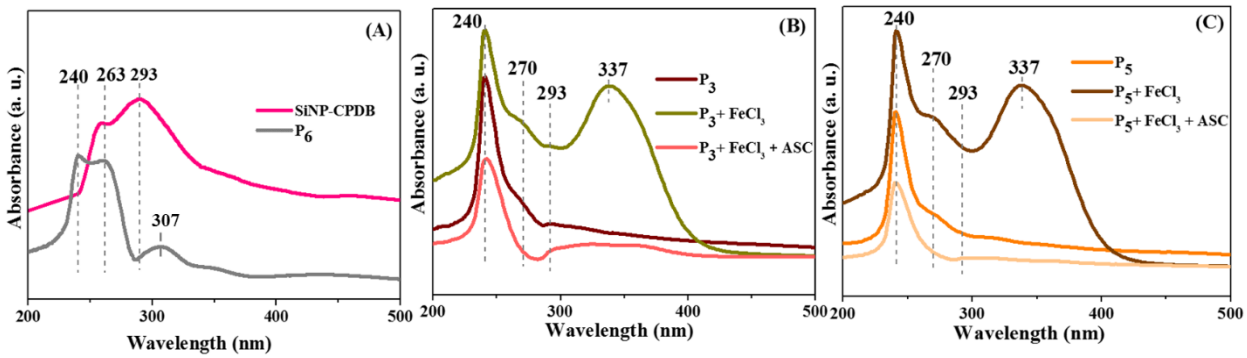

***Figure 5.12**: (A) UV-visible spectra of SiNP-CPDB and P_6, redox responsive study of the polymer grafted silica particles (B) P_3 and (C) P_5 using UV-visible measurements.*

5.4. Conclusion

In this report, we have designed a smart nano silica particle surface *grafted* with poly(2-(methacryloyloxy)ethyl ferrocenecarboxylate) (pFcMA) polymer brushes *via* SI-RAFT polymerization technique using silica nanoparticle as surface. Five different polymer chain length have been grafted over the SiNP surface. The molecular weight measurements and low dispersity and other studies proved the successful RAFT polymerization. The structure of the polymers have been characterized by NMR and IR. Thermal analysis for P_1 to P_5 displayed a nice correlation with the GPC data and also it helped to understand the polymer chain morphology over the particle surface. DLS measurement provided the information about the

swelling behavior of the polymer chain in a suitable solvent like THF and it correlated with the increased chain length. The core-shell morphology of the pFcMA *grafted* particles have been observed by FESEM and TEM images. The CV analysis demonstrated the reversible redox property of the ferrocenyl polymers; finally the redox-responsiveness property of pFcMA chains were investigated by UV-visible spectroscopy. In a conclusive note, it can be stated that we have successfully *grafted* redox-responsive polymer, pFcMA over silica nanoparticles and these are absolutely ready to be used as a probe to evaluate the activity of topoisomerase II during DNA replication and transcription in the anticancer treatment.

References

[1] C. Feng, X. Huang, *Acc. Chem. Res.* **2018**, *51*, 2314–2323.

[2] J. Elbert, M. Gallei, C. Rüttiger, A. Brunsen, H. Didzoleit, B. Stühn, M. Rehahn, *Organometallics* **2013**, *32*, 5873–5878.

[3] T. P. Russell, *Science* **2002**, *297*, 964–967.

[4] Y. Pei, J. Travas-Sejdic, D. E. Williams, *Langmuir* **2012**, *28*, 8072–8083.

[5] J. Hu, H. Meng, G. Li, S. I. Ibekwe, *Smart Mater. Struct.* **2012**, *21*, 053001.

[6] F. Xu, Z. M. Cui, H. Li, Y. L. Luo, *RSC Adv.* **2017**, *7*, 7431–7441.

[7] Y. Ma, W. F. Dong, M. A. Hempenius, H. Möhwald, G. Julius Vancso, *Nat. Mater.* **2006**, *5*, 724–729.

[8] B. Kim, E. L. Ratcliff, N. R. Armstrong, T. Kowalewski, J. Pyun, *Langmuir* **2010**, *26*, 2083–2092.

[9] Y. Li, B. C. Benicewicz, *Macromolecules* **2008**, *41*, 7986–7992.

[10] D. Maillard, S. K. Kumar, A. Rungta, B. C. Benicewicz, R. E. Prud'Homme, *Nano Lett.* **2011**, *11*, 4569–4573.

[11] M. Ballauff, Y. Lu, *Polymer* **2007**, *48*, 1815–1823.

[12] P. Pageni, P. Yang, Y. P. Chen, Y. Huang, M. Bam, T. Zhu, M. Nagarkatti, B. C. Benicewicz, A. W. Decho, C. Tang, *Biomacromolecules* **2018**, *19*, 417–425.

[13] P. Li, H. Kang, N. Che, Z. Liu, C. Zhang, C. Cao, W. Li, R. Liu, Y. Huang, *Polym. Int.* **2015**, *64*, 1015–1022.

[14] M. Lillethorup, K. Shimizu, N. Plumeré, S. U. Pedersen, K. Daasbjerg, *Macromolecules* **2014**, *47*, 5081–5088.

[15] M. Mazurowski, M. Gallei, J. Li, H. Didzoleit, B. Stühn, M. Rehahn, *Macromolecules* **2012**, *45*, 8970–8981.

[16] T. Winter, X. Su, T. A. Hatton, M. Gallei, *Macromol. Rapid Commun.* **2018**, *39*, 1–8.

[17] M. M. Khani, D. Woo, E. L. Mumpower, B. C. Benicewicz, *Polymer* **2017**, *109*, 339–348.

[18] C. Li, J. Han, C. Y. Ryu, B. C. Benicewicz, **2006**, 3175–3183.

[19] M. Baum, W. J. Brittain, *Macromolecules* **2002**, *35*, 610–615.

[20] T. Caykara, *Wiley Blackwell*, **2017,** 97-121.

[21] F. Tang, L. Li, D. Chen, *Adv. Mater.* **2012**, *24*, 1504–1534.

[22] A. Bitar, N. M. Ahmad, H. Fessi, A. Elaissari, *Drug Discov. Today* **2012**, *17*, 1147–1154.

[23] J. T. Sun, J. G. Piao, L. H. Wang, M. Javed, C. Y. Hong, C. Y. Pan, *Macromol. Rapid Commun.* **2013**, *34*, 1387–1394.

[24] S. N. R. Kutcherlapati, R. Koyilapu, U. M. R. Boddu, D. Datta, R. S. Perali, M. J. Swamy, T. Jana, *Macromolecules* **2017**, *50*, 7309–7320.

[25] S. R. Kutcherlapati, R. Koyilapu, T. Jana, *J. Polym. Sci. Part A Polym. Chem.* **2018**, *56*, 365–375.

[26] R. Koyilapu, S. Singha, S. N. R. Kutcherlapati, T. Jana, *Polymer* **2020**, *195*, 122458.

[27] M. Dhara, S. Rudra, N. Mukherjee, T. Jana, *Polym. Chem.* **2021**, DOI 10.1039/D1PY00590A.

[28] Y. Takeuchi, *J. Phys. Ther. Sci.* **2017**, *29*, 112–114.

[29] B. Radhakrishnan, R. Ranjan, W. J. Brittain, *Soft Matter* **2006**, *2*, 386–396.

[30] X. Huang, D. Appelhans, P. Formanek, F. Simon, B. Voit, **2011**, 8351–8360.

[31] Y. Mitsukami, M. S. Donovan, A. B. Lowe, C. L. McCormick, *Macromolecules* **2001**, *34*, 2248–2256.

[32] B. Y. K. Chong, J. Krstina, T. P. T. Le, G. Moad, A. Postma, E. Rizzardo, S. H. Thang, *Macromolecules* **2003**, *36*, 2256–2272.

[33] J. Zhang, L. Ren, C. G. Hardy, C. Tang, *Macromolecules* **2012**, *45*, 6857–6863.

[34] X. Yang, D. Chen, H. Zhao, *Acta Biomater.* **2016**, *29*, 446–454.

[35] T. Steentjes, P. Jonkheijm, J. Huskens, *Langmuir* **2017**, *33*, 11878–11883.

CHAPTER 6

Hollow polymer nanocapsules with ferrocenyl copolymer shell

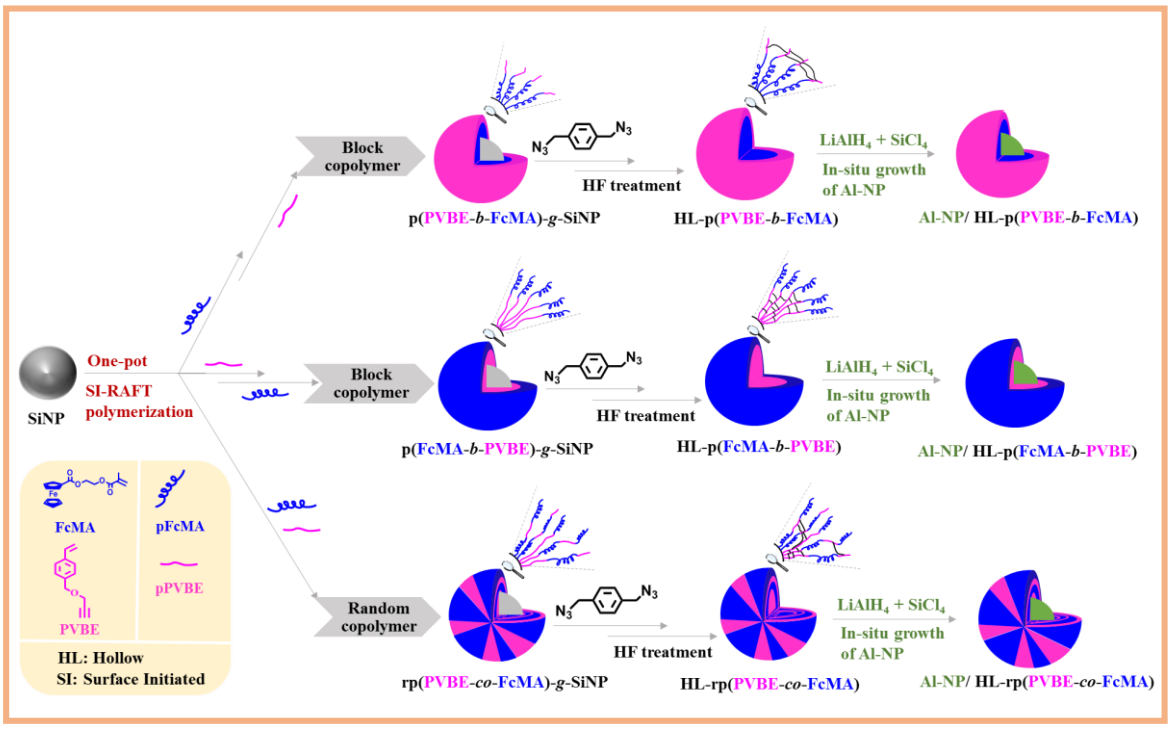

This chapter demonstrates designing of a hollow polymer nanocapsules (HPN) by using silica nanoparticle as a sacrificial template with ferrocenyl copolymer shell after chemically crosslinking the polymer chain and to be used as a dual functional framework in form of fuel cum burn rate catalyst, Al-NP was grown in situ inside the hollow cavity

6.1. Introduction

Hollow polymer nanocapsules (HPN) bring together a fascinating combination of many unique properties owing to nanostructure associated with a robust shell and hollow pore, making them an interesting class of materials as a versatile platform for designing plentiful functional devices. Most significantly, researchers quickly realized the intriguing properties *ca* large surface area, low density, high loading capacity[1] of the unique hollow structures and demonstrated numerous applications including micro/nanoreactors,[2],[3] catalysis,[4],[5] energy storage,[6],[7] biomedicine,[8],[9] sensors,[10],[11] environmental remediation,[12],[13] and so on. The void space within the hollow cavity can be used as template and storage for different substances to design efficient composite materials for catalysis either as a support or as active catalyst.[1] Creation of hollow space within a solid precursor is indeed a challenging task to engineer particularly at the nano/ micro dimension. Among various approaches to make hollow nanostructures, templating of polymer nanoparticles found to be the most favoured methodology owing to the comparable simplicity in selective removal of the templates.[1],[14–20] Bentz et al. covered diverse array of novel synthetic procedures for constructing HPNs and mentioned how HPNs gained tremendous interest compared to their solid counter parts.[21] Several approaches towards this have also been proposed to tailor silica nanoparticle (SiNP) surfaces with polymers *via* surface-initiated living radical polymerization.[22–27] Voit et al. efficiently synthesized hollow nanocapsules by surface initiated RAFT polymerization (SI-RAFT) using SiNP as sacrificial templates with polymer shell of poly[poly (tert-Butyl methacrylate)–*co*-poly(2,3-dimethylmaleic imidopropyl methacrylate)-*b*-poly(2-hydroxypropypl methacrylamide)] (PtBMA-*co*-PDMIPM-*b*-PHPMA) where 2,3-dimethylmaleic imidopropyl methacrylate (DMIPM) was incorporated as a photo crosslinker to stabilize the nanocapsules.[25] They also presented a robust strategy to construct size tunable polymer nanocapsules with [poly(diethylaminoethyl methacrylate)-*co*-poly(pyridyldisulfide ethylmethacrylate)] (PDEAEMA-*co*-PPDSM) as polymer shell on silica template in which factors like pH and the length of the crosslinker, causes a dramatic change in the diameter of the nanocapsule.[26] Chen et al. synthesized poly(N-isopropylacrylamide) (PNIPAm) by RAFT polymerization and then grafted onto silica template *via* thiol-ene click reaction to make

poly(methacrylic acid-*co*-divinylbenzene)-*g*-poly(N-isopropylacrylamide) P(MAA-*co*-DVB)-*g*-PNIPAm nanocapsules with pH-responsive P(MAA-*co*-DVB) inner shell and temperature-responsive PNIPAm brushes.[27] Very recently, vesicle-templated porous polymer nanocapsules,[28] hollow latex (HL) particles of polymers/hybrid polymer/inorganic materials[29], novel hollow and yolk-shell structures[30],[31], supramolecular polymer hollow nanocapsules[32] have been shown as very promising functional materials for numerous applications. Though a lot of studies related to hollow nanocapsules have been reported so far, but there is still scope to tune the shell polymer architecture to see the effect of polymer structure and the chain length on the formation and stability of the HPN. In addition, a suitable shell made up of polymer structure with appropriate functionality can be of huge significance to do various chemical processes inside the core and the shell. Also, the crosslinking among the grafted polymer chains of the particle (intra-crosslinking) and between the chains of the adjacent particles (inter-crosslinking) need to be studied in depth to ensure the robustness of the resulting HPN. In this article, we have made efforts to address all these issues by grafting poly[2-(methacryloyloxy) ethyl ferrocenecarboxylate] (pFcMA) and an alkyne terminated polymer, poly(propargyl 4-vinylbenzyl ether) (pPVBE) in various combinations so that the effect of structural architecture of the shell can be understood on the various physical and chemical aspects of the HPN.

Aluminium nanoparticles (Al-NP) is a known metallic fuel often used in rocket motor, spaceship etc. because of its improved combustion and thermal performances.[33],[34] However, the access to Al-NP is a major concern during and after the synthesis as amorphous oxide layer of Al_2O_3 quickly forms on the surface of Al-NP upon exposure to air or water vapour; thus, a thoughtful passivation of the Al-NP surface is absolute necessity for keeping the combustion properties intact.[35,36] A quite a vast literature efforts have been directed to achieve the effective passivation of the Al-NP though success is quite limited. Murlidharan et al. reported the synthesis and stabilization of aluminum nano particles in various polymeric matrix such as poly (vinylpyrrolidone) or poly (methylmethacrylate) matrices.[37,38] Naypete et al. reported an in situ synthesis of aluminum nanoparticles with the help of a novel titanium (IV) benzyloxide

initiator synthesized within and trapped inside a hollow polymer nanocapsule.[36] Ferrocene (Fc) and its derivative have been regularly used as a promising burn rate catalyst (BRC) in propellants and capable to perform outstanding exothermic thermite reaction with Al powders.[39],[40] So, on this account, encapsulation of Al-NP by ferrocenyl polymer would be a much better choice. Hu et al. prepared a nanocomposite of Al coated with fluoro-containing long-chain Fc polymers in order to tackle migration issue.[33] We envision a dual functional framework comprising of ferrocene a burn rate catalyst and aluminum (Al), a metallic fuel. We took advantage of the hollow space of the HPN to make Al-NP embedded with the polymeric shell consisting of ferrocene. Therefore, the resulting material would be a composite of Al/Fe which is expected to act as burn rate modified cum fuel in the solid composite propellants (CSPs). Recently, our group has reported development of various kinds of polymer chain grafted SiNP using SI-RAFT through grafting from approach and studied carbohydrate-protein interactions, used as very effective nanofiller in improving physical properties of polymer/silica nanocomposites.[41–43] Grafting technique to grow different polymer brushes on to the SiNP surface as per the design after anchoring the chain transfer agent (CTA) onto silica surface has found lot of attention in recent times.[44–46] Motivated by all the development as discussed above, herein we have grown copolymer brush comprising of 2-(methacryloyloxy) ethyl ferrocenecarboxylate (FcMA) and an alkyne terminated monomer, propargyl 4-vinylbenzyl ether (PVBE) onto SiNP surface by using surface initiated one pot RAFT polymerization *via* grafting from approach and after that constructed a hollow polymer nanocapsule by etching out the sacrificial silica core. Further, Al-NP is synthesized in the core in order to make nanoparticles comprised of both Fe and Al which can be used as burn rate catalyst and fuel in CSPs. To investigate the influence of polymer architecture over HPN formation, the copolymer brush on the silica surface was designed in three different structural motifs. Shell polymer intra/ inter-chain crosslinking was performed *via* copper-azide click reaction to make robust HPN. The formation of HPN was ascertained by TEM, confocal laser microscope, fluorescence lifetime imaging microscope. Finally, Al-NP/HPN composite was synthesized following a user-friendly sonochemical process and the encapsulation of Al-NP were validated by IR, PXRD and TGA.

6.2. Experimental Section

All the details about the sources of materials and characterization techniques are included in the **Chapter 2**. Chain transfer agent (CTA), 3-benzylsulfanylthiocarbonylsufanyl-propionic acid (BSPA) was grafted to the SiNP surface via multiple steps followed by our earlier reported procedure and also shown in **Chapter 2**.[47] In the first step, SiNP of size in the range of 45±2 nm was synthesized by Stöber method which was further modified with (3-aminopropyl) triethoxysilane (APTES) to get amine functionalized SiNP (SiNP-NH_2). Then BSPA was activated by N-hydroxysuccinamide (NHS) and attached to the SiNP *via* amine end of triethylamine attached on the SiNP surface as BSPA-NHS. All the detailed synthetic procedures including the complete characterization data of CTA, and monomers FcMA and PVBE are given in the **Chapter 2** and Appendix III.

6.2.1. Grafting of Copolymers of pFcMA and pPVBE on SiNP surface

The copolymerization processes of FcMA and PVBE monomers were performed using grafting from RAFT technique in three different routes to make three varieties *ca* p(FcMA-*b*-PVBE)-*g*-SiNP and p(PVBE-*b*-FcMA)-*g*-SiNP, (two kinds of blocks) and a random copolymer *grafted* SiNP, rp(FcMA-*co*-PVBE)-*g*-SiNP of copolymer structural motifs on the SiNP surface. A representative methodology is described below, synthetic methods for other structures were quite similar except the changes in the monomer addition cycle and the quantity of the monomers added.

100 mg of SiNP-BSPA (2.25 mg of BSPA, 8.27 μmol), calculated amount of FcMA (166 mg; this amount was calculated for the monomer ratio of 1:1 and varied accordingly to obtain different chain lengths), free BSPA (2.25 mg, 8.27 μmol) and 0.679 mg of AIBN (4.18 μmol) were taken in a Schlenk tube and 1.5 mL of dry DMF was added into it in nitrogen atmosphere. Then the reaction mixture was subjected to freeze-pump-thaw cycle for three consecutive times and brought back to room temperature and then it was placed into a preheated oil bath at 90 °C. The reaction was allowed to stir up to 12 hours and then the other monomer, PVBE (166 mg) was added in presence of nitrogen atmosphere and again stirred for another

16 hours at 85 °C. The reactants were added based on the ratio of [SiNP-BSPA]: [free BSPA]: [AIBN] = 1:1:0.25. After completion, the obtained copolymer *grafted* SiNP, designated as p(FcMA-*b*-PVBE)-*g*-SiNP (in short called as P_xQ_y where x and y indicate the monomers weight ratio and altered as 1:1,1:3 and 3:1; see *Scheme 6.1* and *Appendix III-Table 6.1*), was purified by centrifugation at 2000 rpm for 15 minutes with the addition of 5 mL of DCM. This process was repeated until the solution become colourless. Finally the synthesized p(FcMA-*b*-PVBE)-*g*-SiNP (P_1Q_1) particles were collected and dried under vacuum for 24 hours at room temperature. Similar methodology was followed for other two cases by keeping the ratio [SiNP-BSPA]: [free BSPA]: [AIBN] = 1:1:0.25 as constant; only monomers amount (weight ratios) was varied differently as 1:3 and 3:1. Similarly, when PVBE was added first then the particles are named as p(PVBE-*b*-FcMA)-*g*-SiNP (in short called as Q_xP_y ; see *Scheme 6.1* and *Appendix III-Table 6.1*) and when both the monomers were added all together, it yielded random copolymer of FcMA and PVBE of structure rp(FcMA-*co*-PVBE)-*g*-SiNP (in short called as rP_xQ_y ; see *Scheme 6.1* and *Appendix III-Table 6.1*).

6.2.2. Crosslinking of polymer chains grafted on SiNP

Copolymers *grafted* SiNP (80 mg) were dispersed in dry DMF at inert atmosphere and 30 wt% of 1,4-bis(azidomethyl)benzene (24 mg) was added followed by the addition of catalytic amount of CuI. Finally, 0.4 mL of N,N-Diisopropylethylamine (DIPEA) was added as a base and stirred for 16 hours. The cross-linked particle was collected after thorough washing with THF and water *via* centrifugation at 2000 rpm for 15 minutes. This process was repeated until the solution become colourless. Finally, the product was dried under vacuum for 48 hours at room temperature. These particles were designated as CL-p(FcMA-*b*-PVBE)-*g*-SiNP (in short CL-PQ), CL-p(PVBE-*b*-FcMA)-*g*-SiNP (in short CL-QP) and CL- rp(FcMA-*co*-PVBE)-*g*-SiNP (in short CL-rPQ).

6.2.3. Preparation of hollow polymer nanocapsules (HPN)

The crosslinked particles (70 mg) were dispersed in 4 mL of DCM and DMF mixture (3:1 v/v) in a teflon vial. A catalytic amount of phase transfer catalyst tetrabutylammonium

bromide was added to the solution followed by the addition of 1.5 mL of 48% HF. The reaction mixture was stirred for 10 hours at room temperature. The polymer solution was extracted with saturated sodium bicarbonate solution and then finally precipitated with ether. The obtained copolymer was dried under vacuum for 24 hour at room temperature. These particles were referred as hollow polymer nanocapsules (HPN) and abbreviated as HL-p(FcMA-*b*-PVBE)-*g*-SiNP (in short HL-PQ), HL-p(PVBE-*b*-FcMA)-*g*-SiNP (in short HL-QP) and HL- rp(FcMA-*co*-PVBE)-*g*-SiNP (in short HL-rPQ).

6.2.4. Synthesis of Al-NP in the HPN to make Al/ferrocenyl polymer nanocomposite

In a 50 mL three neck round bottom flask fitted with a nitrogen gas inlet and outlet, 15 mL of degassed toluene was stirring under nitrogen environment and placed into an ultrasonic water bath. 0.165 g of $LiAlH_4$ (4.36 mmol) was suspended into it along with 0.058 g of synthesized HPN followed by the drop wise addition of 0.5 mL of $SiCl_4$ (4.36 mmol). The reaction was allowed to continue for 2.5 hours under sonication. The bath temperature was ~60 °C and this temperature was sufficient enough to remove the low boiling silanes and other gaseous by-products formed in this reaction. The weight ratio of $LiAlH_4$ to HPN was 3 : 1 to achieve 100 % of the theoretical yield of metal-polymer nano composite.[37] After 2.5 hours, excess amount of MeOH was added to quench the reaction mixture under cold conditions and filtered to obtain Al-NP encapsulated by HPN. The grey Al-NP/HPN nanocomposite powder was washed with dried methanol to remove impurities. Exactly similar methodology was followed to produce Al-NP without adding HPN and these particles are considered as control (blank) for the comparison purpose.

6.3. Results and Discussion

6.3.1. Synthesis of CTA-anchored SiNP

SI-RAFT polymerization via *grafting-form* technique is one of the most favoured approach among various SI-LRP techniques in order to modify the surface of nanoparticles with polymer chains.[25] In this work, to make HPN using SiNP as sacrificial template, we used

SI-RAFT polymerization technique with *grafting-from* pathway in which BSPA, a trithiobenzoate derivative, is chosen as CTA to perform the RAFT polymerization over SiNP surface. The complete procedure for synthesizing BSPA functionalized SiNP (SiNP-BSPA) is carried out following earlier methods[41–43] and presented detailed in **Chapter 2**. First, silica nanoparticles (SiNP) were prepared using the Stöber method, followed by the reaction with (3-aminopropyl)triethoxy silane (APTES) to obtain amino-functionalized silica nanoparticles (SiNP-NH_2). Finally, activated BSPA was reacted with SiNP-NH_2 to achieve SiNP-BSPA. Activation of BSPA is necessary to enhance the reactivity with amine functionality of SiNP. The amount of grafted amine functionality is kept constant by using a calculated amount of APTES so that a desired amount of BSPA can be loaded over the silica surface.[41,42] All the synthesized particles, SiNP, SiNP-NH_2 and SiNP-BSPA are characterized thoroughly using TGA, FT-IR, microscopic studies and DLS (*Appendix III-Figure 6.1-6.3*). The amount of BSPA loaded over the SiNP particle surface is calculated from TGA by comparing weight loss of SiNP-BSPA with SiNP-NH_2 at 700 ºC (*Appendix III-Figure 6.1*) and found to be equal to 22.5 mg/g which is equal to the BSPA grafting density 0.83 groups/ nm^2 on the SiNP surface. This grafting density calculation is done assuming the density of the silica nanoparticles as 2.65 g/cm^3. The comparison of IR spectra shown in *Appendix III-Figure 6.2* confirms the successful attachment of BSPA over SiNP surface. The characteristic absorption band at 1658 cm^{-1} is attributed to the carbonyl stretching frequency of newly formed amide bond during BSPA attachment over silica surface and the appearance of amide N-H bending vibration at 1568 cm^{-1} supports the attachment [*Appendix III-Figure 6.2(B)*]. The thiocarbonyl stretching peak is not visible due to the overlap with the strong absorption of bare silica at 1064 cm^{-1} [*Appendix III-Figure 6.2(A)*]. The average diameter of the BSPA attached nanoparticle (SiNP-BSPA) is found to be ~ 45 ± 2 nm as measured by FESEM and TEM analysis [*Appendix III-Figure 6.3(A) & (B)*] and 58 nm as obtained from DLS study in THF dispersion [*Appendix III-Figure 6.3(C)*].

6.3.2. Grafting of pFcMA and pPVBE copolymer chains on SiNP

Three series of copolymers (*Scheme 6.1*) with various chain length and three kinds of polymer architectures which include two types of block copolymer structures, p(FcMA-*b*-PVBE) and p(PVBE-*b*-FcMA), and a random copolymer, rp(FcMA-*co*-PVBE) are grafted on the SiNP surface using SI-RAFT polymerization in order to investigate the effect of polymer architecture on the grafting process, grafting density, the morphology of the grafted SiNP and more importantly on the formation of HPN. The SI-RAFT polymerization reactions are carried out to grow the copolymer chains on the CTA anchored SiNP (SiNP-BSPA, which is synthesized as described in the previous section) using AIBN as initiator and in presence of added CTA in the polymerization mixture (*Scheme 6.1*).[25],[41,42] This additional free CTA is used to control the polymerization on the particle surface by allowing efficient exchange reaction between graft and free polymers. As presented in the *Scheme 6.1*, the second monomer was introduced in the polymerization feed just after the completion of the chain propagation of first polymer chain block without any further purification and finally the block copolymer grafted to SiNP are collected after centrifuge. But in case of random copolymer (*Scheme 6.1*), both the polymers are added together in the polymerization feed. The two monomers namely 2-(methacryloyloxy) ethyl ferrocenecarboxylate (FcMA) and propargyl 4-vinylbenzyl ether (PVBE) are chosen for the synthesis of the copolymer chains because the former brings the ferrocenyl functionality, which has catalytic activity as described in the introduction and the later introduces an alkyne functionality in the chain which can be utilized for further modification such as intra and inter-chain crosslinking using click reaction with azide. These two monomers, FcMA and PVBE were synthesized following the procedure as described in the supporting information (*Appendix III-Scheme 6.2 & 6.3*) and their chemical structures are confirmed by ^{1}H, ^{13}C NMR (*Appendix III-Figure 6.4-6.7*) and HRMS characterizations. All the NMR signals are assigned with the chemical structures and detailed in Appendix III description.

All the polymerization reactions were performed in dry DMF solvent by using AIBN as thermal initiator in presence of free BSPA by keeping the mole ratio [SiNP-BSPA]: [free

BSPA]: [AIBN] = 1:1:0.25 as constant. To make different block structure in one case FcMA was added first followed by PVBE and in the second case the order of addition of monomers are changed as depicted in *Scheme 6.1*, however, both FcMA and PVBE are added together in case of random copolymer. In order to synthesize different chain length polymers, [FcMA: PVBE] monomer wt% ratio was varied in three different ways *ca* [1:1], [1:3] and [3:1] where in each case two block-co-polymers and one random-co-polymer are synthesized. Targeted molecular weight of pFcMA part is kept constant as 10,000 in all the cases for the easy calculation and comparison, and thus as a whole total nine different chain lengths of polymers are *grafted* on the silica surface (*Appendix III-Table 6.1*). When pFcMA block (abbreviated as P; *Appendix III-Table 6.1*) is grown first followed by pPVBE (abbreviated as Q in *Appendix III-Table 6.1*), then it is named as p(FcMA-*b*-PVBE)-*g*-SiNP (abbreviated as PQ; *Scheme 6.1*, *Appendix III-Table 6.1*) and similarly when the reverse (pPVBE block is grown first followed by pFcMA) happens to yield p(PVBE-*b*-FcMA)-*g*-SiNP (abbreviated as QP; *Scheme 6.1*, *Appendix III-Table 6.1*). While both pPVBE and pFcMA blocks are grown randomly then the synthesized nanoparticle is having sequence rp(FcMA-*co*-PVBE)-*g*-SiNP (abbreviated as rPQ; *Scheme 6.1*, *Appendix III-Table 6.1*). After many experimental trials, the reaction time to grow the pFcMA block is fixed as 12h and for the pPVBE block it is 16h whereas random copolymer reaction is continued upto 20 hours. Further, for the synthesis of the hollow polymer nanocapsules (HPN), only three of them (P_1Q_1, Q_1P_1, rP_1Q_1), which are having FcMA : PVBE = 1:1, are chosen among nine polymer grafted silica particles as because the molecular weight distribution of these polymer chains grown on the SiNP is quite comparable (*Appendix III-Table 6.1*).

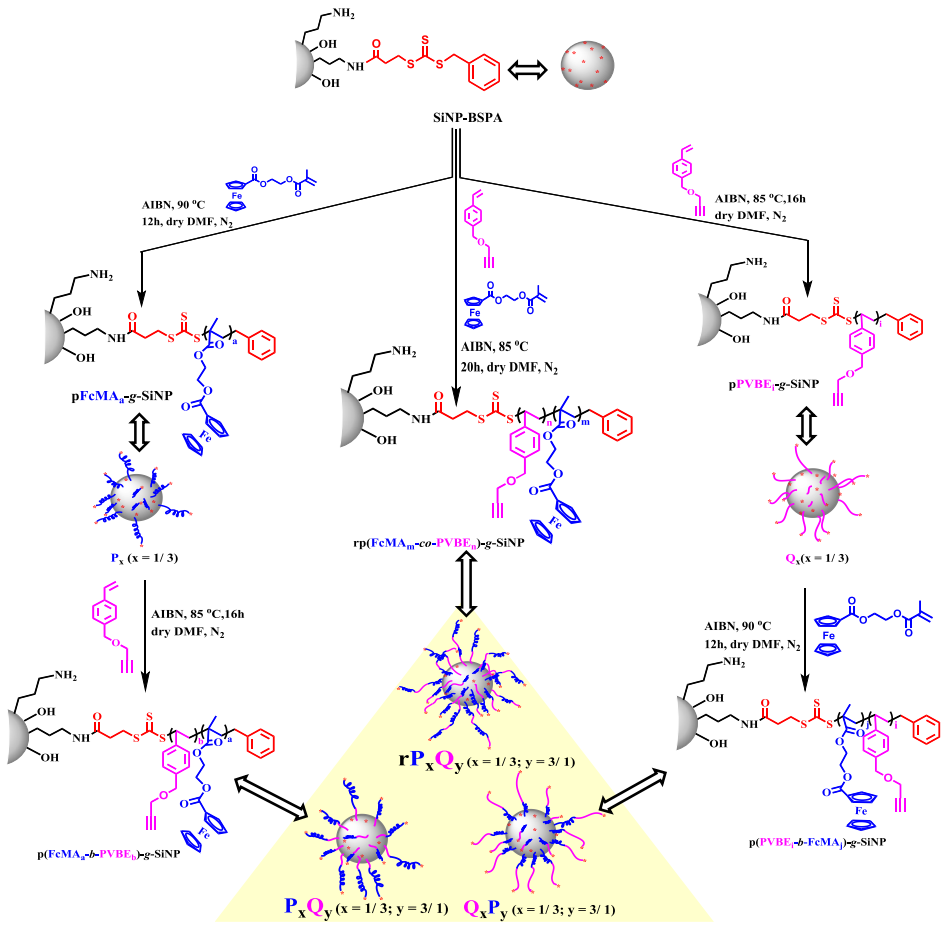

Scheme 6.1: *Pictorial representation of method for synthesizing copolymer grafted SiNP by using one-pot SI-RAFT polymerization via grafting from approach.*

The structural identifications of a block and random copolymers brush *grafted* onto the SiNP surface is investigated by spectroscopic techniques by comparing with the CTA anchored SiNP. The characteristic IR frequencies at 1388 cm^{-1} and 1496 cm^{-1} for ferrocenyl unit is more intense in PQ [p(FcMA-*b*-PVBE)-g-SiNP] samples than in QP [p(PVBE-*b*-FcMA)-g-SiNP] (*Appendix III-Figure 6.8*) while it is not that clearly visible in case of rPQ [rp(FcMA-*co*-PVBE)-g-SiNP]. Similarly peak at 2110 cm^{-1} attributed for the weak stretching frequency of -C≡C- bond in pPVBE chain is seen in the grafted chain. . The ester carbonyl of pFcMA chain

and amide carbonyl peaks get merged together with the peak at 1658 cm^{-1} and displays an intense peak in all the cases.

Further a representative ^{1}H NMR spectrum of random copolymer grafted SiNP is shown in *Figure 6.1* with assigned peaks. The peaks at 4.2 to 4.85 ppm correspond to cyclopentadiene (Cp) ring protons of pFcMA block and the resonance peak for –O-CH_2-CH_2-O- of pFcMA block appears at 4.45 ppm is merged with Cp ring protons. The terminal alkyne hydrogen of pPVBE block shows a singlet at 2.5 ppm. The proton peaks –-CH_2-O-CH- unit of pPVBE are also merged with Cp ring protons. The aromatic ring protons of both the pPVBE and BSPA appear at 6.8 ppm to 7.49 ppm along with $CDCl_3$ solvent peak. The appearance of –CH_3, -CH_2, -CH- resonance peaks at 2.2 ppm to 0.85 ppm (especially –CH_3 of pFcMA can be clearly identified as a singlet at 1.28 ppm as shown in the inset of the *Figure 6.1*; besides the ether peak mentioned in the inset appears as a solvent impurity) is clearly indicated the successful polymerization. The methylene protons of BSPA appears at 3.8-3.9 ppm. A ^{13}C-NMR spectra along with the detailed peak assignments of a representative sample shown in *Appendix III-Figure 6.9* also confirms the structure of the synthesized copolymer.

A detailed analysis is carried out on ^{1}H NMR spectra to identify the differences between block and random copolymer structure (*Appendix III-Figure 6.10*). It is known that a change from one sequence of microstructure to another sequence is possible in case of block copolymer while random copolymer maintains a constant sequence of average composition all along the polymer backbone.[48] In order to investigate the structural difference from block to random copolymers in the current grafted polymer chains, the alkyl region of NMR spectra (2.85 - 0.7

ppm of two synthesized block copolymers are compared with random copolymer and a significant differences in peak distribution are noticed as seen in *Appendix III-Figure 6.10*. In case of block copolymers (PQ and QP), methyl (CH_3, numbered as 4) appears as an intense singlet at 1.28 ppm, methylene (CH_2, abbreviated as 2/1'/3') shows up at 1.65 ppm as relatively broad peak and methine (-CH-, denoted as 2'/4') resonance peak comes as multiplates between 2.17- 2.2 ppm (though difficult to assign exactly). However, in different microstructure, in case

of random copolymer (rPQ), the resonance peaks of CH_2 (2") appears at 1.35- 1.75 ppm as very broad doublet, CH_3 (4") comes at 1.28 ppm as singlet and CH (1") shows as multiplates in the range of 2.1-2.2 ppm. It is important to note that the alkyne proton of pPVBE block is clearly visible at 2.5 ppm for random copolymer while in block copolymer it merges in the region of 2.05 – 2.2 (*Appendix III-Figure 6.10*). All these observations as discussed above clearly points to the fact that there are clear cut microstructural distinctions between the grafted block and random chains.

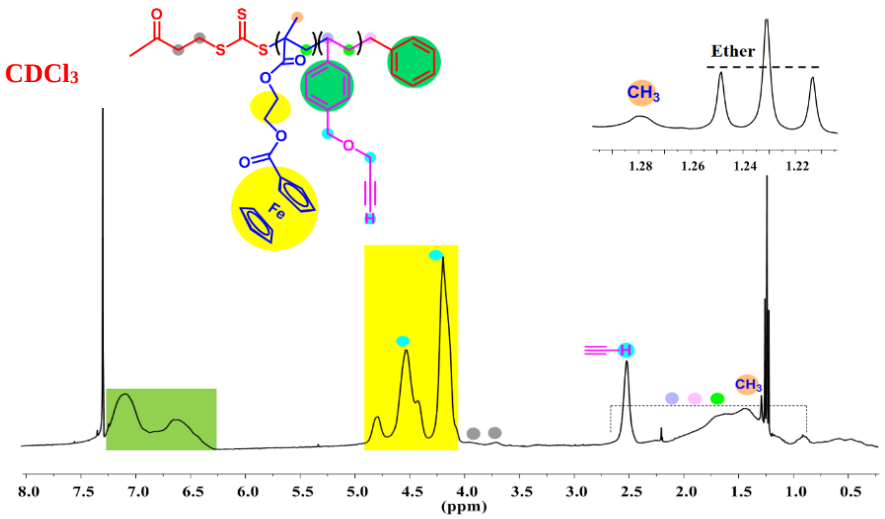

Figure 6.1: *^{1}H NMR spectrum of rp(FcMA-co-PVBE)-g-SiNP. Identification of various peaks are indicated in the figure. Inset: An enlarge portion to show the clarity in the peak integration.*

We also calculated the molecular weight and degree of polymerization (DP) of the copolymers from the peak integrals of ^{1}H NMR (*Appendix III-Figure 6.11*) spectra and tabulated in Table 1. The data clearly indicate that we have achieved the chain length of the copolymer as targeted by the RAFT reaction condition ($\overline{M_n}$ targeted was ~20,000) The molar percentage of FcMA monomer in the copolymer is also calculated from this data and found to be the maximum at ~ 63% in case of random copolymer (rP_1Q_1) whereas conversion is

relatively lower in blocky structure and the values are 57% and 40 % for P_1Q_1 and Q_1P_1, respectively. Furthermore, the molecular weight and polydispersity index (Đ) of all the samples were determined using GPC (*Appendix III-Table 6.1*& *Table 6.1*) and chromatographs of all three type copolymers are shown in *Figure 6.2(A)* and *Appendix III-Figure 6.12*.

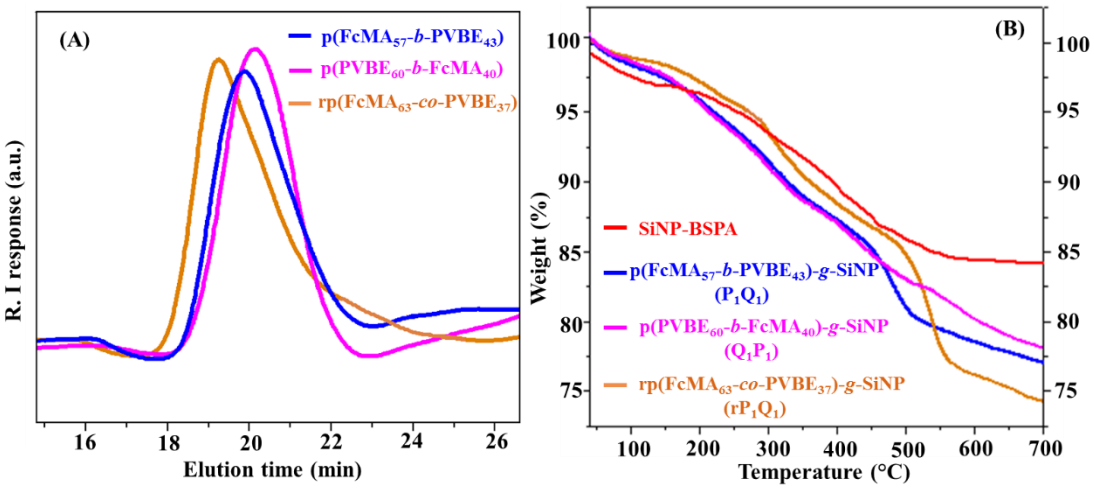

Figure 6.2: *(A) GPC chromatograms of few representative copolymers grafted on the SiNP. All other samples chromatograms are given in Figure S12. Note: The GPC was measured after cleaving the polymer chain from the SiNP by HF treatment. (B) TGA thermogram of SiNP-BSPA and copolymers grafted particles.*

The polymer chains are cleaved and separated from the SiNP surface by HF treatment to perform the GPC analysis. The number-average molecular weight ($\overline{M_n}$) and Đ values of the grafted copolymers clearly indicate that SI-RAFT polymerization over the particle surface is successfully conducted in a well-controlled manner. The molecular weights obtained from GPC data are in well agreement with the targeted molecular weight (see *Appendix III-Table 6.1*& *Table 6.1*) and the best matched in case of random copolymer grafted chain (rPQ). It is also to be noted that the chain length (molecular weight) of all the rPQ samples are higher than both PQ and QP samples irrespective of the monomer composition (see *Appendix III-Table 6.1*). The amount of polymer chain grafted and the polymer chain density (σ) on the SiNP surface are calculated from the thermogravimetric analysis [*Figure 6.2(B)*]. The remaining

weight % of P_1Q_1, Q_1P_1 and rP_1Q_1 grafted SiNP at 700 ºC is 77.08%, 78.41% and 74.11% , respectively. Comparing the weight loss of SiNP-BSPA at 700 ºC, the amount of the grafted polymers P_1Q_1, Q_1P_1 and rP_1Q_1 on the SiNP is calculated to be (in mg/g of SiNP) 83.8, 68.1 and 119.1, respectively (*Table 6.1*).

Table 6.1: *Various parameters obtained from GPC and TGA analysis for different copolymers grafted over SiNP surface.*

Polymer Sample[a]	$\overline{M_n}$ **calculate**[b] **(g/mol)**	$\overline{M_n}$ **achieved**[c] **(g/mol)**	**Đ**[d]	**Amount grafted over surface**[e] **(mg/g)**	**Grafting density (chains/ nm^2)**[f]	**D/R_g**[g]	**Size (TEM) (nm) [Shell diameter (nm)]**[h]	**DLS Size in THF & ethanol**[i] **(nm)**
SiNP-BSPA				22.5	0.83		45	58 & 61
p($FcMA_{57}$-*b*-$PVBE_{43}$)-*g*-SiNP (P_1Q_1)	27,219	18,851	1.3	83.8	0.053	1.15	59 [13]	128 & 105
p($PVBE_{60}$-*b*-$FcMA_{40}$)-*g*-SiNP (Q_1P_1)	24, 312	17,647	1.27	68.1	0.046	1.2	54 [8]	122 & 103
rp($FcMA_{63}$-*co*- $PVBE_{37}$)-*g*-SiNP (rP_1Q_1)	28, 245	21,496	1.4	119.1	0.066	0.98	63 [18]	148 & 112

[a] Degree of polymerization from NMR molecular weighed calculated using ^{1}H NMR peak integrals (*Appendix III-Table 6.11*) and the DP values are indicated in the subscript of the polymer chain [b] ($\overline{M_n}$) calculated based on the integration value obtained from ^{1}H-NMR spectra. [c] $\overline{M_n}$ and [d] dispersity (Đ) are obtained from GPC analysis. [e,f] Estimated from TGA analysis. [g]D represents the distance between the grafted polymer chains; [g]R_g refers the radius of gyration determined by $R_g = 0.5\ N^{0.5}$ nm, [h] measured from the TEM software and the data shown here is the average of at least six measurements, [i] DLS size measured by dispersing the samples in THF and ethanol.

This data clearly suggests that the copolymer structure affects the grafting process which is more evident when grafted copolymer amount is calculated as the polymer chain density (σ), which are found to be 0.053, 0.046 and 0.066 chains/ nm^2 for P_1Q_1, Q_1P_1 and rP_1Q_1, respectively. Higher amount and denser chain grafting happened in case of random copolymer than block-copolymers. It is also to be noted that σ of SiNP-BSPA (0.83 BSPA/nm^2) is much

higher (more than 10 times) compare to grafted chains indicating that copolymer chain growth is not occurring from all the CTA anchored initiating sites on the particle surface.[25] We also calculated the average distance between the neighbouring polymer chains (D), which is equal to $\sigma^{-1/2}$ and radius of gyration (R_g) of the grafted chains, which is calculated as $R_g = 0.5\ N^{0.5}$ nm where N is the degree of polymerization which are considered here as 57, 60 and 63 for P_1Q_1, Q_1P_1 and rP_1Q_1, respectively.[49] A point to be noted here is that to calculate R_g value, the degree of polymerizations of the nearest chain attached to surface is considered. *Table 6.1* shows that the ratio of D to the radius of gyration (D/R_g) values are 1.15, 1.2 and 0.98 for for P_1Q_1, Q_1P_1 and rP_1Q_1, respectively which are less than 2 attributing that the polymer chains grafted on the SiNP are in brush regime.[49]

The morphology of the polymer *grafted* SiNP was inspected by TEM, is shown in *Figure 6.3*, clearly display a well-defined core-shell features in all three cases with the diameter of about 54 to 63 nm (*Table 6.1*). Also the surface of the particles looks less smooth as as compared to SiNP. The increase in particle size, core-shell features and rougher surface compared to SiNP-BSPA (45 nm) supports the event of copolymer chains growth on the particle surface. Also, it is to be noted that the shell thickness, as noted in *Table 6.1*, increases with increasing chain length of the grafted copolymers; maximum shell thickness (~ 18 nm) is obtained in case of rP_1Q_1 which has the highest chain length. This observation also confirms the grafting of the chains. The particle diameter obtained from DLS study in THF dispersion (*Table6.1*) displays quite a significant increase in the size of the copolymer grafted SiNP from the SiNP-BSPA particles attributing the swelling of the grafted chains. Also, the swelled particle size varies with the chain length.

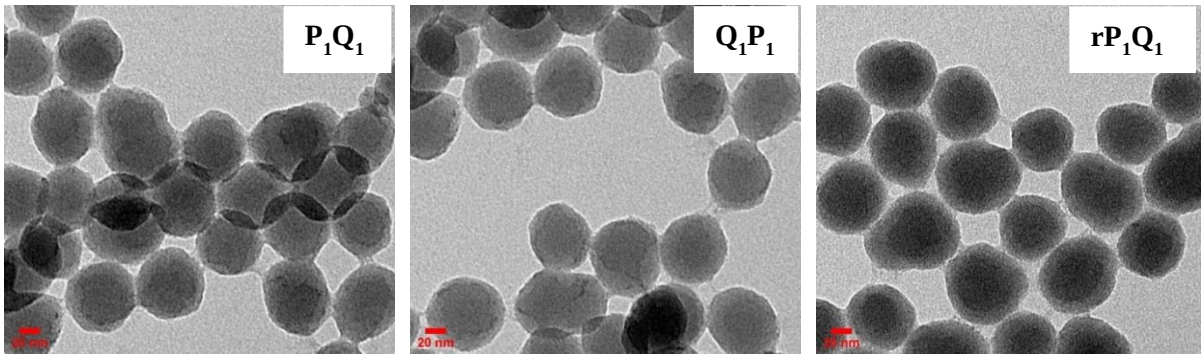

Figure 6.3: *TEM images of copolymer grafted SiNP.*

In order to study the electrochemical properties of ferrocenyl polymer on the particle surface, cyclic voltammetry (CV) was performed with copolymers after cleaving from the particles. At the scan rate of 20 mV S^{-1}, the oxidation peaks ranges from 0.898 to 0.812 V and the corresponding reduction peaks varies from 0.729 V 0.632 V as shown in the *Figure 6.4(A)* with dotted line. The peak potential values are in good agreement with ferrocene containing polymers and also the relatively lower difference between the peak potential is attributed to comparatively less delayed electron transfer process.[50,51] The scan rate dependency study, anodic peak current with the square root of scan rate, shown in *Figure 6.5(B)* matches quite well as linear fit following the Randles-Sevcik equation may be attributed to the involvement of freely diffusing redox species (ferrocene) in the copolymer solution [52,53].

Furthermore, we investigated the swelling behaviour of the polymer chains grafted over the particle surface under two kinds of solvents, ethanol and THF, with wide variation in polarity, where particles are dispersed well. The hydrodynamic radius (R_h) of SiNP-BSPA obtained from DLS study in THF (58 nm) is little less than in case of ethanol (61 nm) (see last column of the first row in *Table 6.1*). As both the polymer blocks are hydrophobic in nature, the brush length (l_b; defined as the difference in hydrodynamic radius of the polymer grafted nanoparticle and the bare silica nanoparticle) is expected to swell more in less polar THF than highly polar ethanol. This is realized from the DLS study (*Appendix III-Figure 6.13*) which

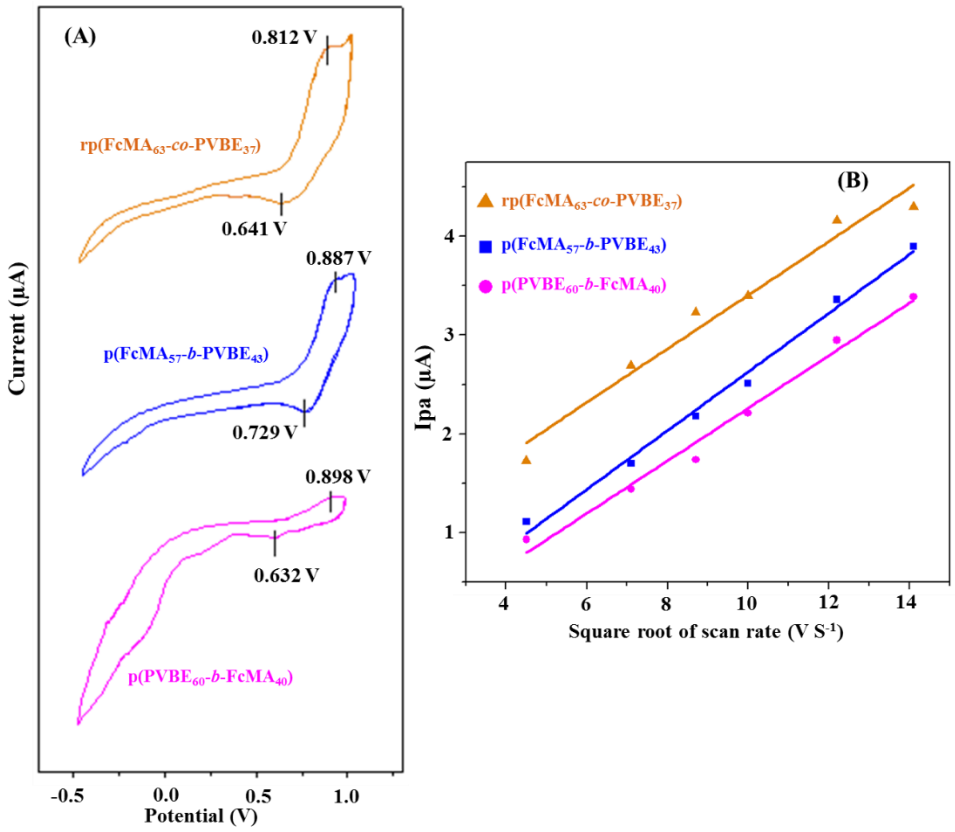

Figure 6.4: *(A) Cyclic voltagramms of copolymers grafted on the particle surface and (B) Anodic peak current vs. square root of scan rate of the redox process of the ferrocenyl copolymers. The experiment was carried out by dissolving (0.5 mg/mL) the copolymers in dry DCM by using Pt wire as working electrode in presence of 0.1(M) TBAP with addition of a Ag wire as reference and Pt wire as counter electrode. The CV chromatogram was obtained by cycling the potential between -0.5 V to +1.0 V at various scan rate ranging from 20 mV S^{-1} to 200 mV S^{-1}.*

shows that the $l_{b,THF}$ are 70 , 64 and 90 nm (these numbers are obtained by subtracting DLS size of polymer grafted nanoparticle in THF from the DLS size of SiNP in THF, see the last column in *Table 6.1*) for three copolymers P_1Q_1, Q_1P_1 and rP_1Q_1, respectively is almost 1.6 - 1.7 times higher than $l_{b,\ ethanol}$ which are found to be 44 , 42 and 51 nm for for three copolymers P_1Q_1, Q_1P_1 and rP_1Q_1, respectively. As chain length differs, l_b also differs accordingly in both

solvent which is evident from the data presented in *Table 6.1* where it is seen that highest number of repeat unit containing polymer rP_1Q_1 has the highest l_b followed by P_1Q_1 and Q_1P_1.

Polymer ligands on the silica nanoparticle surfaces having different grafting densities can have different types of chain conformation resulting unique assembly behaviour.[44,45,54,55] In the current study our synthesized block copolymer tethered brush particles displays a continuous assembled cluster network suggesting the occurrence of self-assembly process in between the polymer chains (*Appendix III-Figure 6.14*). On the other hand, random copolymer *grafted* particles shows more like aggregated cluster network (*Appendix III-Figure 6.14*) and this is most possibly because in the random state the polymer chains are not self-assembled as good as in block copolymer grafted chains.

6.3.3. Crosslinking the grafted copolymer chains

The SiNP functionalized with copolymer chains, p($FcMA_{57}$-b- $PVBE_{43}$), p($PVBE_{60}$-*b*-$FcMA_{40}$) and p($FcMA_{63}$-*co*-$PVBE_{37}$), are covalently cross-linked by coupling with a diazide derivative through click reaction (*Scheme 6.2*) to create the robust particles. The cross-linker, a diazide derivative [1,4-bis(azidomethyl)benzene] was first synthesized from a commercially available dibromo derivative 1,4-bis(bromomethyl)benzene by using sodium azide as base and characterized by IR and NMR spectroscopy (*Appendix III-Figure 6.15 and 6.16*). The CuI mediated click reaction between synthesized 1,4-bis(azidomethyl)benzene and the terminal alkyne functionality of pPVBE block hanging from either side of the polymer chain on the particle surface lead to the formation of two units of triazole units bridged with a benzene ring yielding a highly cross-linked polymer matrix (*Scheme 6.2*). Thus the crosslinking region will be designed as per the position of pPVBE block as schematically presented in *Scheme 6.2* and it will indirectly govern the possibility of pFcMA block to be involved in the strong non-covalent-intra/inter-particle crosslinking owing to very high polarizability of Cp unit.[50] For better clarity, the intra-particles-crosslinked region is pictorially presented in *Appendix III-Figure 6.17(A)*. These cross-linked polymer structures are ascertained by FT-IR [shown in *Appendix III-Figure 6.17(B)* only for p($PVBE_{60}$-*b*- $FcMA_{40}$)-*g*-SiNP as a representative] and

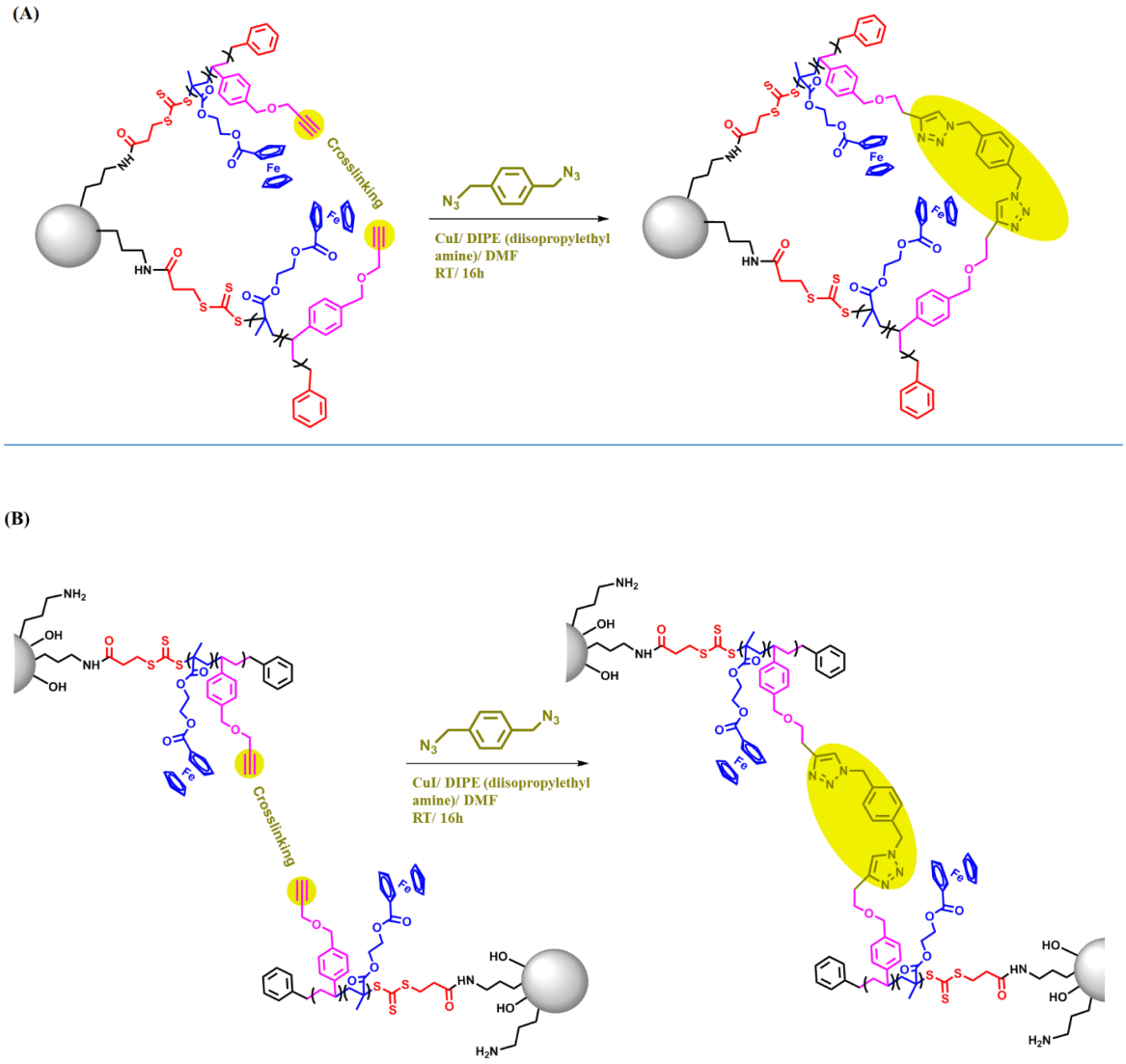

Scheme 6.2: *(A) Intra particle and (B) inter particle crosslinking reaction among the grafted copolymer chains through azide-click reaction. Only reaction between two adjacent chains is shown for the clarity of presentation; reactions are occurring throughout the particle surface wherever the PVBE chains are available.*

confirmed by the disappearance of the peak correspond to -C≡C- stretching at 2110 cm^{-1} and -C≡C-H bending vibration at 661 cm^{-1} while compared with the polymer grafted nanoparticles. The absorption peak for triazole ring gets merged with aromatic benzene ring region 3100

cm^{-1} to 3300 cm^{-1} and hence hard to identify separately. The cross-linked polymer *grafted* nanoparticles tend to agglomerate as can be visualized from the morphological features (*Appendix III-Figure 6.18*) and correlated by the increment in R_h values obtained from DLS study as shown in *Figure 6.5(A)* [DLS plots of cross-linked particles both in THF and ethanol are shown in *Appendix III-Figure 6.19*]. For example, upon crosslinking the R_h of P_1Q_1 sample (CL-P_1Q_1) in THF dispersion increased to 217 nm from 128 nm (P_1Q_1) indicating a change in brush length (l_b) of 89 nm, whereas for Q_1P_1 and rP_1Q_1 this change is 67 nm and 76 nm, respectively. Hence, it is to be noted from the *Figure 6.5(A)* that the increase in R_h values upon cross-linking varies depending on the type of copolymer chain grafted on the SiNP. A comparison of brush length values before (see the discussion in earlier section) and after cross-linking clearly indicates nearly 1.3 fold increase in brush length due to crosslinking in case of P_1Q_1 whereas the increase is much less in case of both Q_1P_1 and rP_1Q_1. This may be due to pFcMA block which remains far from the surface also taking part in strong non-covalent-intra/ inter-particle-interactions owing to very high polarizability of Cp unit[50] during the process of intra/ inter-particle-chemical-crosslinking through pPVBE block. While, in Q_1P_1, intra/ inter-particle-chemical-crosslinking *via* pPVBE block (away from the surface) helps to decrease the tendency of non-covalent-inter-particle-interactions *via* Cp unit of pFcMA block (nearer to the surface) because of steric crowding [*Scheme 6.2(B)*]. A quite similar trend is observed for ethanol dispersed samples as well [*Figure 6.5(A)*].

In order to understand the reason behind the increase in hydrodynamic radius (R_h) and brush length (l_b) of the grafted copolymer chain upon cross-linking, we performed dynamic vapour sorption (DVS) studies of our all the samples before and after cross-linking. It is expected that the water absorption of the cross-linked samples would be more as hydrophilic traizole rings are created upon cross-linking [*Scheme 6.2(A)*]. However, the DVS plots presented in *Appendix III-Figure (6.20 – 6.23)* show that the increase in water absorption upon cross-linking is very minimal for all the cases. CL-P_1Q_1 displayed 0.35 wt% increments in water absorption compared to P_1Q_1 when exposed to 70-92% RH, while Q_1P_1 and rP_1Q_1 showed only 0.03 and 0.05 wt % increment in water absorption in the same RH range after

cross-linking. This negligible water absorption primarily because of the hydrophobic nature of polymer samples which overwhelmed the hydrophilic contribution of the traizole ring. During desorption cycle, the material lost almost similar wt% of water as in sorption phase indicates that it converted back to its original state at 15% RH.[56] All these observations point to the fact that swelling of the particles upon crosslinking as evident from the increase in R_h and l_b is not only owing to cross-linking and must be due to some other cause. We believe this is caused due to agglomeration of the particles as seen from the TEM morphology shown in *Appendix III-Figure 6.18* and strong non-covalent-intra/ inter particle-interactions between Cp unit is most possible reason behind it.

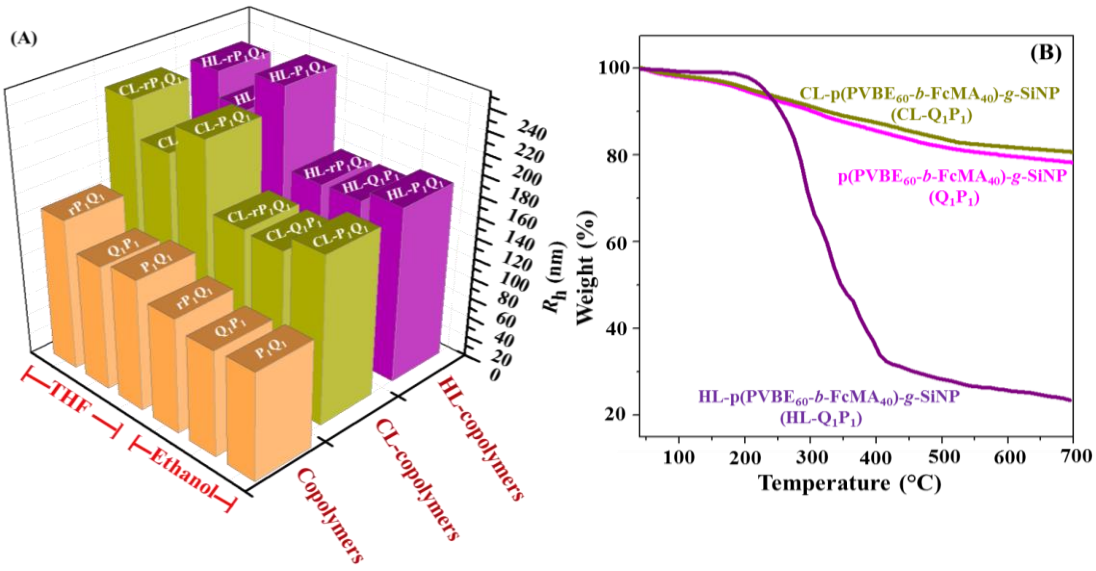

Figure 6.5: *Comparison of (A) the hydrodynamic radius (R_h) in two solvents of different polarity and (B) TGA thermograms of copolymer grafted SiNP before and after cross-linking, and the hollow particles after silica core removal.*

6.3.4. Converting cross-linked polymer grafted particles into hollow polymer nanocapsules (HPN)

The silica core of the cross-linked copolymer grafted SiNP was digested with 48% HF in order to make hollow cavity within the polymeric framework. The removal of silica core is

verified by the disappearance of the characteristic silica stretch peak (1071 cm^{-1}) in the FT-IR spectrum (*Appendix III-Figure 6.17*). A significant weight loss at around 250 °C in case of hollow particles as seen in the TGA plots [*Figure 6.5(B)*] clearly indicates the removal of silica core. Other samples, copolymer grafted SiNP and the cross-linked samples, did not display such a huge weight loss because of the presence of the silica particles which provides the thermal stability to the samples so definitely the degradation observed in case of hollow samples is due to the degradation copolymers chains.

The R_h values [*Figure 6.5(A)*] for the hollow nanocapsules determined from DLS study (*Appendix III-Figure 6.19*) show further increment in l_b compared to the cross-linked (where core is intact) particle suggesting that the release of surface constraints helps in swelling of the particles. HL-P_1Q_1 shows the maximum change (19 nm) in l_b with respect to CL-P_1Q_1 followed by HL- Q_1P_1 (11 nm) and HL-rP_1Q_1 (2 nm) in the good solvent THF. The presence of particles in the size range of 200 nm in THF solution also indirectly attributes the formation of hollow polymer nanocapsules (HPN) which is possible because of the cross-linking of the chains. If the polymer network would not have been cross-linked then after the removal of silica core, the polymer chain would have completely dissolved in the THF solution as both the polymers (pPVBE and pFcMA) like the THF solvent. When the HPN samples are dispersed in ethanol, the change in R_h from the cross-linked samples is much less compared to THF [*Figure 6.5(A)*] and the calculated change in l_b values in comparison to the cross-linked particles for all the samples are almost similar (HL-P_1Q_1, HL-Q_1P_1 and HL-rP_1Q_1 are 7, 11 and 8 nm, respectively) indicating that the ethanol is not good solvent for both the polymer chains. DVS study (*Appendix III-Figure 6.23*) shows that HPN samples adsorbed 0.48, 0.41 and 1.99 wt% for HL-P_1Q_1, HL-Q_1P_1 and HL-rP_1Q_1, respectively more water with respect to cross-linked particles though it was not expected. This indirectly confirms the formation of successful hollow cavity after core removal process where water molecule sit inside the hollow cavity. The highest increment in water sorption in case HL-rP_1Q_1 also indicates the possibility of maximum porous nature of this sample among the three types of HPN developed in this study.

Further the morphology of the HPN samples reveals a well-defined core-shell type

structure obtained from TEM study as indicated in *Figure 6.6(A)*. The thickness of the shell and the size of core depend on the type of the copolymer chains. In case of HL-rP_1Q_1 (the sample with random copolymer structure), a 12 nm thick shell and with 30 nm size hollow cavity core is obtained whereas HL- P_1Q_1 (sample with block copolymer chain) displays highest core size of 36 nm among all three without having any well-defined shell. However, the other block copolymer chain grafted sample i.e. HL-Q_1P_1 has core size of 24 nm with shell thickness of 7 nm. All these observation clearly indicate the effect of chain structure on the morphology. The smaller core diameter than the corresponding precursor particle is attributed for the shrinkage of polymer chains after solid template removal. The presence of particles without shell in case of HL-P_1Q_1 may be owing to the intra/ inter particle chemical crosslinking happening *via* pPVBE chains which are nearer to the particle surface while the pFcMA chains that are away from the surface also involve in agglomeration *via* strong non-covalent-intra/ inter-particle-interactions of Cp unit. And hence after template (silica core) removal we could not see a shell thickness like other cases. On the other contrary, in Q_1P_1, pPVBE block which is away from the surface mainly involvs in intra/ inter particle chemical crosslinking which indirectly decreases the possibility of strong non-covalent-inter-particle-interactions happening *via* pFcMA block (nearer to the surface) between Cp units due to steric crowding and results a very few of agglomerated hollow nanocapsules with well-defined shell. This hollow cavity formation of the nanocapsules is also supported by the agglomerated nano particles with uneven spherical shape observed in FESEM (*Appendix III-Figure 6.24*). Hollow rP_1Q_1 shows most translucent electron micrographs among all while clumsy images appear for P_1Q_1 and Q_1P_1 made us to conclude that the *grafted* random copolymer over a particle surface allows the hollow polymeric nanocapsule formation in much better way with a rigid cross-linker distributed randomly all over the polymer network compared to block copolymer chains. Also randomly distributed pFcMA block indirectly helps to have a best optimized hollow structure in case of rP_1Q_1 *via* non-covalent-intra/ inter-particle-interactions in case of among all three.

The confirmation of the formation of hollow cavity in HPN is further examined by treating the samples with dye and the imaged in Confocal Laser Scanning Microscopy (CLSM).

A comparison of the morphology [*Figure 6.6(B)*] between cross-linked and hollow particles shows the discrete differences in the appearance of dye in the images. The dye is distributed evenly except core in case of cross-linked sample whereas presence of dye is visible in some pockets in case of hollow particles. This indicates the formation of the spherical nanocapsule with dye sited inside the hollow cavity. Similarly, further analysis and imaging of dye treated the particles using fluorescence lifetime imaging microscopic measurements [*Figure 6.6(C)*] also confirm the presence of hollow cavity in HPN and in agreement with other morphological studies as discussed above.

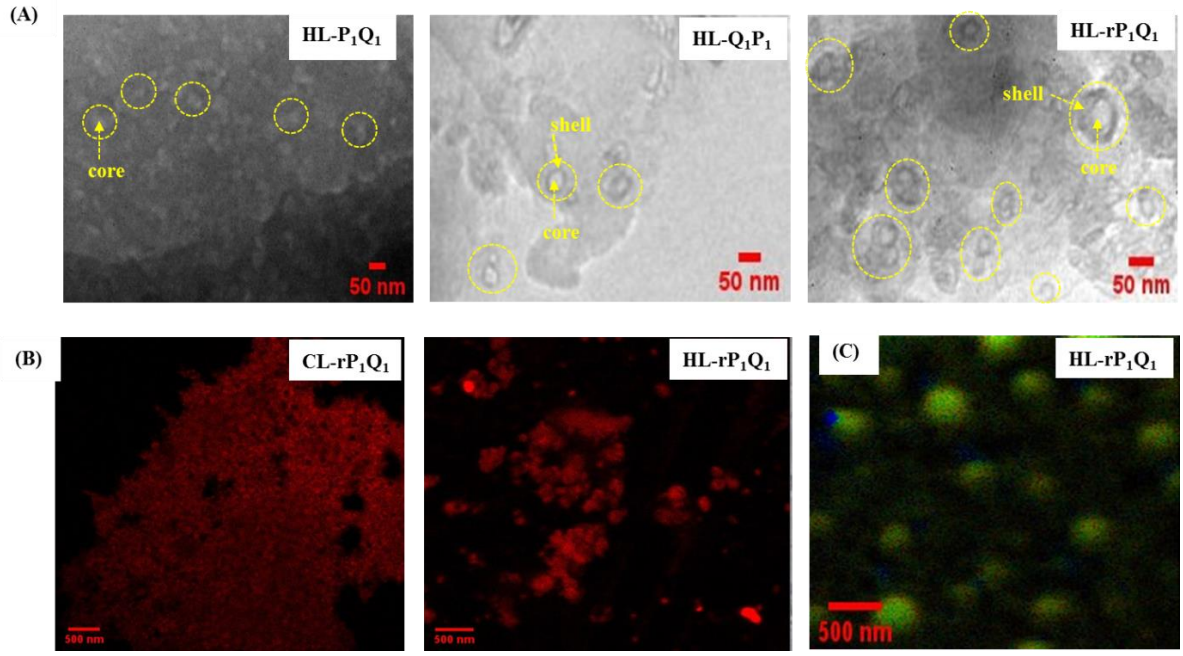

Figure 6.6: *(A) TEM images of hollow polymer nanocapsules. Few HPN particles in each case are identified by dotted circles in the figure. Representative shell and core of the HPN are also shown in the image with arrow marks. (B) CLSM images of dye (Rhodamine B) treated cross-linked and hollow samples and (C) Images obtained from fluorescence lifetime imaging microscopic measurements of Coumarin treated samples.*

Copolymer grafted SiNP, cross-linked and hollow copolymer particles were further

characterized by BET (Brunaer-Emmett-Teller) analysis by using nitrogen adsorption isotherm in order to get a quantitative comparison of porosity parameter of the particles. As shown in *Figure 6.7*, the isotherm of both cross-linked and hollow rP_1Q_1 exhibit hysteresis loop of nitrogen uptake as a function of relative pressure, an indication that is consistent with porous structure.[30]

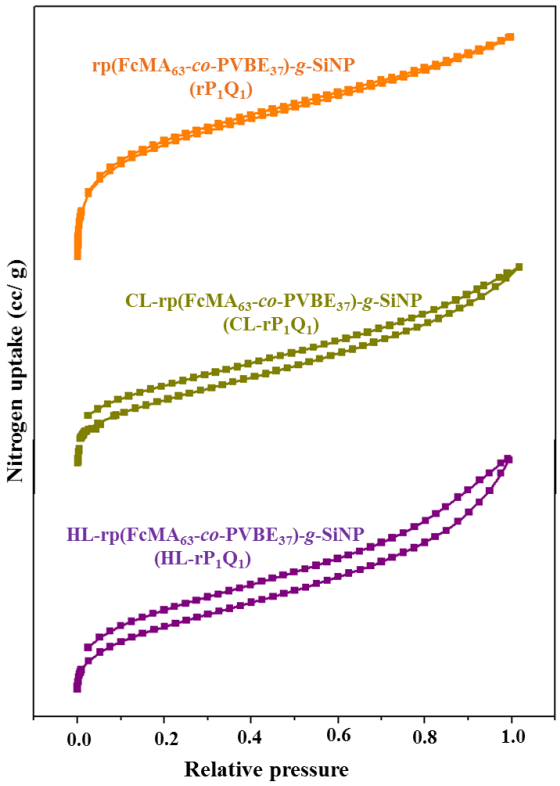

Figure 6.7: *BET isotherms of rp(FcMA$_{63}$-co-PVBE$_{37}$)-g-SiNP (rP_1Q_1), CL-rP_1Q_1, HL-rP_1Q_1.*

The isotherm of rP_1Q_1 (sample before cross-linking) shows no hysteresis loop indicating the absence (or very minimum presence) of porosity in this sample which in turn proves that porosity appears in the sample only after cross-linking the copolymer chain and formation of hollow structure, and it is not due to grafted polymer. The huge increase in surface area, pore volume and pore size (*Table 6.2*) in case of hollow particles in comparison to grafted and cross-

linked particles is the proof of formation of hollow cavity after removal of silica core. The increased values of surface area, pore volume and pore size (*Table 6.2*) of cross-linked particles than uncross-linked particles attributes that some porosity have been also introduced in the particle just because of cross-linking. The better porosity data profile of the hollow rP_1Q_1 (random copolymer sample) compared to hollow P_1Q_1 (block copolymer) confirms again about the better HPN formation in former. As expected, the other kinds of copolymer (Q_1P_1) where PVBE chains are away from the SiNP surface did not give good isotherm and shows very less porous nature.

Table 6.2: *Various porosity related parameters obtained from BET analysis.*

Sample Identity	BET surface area (m^2/g)	Total pore volume (cc/g)	Average pore size (nm)
rP_1Q_1	27.9	0.03	0.38
CL- rP_1Q_1	45.4	0.07	0.61
HL- rP_1Q_1	160.9	0.21	5.2
HL-P_1Q_1	102.9	0.13	5

6.3.5. Hollow polymer nanocapsules embedded aluminum nanoparticles

Numerous efforts have been made to develop aluminum nanoparticles (Al-NP) in recent times owing to its enormous potential as fuel in CSP. These reports found that polymeric matrix can provide a suitable protective layer in stabilizing Al-NP for any further oxidation.[33,35,36] In order to demonstrate the use of HPN developed in this work and also to develop a catalytic material consists of both Al and Fe, herein, we have synthesized Al-NP inside the hollow cavity of ferrocenyl polymer containing HPN by following a simple, user-friendly sono-chemical synthetic procedure reported earlier.[37] In this process in presence of HPN, $LiAlH_4$ reduces $SiCl_4$ to silanes along with LiCl and AlH_3 which further decomposes to yield Al and H_2 at the temperature range of ~60°C under sonication. This is an *in-situ* synthesized Al-NP

which gets stabilized by HPN and grown inside the HPN hollow nano-cavity . In addition, as the shell of the HPN is the ferrocenyl polymer hence the resulting Al-NP is embedded with Fe containing polymers resulting nanostructured materials consists of both Fe and Al which can be used as fuel cum burn rate catalyst in CSP.

The formation of Al-NP/HPN composite is structurally verified by noting the peak shifting of the characteristic IR frequency for C=O functionality, owing to the presence of pFcMA chains, of hollow sample from 1715 to 1698 cm^{-1} [*Figure 6.8(A)*] after encapsulated with Al-NP. This observation suggests the presence of interaction between C=O bond and the formed Al-NP which occurred through the partial donation of the oxygen lone pair to form a coordination interaction at the interface of Al-NP and the polymer.[37] Coordination of Al-NP is also possible *via* nitrogen lone pair at the cross-linked region, but no significant peak shifting is observed in FTIR spectra. The PXRD pattern of Al-NP/HPN [*Figure 6.8(B)*] also confirms the formation of Al-NP nanoparticle as the diffraction peaks are matching well with JCPDS No. 89-4037 of crystalline Al.[37] The PXRD pattern [*Figure 6.8(B)*] of Al-NP/HL-p($FcMA_{57}$-*b*- $PVBE_{43}$) (HL-P_1Q_1) Hollow) nanocomposite displays the diffraction peaks of both Al-NP (marked using squares) and polymer (indicated using # and $). The crystalline peak at 16.34º corresponds to ferrocenyl polymeric block and the broad peak at 2θ 19.8º –27.5º are observed because of the amorphous nature of PVBE matrix. On the other hand, a number of crystalline peaks in addition to crystalline Al peaks appeared in case of Al-NP/rp($FcMA_{63}$-*co*- $PVBE_{37}$) (HL-rP_1Q_1) nanocomposite. These peaks are may be due to the random distribution of ferrocenyl functionality all over the polymer matrices. A very little shift of the Al crystalline peaks in case of nanocomposite samples is observed which may be because of the coordination interaction with the polymer chain. The higher intensity of the diffraction peaks for the crystalline Al-NP in case of random polymer coated HPN compared to block HPN suggests the higher amount of Al-NP encapsulation in the former. This once again reconfirms the fact that random copolymer is better when chosen as a shell than block copolymer for synthesizing HPN. It is to be noted that the encapsulation of Al-NP is successful only when the *in-situ* synthesis process (as described above) was carried out with the hollow sample. An attempt to

make Al-NP in the cross-linked sample did not result the formation Al-NP as evident from the absence of any crystalline peak in PXRD pattern of Al/CL-rP$_1$Q$_1$ sample (*Appendix III-Figure S25*). This clearly demonstrates that significant amount of *in-situ* formed Al-NP is encapsulated after hollow cavity formation only. As per BET data, crosslinked particle could have interacted with Al-NP *via* the interaction with C=O functionality and nitrogen lone pair, most possibly the nanocomposite formation is too poor to be detected as a diffraction peaks in PXRD.

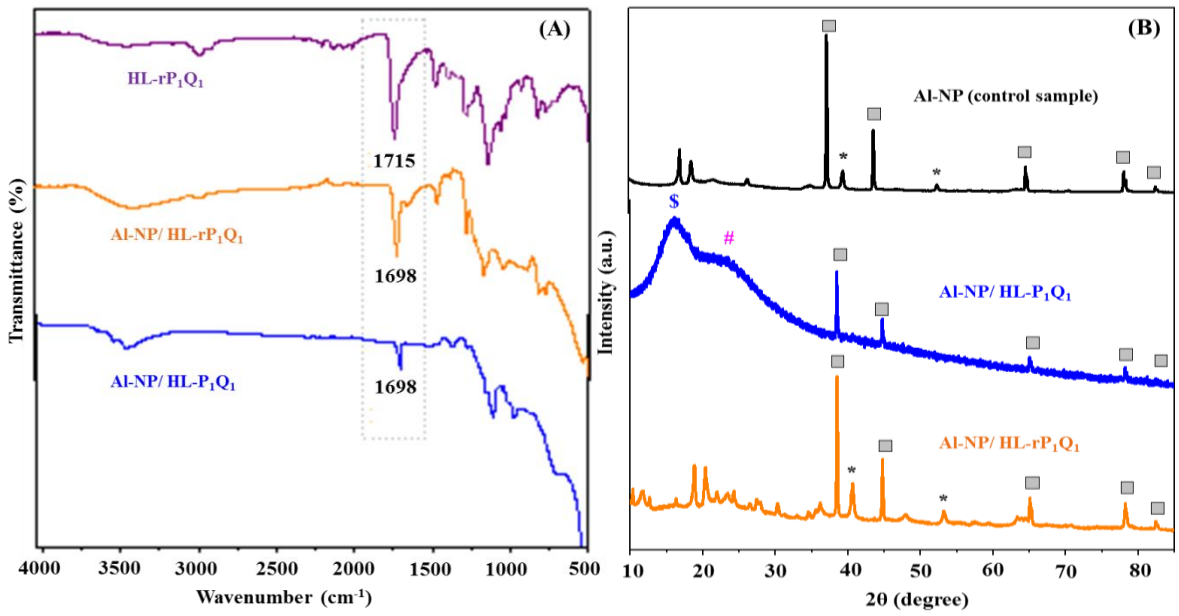

Figure 6.8: *(A) Comparison of FTIR spectra of HPN with the Al-NP/HPN composites and (B) (B) PXRD plots of Al-NP (a control sample prepared in absence of polymer) and Al-NP/HPN nanocomposite samples. Peaks are assigned with various symbols: filled square, *, $ and # are for Al, AlH$_3$, pFcMA and pPVBE, respectively.*

Subsequently encapsulation of Al-NP in HPN further is reconfirmed by Al_2O_3 formation during thermal analysis. Al-NP/HPN nanocomposites and the control sample were subjected to TGA analysis under nitrogen environment at a heating rate of 50 ºC min^{-1} from 25 to 1100 ºC. The thermogram of Al-NP/HL-rP$_1$Q$_1$ shows almost 39% weight loss up to 580 ºC indicateing the

decomposition of HPN backbone which in turn exposes Al-NP to get oxidized and yielding ~ 4 % weight gain up to 1100ºC which is ascribed to Al oxidation (*Appendix III-Figure 6.26*). In case of Al-NP/HL-P_1Q_1 sample less than 1 wt % weight is observed, however, for control Al-NP sample (synthesized without HPN), the weight gain is about 16 % and no weight gain is detected for cross-linked case (Al-NP/CL-P_1Q_1) which again supports the fact that possibility of Al-NP formation in crosslinked region is insignificant. All these observations on weight gain clearly prove that without silica core nanocomposite formation is not feasible or other words suggests the successful encapsulation of Al-NP in HPN. In addition, higher weight gain also indicates that the encapsulation is better for random copolymer grafted HPN. The amount of active Al content is calculated from this weight gain region following the reported literature[37] and it is found to be 4.34% for rP_1Q_1, 0.9% for P_1Q_1. The presence of higher amount of active Al content when random copolymer is shell, is also in agreement with the PXRD data where the peak higher intensity is seen.

6.4. Conclusion

In this report, we presented an efficient method to synthesize hollow polymer nanocapsules (HPN) by using one pot surface initiated RAFT polymerization via *grafting from* approach based on silica as a sacrificial template. Further, the cavity of HPN has been used to make aluminum nanoparticles (Al-NP) embedded by the polymer chains. The whole process has been carried out in four stages: first copolymer chains consist of poly [2-(methacryloyloxy) ethyl ferrocenecarboxylate] (FcMA) and poly(propargyl 4-vinylbenzyl ether) (PVBE) of various chain length, composition and microstructures have been grafted on the silica nanoparticle (SiNP) surface, in the second stage the grafted chains have been chemically cross-linked via click reaction between the proapgyl functionality of the pPVBE chains and 1,4-bis(azidomethyl)benzene cross-linker in order to impart the robustness in the particle. Then, the silica core of the crosslinked copolymer grafted particles has been removed by HF etching to create the cavity in the grafted particles so that HPN is formed. Finally, Al-NP/HPN nanocomposites have been synthesised by embedding Al-NP inside the cavity of the HPN using readily doable chemical methods. All the materials prepared in various stages of the whole

process have been characterized thoroughly using various techniques to confirm the formation of desired materials. The detailed structural analysis found that the random copolymer grafted chains is better than the block copolymer grafted chains in making HPN. In a summary, we believe that the current methodology to synthesize Al/ ferrocenyl HPN nanocomposite is a very innovative way to encapsulate Al fuel with a polymeric ferrocenyl shell as burn rate catalyst and can be used as a dual functional framework in solid composite propellants (CSPs).

Appendix II

Monomer feed ratio, samples abbreviations and various parameters obtained from GPC analysis, structural, thermal and morphological characterizations of SiNP-BSPA, NMR spectra of monomers FcMA and PVBE, IR and NMR analysis of the synthesized copolymers, GPC chromatograms of copolymers (with monomer ratio of 1:3 and 3:1), DLS plots and TEM images of copolymers grafted SiNP, FT-IR and NMR spectra of cross-linker, IR spectra and TEM images of cross-linked particles, DLS plots of cross-linked and hollow particles dispersed in THF and ethanol, DVS plots of copolymers grafted particles, CL-particles and HL-particles, FESEM images of HL-particles, PXRD plot of Al-NP/ CL-rP_1Q_1 nanocomposite and TGA plot of Al (control sample), Al-NP/ HL- P_1Q_1, Al-NP/ HL- rP_1Q_1 and Al/ CL- rP_1Q_1. All these are included in Appendix II (page no. 242-261).

References

[1] X. Wang, J. Feng, Y. Bai, Q. Zhang, Y. Yin, *Chem. Rev.* **2016**, *116*, 10983–11060.

[2] J. Liu, S. Z. Qiao, S. B. Hartono, G. Q. Lu, *Angew. Chemie - Int. Ed.* **2010**, *49*, 4981–4985.

[3] P. Tanner, P. Baumann, R. Enea, O. Onaca, C. Palivan, W. Meier, *Acc. Chem. Res.* **2011**, *44*, 1039–1049.

[4] C. C. Nguyen, N. N. Vu, T. O. Do, *J. Mater. Chem. A* **2015**, *3*, 18345–18359.

[5] X. Xu, Z. Zhang, X. Wang, *Adv. Mater.* **2015**, *27*, 5365–5371.

[6] Q. Su, S. Han, X. Xie, H. Zhu, H. Chen, C. K. Chen, R. S. Liu, X. Chen, F. Wang, X. Liu, *J. Am. Chem. Soc.* **2012**, *134*, 20849–20857.

[7] J. Luo, X. Xia, Y. Luo, C. Guan, J. Liu, X. Qi, C. F. Ng, T. Yu, H. Zhang, H. J. Fan, *Adv. Energy Mater.* **2013**, *3*, 737–743.

[8] H. Wu, S. Zhang, J. Zhang, G. Liu, J. Shi, L. Zhang, X. Cui, M. Ruan, Q. He, W. Bu, *Adv. Funct. Mater.* **2011**, *21*, 1850–1862.

[9] Y. Zhao, L. N. Lin, Y. Lu, S. F. Chen, L. Dong, S. H. Yu, *Adv. Mater.* **2010**, *22*, 5255–5259.

[10] L. Wang, Z. Lou, T. Fei, T. Zhang, *J. Mater. Chem.* **2011**, *21*, 19331–19336.

[11] W. Yang, K. R. Ratinac, S. R. Ringer, P. Thordarson, J. J. Gooding, F. Braet, *Angew. Chemie - Int. Ed.* **2010**, *49*, 2114–2138.

[12] Y. Wang, G. Wang, H. Wang, C. Liang, W. Cai, L. Zhang, *Chem. - A Eur. J.* **2010**, *16*, 3497–3503.

[13] J. H. Pan, X. Zhang, A. J. Du, D. D. Sun, J. O. Leckie, *J. Am. Chem. Soc.* **2008**, *130*, 11256–11257.

[14] J. Hu, M. Chen, X. Fang, L. Wu, *Chem. Soc. Rev.* **2011**, *40*, 5472–5491.

[15] X. Liu, A. Basu, *J. Am. Chem. Soc.* **2009**, *131*, 5718–5719.

[16] K. Kondo, T. Kida, Y. Ogawa, Y. Arikawa, M. Akashi, *J. Am. Chem. Soc.* **2010**, *132*, 8236–8237.

[17] T. Chen, B. Du, Z. Fan, *Langmuir* **2012**, *28*, 11225–11231.

[18] H. Hou, D. Yu, Q. Tian, G. Hu, *Langmuir* **2014**, *30*, 1741–1747.

[19] Z. Dong, J. Mao, D. Wang, M. Yang, X. Ji, *Langmuir* **2015**, *31*, 8930–8939.

[20] K. C. Bentz, M. Ejaz, S. Arencibia, N. Sultan, S. M. Grayson, D. A. Savin, *Polym. Chem.* **2017**, *8*, 5129–5138.

[21] K. C. Bentz, D. A. Savin, *Polym. Chem.* **2018**, *9*, 2059–2081.

[22] S. Blomberg, S. Ostberg, E. Harth, A. W. Bosman, B. Van Horn, C. J. Hawker, *J. Polym. Sci. Part A Polym. Chem.* **2002**, *40*, 1309–1320.

[23] G. D. Fu, Z. Shang, L. Hong, E. T. Kang, K. G. Neoh, *Macromolecules* **2005**, *38*, 7867–7871.

[24] T. Morinaga, M. Ohkura, K. Ohno, Y. Tsujii, T. Fukuda, *Macromolecules* **2007**, *40*, 1159–1164.

[25] X. Huang, D. Appelhans, P. Formanek, F. Simon, B. Voit, *Macromolecules* **2011**, *44*, 8351–8360.

[26] X. Huang, D. Appelhans, P. Formanek, F. Simon, B. Voit, *ACS Nano* **2012**, *6*, 9718–9726.

[27] L. Chen, Z. Peng, Z. Zeng, Y. She, J. Wei, Y. Chen, *J. Polym. Sci. Part A Polym. Chem.* **2014**, *52*, 2202–2216.

[28] S. A. Dergunov, M. D. Kim, S. N. Shmakov, E. Pinkhassik, *Acc. Chem. Res.* **2019**, *52*, 189–198.

[29] W. Wichaita, D. Polpanich, P. Tangboriboonrat, *Ind. Eng. Chem. Res.* **2019**, *58*, 20880–20901.

[30] Y. Xu, Y. Yao, H. Yu, B. Shi, S. Gao, L. Zhang, A. L. Miller, J. C. Fang, X. Wang, K. Huang, *ACS Macro Lett.* **2019**, *8*, 1263–1267.

[31] Y. Liang, W. Mai, J. Huang, Z. Huang, R. Fu, M. Zhang, D. Wu, K. Matyjaszewski, *Chem. Commun.* **2016**, *52*, 2489–2492.

[32] S. Liu, Z. Huang, F. Li, T. Yan, S. Fu, R. Tian, C. Hou, Q. Luo, J. Xu, J. Liu, *Polym. Chem.* **2019**, *10*, 3566–3570.

[33] Y. Hu, D. Hao, B. Tao, F. Wang, D. Wang, R. Fan, D. Xia, P. Wang, Y. Yang, A. Pang, K. Lin, *Chem. Eng. J.* **2020**, *394*, 124884.

[34] Q. L. Yan, F. Q. Zhao, K. K. Kuo, X. H. Zhang, S. Zeman, L. T. DeLuca, *Prog. Energy Combust. Sci.* **2016**, *57*, 75–136.

[35] W. Zeng, S. W. Buckner, P. A. Jelliss, *ACS Omega* **2017**, *2*, 2034–2040.

[36] C. O. Nyapete, A. H. H. Benziger, S. W. Buckner, P. A. Jelliss, *Nano-Structures and Nano-Objects* **2018**, *16*, 282–287.

[37] S. Gottapu, S. K. Padhi, M. G. Krishna, K. Muralidharan, *New J. Chem.* **2015**, *39*, 5203–5207.

[38] S. R. Ghanta, K. Muralidharan, *Nanoscale* **2010**, *2*, 976–980.

[39] M. Usman, L. Wang, H. Yu, F. Haq, M. Haroon, R. Summe Ullah, A. Khan, S. Fahad, A. Nazir, T. Elshaarani, *J. Organomet. Chem.* **2018**, *872*, 40–53.

[40] B. U. Amin, H. Yu, L. Wang, A. Nazir, S. Fahad, F. Haq, S. Mahmood, R. Liang, M. A. Uddin, T. Lin, *J. Organomet. Chem.* **2020**, 121368.

[41] S. N. R. Kutcherlapati, R. Koyilapu, U. M. R. Boddu, D. Datta, R. S. Perali, M. J. Swamy, T. Jana, *Macromolecules* **2017**, *50*, 7309–7320.

[42] S. R. Kutcherlapati, R. Koyilapu, T. Jana, *J. Polym. Sci. Part A Polym. Chem.* **2018**, *56*, 365–375.

[43] R. Koyilapu, S. Singha, S. N. R. Kutcherlapati, T. Jana, *Polymer* **2020**, *195*, 122458.

[44] Y. Liu, W. Hou, H. Zhao, *Macromolecules* **2020**, *53*, 5001–5014.

[45] C. Koh, G. S. Grest, S. K. Kumar, *ACS Nano* **2020**, *14*, 13491–13499.

[46] Z. M. Abbas, M. M. Khani, M. Tawfilas, Z. M. Marsh, M. Stefik, B. C. Benicewicz, *J. Polym. Sci.* **2020**, *58*, 417–427.

[47] N. Yeole, S. N. R. Kutcherlapati, T. Jana, *J. Colloid Interface Sci.* **2015**, *443*, 137–142.

[48] L. Tripathi, L. P. Wu, D. Meng, J. Chen, G. Q. Chen, *Biomacromolecules* **2013**, *14*, 862–870.

[49] X. Yang, D. Chen, H. Zhao, *Acta Biomater.* **2016**, *29*, 446–454.

[50] M. Dhara, N. Giri, B. Narasimha Rao, A. K. Patra, P. U. Sastry, M. S. Ingole, T. Jana, *Eur. Polym. J.* **2020**, *122*, 109380.

[51] M. Dhara, N. Giri, A. Dutta, A. K. Patra, P. U. Sastry, M. S. Ingole, T. Jana, *Polymer* **2020**, *204*, 122807.

[52] N. Elgrishi, K. J. Rountree, B. D. McCarthy, E. S. Rountree, T. T. Eisenhart, J. L. Dempsey, *J. Chem. Educ.* **2018**, *95*, 197–206.

[53] T. Steentjes, P. Jonkheijm, J. Huskens, *Langmuir* **2017**, *33*, 11878–11883.

[54] Z. Wang, J. Lee, Z. Wang, Y. Zhao, J. Yan, Y. Lin, S. Li, T. Liu, M. Olszewski, J. Pietrasik, M. R. Bockstaller, K. Matyjaszewski, M. R. Bockstaller, K. Matyjaszewski, *ACS Macro Lett.* **2020**, 806–812.

[55] A. S. Altorbaq, A. M. Jimenez, J. Pribyl, B. Benicewicz, A. J. Mu, S. K. Kumar, *Macromolecules* **2021,** *54*, 1063–1072.

[56] K. Suresh, U. B. R. Khandavilli, A. Gunnam, A. Nangia, *CrystEngComm* **2017**, *19*, 918–929.

CHAPTER 7

Porous multi compartment morphologies of ferrocene containing diblock copolymer

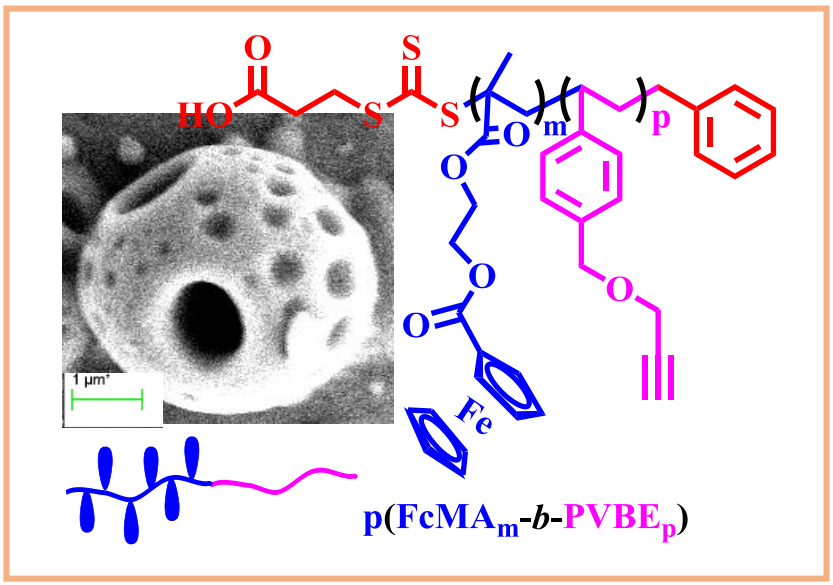

This chapter deals with the construction of multicompartment morphologies like vesicles and fibres with several nanopores from ferrocenyl diblock copolymers after employing heat-cool process in a similar line as associated with crystallization-driven self-assembly.

7.1. Introduction

Multi compartment block copolymer nanoparticles (MCBNs) consist of very intricate inner structure of several phase-segregated micro domains[1], these are esteemed to have wide range of applications in drug delivery, nanotechnology, catalysis and so on. The perception of multi compartment micelles is outlined from naturally occurring blood proteins like serum albumin which is responsible for the circulatory transport to the sparingly soluble compounds including vitamins, lipids, hormones and metals.[2] Helmut Ringsdorf envisioned that multi compartment micelles can mimic various biological structures and feature and act as a bridge between material sciences to life sciences.[3] The evolution of multi compartment micelles definitely an intriguing effort for mimicking biological systems in a most trivial and tailorable fashion, at the same time setting up a lots of scope within nanotechnology applications to carry on several hierarchical self-assembly with myriad functions and architectures on various length scale.[4]

Generally, modulating copolymer parameters like monomer structure, block molecular weights, copolymer architectures can yield to several micellar structures more like worm, spherical, vesicles, cylindrical, or bilayers.[5–8] Whereas, MCBNs is constructed by employing linear ABC triblock terpolymers[9,10] for example, fluorinated triblock terpolymers[11,12], miktoarm star polymers[13,14] in which A is assigned to solvophilic block and B and C stand for two incompatible solvophobic block, respectively. MCBNs having particle size in nanoscale have been achieved either *via* micellization strategy, blending strategy or *via* two macro RAFT agents mediated dispersion polymerization pathway.[15–17] Fluorinated block copolymers or miktoarm star polymers mediated MCBNs are very limited since preparation of these complex structures requires laborious synthesis; so convenient synthetic methodology of MCBN assemblies with more advanced morphology is always challenging task. Zhang *et al* introduced the redox-responsive multi compartment vesicles of the poly[2-(dimethylamino) ethyl methacrylate]-*block*-poly(benzylmethacrylate)-*block*-poly(4-vinylbenzylferoenecarboxylate) (PDMAEMA-*b*-PBzMA-bPVFC) triblock terpolymer prepared by seeded RAFT polymerization through PISA.[18]

In a conventional solution self-assembly, generally, a specific solvent is chosen selectively for one of the blocks in which the self-assembly process is governed *via* balancing of energy allied with the solvation of corona and chain packing of the core block[19] and thus very often distinct micellar morphological transition can be tuned by changing their block ratio or solvent characteristics.[20–23] While it has been stated that, crystallization-driven self-assembly (CDSA) employs block copolymers (BCPs) with semi-crystalline core-forming block to form anisotropic 1D, 2D and 3D morphology with high precision where the crystallization of the BCP core is the commanding force of self-assembly.[24–31] In CDSA, normally the polymer is dissolved in a specific solvent to allow the insoluble block to crystalize slowly[29,32] and often it is followed the heat-cool cycle to control the crystallization process.[25,32,33] In 2000, Manners and Winnik et al. studied the solution self-assembly of ferrocene containing BCP with a core forming polyferrocenyldimethylsilane (PFS) metalloblock[34], later they concluded that the core crystallization helps to form either cylindrical micelles or platelet nanostructures depending upon the ratio of crystallizable core to amorphous corona-forming block.[35,36] Though, extensive CDSA studies have been well scrutinized, the crystalline cores mentioned to date are limited to main chain polymers only, among them polyferrocenylsilanes are most well-documented. In this Chapter we are employing CDSA techniques for a polyferrocenyl BCP where the ferrocenyl block remains as a side chain. It has been found out that, main chain polymer architectures construct themselves in such a manner that provide opportunities to form nice semi crystalline ferrocene-containing polymers[37–40] which are not easily feasible with side-chain ferrocene-containing topologies.[41] May be this is the reason why CDSA not yet explored enough for pendant ferrocene containing block copolymers (FcBCPs). In this report, we have exploited crystallization driven self-assembly (CDSA) technique to achieve multi compartment vesicles from pendant ferrocenyl diblock copolymers.

FcBCP is very well known and widely used to fabricate variety of functional nanomaterials owing to their redox and electro-chemical properties to serve the needs of plentiful applications.[42,43] However, main chain ferrocene based polymers like

polyferrocenylsilanes were mainly synthesized *via* anionic, cationic, and photolytic anionic ring-opening polymerization methodologies[44], which inflicted hurdles in their applications in consequence of the harsh preparation condition required. On the contrary, well-defined side-chain FcBCP can be synthesized in a much simpler pathway named as reversible addition fragmentation chain transfer (RAFT) polymerization.[41,45] It's been a decade, our group has reported a novel approach to synthesis core-shell nanoparticles *via* surfactant free emulsion polymerization using macro-chain transfer agent (CTA)[46] and over the time, we have established a very simple and robust one-pot methodology for the synthesis of colloidal particles with tunable core-shell morphology using RAFT polymerization techniques where initially generated hydrophilic macro-CTA were chain-extended *in situ* with a hydrophobic monomer.[47–49] Since past few years, we mainly focused on surface modification *via* surface-initiated RAFT (SI-RAFT) polymerization and very recently we have developed to engineer block/ random copolymer on the particle surface *via* one pot SI-RAFT polymerization technique.[50–53]

Because of the possibilities of strong non-covalent interactions between ferrocene moieties[54,55], it is expected to have some crystalline region within a pendant ferrocenyl polymer matrix even though it is not behaving like a typical crystalline or even semicrystalline polymer. So, pendant ferrocenyl polymers how rearrange themselves in a solution after employing CDSA technique, can be an interesting objective to be explored. In the present study, we have demonstrated how CDSA technique can induce the morphological transition for a pendant FcBCPs. In order to do this, two types of FcBCPs with different chain length were synthesized namely poly(2-methacryloyloxy ethylferrocenecarboxylate)-*b*-poly(propargyl 4-vinylbenzylether) (pFcMA-*b*-pPVBE) and poly(2-methacryloyloxy ethylferrocenecarboxylate)-*b*-poly(sodium styrene sulfonate) (pFcMA-*b*-pNaSS). The FcBCPs were synthesized *via* sequential RAFT polymerization technique by using BSPA and CPDB as chain transfer agent (CTA), respectively. The synthesized FcBCPs were fully characterized *via* NMR, UV, GPC, DSC, PXRD and CV analysis. At the end, the self-assembly study was carried out *via* crystallization-driven self-assembly pathway by selecting THF as a

common solvent for both block and acetone/ water as a selective solvent for pPVBE/ pNaSS unit. FESEM analysis revealed hollow patchy nanocapsules to multi compartment vesicle morphology having several nanopores in the micellar membrane wall. The variation in morphology has been evaluated based on the degree of polymerization (DP) of pFcMA block. The switchability of nanopores has been explored based on redox responsiveness of pFcMA block. Definitely, our current investigation is expected to explore a new pathway to fashion multi compartment structures in even more proficiently for ferrocene containing block copolymers with ferrocene as a side chain.

7.2. Experimental section

Various chain length of ferrocene containing block copolymers (FcBCP) were synthesized *via* RAFT polymerization. 2-(methacryloyloxy)ethyl ferrocenecarboxylate (FcMA) was selected as a ferrocene containing monomer whereas propargyl 4-vinylbenzyl ether (PVBE) and sodium 4-styrenesulfonate (NaSS) are the other two monomers which were used as a second monomer to achieve the targeted BCPs. As per the reactivity compatibility with the chosen monomers, two different chain transfer agent (CTA) 3-benzylsulfanylthiocarbonylsufanyl-propionic acid (BSPA) and 4-cyanopentanoic acid dithiobenzoate (CPDB) were used. These monomers (except NaSS) and CTAs were synthesized in our laboratory as shown in **Chapter 2**. All the materials used with in this chapter are previously mentioned in **Chapter 2** including the synthesis of monomers FcMA and PVBE, chain transfer agents BSPA and CPDB; while the another monomer NaSS was used as received from sigma Aldrich, India. All the characterization techniques like NMR, UV, GPC, CV, DSC, PXRD, DLS and FESEM are addressed in details in **Chapter 2**.

7.2.1. Synthesis of poly[2-(methacryloyloxy)ethyl ferrocenecarboxylate] (pFcMA)

In a typical experiment, 1 g of FcMA (2.92 mmol), calculated amount of BSPA (14 mg, 51.39 µmol; this particular amount was calculated for the chain length of 20K and varied as per the calculations for the other chain lengths) and calculated amount of AIBN (2.05 mg, 12.48 µmol; this is also calculated for synthesizing the chain length of 20K and varied

accordingly as per requirements) were dissolved in 1 mL of dry DMF in a small pressure tube, then degassed by three cycles of freeze–pump–thaw techniques. The whole reaction mixture was then stirred at 90 ^{o}C for 10 hours in an inert atmosphere. The reactants were added according to the ratio of [BSPA]: [AIBN] = 1:0.25. After cooling down to room temperature, the reaction mixture was precipitated in ether, the precipitated product further redissolved in least amount of DMF and reprecipitated in ether; this process was repeated twice more to get rid of impurity completely. Finally, the purified polymer was dried under vacuum for 24 hours.

7.2.2. Synthesis of poly[2-(methacryloyloxy)ethyl ferrocenecarboxylate-*b*-propargyl 4-vinylbenzyl ether] [p(FcMA-*b*-PVBE)]

30 mg of pFcMA (1.2 µmol; estimated with respect to molecular weight 24,650 KDa as obtained from GPC analysis), 60 mg of PVBE [0.35 mmol; amount of PVBE was calculated based on the macro-CTA (pFcMA-BSPA) : monomer (PVBE) ratio of 1: 2 wt% and it was varied further to achieve different chain length] and 0.6 mg of AIBN (3.6 µmol; calculated as 1 wt% of PVBE amount and this value was also changed accordingly) were placed in a schlenk tube containing 1 mL of dry DMF and subjected to three times of freeze-thaw cycles. Next, the whole reaction mixture was continued to stir for 12 hours at 85 °C in presence of nitrogen atmosphere. After the completion of the reaction, the synthesized block copolymers were collected by precipitating from large amount of ether and it further purified by redissolving in minimum amount of DMF followed by reprecipitation in ether. Finally, the polymers were dried under vacuum for 24 hours and the synthesized block copolymer is assigned as p(FcMA-*b*-PVBE).

7.2.3. Synthesis of poly[2-(methacryloyloxy)ethyl ferrocenecarboxylate-*b*-sodium 4-styrenesulfonate] [p(FcMA-*b*-NaSS)]

30 mg of pFcMA (0.79 µmol; estimated with respect to molecular weight 38,172 KDa as obtained from GPC analysis), 60 mg of NaSS [0.29 mmol; amount of PVBE was calculated based on the macro-CTA (pFcMA-CPDB) : monomer (NaSS) ratio of 1: 2 wt% and it was varied further to achieve different chain length of pNaSS] and 0.6 mg of ACP (2.1 µmol; calculated as 1 wt% of NaSS amount and this value was also changed accordingly) were placed

in a schlenk tube containing 1 mL of dry DMF and subjected to three times of freeze-thaw cycles. Next the whole reaction mixture was continued to stir for 7 hours at 75 °C in presence of nitrogen atmosphere. After the reaction completed the synthesized block copolymers were collected by precipitating from larger amount of ether and it further purified by redissolving in minimum amount of DMF followed by reprecipitation in ether. Finally, the polymers were dried under vacuum for 24 hours and the synthesized block copolymer was assigned as p(FcMA-*b*-NaSS).

7.2.4. Self-assembly of FcBCPs followed *via* CDSA technique

1 mg/ mL of p(FcMA-*b*-PVBE) solution in THF was added drop wise over the period of 5 hours into 1 mL of acetone to get final solution concentration of 0.5 mg/ mL. After completion of whole addition process, the resulting solution was heated to 54 °C for first 1 hour and then at 48 °C for another 2 hours. Finally it allowed to cool to room temperature and kept 48 hours for maturing. The solution was subjected to morphology study by drop casting it onto a glass plate. In case of p(FcMA-*b*-NaSS), exactly similar methodology was followed except the other solvent chosen was water instead of acetone in which the polymer solution in THF was added drop wise over the similar period of time and the resulting solutions are heated at 60 °C.

7.3. Results and discussion

7.3.1. Synthesis of Ferrocenyl Polymer

Ferrocenyl monomer (FcMA) was synthesized *via* DCC/DMAP coupling mediated esterification reaction by modifying the reported protocol and mentioned earlier in **Chapter 2**. Commercially available monofunctional ferrocenyl compound, i.e, ferrocenemonocarboxylic acid (FcCOOH) and methacrylate derivative, 2-hydroxyethyl methacrylate (HEMA) were used as a precursor materials to form FcMA monomer. The monomer structure was confirmed by NMR technique which mentioned in Chapter 6_Appendix III. After the synthesis of ferrocenyl monomer FcMA, RAFT polymerization, a versatile polymerization technique for the synthesis

of block-co-polymers (BCP)[56] was employed to synthesize side-chain ferrocenene containing homopolymers. The polymerization reactions were performed using AIBN as an initiator in dry DMF solvent at 90 ºC for 10 hours. The reaction scheme for this synthesis is outlined in *Scheme 7.1*. Depending on the compatibility of the counter block towards CTA, two different kind of chain transfer agent (CTA), one dithiobenzoate derivative CPDB and another trithiobenzoate derivative BSPA were used to obtain pFcMA as a macro CTA. At first the two CTA, CPDB and BSPA were synthesized and the structures were confirmed by NMR spectroscopy. Followingly, the obtained CTAs were used to synthesize pFcMA as macro CTA with constant feed ratios of CTA to AIBN as 1:0.25 and by using these two CTA five different chain length of macro CTA was prepared as presented in *Table 7.1* (P_1 to P_5).

Disappearance of vinyl proton signals of FcMA at ~5.68 and ~6.23 ppm in ^{1}H-NMR spectra (*Figure 7.1*, all the square box) clearly indicated the successful polymerization of FcMA monomer. ^{1}H-NMR spectra of P_3, P_5 are shown here as a representative of all the synthesized side-chain ferrocene-containing homopolymers (macro-CTAs), similar spectra are obtained for other polymers (P_1, P_2, P_4) as well. These spectra with peak integration are shown in *Figure 7.2*. After polymerization the Cp proton signals appeared as a broad peak with higher integration values compared to FcMA monomer at the similar position between 4.2 ppm to 4.85 ppm (*Figure 7.1, shown in the box and Figure 7.2*).

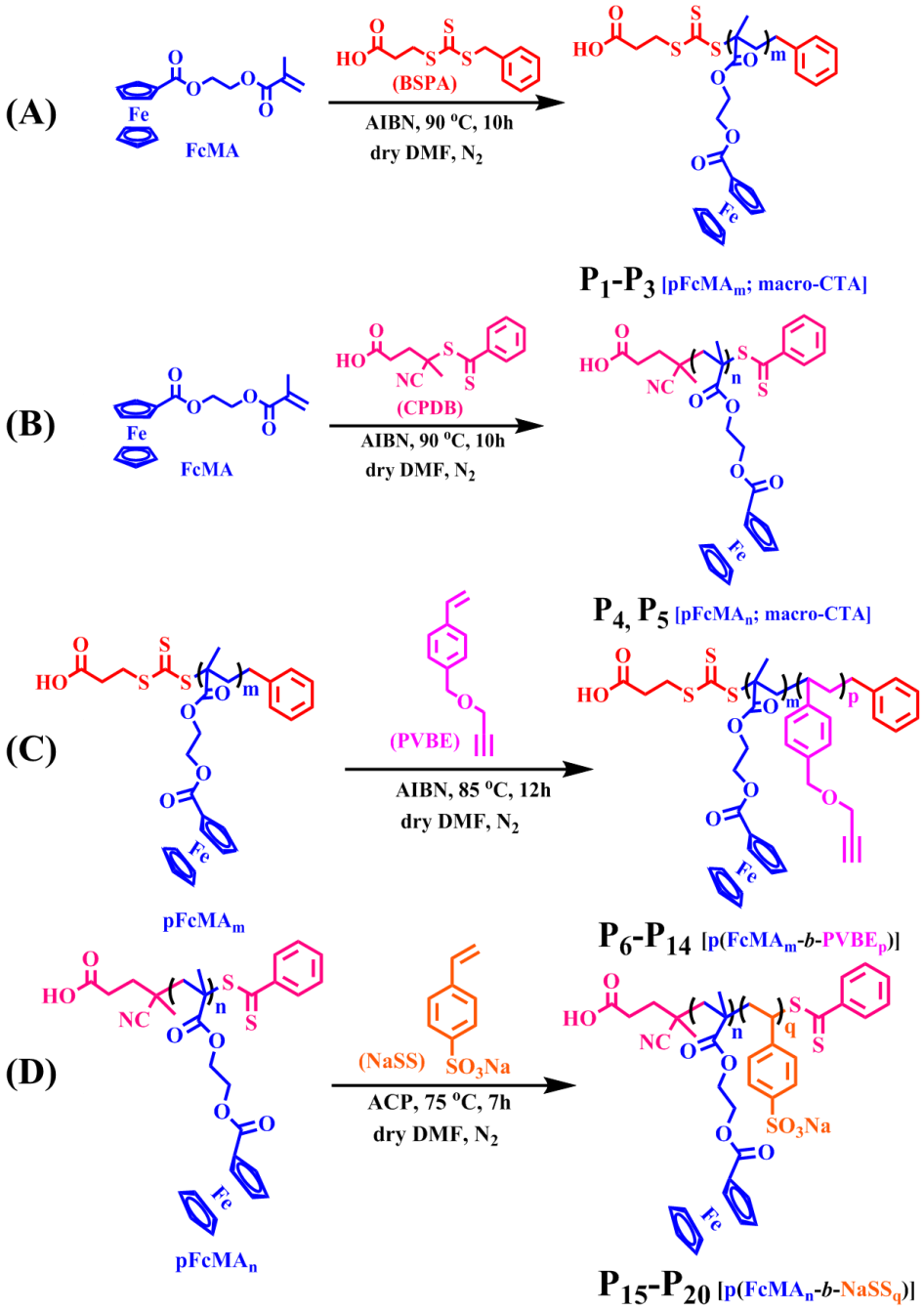

Scheme 7.1: *Synthetic routes of synthesizing ferrocene containing block copolymers. (A) macro-CTA P1-P3 prepared using BSPA as a RAFT reagent (B) P4 and P5 macro-CTA were prepared using CPDB as RAFT reagent. (C) BSPA based macro-CTA ($pFcMA_m$) was used to make BCPs with PVBE (D) CPDB based macro-CTA ($pFcMA_n$) was used to synthesis BCPs with NaSS.*

The resonance peaks at 1.6 to 2.2 ppm in the aliphatic region of spectra assigned to –CH_2 and –CH_3 protons, difficult to assign separately after polymerization. The molecular weight calculated from ^{1}H-NMR with the help of end-group analysis found to be in a well agreement with the GPC data for all the ferrocenyl homopolymers (P_1 and P_5) and mentioned in *Table 7.1*. The discussion of the spectra of block copolymers (P_{12} and P_{19}) as shown in *Figure 7.1* will be done at later section.

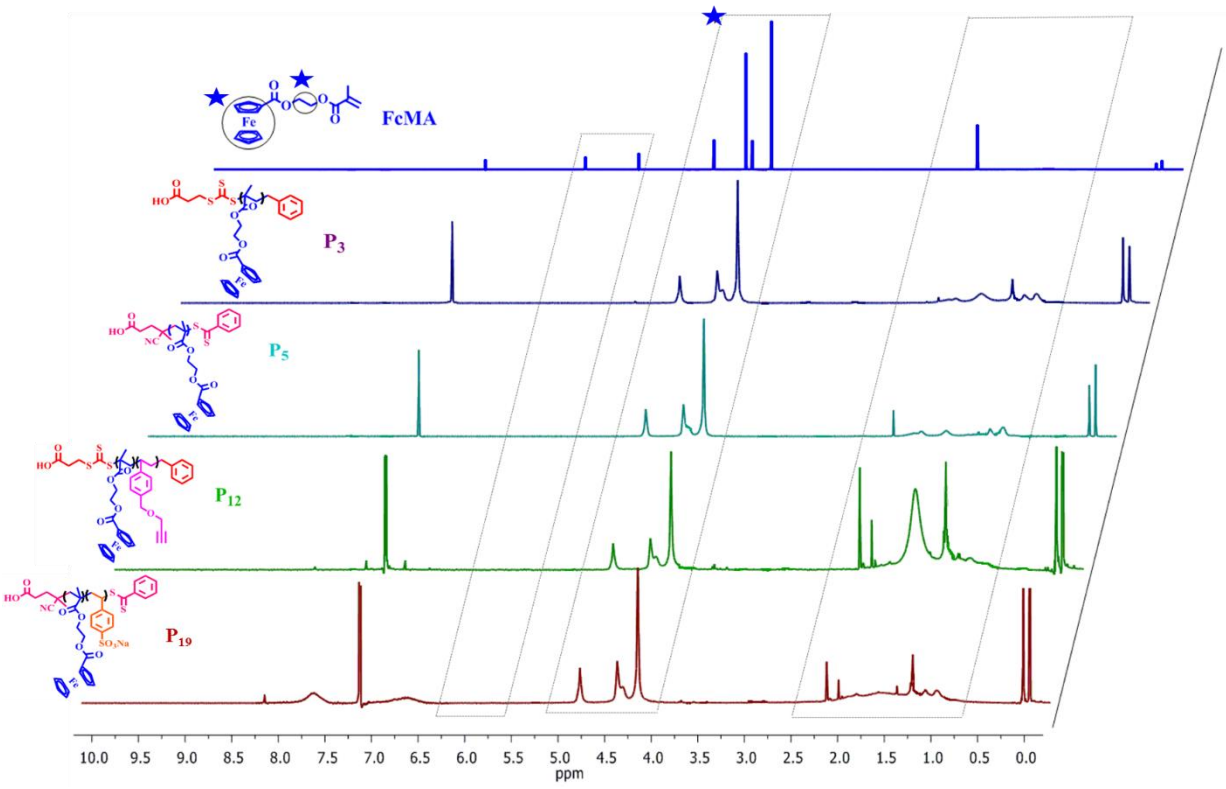

Figure 7.1: *^{1}H-NMR spectra of FcMA and ferrocene containing polymers and block copolymers.*

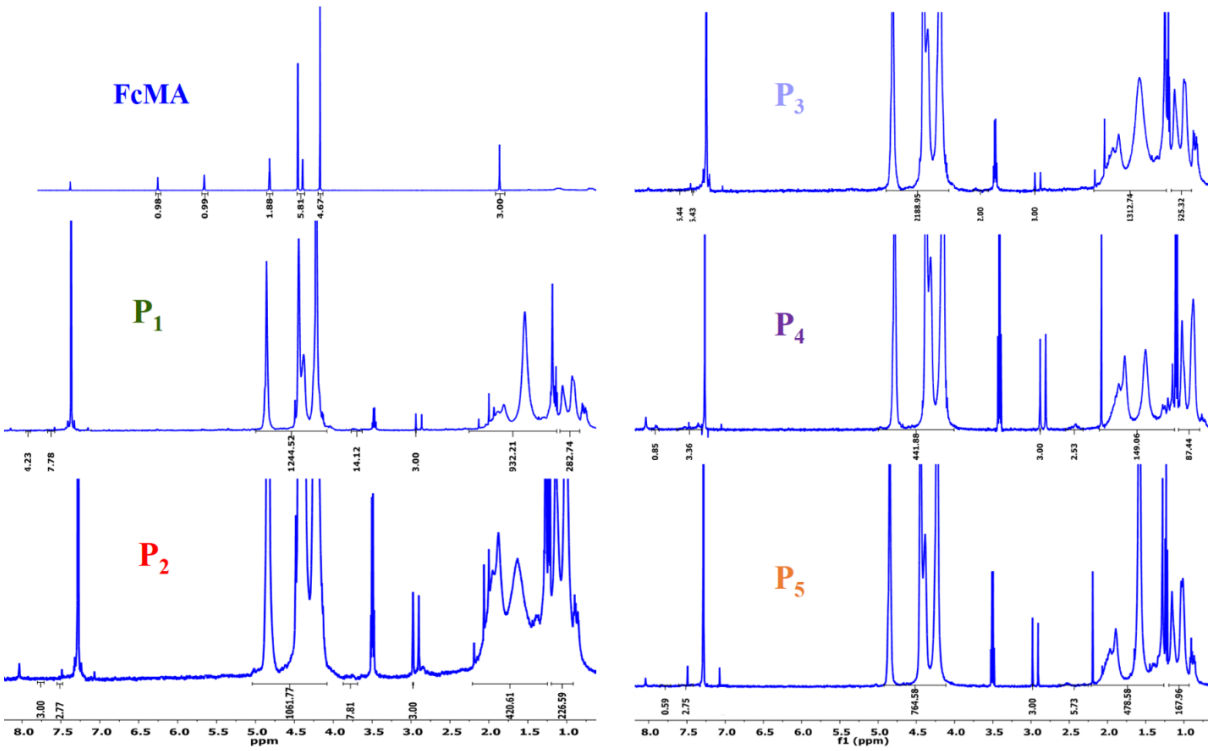

Figure 7.2: *^{1}H-NMR spectra with well-defined integral values of FcMA and all ferrocene containing polymers homo/ macro-CTAs (P_1 to P_5). The peak integration values are used to calculate $\overline{M_n}$ value of P_1-P_5 polymers (see Table 7.1).*

GPC experiment was performed to see the molecular weight distribution of all the ferrocene based homopolymers (P_1 to P_5). *Figure 7.3* shows the GPC curves and the molecular weights with dispersities obtained are summarized in *Table 7.1*. A good control in polymerization with narrow molecular weight distribution is observed which fulfils the basic criteria of RAFT technique. Dispersity (Đ) value found to be in acceptable range for all the homopolymers clarifies about the suitability of FcMA towards RAFT polymerization; though a little higher value of PDI in these cases compared to earlier work presented in Chapter 5 and 6 where polymerization was carried out in a particle surface, confirms the effectiveness of surface-initiated RAFT polymerization in comparison to solution RAFT polymerization

process. In this chapter, the presence of a shoulder in every cases refers to the dead polymer chains formed during RAFT polymerization.

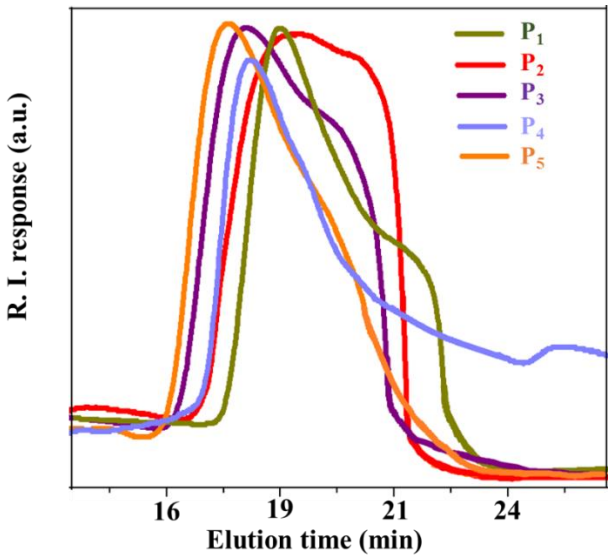

Figure 7.3: *GPC of all the pFcMA homopolymers (macro-CTA, P1-P5). GPC was carried out using LiBr-DMF as carrier solvent.*

7.3.2. Chain extension to prepare diblock copolymers

Side-chain ferrocene containing diblock copolymers were synthesized by utilizing pFcMA as a macro-CTA (*Scheme 7.1*). Two different monomers sodium 4-styrenesulfonate (NaSS) and propargyl 4-vinylbenzyl ether (PVBE) were used to prepare diblock copolymers. NaSS monomer was commercially available whereas nucleophilic aromatic substitution reaction of 4-vinylbenzylchloride with propargyl alcohol resulted an ether derivative monomer called PVBE. PVBE structure was confirmed by ^{1}H-NMR and shown in Chapter 6_Appendix III. All the polymerization reactions were performed under inert atmosphere in dry DMF with a constant wt% ratio of [monomer]:[AIBN/ACP] = 1:0.1 and to get different chain length of block copolymer further this ratio was varied accordingly. To get chain extended block copolymer the monomer addition was altered as per the wt% ratio of [pFcMA]:[PVBE/ NaSS] as [1:2], [1:1] and [1:0.5] respectively and thus total fifteen numbers of ferrocene containing block copolymers (FcBCPs) were synthesized displayed in *Table 7.1* as P_6 to P_{20}. The reaction

conditions like temperature, reaction duration, radical initiator and all other condition, all were optimized after many trials (*Scheme 7.1*) and finally block copolymers p(FcMA-*b*-PVBE) and p(FcMA-*b*-NaSS) were achieved successfully. ^{1}H-NMR spectra of P_{12} and P_{18} are shown in *Figure 7.1* as a representative of p(FcMA-*b*-PVBE) and p(FcMA-*b*-NaSS), respectively. In P_{12} the -CH_2-O-proton peaks of PVBE is merged with Cp proton signals at 4.2 and 4.45 ppm. The terminal alkyne proton signal also coalesced with aliphatic region of the spectrum at ~2.38 ppm. P_{18} clearly indicated the appearance of broad signals of Ph ring protons at 6.5 and 7.6 ppm, confirms the formation of pNaSS block. In each block, relative molar amount of FcMA and PVBE/ NaSS is estimated from well-defined integrated peaks in ^{1}H-NMR analysis (shown in *Figure 7.4).*

The formation of BCPs (P_6 to P_{20}) after chain extension from macro-CTA pFcMA is ascertained again by clear shift in GPC chromatograms towards higher molecular weight though the molecular weight distribution became more broadened than earlier (*Figure 7.5*). One interesting point can be noted that in most of the cases the dispersity is relatively low for higher molecular weight polymers indicating better control of RAFT polymerization in these cases compared to lower molecular weight polymers. The chain length variation in each series of BCPs (for example P_1 and P_6-P_8) also can be clearly visible from GPC peak separation presented in [*Figure 7.5(A, B, C, D and E)*]. In most of the cases, a small fraction of homo-polymer is retained in the final product which can be clearly visible as a little hump at the higher elution time. The all data like molecular weight, dispersities etc. obtained from GPC and NMR are tabulated in *Table 7.1*. The data clearly show that the achieved molecular weight (obtained both from NMR and GPC) are matching very well with the targeted molecular weight for all the cases. It is important to note that (from *Table 7.1*) a wide variety of BCPs are made using P_1 to P_5 macro-CTAs by altering PVBE and NaSS block chain lengths. A clearer picture of the chain length variation can be seen from the DP values as shown in the *Table 7.1*.

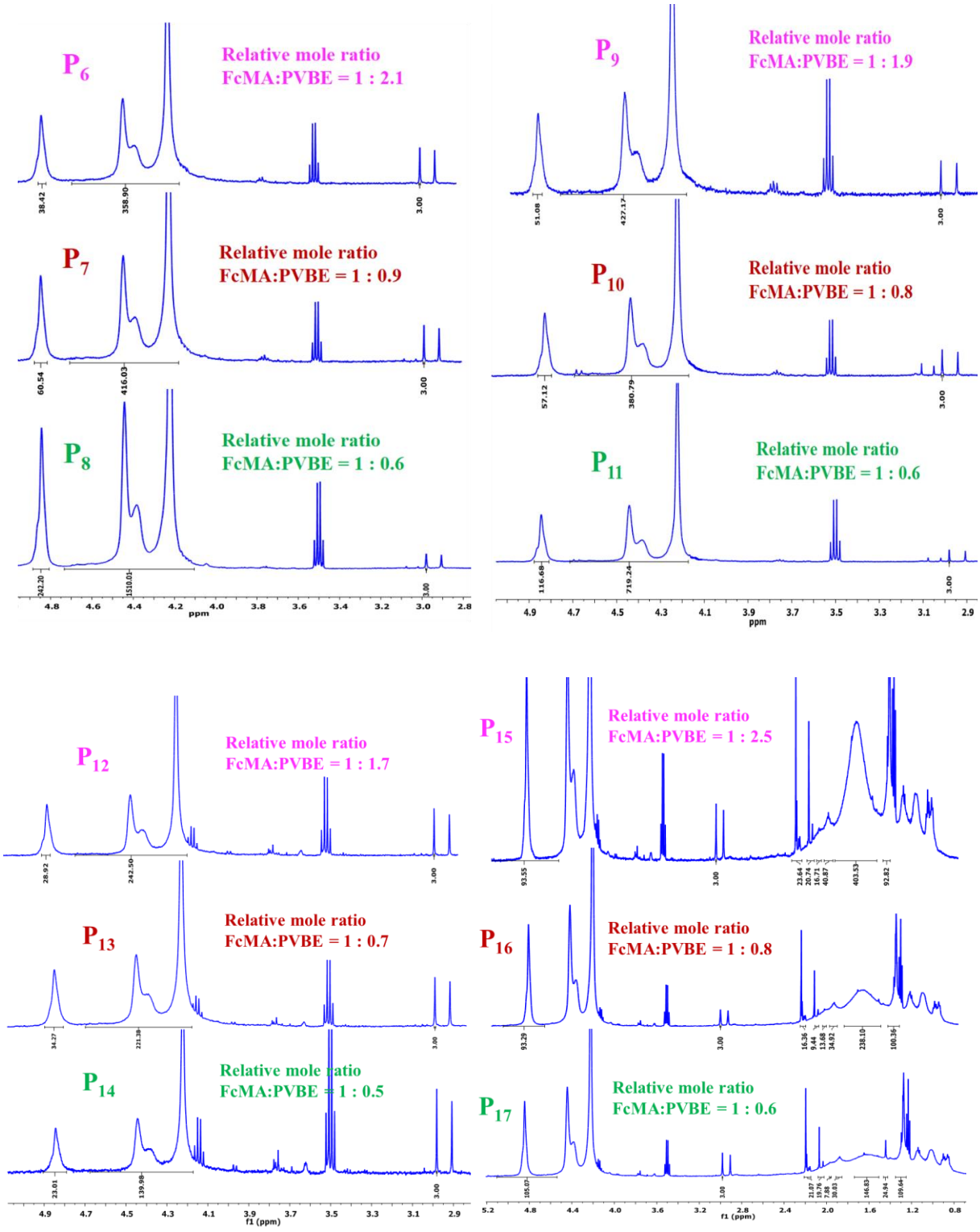
P6
Relative mole ratio
FcMA:PVBE = 1 : 2.1
P7
Relative mole ratio
FcMA:PVBE = 1 : 0.9
P8
Relative mole ratio
FcMA:PVBE = 1 : 0.6
P9
Relative mole ratio
FcMA:PVBE = 1 : 1.9
P10
Relative mole ratio
FcMA:PVBE = 1 : 0.8
P11
Relative mole ratio
FcMA:PVBE = 1 : 0.6
ppm
P12
Relative mole ratio
FcMA:PVBE = 1 : 1.7
P13
Relative mole ratio
FcMA:PVBE = 1 : 0.7
P14
Relative mole ratio
FcMA:PVBE = 1 : 0.5
P15
Relative mole ratio
FcMA:PVBE = 1 : 2.5
P16
Relative mole ratio
FcMA:PVBE = 1 : 0.8
P17
Relative mole ratio
FcMA:PVBE = 1 : 0.6
f1 (ppm)

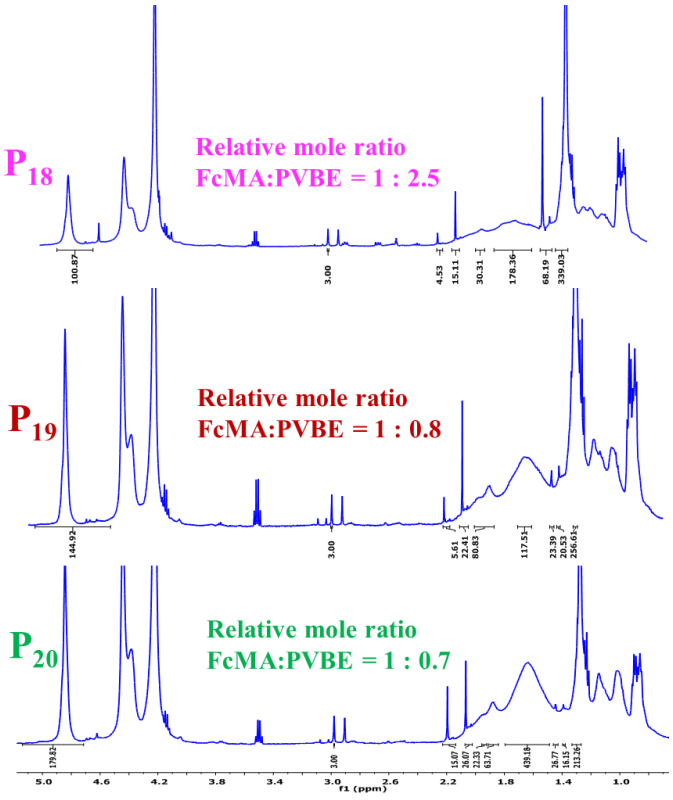

Figure 7.4: *^{1}H-NMR spectra with integral values of FcMA and all ferrocene containing polymers (P_6 to P_{20}). Feed mole ratios are mentioned in the Figure.*

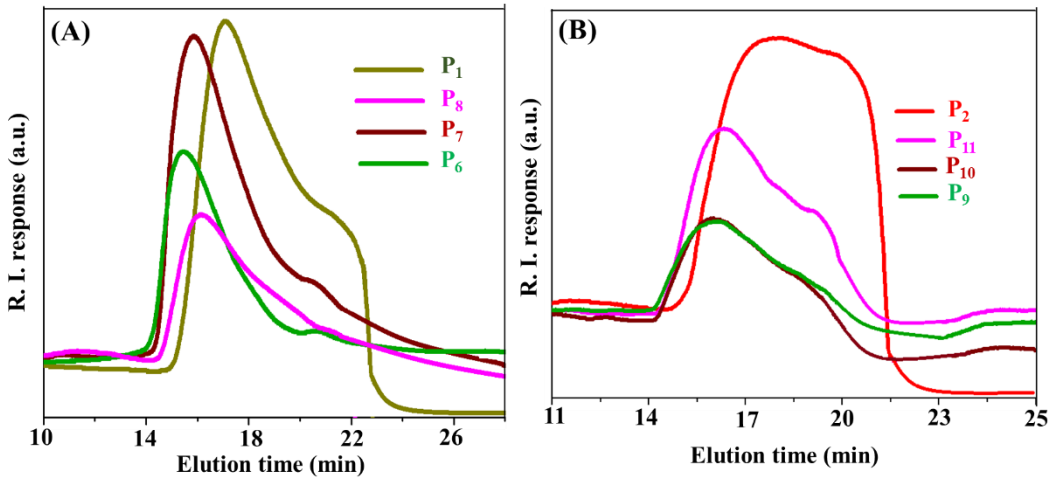

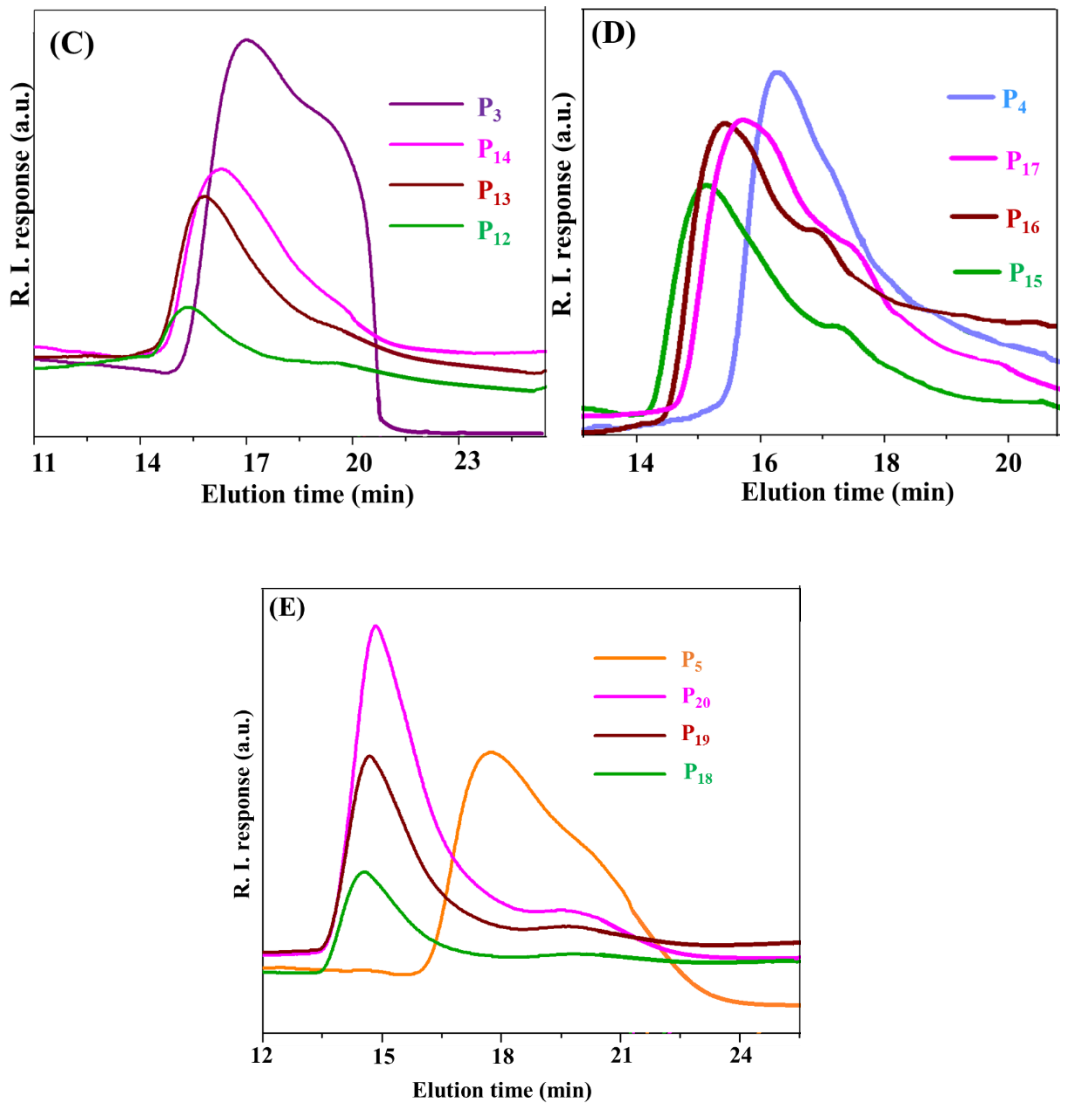

Figure 7.5: *GPC plots of ferrocene containing block copolymers (FcBCPs). In each sub figure FcBCPs are compared with the corresponding pFcMA homopolymer macro-CTA.*

Table 7.1: *Various parameters obtained from GPC and ^{1}H-NMR analysis for different chain length of ferrocene containing block copolymers.*

Polymer Sample identity	Sample composition[a]	[FcMA]:[PVBE]/ [NaSS] (weight % ratio)	$\overline{M_n}$ targeted[b] (g/mol)	$\overline{M_n}$ achieved[c] (g/mol)	Đ[d]	$\overline{M_n}$ from ^{1}H-NMR[e] (g/mol)
P_1	[f]pFcMA$_{71}$	--	20,000	24,650	1.55	24,282
P_2	[f]pFcMA$_{101}$	--	40,000	34,906	1.38	38,688
P_3	[f]pFcMA$_{120}$	--	60,000	47,509	1.4	49,577
P_4	[g]pFcMA$_{110}$	--	40,000	38,172	1.41	42,441
P_5	[g]pFcMA$_{151}$	--	60,000	52,052	1.35	57,553
P_6	p(FcMA$_{71}$-*b*-PVBE$_{247}$)	1:2	73,950	53,462	1.49	35,131
P_7	p(FcMA$_{71}$-*b*-PVBE$_{109}$)	1:1	49,650	43,711	1.54	31,515
P_8	p(FcMA$_{71}$-*b*-PVBE$_{54}$)	1:0.5	37,150	33,982	1.68	30,309
P_9	p(FcMA$_{101}$-*b*-PVBE$_{294}$)	1:2	1,04,718	57,807	1.39	49,882
P_{10}	p(FcMA$_{101}$-*b*-PVBE$_{118}$)	1:1	70,200	51,549	1.35	46,437
P_{11}	p(FcMA$_{101}$-*b*-PVBE$_{39}$)	1:0.5	52,553	41,845	1.43	45,232
P_{12}	p(FcMA$_{120}$-*b*-PVBE$_{298}$)	1:2	1,24,527	77,108	1.39	61,287
P_{13}	p(FcMA$_{120}$-*b*-PVBE$_{192}$)	1:1	83,175	70,727	1.41	57,843
P_{14}	p(FcMA$_{120}$-*b*-PVBE$_{114}$)	1:0.5	62,342	61,465	1.42	56,121
P_{15}	p(FcMA$_{110}$-*b*-NaSS$_{286}$)	1:2	1,14,516	59,404	1.5	57,287
P_{16}	p(FcMA$_{110}$-*b*-NaSS$_{176}$)	1:1	76,633	54,795	1.61	53,988
P_{17}	p(FcMA$_{110}$-*b*-NaSS$_{16}$)	1:0.5	57,402	41,843	1.57	50,276
P_{18}	p(FcMA$_{151}$-*b*-NaSS$_{330}$)	1:2	1,56,218	74,481	1.33	72,193
P_{19}	p(FcMA$_{151}$-*b*-NaSS$_{186}$)	1:1	1,04,104	71,583	1.39	69,512
P_{20}	p(FcMA$_{151}$-*b*-NaSS$_{40}$)	1:0.5	78,093	69,622	1.37	66,419

[a] Degree of polymerization (DP) obtained from GPC analysis and the DP values are indicated in the subscript of the polymer chain. [b] Targeted molecular weight as per the calculation using in RAFT method. [c] $\overline{M_n}$ and [d] dispersity (Đ) are obtained from GPC analysis. [e] ($\overline{M_n}$) calculated based on the integration value obtained from ^{1}H-NMR spectra [f, g] synthesized by using BSPA and CPDB as CTA, respectively.

Figure 7.6 presents the UV-vis absorption spectra of ferrocene based homopolymers (P_3, P_5) as well as block copolymers (P_{12}, P_{19}) along with FcMA. Three absorption peaks appear at 240, 263, and 450 nm are ascribed to π - π* and d – d transitions of Cp rings, which are a well-known characteristic of ferrocene functionalized moiety. Two additional electronic transition of FcMA unit at 307 and 350 nm are also observed and assigned to thio carbonyl based transitions. After polymerization, both P_3 and P_5 (macro-CTA, pFcMA) shows all the identical absorption peaks like FcMA confirming the presence of ferrocene moiety intact in the homopolymers. Later on, in BCPs P_{12} and P_{19}, the π - π* transition due to phenyl ring of PVBE and NaSS made 240 nm peak even more intense in comparison to the 263 nm than the homopolymer cases. Ferrocene based transition peaks can be seen prominently at the similar position which is an indirect proof of successful synthesis of ferrocene based homopolymers as well as BCPs.

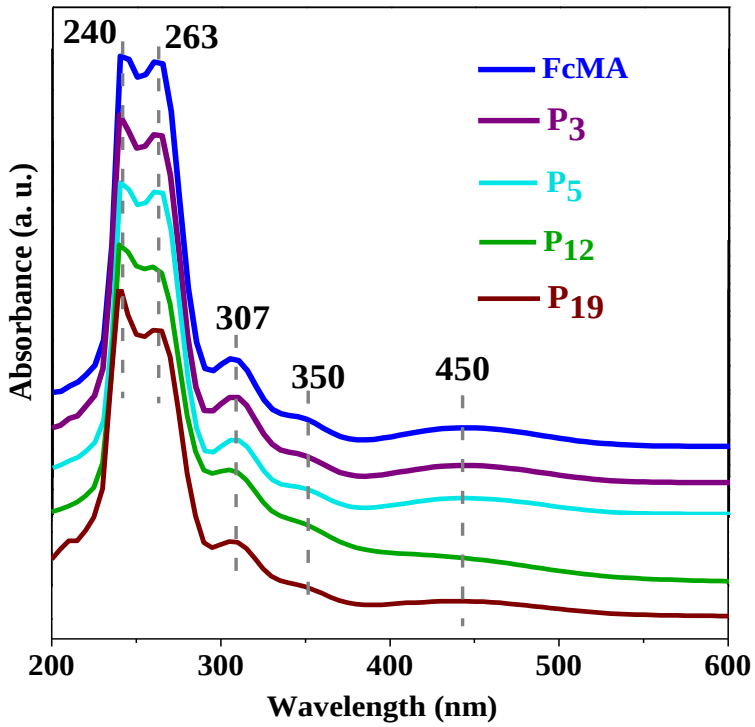

Figure 7.6: *UV-visible absorption spectra of ferrocene based homopolymers and BCPs along with monomer FcMA. Spectra were recorded using 0.5 mg/ mL sample solution in THF.*

The redox properties of FcMA based homopolymers and BCPs were inspected *via* cyclic voltammetry (CV) analysis by using Pt as a working electrode and tetrabutyl ammonium perchlorate (TBAP) as an electrolyte in dry THF at room temperature. All the voltammograms were obtained at the scan rate of 150 VS^{-1} with the sample concentration of 0.5 mg/ mL and shown in *Figure 7.7(A)* into a plot of current versus applied potential. A typical ferrocene based CV diagram is obtained which is an indirect proof of presence of ferrocene in all the cases.

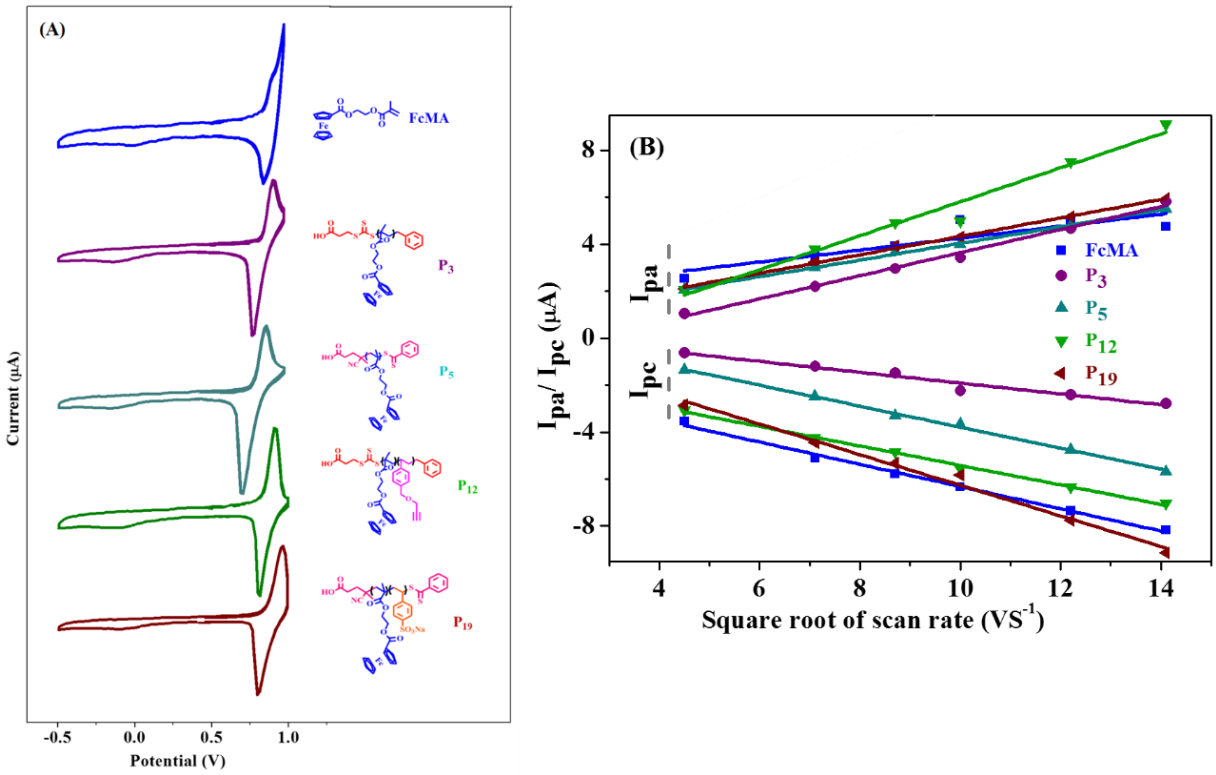

Figure 7.7*: (A) CV diagram of FcMA based homopolymers (P_3, P_5)and block copolymers (P_{12} and P_{19} as taken as a representative samples. (B) Anodic peak current (I_{pa}) or cathodic peak current (I_{pc}) vs. square root of scan rate of the redox process.*

The electrochemical parameters determined from the CV diagrams are tabulated in *Table 7.2*. Strong electron withdrawing effect of –CN group present in CPDB triggered P_5 to make a positive shift in oxidation potential (E_{pa}) compared to P_3 and NaSS having electron withdrawing nature, further shifted this particular potential peak in P_5 towards more positive

side in P_{19}. All this supports the fact of delaying in electron releasing process while oxidation occurs. Exactly similar observation is obtained in case of reduction potential (E_{pc}). BCP composed of PVBE in P_{12} followed the similar trend like P_{19}. But as a whole, the electron donating effect of sulphur (S) linked to the repeat unit after polymerization exhibits a negative shift in both oxidation and reduction potential if all polymers (P_3 to P_{18}) compared to FcMA. As chain length increases from P_3 to P_5, both I_{pa} and I_{pc} also increases simultaneously indicating the involvement of even higher number of electroactive ferrocene uniti P_5 than P_3. The scan rate dependency study carried out for both anodic current (I_{pa}) and cathodic current (I_{pc}) presented in *Figure 7.7(B)* clearly attributing to the fact that the redox process involving our synthesized ferrocene based monomer, homopolymer as well as BCP are following Randles-Sevcik equation.

Table 7.2: *Various parameters obtained from CV analysis for ferrocene based monomer, homopolymers and BCPs.*

Polymer Sample	**E_{pa} (V)**	**E_{pc} (V)**	**ΔE_p (V)**	**$E_{1/2}$[a] (V)**	**I_{pa} (µA)**	**I_{pc} (µA)**
FcMA	0.988	0.861	0.127	0.925	4.97	2.4
P_3	0.868	0.719	0.149	0.794	4.79	6.34
P_5	0.923	0.778	0.145	0.851	5.17	7.35
P_{12}	0.909	0.813	0.096	0.861	5.83	5.68
P_{19}	0.954	0.861	0.093	0.908	7.52	7.76

[a] $E_{1/2}$ values were determined as the average values of E_{pa} and E_{pc}.

7.3.3. Porous multi compartment micelles formation followed *via* crystallization driven self-assembly (CDSA) technique

The series of samples from P_6 to P_{20} were subjected to self-assembly experiment *via* crystallizable driven self-assembly (CDSA) in order to figure out how pendant ferrocenyl block copolymers rearranged themselves during heating-cooling processes employed in CDSA. For P_6 to P_{14} those are comprised with PVBE as other block, THF was used as a common solvent, and acetone in which pFcMA is insoluble was selected as a good solvent for pPVBE block. To conduct the self-assembly study, each BCP solution in THF (1 mg/ mL) was injected to 1 mL of acetone at a rate of 0.2 mL/ h at ambient temperature resulting a final solution concentration of 0.5 mg/ mL. Thereafter, the prepared solution was annealed for 1 h at 54 ºC followed by additional 2 h at 48 ºC and then left to slowly cool down to room temperature after while the solution was matured for 48 h at the refrigerator. This resulted a turbid suspension in each case which was then sonicated (~2 seconds) to disperse better prior to FESEM analysis by drop casting the colloidal solution onto the glass plate followed by subsequent solvent evaporation. Similar methodology was followed in case of P_{15} to P_{20} except the solvent water which is chosen as the good solvent for pNaSS block. For the convenience pFcMA, pPVBE and pNaSS are assigned as F, P and S, respectively for further discussion and thus p(FcMA-*b*-PVBE) and p(FcMA-*b*-NaSS) are considered as FP and FS, respectively. Thorough inspection unveiled predominantly a multi compartment vesicles of size 150 nm to 3 µm containing several nanopores in the wall with size ranging from 50 nm to 600 nm for P_6 to P_{14}. The very high incompatibility between F i.e. pFcMA and P i.e. pPVBE block triggers a strong microphase separation within the micelle formed after CDSA treatment and results a porous phase-segregated assemblies (*Figure 7.8*). The contrast in electron density between F and P blocks assists to detect the phase-segregated assemblies within the multi compartment vesicles easily by FESEM in which the little darker spots corresponds to P domain while the remaining bright grey areas stands for F domain (*Figure 7.8*). The competition between very high interfacial energy and chain conformation of both F and P block makes internal segregation so strong that it pushes the whole system towards a super strong micro-phase separation within the micelles membrane leading to formation of porous multi compartment vesicles. The morphology has

found to be varying with the degree of polymerization (DP) of pFcMA block (F). The FESEM images of FP vesicles shown in *Figure 7.8* changes its morphology from DP 71 to 101 of F block, for example $F_{101}P_{294}$, $F_{101}P_{118}$ and $F_{101}P_{39}$ (shown in *Table 1* for the DP mentioned in the subscript of F and P for the corresponding sample) have a porous phase-segregated vesicle membrane (P_9, P_{10}, P_{11}) whereas $F_{71}P_{247}$, $F_{71}P_{109}$ and $F_{71}P_{54}$ have vesicles with crinkly membrane (P_6, P_7, P_8). Both $F_{71}P_{54}$ (P_8) and $F_{101}P_{39}$ (P_{11}) with least amount of pPVBE block showed formation of comparatively less aggregated discrete micelles. There are some curved micelles in both P_8 and P_{11} which might have been appeared as a broken microstructure while doing sonication and this clearly confirms the presence of hollow cavity inside. Again with the change in DP of pFcMA block to 120 the samples $F_{120}P_{298}$, $F_{120}P_{192}$ and $F_{120}P_{114}$ display fibre morphology having width size of 50 nm to 350 nm in all three cases. Most likely with higher number of DP of pFcMA, during heat-cool process the crystalline region of pFcMA rearranged themselves in such a manner that it looks like a long cylindrical axes oriented in a perpendicular direction and the pPVBE block remains inside as a core helping to form multi compartment region within the long fibre [*Figure 7.8 third panel (P_{12}-P_{14}) and Figure 7.9D*]. If we see carefully [zoomed image of P_{12} in *Figure 7.9(D)]*, P_{12} also reveals the presence of pores with sizes ranges from 10 nm 100 nm throughout the matrix. A major point to be noted here is that both the F and P blocks are hydrophobic in nature while in case of P_{15} to P_{20}, the F and S (pNaSS) blocks are hydrophobic and hydrophilic in nature respectively. $F_{110}S_{286}$, $F_{110}S_{176}$ and $F_{110}S_{16}$ have 3D micellar morphology with F block as a core with little darker in colour and S block as a corona with brighter colour and the sizes varies from 300 nm to 3 µm (*Figure 7.8, fourth panel, P_{15}-P_{17}*). Further with increase in DP of F block morphology of to the samples $F_{151}S_{330}$, $F_{151}S_{186}$ and $F_{150}S_{40}$ transform into a hollow vesicles (P_{18}, P_{19}, P_{20}) with sizes of 200 nm to 1 µm (*Figure 7.8, fifth last lower panel, P_{18}-P_{20}*). Most likely the presence of a hydrophilic S block differs much in the microphase segregation owing to the difference in interfacial energy balances in FS sample series with hydrophobic F block than in presence of a hydrophobic P block in FP types of samples and end up with a single compartment hollow vesicle formation instead of producing multi compartment hollow vesicles. Though aggregated hollow structure in $F_{151}S_{330}$ makes whole matrix looks like a hollow multi compartment

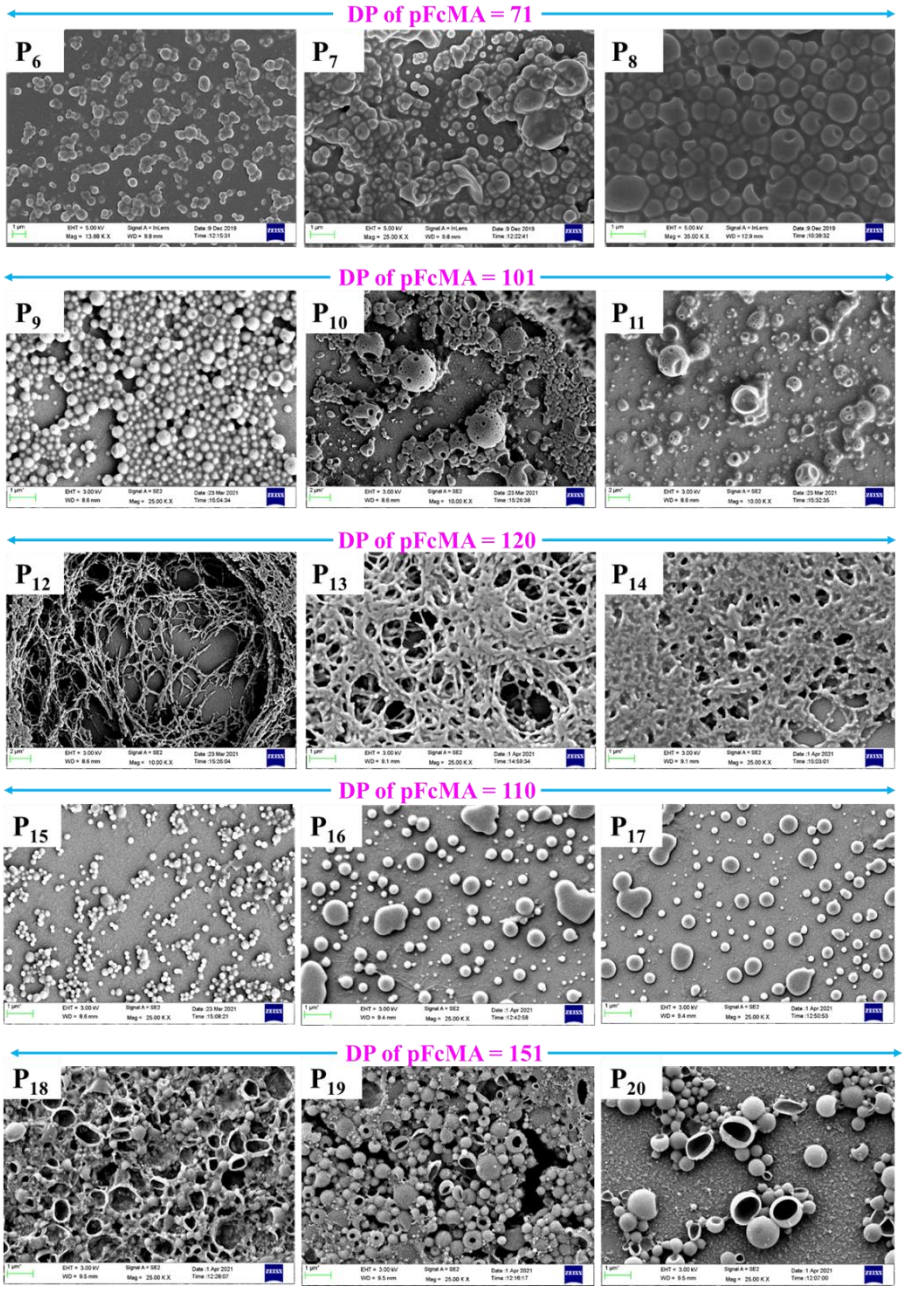

Figure 7.8: *FESEM images after CDSA treatment of each ferrocene containing block copolymers. P_6-P_8 (upper top first panel); P_9-P_{11} (second panel from top); P_{12}-P_{14} (third panel from top); P_{15}-P_{17} (fourth panel from top); P_{18}-P_{20} (fifth panel last one). For each panel the related degree of polymerization (DP) of pFcMA block is mentioned at the extreme right hand side.*

micelles (P_{18}, *Figure 7.8, fifth last lower panel*) but if we see carefully, (P_{18}-P_{20}) each of the micelle is actually a single compartment vesicle which appeared as a 3D hollow bowl shaped morphology after rapture of the actual shape. The main reason behind this structural breakdown is most likely the strong phase segregation between F and S block. There are some vesicles intact in shape can be seen clearly (*Figure 7.8, fifth last lower panel*) where the darker patchy grown towards inner side of the vesicle membrane correspond to S block and the vesicle membrane wall consist of F block. In this series of samples with FS type also we can see the formation of less aggregated discrete micelles for $F_{110}S_{16}$ (P_{17}) and $F_{150}S_{40}$ (P_{20}) much like $F_{71}P_{54}$ (P_{10}) and $F_{101}P_{39}$ (P_{11}).

To ascertain the role of CDSA in forming the complex porous multi compartment micelles, vesicles and fibres as well as single compartment vesicles, the micelles of FP and FS series were prepared as a reference *via* controlled experiment and the morphologies were thoroughly studied [*Figure 7.9(A to F)*]. In control experiment, the BCP solutions were subjected to do self-assembly study without subsequent heat-cool process. To do so, exactly similar protocol was followed to inject the BCP solution in THF in 1 mL of acetone/ water at a rate of 0.2 mL/ h at room temperature and then left for 48 h to be matured at the refrigerator. FESEM data [*Figure 7.9(A, C, E)*] revealed that the control experiment of all three $F_{101}P_{294}$ (P_9), $F_{120}P_{298}$ (P_{12}) and $F_{151}S_{330}$ (P_{18}) is not enough to achieve well defined complex porous multi compartment micelles, vesicles and fibre type morphology. The very slow addition of F block solution either into P or S block solution, the self-assembly process proceeded *via* the formation of micellar sheet with irregular shape and size [*Figure 7.9: (A), (C) and (E)*] which after CDSA treatment evolved into a complex well defined multi compartment vesicles and fibres with nano pores in the micellar membrane wall [*Figure 7.9: (B), (D) and (F)*]. During heating process to perform CDSA, the non-solvent acetone/ water helped F block to rearrange its crystalline region slowly among themselves to form a micellar membrane wall and further directed a spatial self-assembly to form 3D multi compartment vesicles or fibres. The P block seemed to be remained as a separate phase in the form of white colour small globules in P_9 [*Figure 7.9(A)*] which after CDSA due to strong microphase separation appears as a darker

patchy grown towards the inner wall of the F micellar membrane [*Figure 7.9(B)*] with subsequent pore formation in the wall. To demonstrate the crucial role of the presence of P or S as a second block with F behind strong microphase segregation during heat-cool process, CDSA was carried out only with F blocks for example F_{71} (P1) and F_{110} (P4) as a representative and only a flat kind micellar membrane formation can be seen [*Figure 7.9(G) and (H)*]. This suggests that the microphase separation of the incompatible F and P/ S blocks leads to the formation of the porous multi compartment vesicles or fibres.

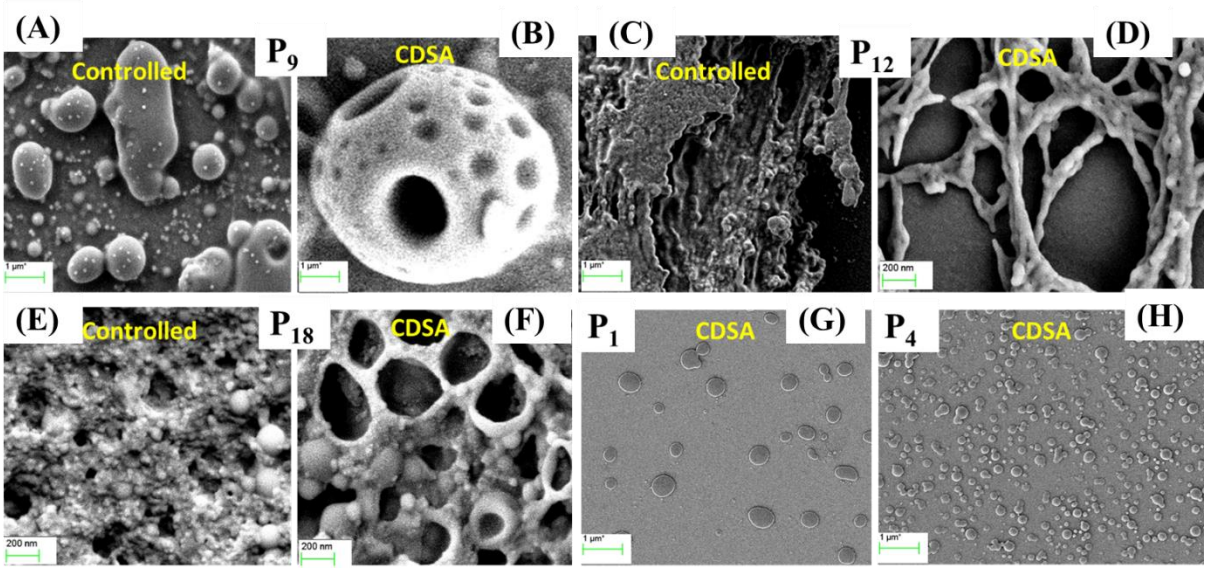

Figure 7.9: *Comparison of the FESEM the images obtained after controlled and CDSA experiment: (A, B) P_9; (C, D) P_{12}; (E, F) P_{18} and (G, H) CDSA experiment images of P_1 and P_4. Each images in the figure is labelled as controlled or CDSA to indicate the nature of experiment.*

Ferrocenyl polymers are very well-known as a redox-responsive materials. It is established that the oxidation of ferrocene unit into its cationic species is fully reversible. And this redox-responsiveness of this is widely utilized to tune the self-assembly or disassembly process of ferrocenyl polymers. *Figure 7.10* shows that $F_{101}P_{118}$ (P_{10}) porous multi compartment vesicles transforms into a simple micellar membrane after oxidation with $FeCl_3$

and showing no porous nature of the membrane and the oxidized micellar membrane reversibly goes back into its initial porous nature of the micellar membrane after reduction with $SnCl_2$.

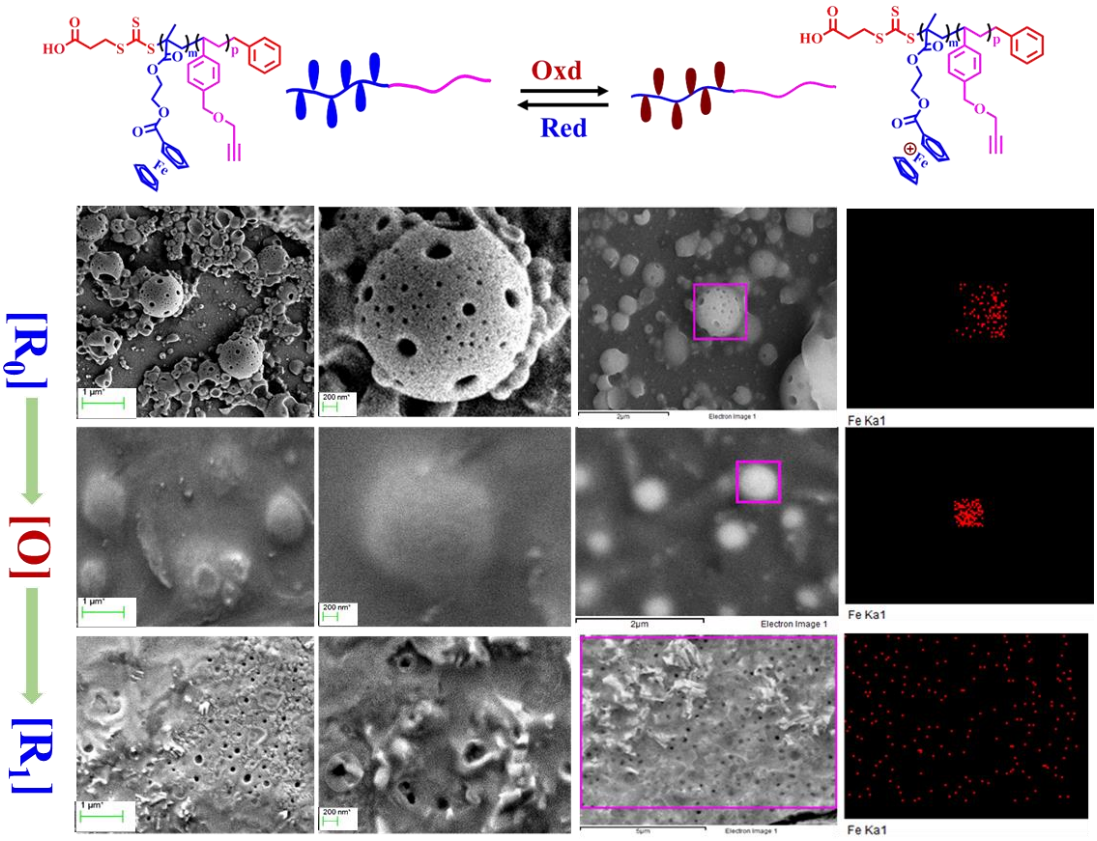

Figure 7.10: *FESEM analysis to study the redox responsiveness of P_{10}. At the top a general scheme for the oxidation and reduction process of ferrocenyl block copolymers is presented. FESEM images of (upper top panel) P_{10} in its original state, mentioned as [R_0]; (middle panel) after oxidation with $FeCl_3$, assigned as [O]; (lower panel) after reduction with $SnCl_2$, assigned as [R_1]. In all three panels the related iron distribution mapping also shown at the last row.*

Though porous multicompartment vesicle shape got raptured in the reduced state which can be clearly seen by the presence of membrane layer around the pores (*Figure 7.10, lower panel*), but the reappearance of pore throughout the matrix confirms the happening of microphase

segregation in the micellar membrane wall. The presence of iron as an aggregated form and as dispersed condition in *Figure 7.10* in the iron distribution mapping images reconfirms the successful redox responsive nature of F block in this case. It is believed that oxidation of the ferrocene moiety helps to change the solvophobic character of the micellar membrane forming F block and provoke the F^+ and P block to be rearranged themselves to form a uniform micellar membrane as schematically shown in *Figure 7.10*. After this successful redox response of this multicompartment porous vesicles it can be envisioned that these kind of micelles where membrane pores can be designed as an on-off switchable pore triggered *via* redox-response, can be engineered as a host to load and release various guests, when the guest size is smaller than the pore diameter.

7.4. Conclusion

A series of ferrocene based homopolymers and block copolymers has been synthesized where ferrocene block remains as a pendant chain *via* sequential RAFT polymerization technique. 2-(methacryloyloxy)ethyl ferrocenecarboxylate (FcMA) was chosen as a ferrocenyl monomer whereas propargyl 4-vinylbenzyl ether (PVBE) and sodium 4-styrenesulfonate (NaSS) were used to get the desired chain extended block copolymer. All the synthesized polymers were well characterized by ^{1}H-NMR and UV-visible spectroscopy. The molecular weight obtained from the well-defined peak integral values in ^{1}H-NMR spectroscopy shows good correlation with the GPC data. The GPC curves with narrow molecular weight distribution refers the successful RAFT polymerization of FcMA based monomer. CV analysis indicates the reversible redox properties of all the synthesized Fc based polymers. Finally, a new kind of porous multicompartment assemblies are prepared by employing crystallization-driven-self-assembly (CDSA) process. The presence of imcompatible pPVBE/ pNaSS causes strong microphase segregation in the uniform micellar membrane wall of pFcMA block during CDSA and end up with a formation of porous multi compartment vesicles and fibres. It is found out that structure of the phase segregated multi compartment micelles formation is firmly dependent on the degree of polymerization of pFcMA block. These multi compartment porous vesicles are redox-responsive in nature owing to the presence of ferrocenyl moiety and the

micellar membrane pores can be reversibly on-off triggered by the redox-response. These redox-responsive porous multicompartment vesicles are expected to be a new kind assemblies of ferrocenyl diblock copolymer achieved via CDSA technique and can be treated as a smart host to load and release the guests.

References

[1] A. O. Moughton, M. A. Hillmyer, T. P. Lodge, *Macromolecules* **2012**, *45*, 2–19.

[2] A. Laschewsky, *Curr. Opin. Colloid Interface Sci.* **2003**, *8*, 274–281.

[3] O. July, H. Ringsdorf, *Macromolecules* **2004**, *37*, 8485–8486.

[4] H. Ringsdorf, B. Schlarb, J. Venzmer, *Angew. Chemie Int. Ed. English* **1988**, *27*, 113–158.

[5] Y. Pei, L. Thurairajah, O. R. Sugita, A. B. Lowe, *Macromolecules* **2015**, *48*, 236–244.

[6] Y. Han, H. Yu, H. Du, W. Jiang, *J. Am. Chem. Soc.* **2010**, *132*, 1144–1150.

[7] O. Colombani, M. Ruppel, M. Burkhardt, M. Drechsler, M. Schumacher, M. Gradzielski, R. Schweins, A. H. E. Müller, *Macromolecules* **2007**, *40*, 4351–4362.

[8] Y. Mai, A. Eisenberg, *Chem. Soc. Rev.* **2012**, *41*, 5969–5985.

[9] G. Sun, H. Cui, L. Y. Lin, N. S. Lee, C. Yang, W. L. Neumann, J. N. Freskos, J. J. Shieh, R. B. Dorshow, K. L. Wooley, *J. Am. Chem. Soc.* **2011**, *133*, 8534–8543.

[10] S. Kubowicz, J. F. Baussard, J. F. Lutz, A. F. Thünemann, H. Von Berlepsch, A. Laschewsky, *Angew. Chemie - Int. Ed.* **2005**, *44*, 5262–5265.

[11] Y. Gao, X. Li, L. Hong, G. Liu, *Macromolecules* **2012**, *45*, 1321–1330.

[12] B. Fang, A. Walther, A. Wolf, Y. Xu, J. Yuan, A. H. E. Müller, *Angew. Chemie - Int. Ed.* **2009**, *48*, 2877–2880.

[13] A. Hanisch, A. H. Gröschel, M. Förtsch, M. Drechsler, H. Jinnai, T. M. Ruhland, F. H. Schacher, A. H. E. Müller, *ACS Nano* **2013**, *7*, 4030–4041.

[14] T. P. Lodge, A. Rasdal, Z. Li, M. A. Hillmyer, *J. Am. Chem. Soc.* **2005**, *127*, 17608–17609.

[15] M. Williams, N. J. W. Penfold, S. P. Armes, *Polym. Chem.* **2016**, *7*, 384–393.

[16] S. Li, X. He, Q. Li, P. Shi, W. Zhang, *ACS Macro Lett.* **2014**, *3*, 916–921.

[17] A. H. Gröschel, F. H. Schacher, H. Schmalz, O. V. Borisov, E. B. Zhulina, A. Walther, A. H. E. Müller, *Nat. Commun.* **2012**, *3*, 710.

[18] P. Shi, Y. Qu, C. Liu, H. Khan, P. Sun, W. Zhang, *ACS Macro Lett.* **2016**, *5*, 88–93.

[19] A. Blanazs, S. P. Armes, A. J. Ryan, *Macromol. Rapid Commun.* **2009**, *30*, 267–277.

[20] L. Shen, H. Wang, G. Guerin, C. Wu, I. Manners, M. A. Winnik, *Macromolecules* **2008**, *41*, 4380–4389.

[21] F. He, T. Gädt, I. Manners, M. A. Winnik, *J. Am. Chem. Soc.* **2011**, *133*, 9095–9103.

[22] N. Fairley, B. Hoang, C. Allen, *Biomacromolecules* **2008**, *9*, 2283–2291.

[23] A. M. Mihut, M. Drechsler, M. Möller, M. Ballauff, *Macromol. Rapid Commun.* **2010**, *31*, 449–453.

[24] A. Pitto-Barry, N. Kirby, A. P. Dove, R. K. O'Reilly, *Polym. Chem.* **2014**, *5*, 1427–1436.

[25] W. Yu, M. Inam, J. R. Jones, A. P. Dove, R. K. O'Reilly, *Polym. Chem.* **2017**, *8*, 5504–5512.

[26] M. Inam, G. Cambridge, A. Pitto-Barry, Z. P. L. Laker, N. R. Wilson, R. T. Mathers, A. P. Dove, R. K. O'Reilly, *Chem. Sci.* **2017**, *8*, 4223–4230.

[27] N. Petzetakis, D. Walker, A. P. Dove, R. K. O'Reilly, *Soft Matter* **2012**, *8*, 7408–7414.

[28] T. Vilgis, A. Halperin, *Macromolecules* **1991**, *24*, 2090–2095.

[29] W. N. He, J. T. Xu, *Prog. Polym. Sci.* **2012**, *37*, 1350–1400.

[30] P. J. Hurst, A. M. Rakowski, J. P. Patterson, *Nat. Commun.* **2020**, *11*, 1–12.

[31] G. Guerin, M. Cruz, Q. Yu, *Sci. Adv.* **2020**, *6*, 1-10.

[32] S. Ganda, M. H. Stenzel, *Prog. Polym. Sci.* **2019**, 101195.

[33] C. E. Boott, J. Gwyther, R. L. Harniman, D. W. Hayward, I. Manners, *Nat. Chem.* **2017**, *9*, 785-792.

[34] G. R. Whittell, M. D. Hager, U. S. Schubert, I. Manners, *Nat. Publ. Gr.* **2011**, *10*, 176–188.

[35] J. A. Massey, K. Temple, L. Cao, Y. Rharbi, J. Raez, M. A. Winnik, I. Manners, *J. Am. Chem. Soc.* **2000**, *122*, 11577–11584.

[36] L. Cao, I. Manners, M. A. Winnik, *Macromolecules* **2002**, *35*, 8258–8260.

[37] D. J. Lunn, J. R. Finnegan, I. Manners, *Chem. Sci.* **2015**, *6*, 3663–3673.

[38] U. Tritschler, S. Pearce, J. Gwyther, G. R. Whittell, I. Manners, *Macromolecules* **2017**, *50*, 3439–3463.

[39] J. Massey, K. N. Power, I. Manners, M. A. Winnik, **1998**, *7863*, 9533–9540.

[40] R. L. N. Hailes, A. M. Oliver, J. Gwyther, G. R. Whittell, I. Manners, *Chem. Soc. Rev.* **2016**, *45*, 5358–5407.

[41] C. G. Hardy, J. Zhang, Y. Yan, L. Ren, C. Tang, *Prog. Polym. Sci.* **2014**, *39*, 1742–1796.

[42] G. R. Whittell, I. Manners, *Adv. Mater.* **2007**, *19*, 3439–3468.

[43] R. D. A. Hudson, *J. Organomet. Chem.* **2001**, *637–639*, 47–69.

[44] V. Bellas, M. Rehahn, *Angew. Chemie - Int. Ed.* **2007**, *46*, 5082–5104.

[45] C. G. Hardy, L. Ren, J. Zhang, C. Tang, *Isr. J. Chem.* **2012**, *52*, 230–245.

[46] N. Yeole, D. Hundiwale, T. Jana, *J. Colloid Interface Sci.* **2011**, *354*, 506–510.

[47] N. Yeole, S. N. R. Kutcherlapati, T. Jana, *RSC Adv.* **2014**, *4*, 2382–2388.

[48] S. N. Raju Kutcherlapati, N. Yeole, M. R. Gadi, R. S. Perali, T. Jana, *Polym. Chem.* **2017**, *8*, 1371–1380.

[49] K. Pawar, S. N. R. Kutcherlapati, N. Yeole, D. Hundiwale, T. Jana, *J. Appl. Polym. Sci.* **2018**, *135*, 1–10.

[50] S. N. R. Kutcherlapati, R. Koyilapu, U. M. R. Boddu, D. Datta, R. S. Perali, M. J. Swamy, T. Jana, *Macromolecules* **2017**, *50*, 7309–7320.

[51] S. R. Kutcherlapati, R. Koyilapu, T. Jana, *J. Polym. Sci. Part A Polym. Chem.* **2018**, *56*, 365–375.

[52] R. Koyilapu, S. Singha, S. N. R. Kutcherlapati, T. Jana, *Polymer* **2020**, *195*, 122458.

[53] M. Dhara, S. Rudra, N. Mukherjee, T. Jana, *Polym. Chem.* **2021**, DOI

10.1039/D1PY00590A.

[54] M. Dhara, N. Giri, B. Narasimha Rao, A. K. Patra, P. U. Sastry, M. S. Ingole, T. Jana, *Eur. Polym. J.* **2020**, *122*, 109380.

[55] M. Dhara, N. Giri, A. Dutta, A. K. Patra, P. U. Sastry, M. S. Ingole, T. Jana, *Polymer* **2020**, *204*, 122807.

[56] J. Zhang, L. Ren, C. G. Hardy, C. Tang, *Macromolecules* **2012**, *45*, 6857–6863.

CHAPTER 8

Summary and Conclusions

8.1. Summary

Thesis entitled "***Polymers with Pendant Ferrocenyl units as Burn Rate Catalyst and Redox Responsive Material***" illustrates the synthesis and characterization of pendant ferrocenyl polymers to be used as a burn rate catalyst and redox responsive material. Two different pathway namely polyurethane chemistry and RAFT polymerization technique have been chosen to synthesize all the ferrocenyl polymers discussed in the thesis. The whole thesis work comprises of total eight chapters that starts with an introductory chapter then materials, synthesis and methods followed by five working chapters. A brief summary of each chapter is mentioned below.

CHAPTER 1

This chapter is associated with a historical background of ferrocene containing polymer besides their systematic evolvement as a side chain by following a variety of well-established polymerization technique since their discovery. Further the problems dealing with ferrocene-based polymers as a burn rate catalyst in composite solid propellant have been thoroughly described along with proposing most beneficial pathway. In the later part the utility of designing the ferrocenyl polymers as a well-defined controlled polymer chain on a particle surface has been demonstrated and as an extension the possibilities of producing hollow polymer nanocapsules has been outlined. Towards the end, the complex morphologies related to ferrocene containing polymers have been developed. Finally, conclusions and scope of this thesis work have been summarized.

CHAPTER 2

This particular chapter includes all the materials those were used for whole thesis work, details of synthesis of precursor materials and various instrumentation methods employed for the synthesis and characterization of all the materials mentioned in the thesis.

CHAPTER 3

Series of metal based polyurethanes (PUs) have been synthesized from hydroxyl terminated polybutadiene (HTPB) with combination of a potential energetic material, 2,4-dinitrobenzene (DNB) and burn rate (BR) enhancer, ferrocene with two objectives: (1) exerting flexibility into otherwise brittle PU film and (2) increasing BR of composite solid propellant (CSP). HTPB was first functionalized with DNB at the terminal carbons and then ferrocene was grafted radically as poly (vinyl ferrocene) (PVF) chain onto the pendant vinyl bond of HTPB. The degree of PVF grafting was altered by appropriate reaction recipes to find out the effect of Fe content on various physical properties including fluidity of the HTPB. Density function theory (DFT) calculation showed that the dominating intra-chain interactions over inter-chain owing to the strong interactions between NO_2 of DNB and cyclopentadiene of ferrocene are the driving force for improvement in various physical properties of PVF grafted-HTPB-DNB. Cyclic voltammetry (CV) measurement showed one electron reversible redox behaviour of the grafted PVF polymer chain with slow electron transfer process. Further the mechanical stability, thermal stability and properties of PUs have been studied thoroughly; the results indicated a strong influence of DNB and ferrocene in the chains on the physical properties. All the DNB modified PU membranes displayed exceptionally enhanced flexibility along with much lower Tg value compared to neat PVF-g-HTPB-PU. The presence of DNB at the chain end of soft segment (SS) causes strong segmental mixing between SS and hard segment (HS) domains which helps in enhancing the elasticity of SS chain by increasing the inter polymer chain distance. Morphology of the hard segment domains formation has been probed by small angle X-ray scattering (SAXS) and further confirmed by FESEM. Burn rate of composite solid propellant made from the HTPB-DNB-g-PVF binder is found to be ~18% larger than the HTPB-DNB.

CHAPTER 4

This chapter addresses the effect of enhanced segmental mixing on various physical properties of ferrocenylsilane tethered polybutadiene based polyurethane (PU). To study this, 2-(ferrocenylpropyl) dimethylsilane (FPDS) has been *grafted* to the pendant vinyl double bond

of hydroxyl terminated polybutadiene (HTPB) and 2, 4-dinitrobenzene attached HTPB (HTPB-DNB) through hydrosilylation reaction and then this resulting diols (FPDS-*g*-HTPB and FPDS-*g*-HTPB-DNB) were polymerized with isophorone diisocyanate (IPDI) to obtain FPDS-*g*-HTPB-PU and FPDS-*g*-HTPB-DNB-PU. Spectral (NMR, IR) analysis, molecular weight measurements and estimation of free hydroxyl contents were carried out to confirm the formation of these new diols. The careful variation of the grafting conditionaltered the extent of FPDS tethering on the diols which resulted varying amount of Si and Fe contents in these modified HTPBs. Density functional theory (DFT) calculation revealed the presence of various interactions of Si with various functionalities including ferrocene of the chain which resulted highly cross-linked polymer matrix. Cyclic voltammetry (CV) measurements of FPDS-*g*-HTPB-DNB displayed non-Nerstain reversible redox system with slow electron transfer process owing to the presence of DNB. Further, the PUs obtained from these HTPBs were prepared and characterized thoroughly in terms of thermal, mechanical, structural and tensile properties to study the segmental mixing between hard and soft segments of PUs owing to the presence of Si, Fe and DNB in the PU chain. Higher degree of segmental mixing was noticed when Si, Fe in the diol increased and also presence of DNB in the diol played a significant role in inducing the segmental mixing. The co-existence of segmental mixing and phase separation has been confirmed by small-angle x-ray scattering studies which further reaffirmed by FESEM analysis. Finally, composite solid propellants (CSPs) were prepared from these modified HTPBs and burn rate measurements were carried out. We found that CSPs obtained from FPDS-*g*-HTPB-DNB displayed ~10% higher burn rate than the CSP made from bare HTPB-DNB.

CHAPTER 5

A smart nanosurface has been developed by constructing a well-defined poly(2-(methacryloyloxy)ethylferrocenecarboxylate) (pFcMA) brush over silica nanoparticle (SiNP) surface via surface-initiated reversible addition fragmentation chain transfer (SI-RAFT) polymerization technique. Five different chain length of pFcMA was successfully varied on the particle surface and in each case the molar mass of the polymer was nearly achieved as targeted

with good control in dispersity. The amount of polymer grafted on the surface was calculated by using TGA analysis and even in lower modification the polymers showing "brush-like" regime. The swelling behaviour of the grafted polymer chains in a suitable solvent was investigated by DLS studies; it was concluded that THF is a good solvent for pFcMA block rather than ethanol by analysing the brush length variation with the increasing chain length. Well-defined core-shell morphology obtained from TEM and FESEM study indirectly proves the successful formation of pFcMA layer on the particle surface. The redox property of ferrocenyl polymer was thoroughly inspected by CV analysis and it showed reversible oxidation-reduction properties. Finally, the redox-responsive behaviour of the pfcMA shell was studied by UV-visible absorption spectroscopy.

CHAPTER 6

Hollow polymer nanocapsules (HPN) consist of ferrocenyl shell have been developed by crosslinking the polymer chains *grafted* over silica nanoparticles (SiNP) which were synthesized *via* one pot *grafting from* surface initiated reversible addition fragmentation chain transfer (RAFT) approach followed by removal of the sacrificial silica template. Copolymer brushes composed of ferrocene containing polymer, poly[2-(methacryloyloxy) ethyl ferrocenecarboxylate] (pFcMA) and an alkyne terminated polymer, poly(propargyl 4-vinylbenzyl ether) (pPVBE), were constructed in three different motifs on the SiNP surface as a shell. Two types of block copolymer *grfated* SiNP, p(FcMA-*b*-PVBE)-*g*-SiNP and p(PVBE-*b*-FcMA)-*g*-SiNP, and a random copolymer *grafted* SiNP, rp(FcMA-co-PVBE)-*g*-SiNP were chosen to investigate the influence of polymer architecture on the HPN morphology. Various structural characterizations of all the copolymer *grafted* SiNP confirmed the brush morphology on the particle surface consisting of core-shell structure. In order to bring robustness to the copolymer shell, crosslinking of the polymer chains were performed using a diazide crosslinker, 1,4-bis(azidomethyl)benzene and pPVBE *via* copper-azide click reaction. Various microscopic studies showed that the incorporation of 30 wt% of cross-linker yielded sufficient structural stability leading to HPN formation with ferrocenyl shell after etching away silica with HF treatment. Random copolymer skeleton was found to be the best choice as a polymer

shell to engineer a successful HPN structure compared to block copolymer shell. In addition, encapsulation of oxide free aluminum nanoparticles (Al-NP) inside the hollow cavity of both block and random copolymer was successfully carried out to make a composite materials consisting of both Al and Fe.

CHAPTER 7

A series of ferrocene containing block copolymers were synthesized by employing 2-(methacryloyloxy)ethyl ferrocenecarboxylate (FcMA) as a ferrrocenyl block and propargyl 4-vinylbenzyl ether (PVBE)/ sodium 4-styrenesulfonate (NaSS) as the other block *via* sequential RAFT polymerization. All the synthesized polymers were well characterized by ^{1}H-NMR, UV-visible spectroscopy, GPC measurement and CV analysis. After employing the heat-cool process in a similar line with crystallization driven self-assembly (CDSA) technique, these block polymers produces porous multicompartment micelles and these micellar morphology was found to vary from vesicles to fibre with the change in degree of polymerization of pFcMA block, even with the change in hydrophobic (pPVBE) to hydrophilic (pNaSS) nature of the other block, morphology seemed to varies from multicompartment to single compartment types. The porous morphology is attributed for the strong microphase segregation between the two incompatible polymer block (pFcMA/ pPVBE and pFcMA / pNaSS) which was further investigated for redox-responsive ness study owing to the presence of ferrocenyl block. It was found out that the pores on the micellar wall can be reversibly on-off triggered by redox response and thus can be considered highly useful to enact as a smart host.

CHAPTER 8

This chapter deals with summery and conclusion of the whole thesis work in addition future scopes of these work are also outlined.

8.2. Conclusions

In a conclusion note, we can say that we have successfully synthesized pendant

ferrocenyl polymers and utilized those as an efficient burn rate catalyst and redox-responsive material. Here are some conclusive points those are outlined based on the work carried out for this thesis work (**Chapter 3** to **Chapter 7**).

1. Viscosity build-up rate for PVF-*g*-HTPB-DNB were successfully controlled by incorporating a suitable functionality, DNB at the terminal end of HTPB backbone which was also theoretically proven.
2. In addition, DNB enhanced segmental compatibility between hard and soft segment of PVF-*g*-HTPB-DNB and resulted a very significant improvement in mechanical properties of the PU film.
3. With 18% increment in burn rate compared to HTPB-DNB, PVF-*g*-HTPB-DNB is expected to be a suitable binder cum burn rate catalyst.
4. Almost a similar trend was observed alike for PVF-*g*-HTPB-DNB after functionalization with DNB at the end in case of a ferrocenylsilane tethered HTPB i.e, FPDS-*g*-HTPB-DNB.
5. Even though viscosity build-up rate was not controlled but with significant improvement in mechanical properties for PU film as well as 10% increment in burn rate of CSP than HTPB-DNB, FPDS-*g*-HTPB-DNB also has potential to be a worthy binder cum burn rate catalyst.
6. Furthermore, pFcMA polymer brushes were effectively grown on the SiNP surface by following SI-RAFT polymerization technique.
7. The redox-responsiveness of the pFcMA polymer brushes were ascertained by UV-visible spectroscopy and thus pFcMA-*g*-SiNP particle was entitled as a smart nanosurface which are under inspection at present for its effectiveness as a DNA-topoisomerase inhibitor.
8. To make use of this silica template for the synthesis of a hollow polymer nanocapsules, pFcMA based block and random copolymers were designed on the particle surface in such a way that after chemically crosslinking the polymer chains, the silica was easily etched out to create the hollow cavity surrounded with ferrocenyl copolymer shell.
9. To make a fuel-cum burn rate catalyst, the hollow cavity further used to encapsulate *in-situ* synthesized Al nanoparticles to make Al-NP/ HPN nanocomposite.

which can be a very potential additives in composite solid propellant applications.

10. In the final chapter a variety of chain length of pendant pFcMA based homopolymers and block copolymers were synthesized and their morphology in solution was explored by employing heat-cool process exactly in similar way with CDSA technique.

11. We have achieved complex porous multicompartment micelles, vesicles as well as fibre types morphology and theses vesicle morphologies was further subjected to redox-responsive analysis which made us to conclude to have a switchable pores on the vesicle membrane wall.

12. Till today CDSA technique has been limited to only main-chain ferrocenyl based polymers but our investigation reveals that this technique equally effective to achieve very complex intricate morphologies even for pendant ferrocenyl polymers.

8.3. Scope for future work

This thesis addresses the effectiveness of pendant ferrocenyl polymers as a burn rate catalyst as well as redox responsive material by expecting to create the possibilities for commercialization of ferrocene based polymers. Our findings reveal the fair approaches to resolve many issues related to ferrocenyl polymers while using as a burn rate catalyst in CSP, also explores a new direction to design the complex structural motifs with switchable properties triggered *via* redox-response. And, we presume that our analysis based on the work was presented in this thesis opens up a vast area to be worked for the advancement of ferrocene containing polymer materials. Some of these scopes are mentioned below which are essential to be addressed by the researchers in future.

1. Efforts may be made on to check whether the placement of a suitable functionality at the end position of HTPB backbone, able to improve the various physical properties specially viscosity build-up rate and mechanical properties for other reported ferrocenyl functionalized at the vinylic position of HTPB.

2. The reaction condition for grafting of ferrocenyl materials can be optimized like concentration of the precursor ferrocenyl monomer can be even decreased compared to

what we have used in **Chapter 3** to achieve better viscosity value by targeting to acquire higher burn rate in the final propellant formulation. In addition, designing of a new ferrocene based HTPB as a binder cum burn rate catalyst is always desirable preferably with modification at the end of the HTPB backbone.

3. Ferrocenyl derivatives are well known to be used in variety of application including anti-malaria and anti-cancer drug. Various new kind of ferrocenyl monomer can be designed on the silica nanoparticle surface the way we did in **Chapter 5** so that with the beneficial of surface grafted polymers having redox-responsive properties, many smart materials can be developed as per requirement.

4. We have synthesized a hollow polymer nanocapsules (HPN) with ferrocenyl copolymer shell and encapsulated with Al nanoparticles (Al-NP). The final yield of the Al-NP/ HPN nanocomposite is too less to proceed further for analysing its efficiency as a fuel-cum burn rate catalyst in the binder formulation in CSP. Therefore, there is a huge scope to fabricate the HPN exactly in a fashion we have pursued mentioned in **Chapter 6** by increasing the SiNP core size together with increasing the copolymer chain length.

5. The HPN can also be constructed with newly designed ferrocene based copolymers where the nature of crosslinking can be varied from chemical to photocrosslinking as because the yield of the final HPN also related with better crosslinking of the polymer chains.

6. In the final chapter we have employed CDSA technique on the pendant ferrocenyl block copolymers and successfully achieved porous multicompartment morphologies and our proposed methodology further need to be established with other ferrocenyl based block copolymers.

Appendix

Appendix I

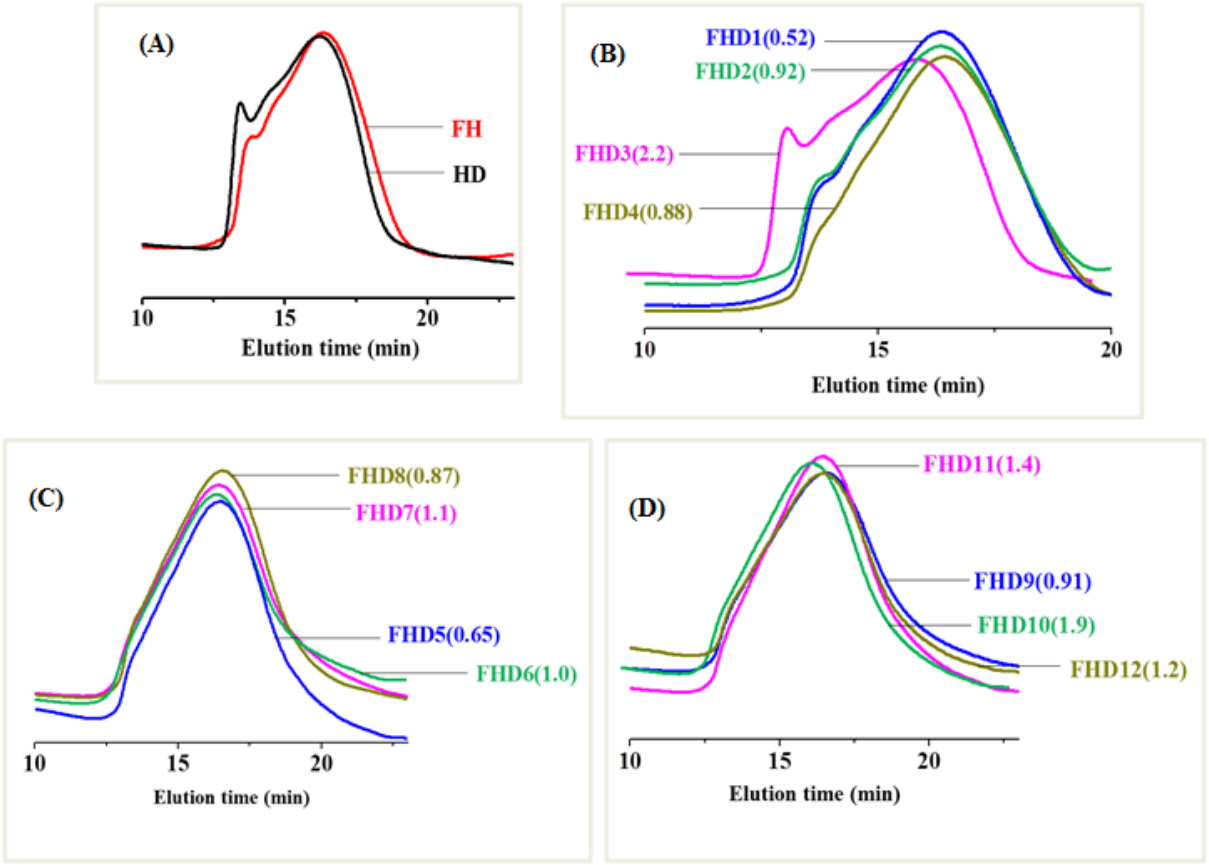

Appendix I-Figure 3.1: *GPC chromatogram of (A) HTPB-DNB (HD) and PVF-g-HTPB (FH), (B) HTPB-g-PVF-DNB (FHD1-4) (C) PVF-g-HTPB-DNB (FHD 5-8) (D) PVF-g-HTPB-DNB (FHD9-12). FHD samples Fe content are indicated in the parenthesis after the sample identification.*

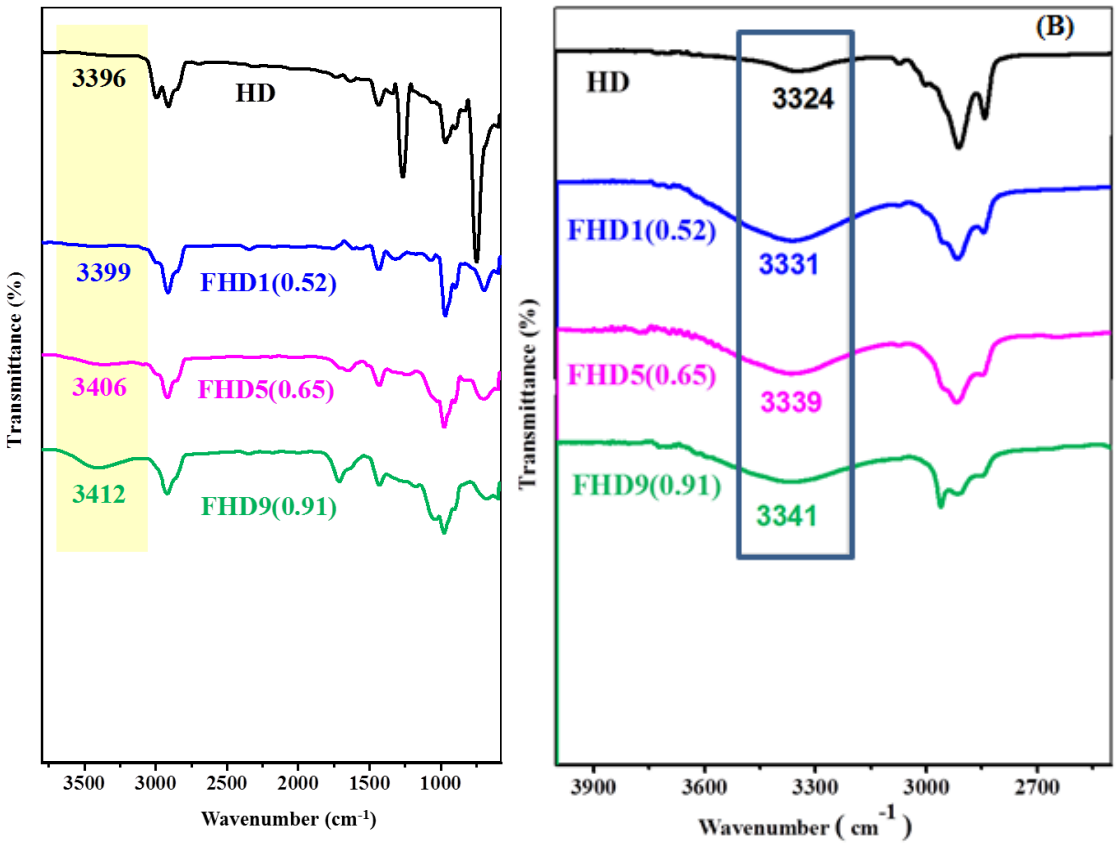

Appendix I-Figure 3.2: *FT-IR spectra of (A) HTPB-DNB (HD) and PVF-g-HTPB-DNB (FHD) and (B) HTPB-DNB-PU (HDPU) and PVF-g-HTPB-DNB-PUs (FHDPUs). FHD and FHDPU samples Fe content are indicated in the parenthesis after the sample identification.*

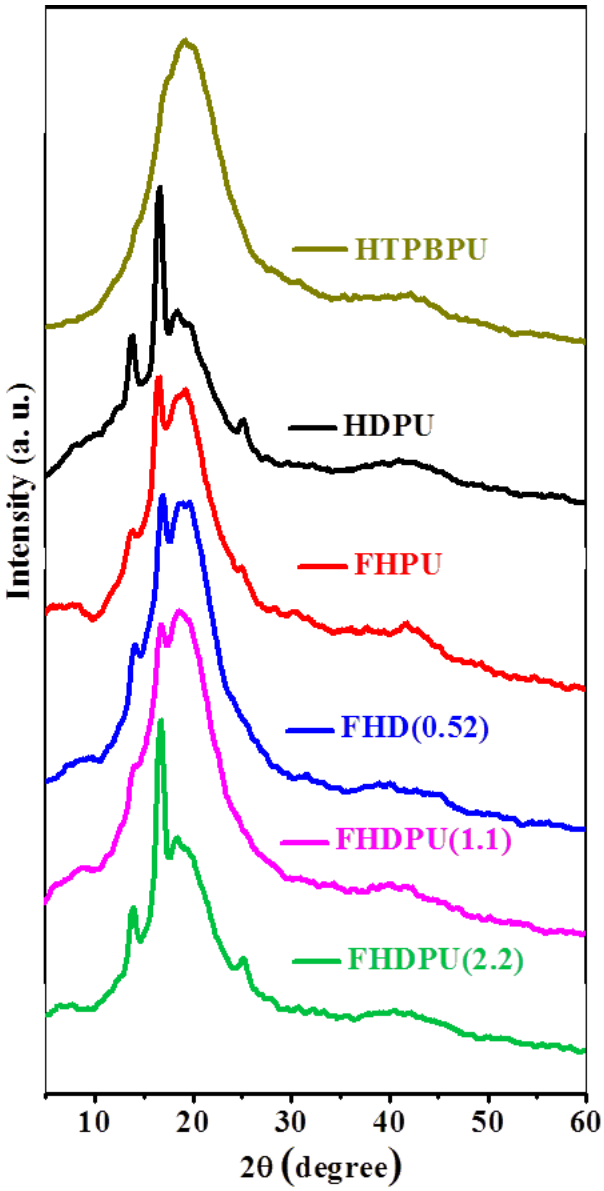

Appendix I-Figure 3.3: *Wide angle X-ray diffraction pattern of HTPB and all modified HTPB polyurethanes: HDPU, FHPU, FHDPUs.*

Appendix II

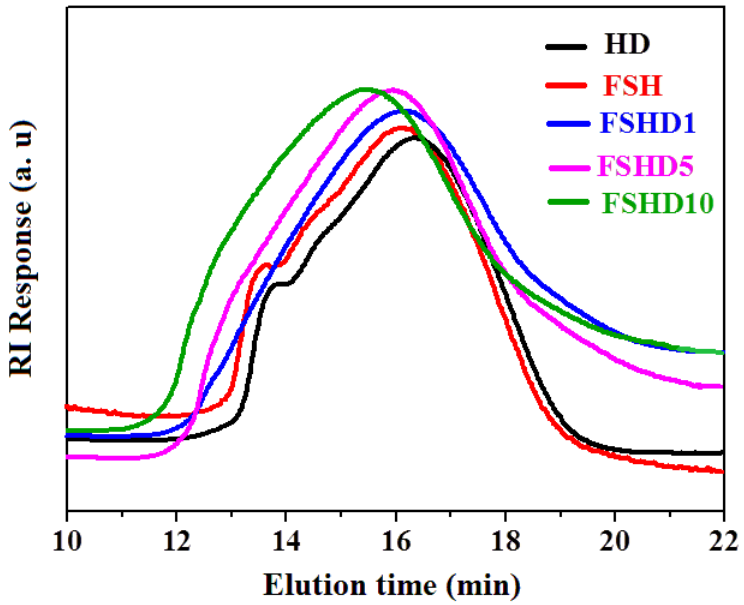

Appendix II-Figure 4.1: *GPC chromatograms of HTPB-DNB (HD), FPDS-g-HTPB (FSH) and FPDS-g-HTPB-DNB (FSHD) samples.*

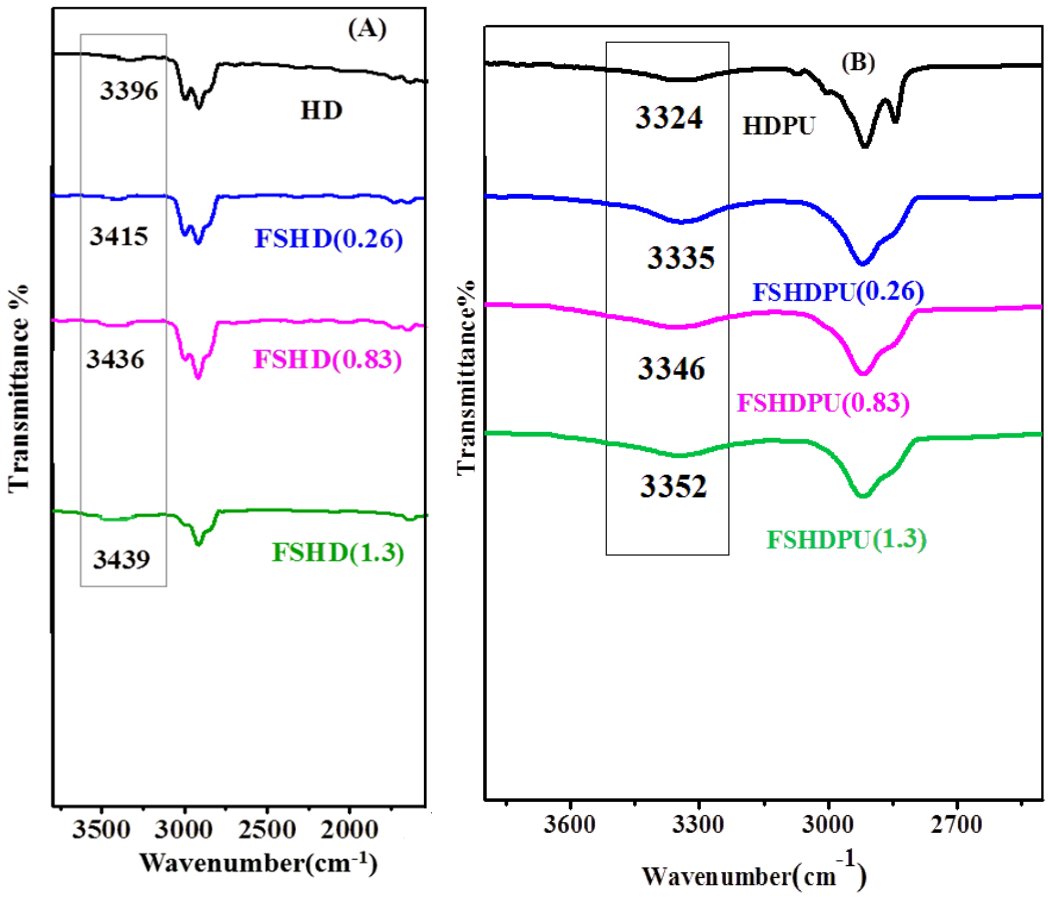

Appendix II-Figure 4.2: *FT-IR spectra of (A) HTPB-DNB (HD) and FPDS-g-HTPB-DNB (FSHD) and (B) HTPB-DNB-PU (HDPU) and FPDS-g-HTPB-DNB-PUs (FSHDPUs). FSHD and FSHDPU samples Fe content are indicated in the parenthesis after the sample identification.*

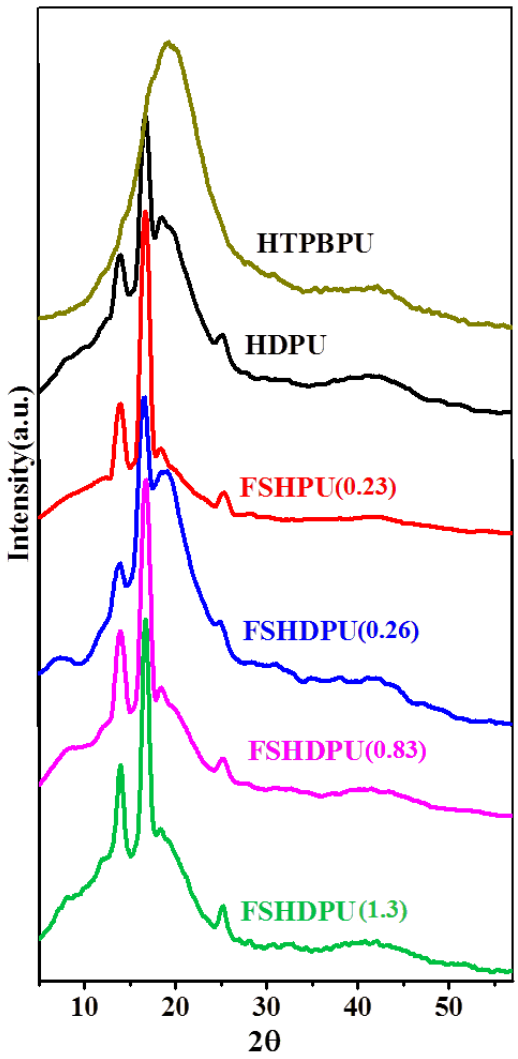

Appendix II-Figure 4.3: *Wide angle X-ray diffraction pattern of HTPB and all modified HTPB polyurethanes: HDPU, FSHPU, FSHDPUs. FSHD and FSHDPU samples Fe content are indicated in the parenthesis after the sample identification.*

Appendix III

Appendix III-Table 6.1: *Monomer feed ratio, samples abbreviations and various parameters obtained from GPC analysis for different copolymers grafted over SiNP surface.*

(FcMa:PVBE) (wt %)	Sample name[a]	$\overline{M_n}$ targeted[b]	$\overline{M_n}$ achieved[c]	Đ[d]
1:1	P_1Q_1	10K10K	18,851	1.27
1:1	Q_1P_1	10K10K	17,647	1.3
1:1	rP_1Q_1	10K10K	21,496	1.4
1:3	P_1Q_3	10K30K	32,304	1.35
1:3	Q_3P_1	30K10K	28,326	1.3
1:3	rP_1Q_3	10K30K	42,394	1.44
3:1	P_3Q_1	10K3K	10,455	1.34
3:1	Q_1P_3	3K10K	10,461	1.24
3:1	rP_3Q_1	10K3K	13,038	1.31

[a]P corresponds to FcMA block and Q is PVBE block. The detailed of the sample abbreviations are discussed in the experimental section [b] Targeted number average molecular weight ($\overline{M_n}$) calculated based on the equation often used in RAFT polymerization and K indicates thousands. [c] $\overline{M_n}$ and [d] dispersity (Đ) are obtained from GPC analysis.

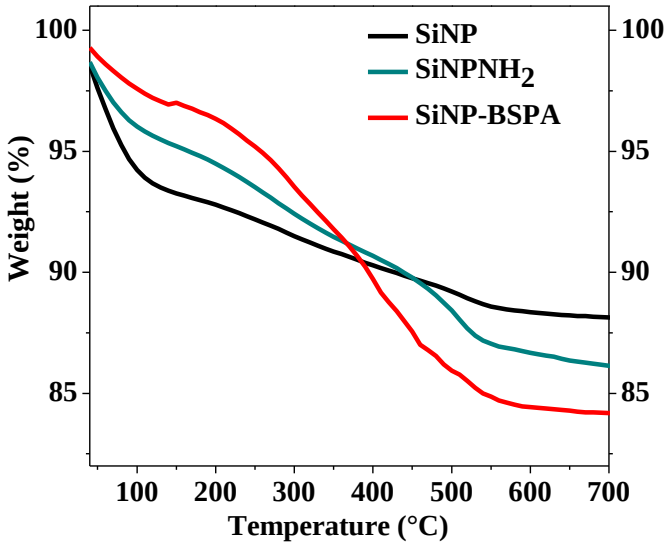

Appendix III-Figure 6.1: *TGA plots of SiNP, SiNP-NH_2 and SiNP-BSPA.*

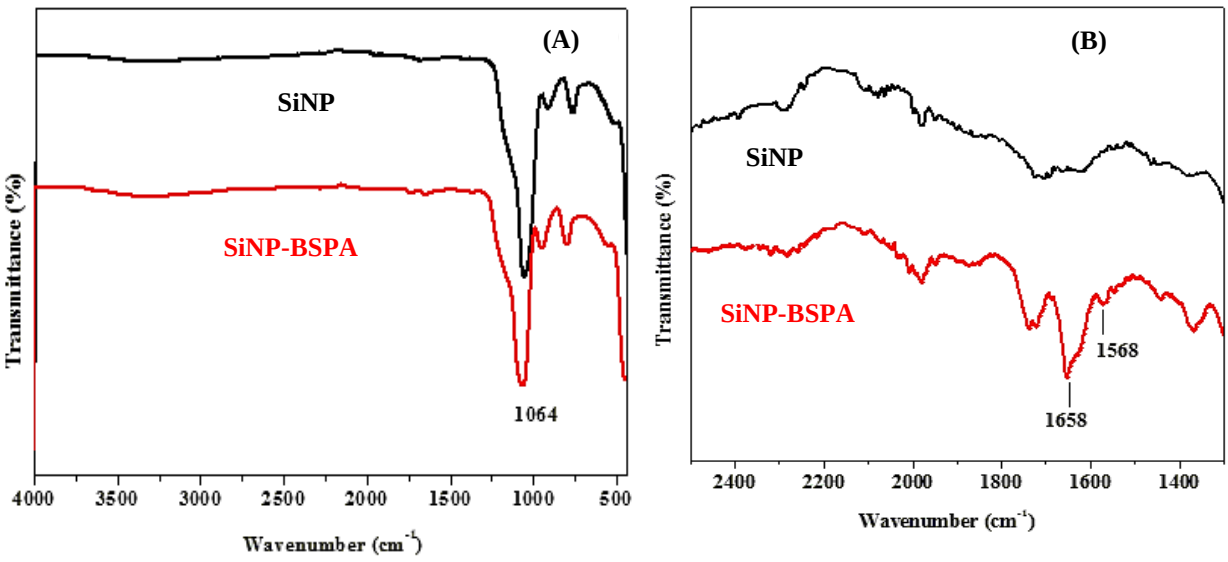

Appendix III-Figure 6.2: *FTIR spectra (A) of SiNP and SiNP-BSPA and (B) zoomed portion to show the BSPA functional group peaks.*

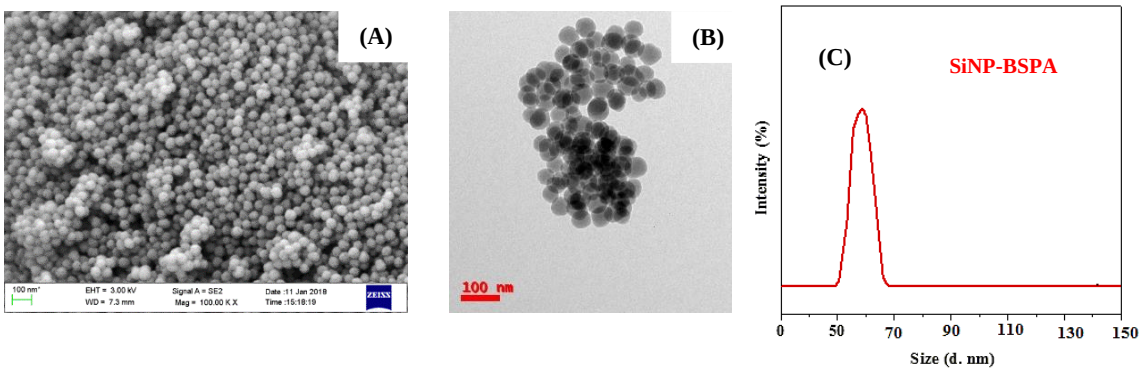

Appendix III-Figure 6.3: *(A) FESEM, (B) TEM images and (C) DLS plot of SiNP-BSPA.*

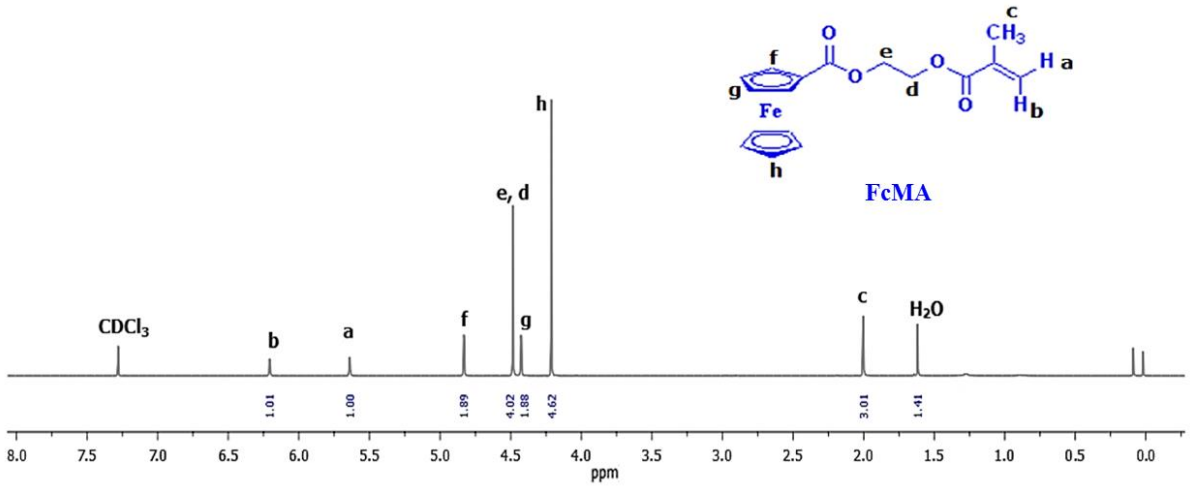

Appendix III-Figure 6.4: *^{1}H-NMR spectra of 2-(methacryloyloxy)ethyl ferrocenecarboxylate (FcMA)*

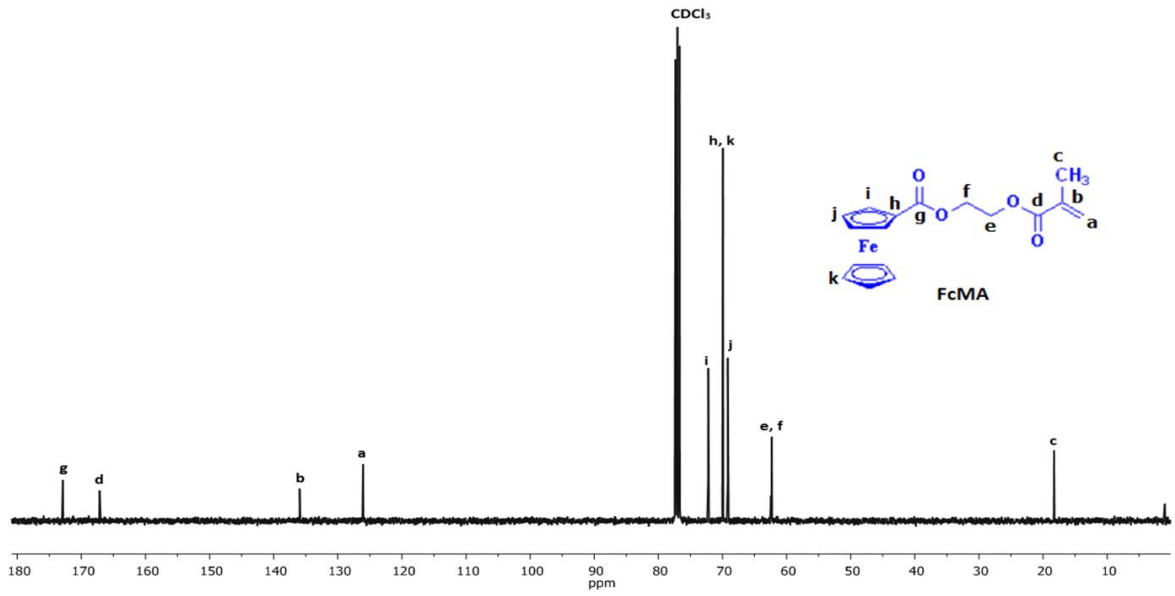

Appendix III-Figure 6.5: *^{13}C-NMR spectra of FcMA*

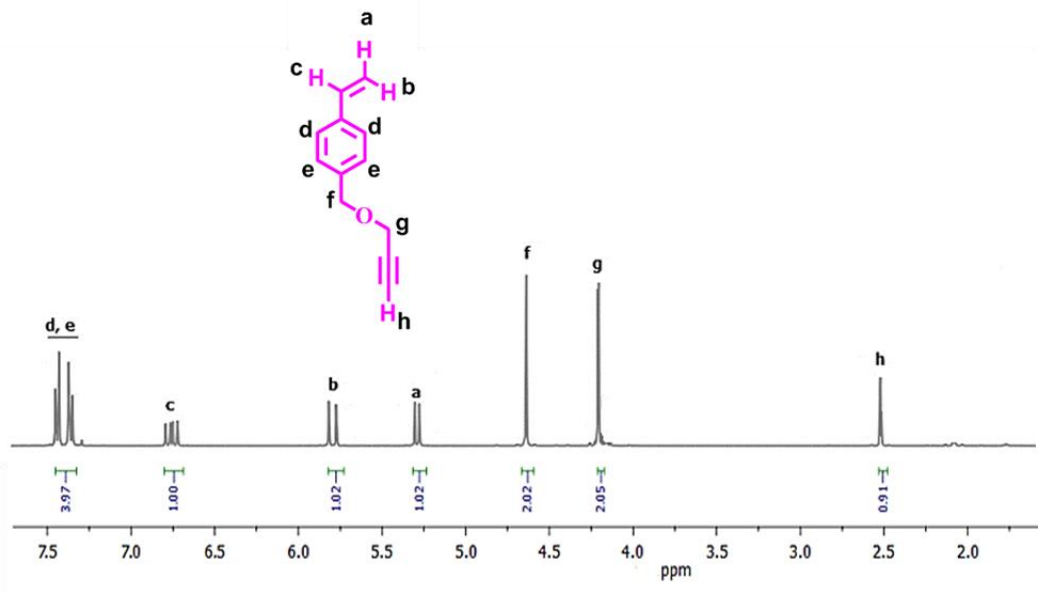

Appendix III-Figure 6.6: *^{1}H-NMR spectra of Propargyl 4-vinylbenzyl ether (PVBE)*

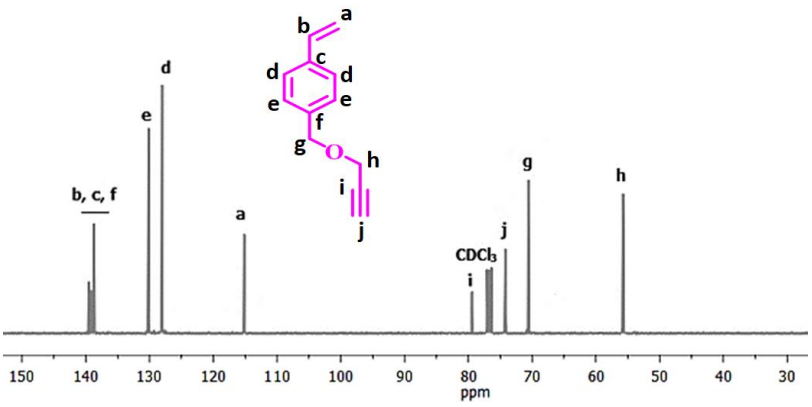

Appendix III-Figure 6.7: *^{13}C-NMR spectra of PVBE*

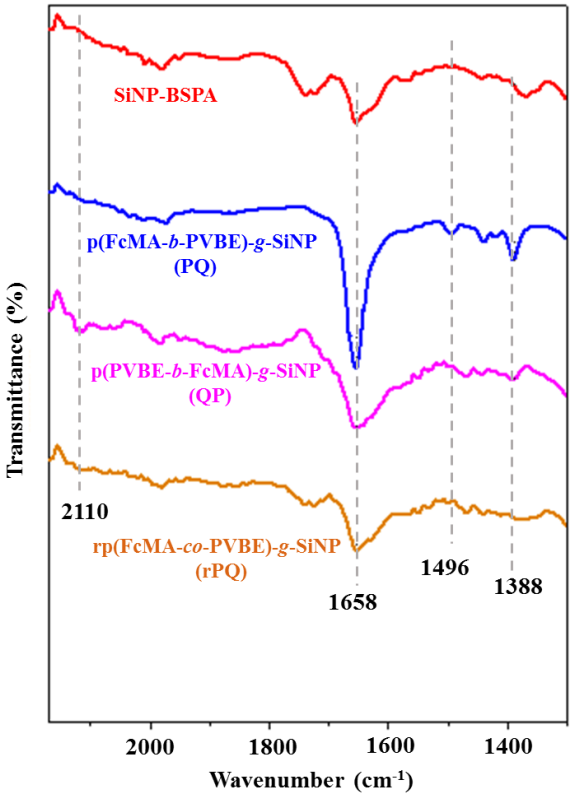

Appendix III-Figure 6.8: *A comparison of FT-IR spectra of copolymers grafted on SiNP surface along with CTA anchored SiNP.*

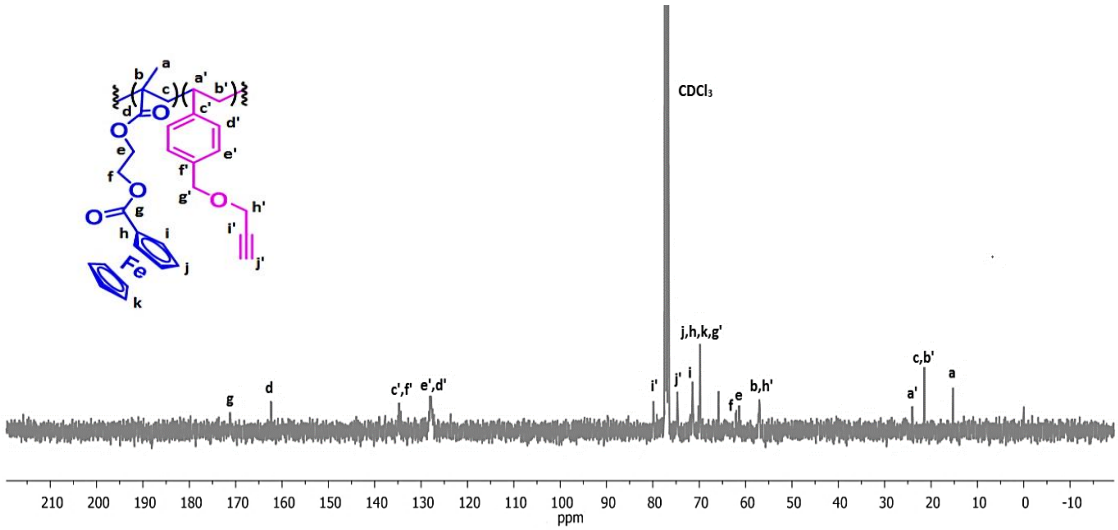

Appendix III-Figure 6.9: *^{13}C-NMR spectrum of random copolymer grafted on SiNP surface. All the peak position are assigned as indicated in the structure and the spectrum.*

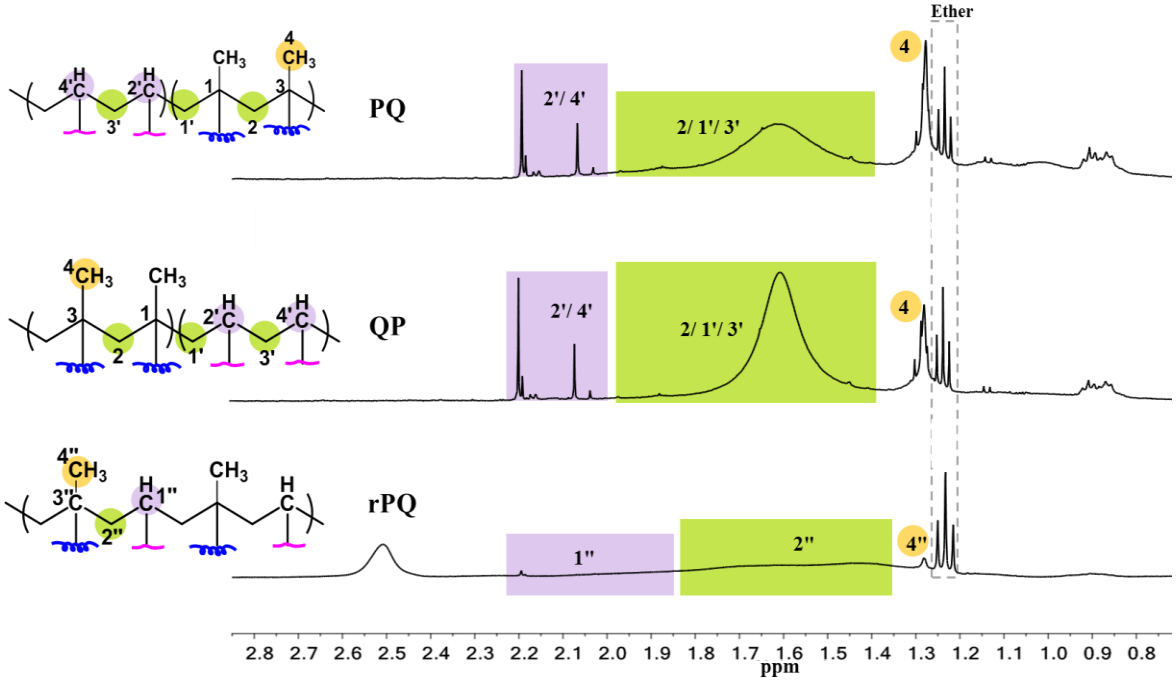

Appendix III-Figure 6.10: *Comparative analysis of ^{1}H-NMR spectra of copolymers to differentiate structurally a block and a random copolymer. All the peak intensities in all the spectra are normalized with respect to solvent peak.*

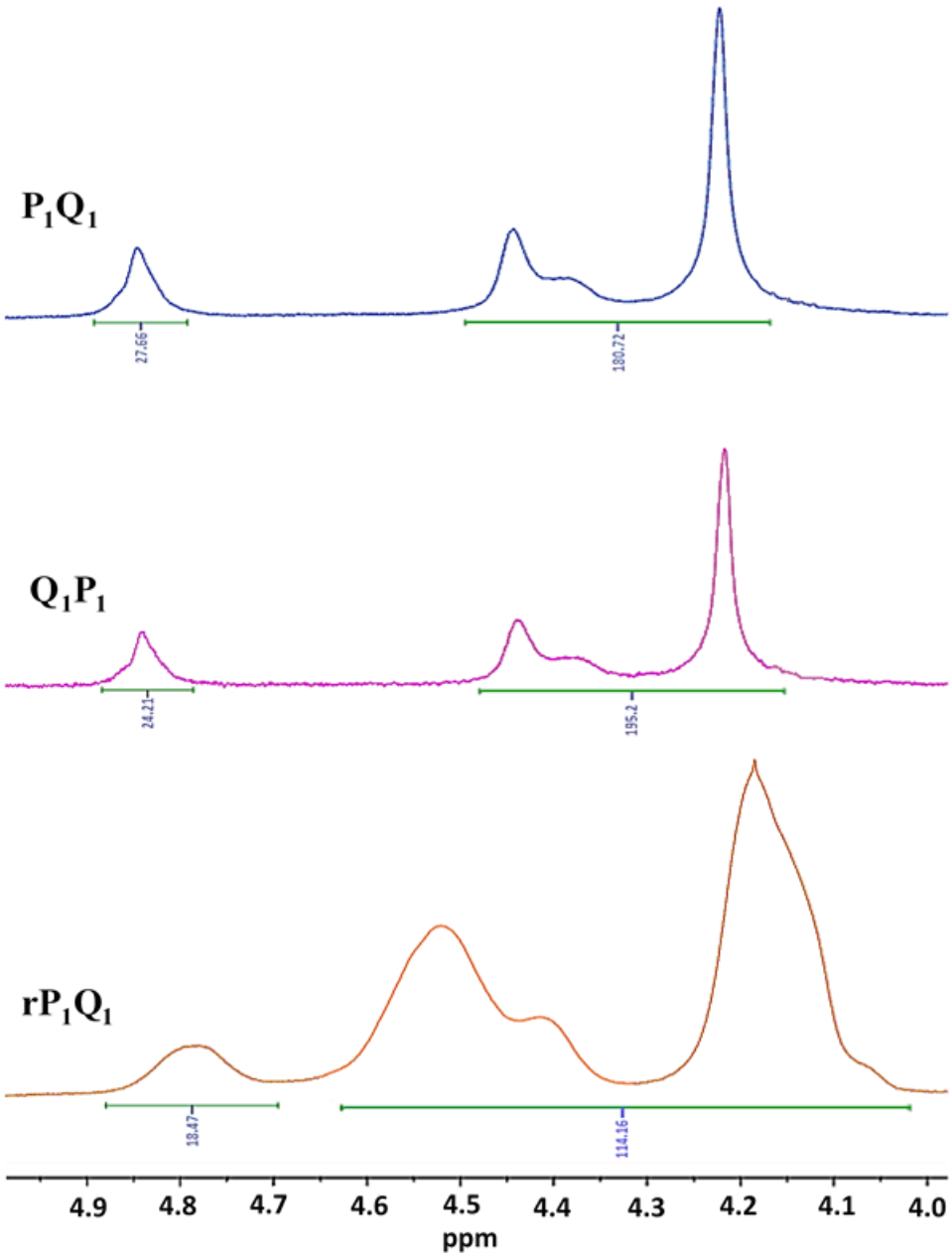

Appendix III-Figure 6.11: *Peak integrals of ^{1}H-NMR spectra of copolymers for calculating the molecular weight, degree of polymerization and % of monomer conversion.*

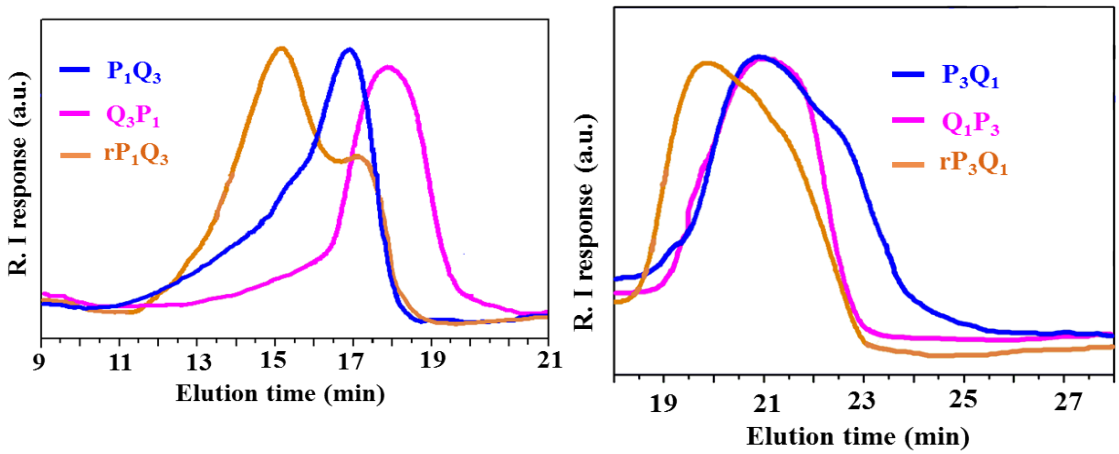

Appendix III-Figure 6.12: *GPC chromatograms of copolymers (with monomers ratio of 1:3 and 3:1) grafted on the particle surface.*

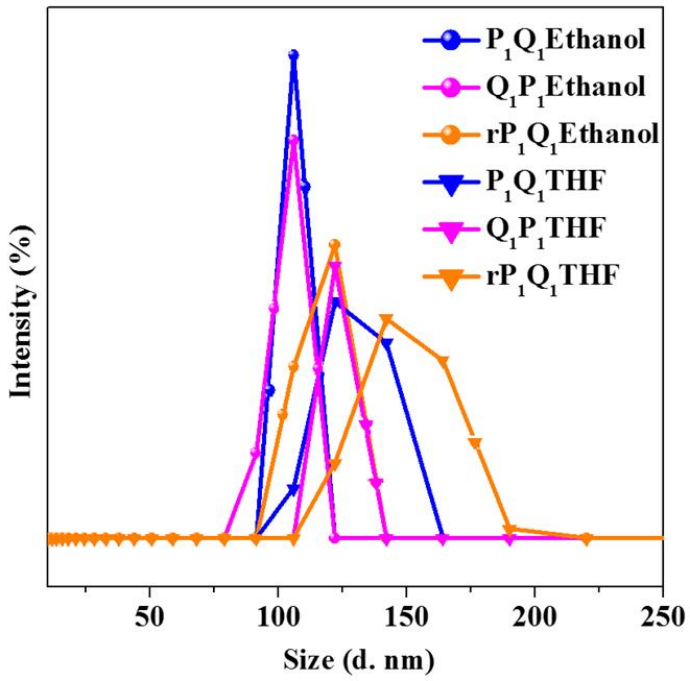

Appendix III-Figure 6.13: *DLS plots of copolymers grafted SiNP in THF and ethanol.*

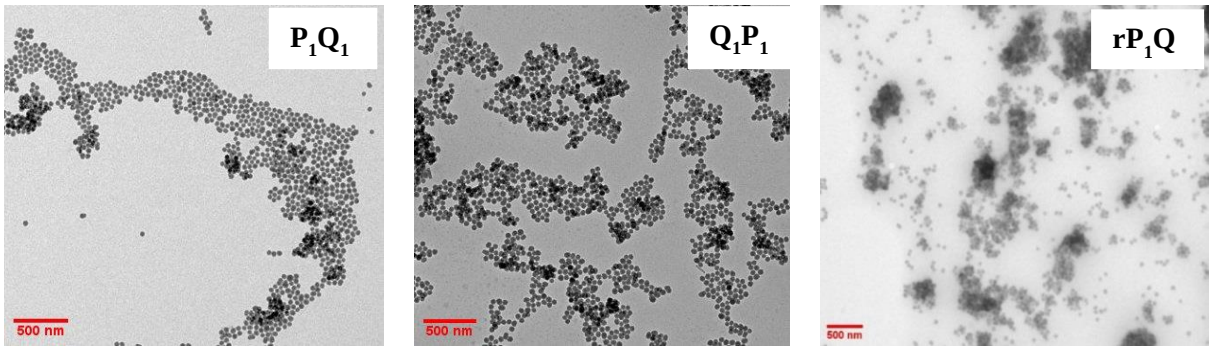

Appendix III-Figure 6.14: *TEM images (lower magnifications in comparison to Figure 3 of the manuscript) of copolymer grafted SiNP to see the self-assembled/ aggregated features of copolymers brush tethered particles.*

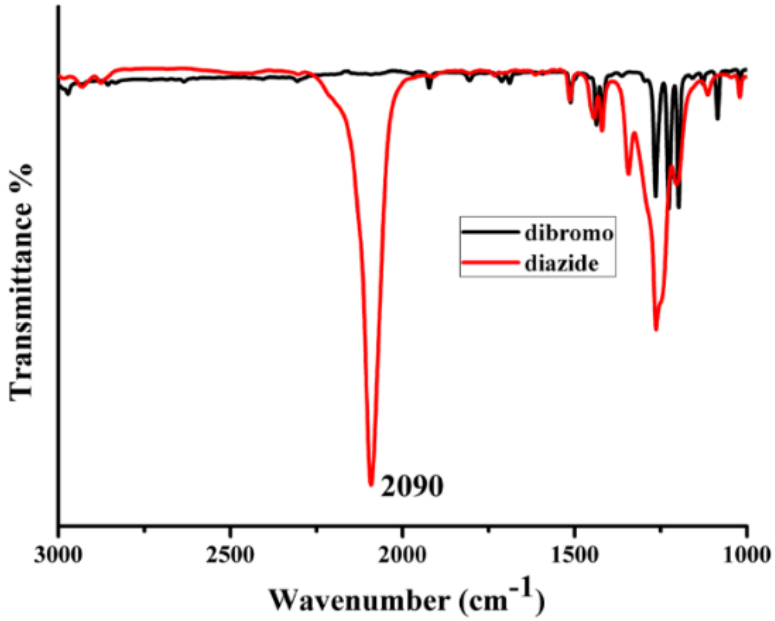

Appendix III-Figure 6.15: *IR spectra of 1,4-bis(azidomethyl)benzene.*

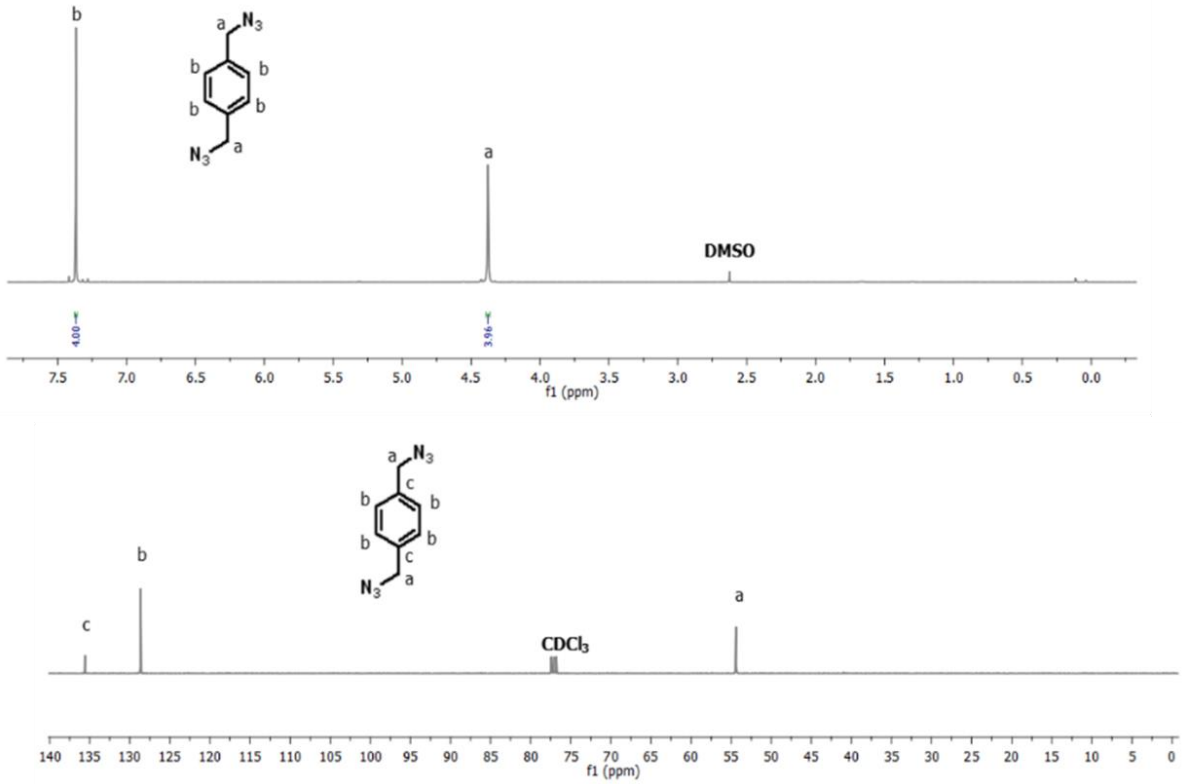

Appendix III-Figure 6.16: *^{1}H-NMR and ^{13}C-NMR spectra of 1,4-bis(azidomethyl)benzene.*

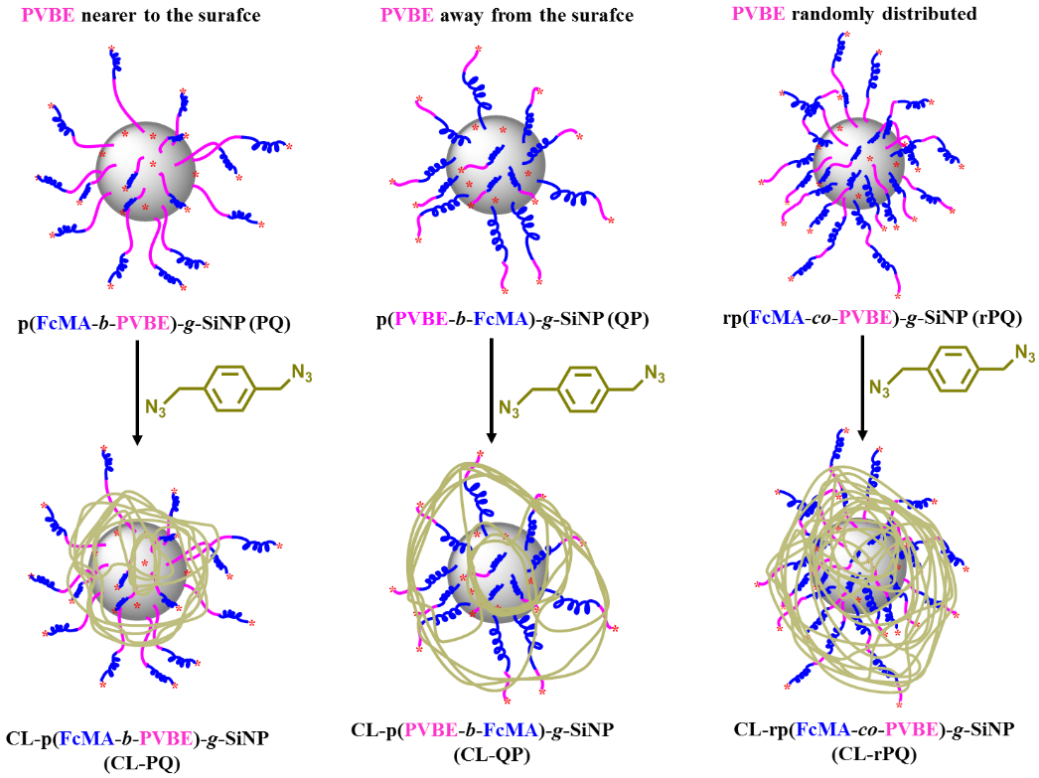

Appendix III-Figure 6.17(A): *A pictorial presentation crosslinking proces and structural differences arises in the cross-linked chain grafted SiNP because of the difference in the grafted chain sequence.*

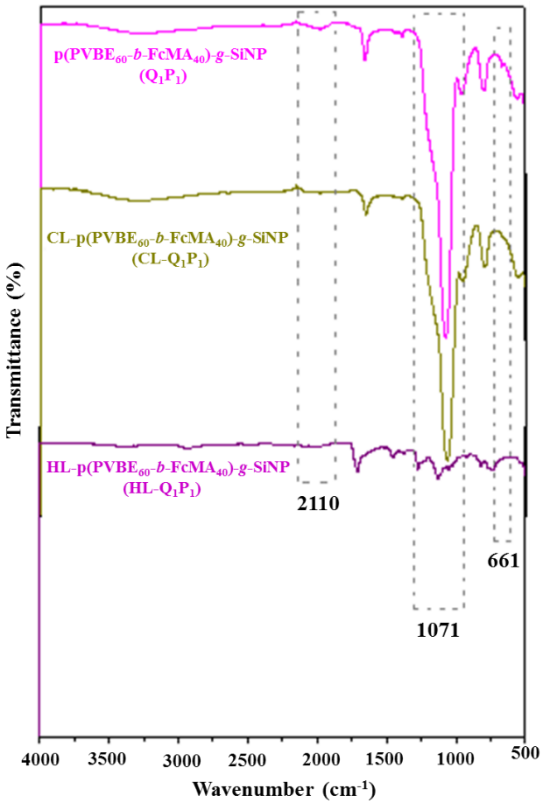

Appendix III-Figure 6.17 (B): *IR spectra of p(FcMA$_{40}$-b-PVBE$_{60}$)-g-SiNP (Q$_1$P$_1$), cross-linked p(FcMA$_{40}$-b-PVBE$_{60}$)-g-SiNP (CL-Q$_1$P$_1$) and hollow p(FcMA$_{40}$-b-PVBE$_{60}$)-g-SiNP (HL-Q$_1$P$_1$).*

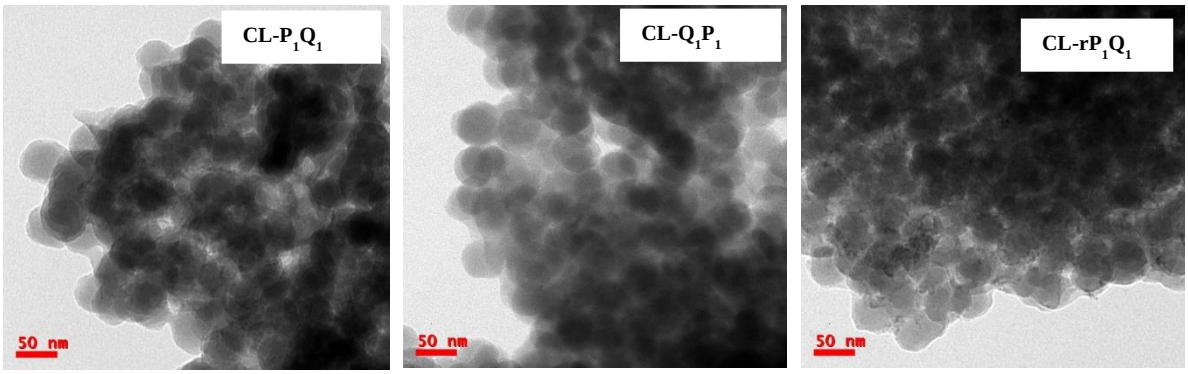

Appendix III-Figure 6.18: *TEM images of cross-linked copolymer grafted SiNP.*

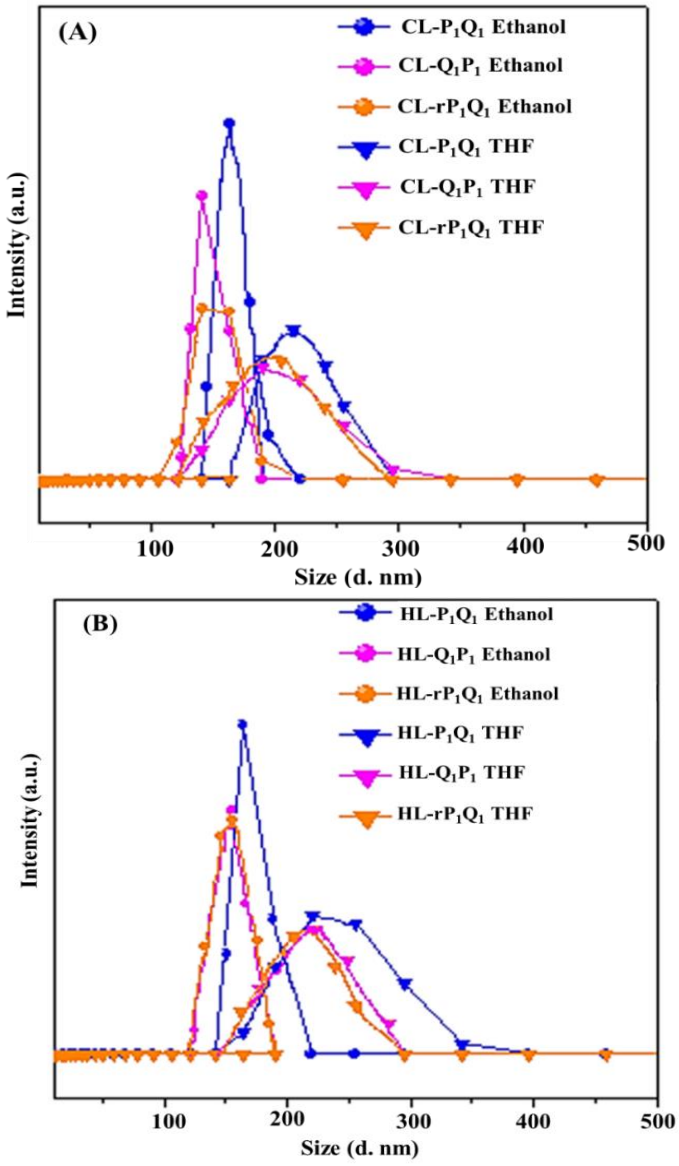

Appendix III-Figure 6.19: *DLS plots of (A) cross-linked and (B) hollow particles dispersed in THF and ethanol.*

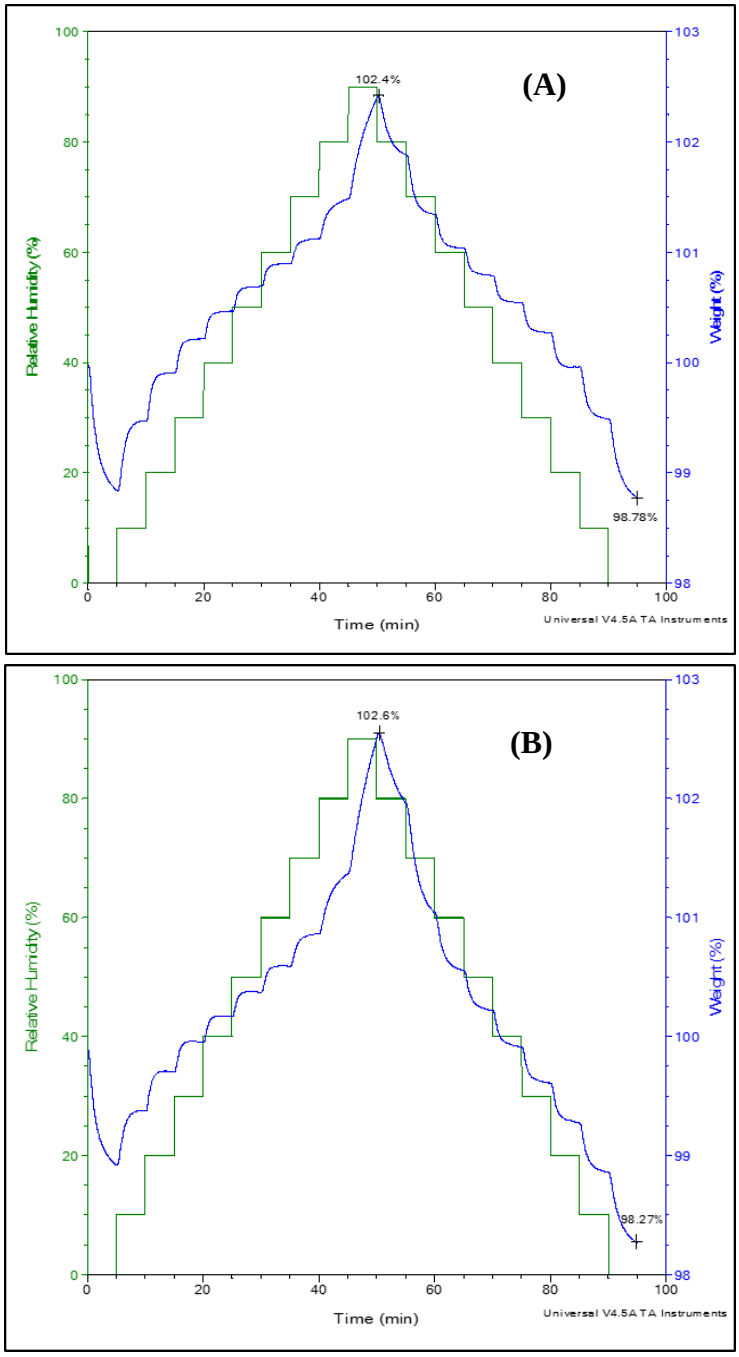

Appendix III-Figure 6.20: *DVS plots of (A) p(PVBE$_{43}$-b-FcMA$_{57}$)-g-SiNP (P_1Q_1) and (B) CL-P_1Q_1 samples. The absorbed water for P_1Q_1 and CL-P_1Q_1 are 0.9 and 1.25 wt%, respectively in the RH range 70-92% which means the net increment in water adsorption upon cross-linking is 0.35 wt%.*

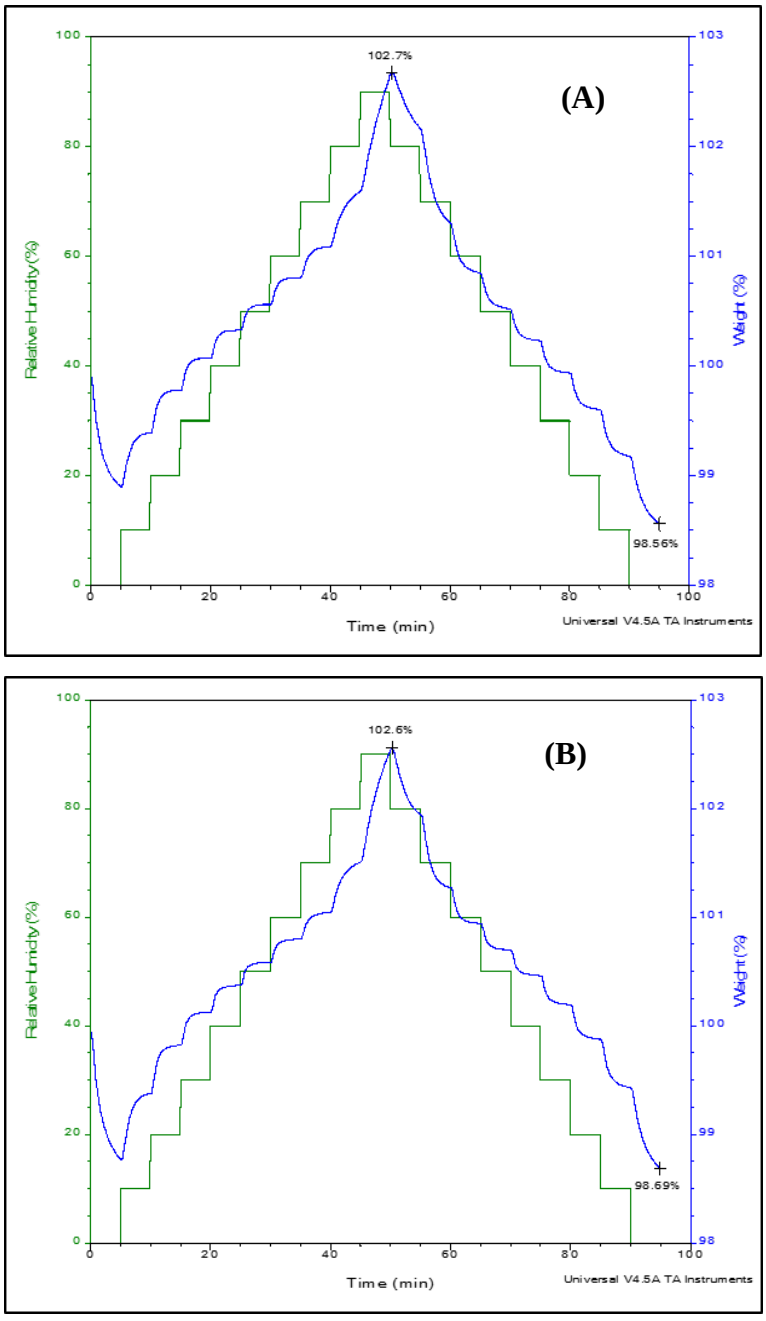

Appendix III-Figure 6.21: *DVS plots of (A) p(FcMA$_{40}$-b-PVBE$_{60}$)-g-SiNP (Q$_1$P$_1$) and (B) CL-Q$_1$P$_1$ samples. The adsorbed water for Q$_1$P$_1$ and CL-Q$_1$P$_1$ are 1.07 and 1.1 wt%, respectively in the RH range 70-92% which means the net increment in water adsorption upon cross-linking is 0.03 wt%.*

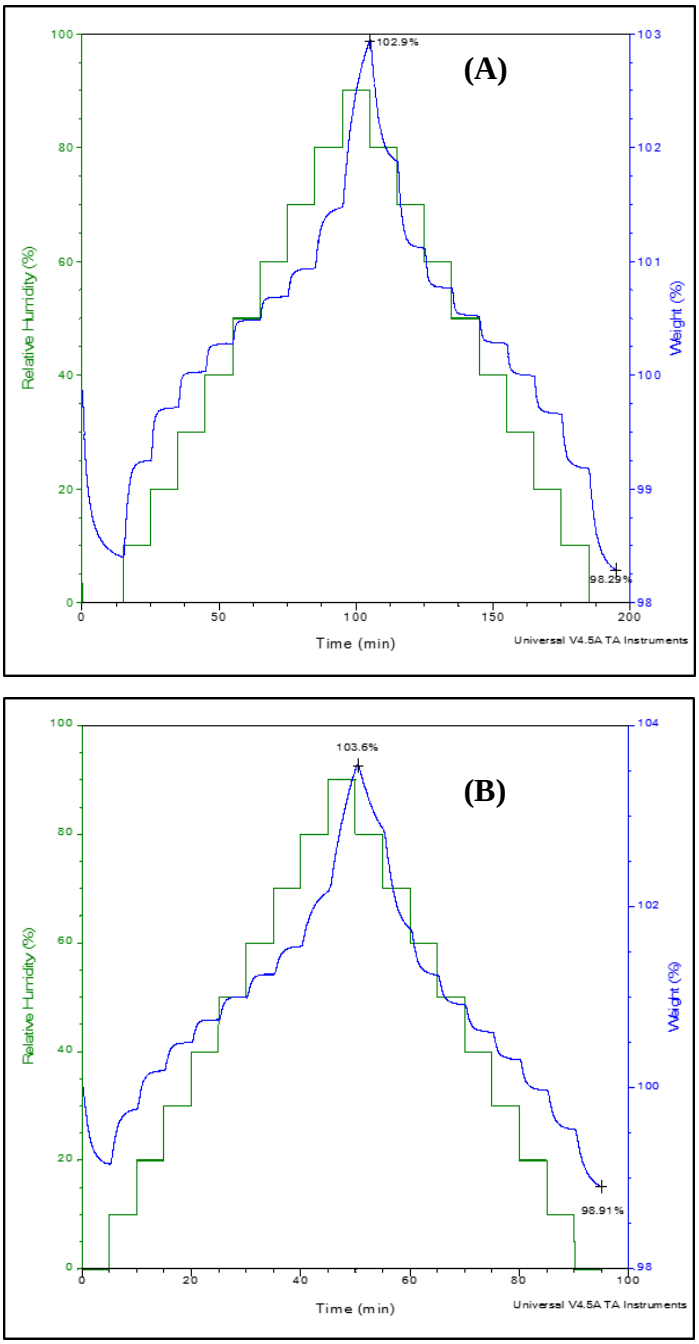

Appendix III-Figure 6.22: *DVS plots of (A) rp(PVBE$_{37}$-co-FcMA$_{63}$)-g-SiNP (rP$_1$Q$_1$) and (B) CL-rP$_1$Q$_1$ samples. The adsorbed water for rP$_1$Q$_1$ and CL-rP$_1$Q$_1$ are 1.44 and 1.49 wt%, respectively in the RH range 70-92% which means the net increment in water adsorption upon cross-linking is 0.05 wt%.*

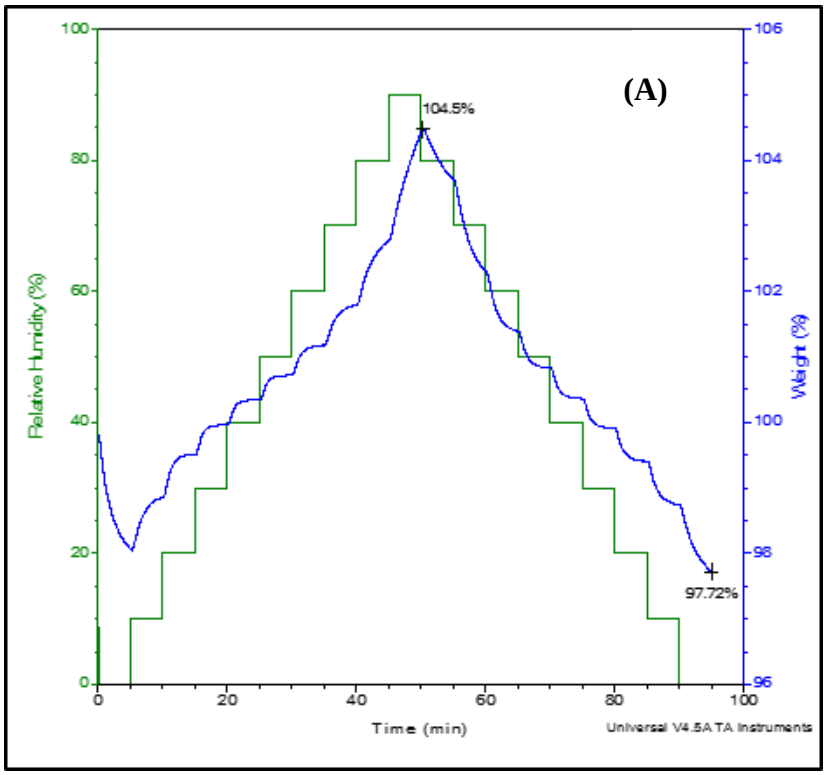
(A)
104.5%
97.72%
Relative Humidity (%)
Weight (%)
Time (min)
Universal V4.5A TA Instruments

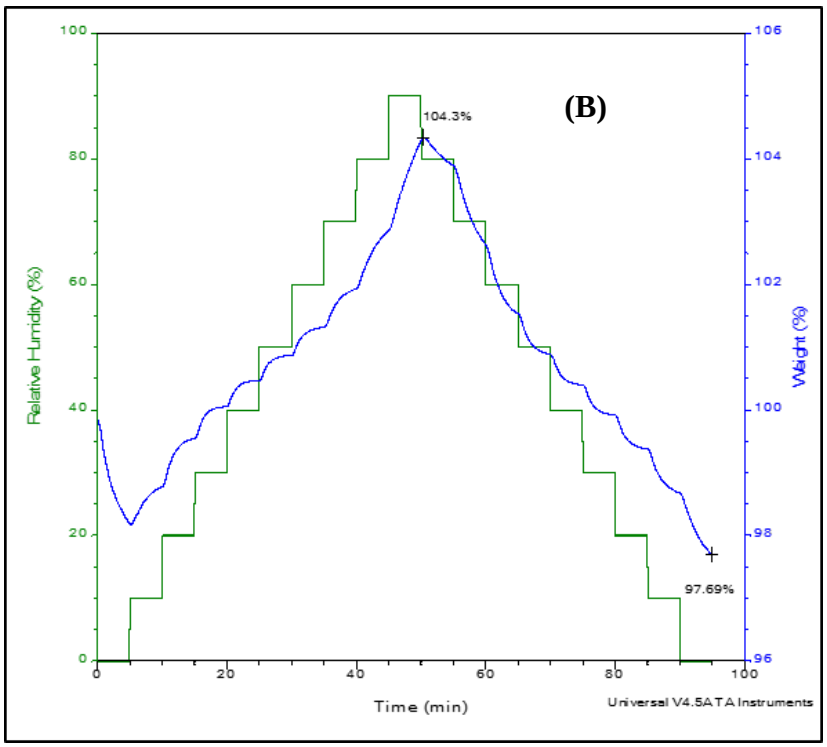
(B)
104.3%
97.69%
Relative Humidity (%)
Weight (%)
Time (min)
Universal V4.5A TA Instruments

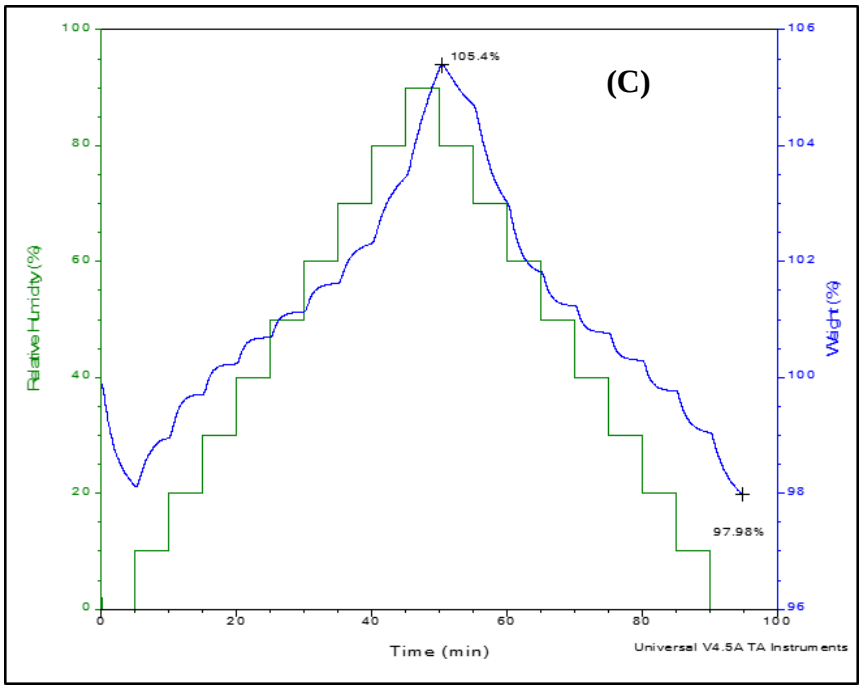

Appendix III-Figure 6.23: *DVS plots of (A) HL-P_1Q_1 (B) HL-Q_1P_1 (C) HL-r P_1Q_1. The net increment in HL-P_1Q_1, HL-Q_1P_1 and HL-rP_1Q_1 water adsorption upon cross-linking are 0.48, 0.41 and 1.99 wt%, respectively in the RH range 70-92%.*

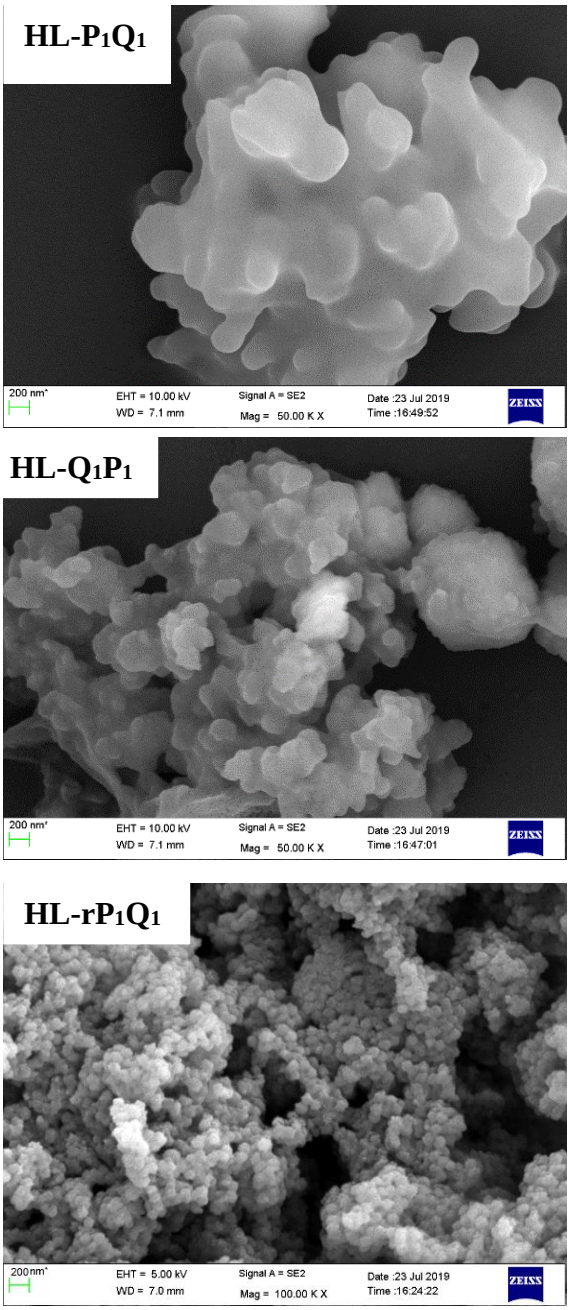

Appendix III-Figure 6.24: *FESEM images of HL particles.*

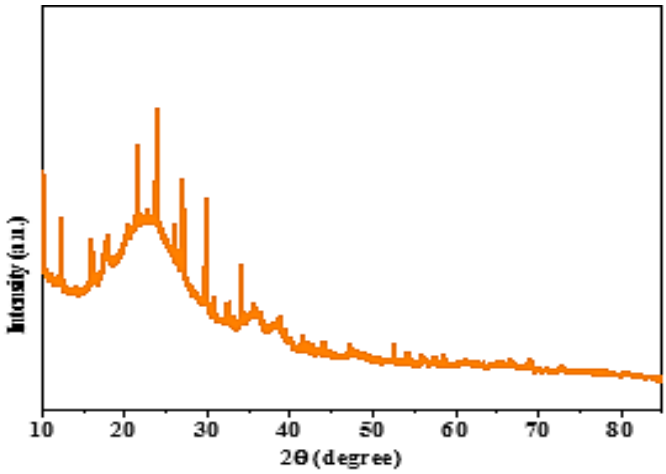

Appendix III-Figure 6.25: *PXRD plot of Al-NP/ CL-p(FcMA$_{63}$-co- PVBE$_{37}$) nanocomposite.*

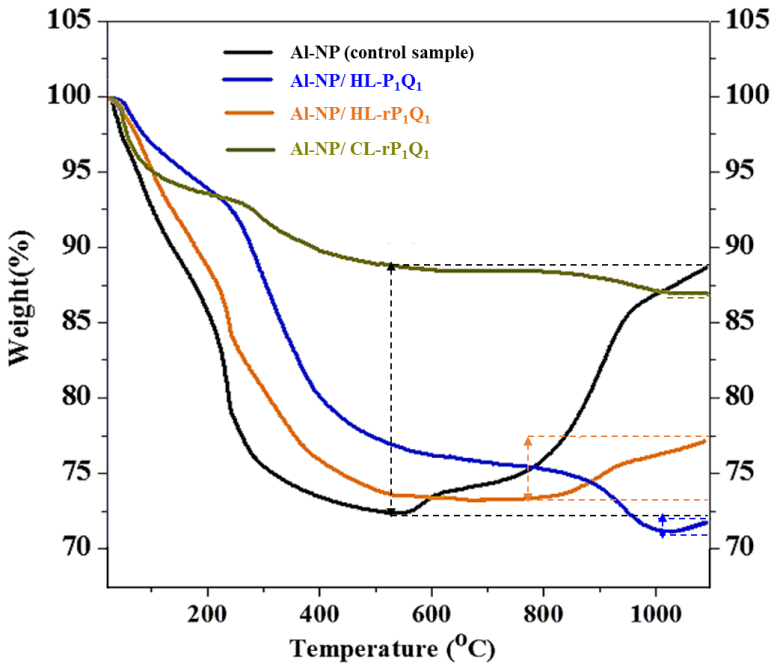

Appendix III-Figure 6.26: *TGA plots of Al (control sample), Al-NP/ HL-p(FcMA$_{57}$-b-PVBE$_{43}$) nanocomposite, Al/ HL-rp(FcMA$_{63}$-co- PVBE$_{37}$) nanocomposite and Al/ CL-rp(FcMA$_{63}$-co-PVBE$_{37}$) nanocomposite. Weight gain is shown in the figure by dotted lines and double sided arrow.*

Publications & Presentations

PUBLICATIONS

Thesis Chapter Publications

1. **M. Dhara**, N. Giri, B. N. Rao, A. K. Patra, P. U. Sastry, M. S. Ingole, T. Jana, Effect of segmental compatibility imposed over metal based polybutadiene polyurethane, ***Euro. Polym. J.***, **2020**, *122* 109380.

2. **M. Dhara**, N. Giri, A. Dutta, A. K. Patra, P. U. Sastry, M. S. Ingole, T. Jana, Enhancement of segmental compatibility and tuning the structure-property relationship of ferrocenylsilane grafted polybutadiene polyurethane, ***Polymer***, **2020**, *204*, 122807.

3. **M. Dhara**, and T. Jana, Ferroceneyl polymer grafted smart nano surface *via* surface initiated RAFT polymerization. (To be communicated)

4. **M. Dhara**, S. Rudra, N. Mukherjee and T. Jana, Hollow polymer nanocapsules with ferrocenyl copolymer shell (***Polymer Chemistry*****, 2021,** doi.org/10.1039/D1PY00590A).

5. **M. Dhara**, and T. Jana, Porous multicompartment morphologies of ferrocene containing diblock copolymer. (To be communicated)

Other Publications

6. B. K. Sikder, **M. Dhara**, T. Jana, Hydroxy terminated polybutadiene (HTPB) based polyurethanes, **Indian Patent No.: 333215**.

7. N. Mukherjee, A. Das, **M. Dhara** and T. Jana, Block Copolymer grafted Silica Nanoparticles: Designer Nanofiller for Improving Proton Exchange Membrane Properties. (Communicated to ***ACS Applied Polymer Materials***).

8. MN Ganivada, **M. Dhara** and T. Jana, Various synthetic approaches for the modification of HTPB and their potential applications. (To be communicated)

Note: Only publication numbers 1, 2, 3, 4 and 5 are included in this thesis as Chapter 3, 4, 5, 6 and 7, respectively.

PRESENTATIONS

1. **Poster presented** on "The Effect of Segmental compatibility imposed over Metal based Polybutadiene Polyurethane" at 15th international conference on Polymer Science and Technology conducted by the society for polymer science (India) (**SPSI MACRO, 2018**) at IISER-Pune, Pune, Maharashtra, India.

2. **Poster presented** on "The effect of Segmental Compatibility imposed over Metal based Polybutadiene Polyurethane" during 16th annual in-house symposium (**CHEMFEST, 2019**) at School of Chemistry, University of Hyderabad, Hyderabad, India.

3. **Poster presented** on "Polymers with Pendant Ferrocenyl unit" at INSPIRE Fellowship review meeting-2019 jointly organised by Department of Science & Technology, New Delhi and K L Deemed to be University, held at Guntur, Andhra Pradesh, India.

4. **Oral talk presented** on "Polymeric hollow nanocapsule with ferrocenyl cell as catalyst" at international conference on Functional Materials (**ICFM, 2020**) conducted by Materials science centre, IIT Kharagpur, at Kharagpur, West Bengal, India.

5. **Oral talk presented** on "Polymeric hollow nanocapsule with ferrocenyl cell as catalyst" 17th annual in-house symposium (**CHEMFEST, 2020**) at School of Chemistry, University of Hyderabad, Hyderabad, India.

Polymers with Pendant Ferrocenyl units as Burn Rate Catalyst and Redox Responsive Material

by Moumita Dhara

Submission date: 02-Jul-2021 02:38PM (UTC+0530)
Submission ID: 1614886003
File name: Moumita_Dhara.pdf (12.67M)
Word count: 54945
Character count: 288891

12 th. July 2021

Prof. TUSHAR JANA
School of Chemistry
University of Hyderabad
HYDERABAD-500 046. INDIA.

Polymers with Pendant Ferrocenyl units as Burn Rate Catalyst and Redox Responsive Material

ORIGINALITY REPORT

50%	6%	49%	3%
SIMILARITY INDEX	INTERNET SOURCES	PUBLICATIONS	STUDENT PAPERS

PRIMARY SOURCES

1	Moumita Dhara, Somdatta Rudra, Nilanjan Mukherjee, Tushar Jana. "Hollow polymer nanocapsules with ferrocenyl copolymer shell", Polymer Chemistry, 2021 Publication	17%
2	Moumita Dhara, Nitai Giri, Arunava Dutta, A.K. Patra, P.U. Sastry, Mahesh Shrikishan Ingole, Tushar Jana. "Enhancing segmental compatibility and tuning the structure-property relationship in ferrocenylsilane tethered polyurethane", Polymer, 2020 Publication	13%
3	Moumita Dhara, Nitai Giri, B. Narasimha Rao, A.K. Patra, P.U. Sastry, Mahesh Shrikishan Ingole, Tushar Jana. "Effect of segmental compatibility imposed over metal based polybutadiene polyurethane", European Polymer Journal, 2020 Publication	12%

Prof. TUSHAR JANA
School of Chemistry
University of Hyderabad
HYDERABAD-500 046. INDIA.

Prof. TUSHAR JANA
School of Chemistry
University of Hyderabad
HYDERABAD-500 046. INDIA.

Prof. TUSHAR JANA
School of Chemistry
University of Hyderabad
HYDERABAD-500 046. INDIA.

4	Submitted to University of Hyderabad, Hyderabad Student Paper	1 %
5	onlinelibrary.wiley.com Internet Source	1 %
6	pubs.rsc.org Internet Source	<1 %
7	Adam O. Moughton, Marc A. Hillmyer, Timothy P. Lodge. "Multicompartment Block Polymer Micelles", Macromolecules, 2011 Publication	<1 %
8	Pengfei Shi, Yaqing Qu, Chonggao Liu, Habib Khan, Pingchuang Sun, Wangqing Zhang. "Redox-Responsive Multicompartment Vesicles of Ferrocene-Containing Triblock Terpolymer Exhibiting On–Off Switchable Pores", ACS Macro Letters, 2015 Publication	<1 %
9	S. N. Raju Kutcherlapati, Rambabu Koyilapu, Uma Maheswara Rao Boddu, Debparna Datta et al. "Glycopolymer-Grafted Nanoparticles: Synthesis Using RAFT Polymerization and Binding Study with Lectin", Macromolecules, 2017 Publication	<1 %
10	hdl.handle.net Internet Source	<1 %

11	Billa Narasimha Rao, Kuruma Malkappa, Nagendra Kumar, Tushar Jana. "Ferrocene grafted hydroxyl terminated polybutadiene: A binder for propellant with improved burn rate", Polymer, 2019 Publication	<1 %
12	Christopher G. Hardy, Lixia Ren, Jiuyang Zhang, Chuanbing Tang. "Side-Chain Metallocene-Containing Polymers by Living and Controlled Polymerizations", Israel Journal of Chemistry, 2012 Publication	<1 %
13	Justin O. Zoppe, Nariye Cavusoglu Ataman, Piotr Mocny, Jian Wang, John Moraes, Harm-Anton Klok. "Surface-Initiated Controlled Radical Polymerization: State-of-the-Art, Opportunities, and Challenges in Surface and Interface Engineering with Polymer Brushes", Chemical Reviews, 2017 Publication	<1 %
14	Paul J. Hurst, Alexander M. Rakowski, Joseph P. Patterson. "Ring-opening polymerization-induced crystallization-driven self-assembly of poly-L-lactide-block-polyethylene glycol block copolymers (ROPI-CDSA)", Nature Communications, 2020 Publication	<1 %

15	Xin Huang, Dietmar Appelhans, Petr Formanek, Frank Simon, Brigitte Voit. "Synthesis of Well-Defined Photo-Cross-Linked Polymeric Nanocapsules by Surface-Initiated RAFT Polymerization", Macromolecules, 2011 Publication	<1 %
16	pubs.acs.org Internet Source	<1 %
17	Kuruma Malkappa, Tushar Jana. "Simultaneous Improvement of Tensile Strength and Elongation: An Unprecedented Observation in the Case of Hydroxyl Terminated Polybutadiene Polyurethanes", Industrial & Engineering Chemistry Research, 2013 Publication	<1 %
18	Markus Mazurowski, Markus Gallei, Junyu Li, Haiko Didzoleit, Bernd Stühn, Matthias Rehahn. "Redox-Responsive Polymer Brushes Grafted from Polystyrene Nanoparticles by Means of Surface Initiated Atom Transfer Radical Polymerization", Macromolecules, 2012 Publication	<1 %
19	Zheng Deng, Haojie Yu, Li Wang, Xiaoting Zhai, Yongsheng Chen, Sergey Z. Vatsadze. "Construction of ferrocene-containing	<1 %

nanomaterials via self-assembly of ferrocenyl hyperbranched polyethylene", Journal of Organometallic Chemistry, 2016
Publication

20	Zhao, Sébastien Perrier. "Synthesis of Well-Defined Homopolymer and Diblock Copolymer Grafted onto Silica Particles by Z-Supported RAFT Polymerization", Macromolecules, 2006 Publication	<1 %
21	scholarbank.nus.edu.sg Internet Source	<1 %
22	Chun Feng, Xiaoyu Huang. "Polymer Brushes: Efficient Synthesis and Applications", Accounts of Chemical Research, 2018 Publication	<1 %
23	www.eurekaselect.com Internet Source	<1 %
24	dokumen.pub Internet Source	<1 %
25	doaj.org Internet Source	<1 %
26	Ing Kong. "Polymers with Nano-Encapsulated Functional Polymers", Elsevier BV, 2016 Publication	<1 %
27	www.beilstein-journals.org Internet Source	<1 %

28	www.patentsencyclopedia.com Internet Source	<1 %
29	Rambabu Koyilapu, Shuvra Singha, S.N.Raju Kutcherlapati, Tushar Jana. "Grafting of vinylimidazolium-type poly(ionic liquid) on silica nanoparticle through RAFT polymerization for constructing nanocomposite based PEM", Polymer, 2020 Publication	<1 %
30	Ye Sha, Yudi Zhang, Tianyu Zhu, Shaobo Tan, Yujin Cha, Stephen L. Craig, Chuanbing Tang. "Ring-Closing Metathesis and Ring-Opening Metathesis Polymerization toward Main-Chain Ferrocene-Containing Polymers", Macromolecules, 2018 Publication	<1 %
31	D. Scheid, C. Lederle, S. Vowinkel, C. G. Schäfer, B. Stühn, M. Gallei. "Redox- and mechano-chromic response of metallopolymer-based elastomeric colloidal crystal films", Journal of Materials Chemistry C, 2014 Publication	<1 %
32	Feng Xu, Zhuo-Miao Cui, He Li, Yan-Ling Luo. "Electrochemical determination of trace pesticide residues based on multiwalled carbon nanotube grafted acryloyloxy	<1 %

ferrocene carboxylates with different spacers", RSC Advances, 2017
Publication

33	idoc.pub Internet Source	<1 %
34	Kyle C. Bentz, Daniel A. Savin. "Hollow polymer nanocapsules: synthesis, properties, and applications", Polymer Chemistry, 2018 Publication	<1 %
35	www.chemistry.ohio-state.edu Internet Source	<1 %
36	tel.archives-ouvertes.fr Internet Source	<1 %
37	Bikash Kumar Sikder, Tushar Jana. "Effect of Solvent and Functionality on the Physical Properties of Hydroxyl-Terminated Polybutadiene (HTPB)-Based Polyurethane", ACS Omega, 2018 Publication	<1 %
38	Elisa G. Doyagüez, Juan Rodríguez-Hernández, Guillermo Corrales, Alfonso Fernández-Mayoralas, Alberto Gallardo. "Water-Soluble Pendant Copolymers Bearing Proline and Permethylated β-Cyclodextrin: pH-Dependent Catalytic Nanoreactors", Macromolecules, 2012 Publication	<1 %

39	Markus Gallei. "The Renaissance of Side-Chain Ferrocene-Containing Polymers: Scope and Limitations of Vinylferrocene and Ferrocenyl Methacrylates", Macromolecular Chemistry and Physics, 2014 Publication	<1 %
40	Martina H. Stenzel, Thomas P. Davis. "Star polymer synthesis using trithiocarbonate functional ?-cyclodextrin cores (reversible addition-fragmentation chain-transfer polymerization)", Journal of Polymer Science Part A: Polymer Chemistry, 2002 Publication	<1 %
41	royalsocietypublishing.org Internet Source	<1 %
42	Dusadee Tumnantong, Garry L. Rempel, Pattarapan Prasassarakich. "Synthesis of polystyrene-silica nanoparticles via RAFT emulsifier-free emulsion polymerization", European Polymer Journal, 2016 Publication	<1 %
43	Yi Yan, Jiuyang Zhang, Yali Qiao, Mitra Ganewatta, Chuanbing Tang. "Ruthenocene-Containing Homopolymers and Block Copolymers via ATRP and RAFT Polymerization", Macromolecules, 2013 Publication	<1 %

44	worldwidescience.org Internet Source	<1 %
45	orbit.dtu.dk Internet Source	<1 %
46	vtechworks.lib.vt.edu Internet Source	<1 %
47	Sylvia Ganda, Martin Dulle, Markus Drechsler, Beate Förster, Stephan Förster, Martina H. Stenzel. "Two-Dimensional Self-Assembled Structures of Highly Ordered Bioactive Crystalline-Based Block Copolymers", Macromolecules, 2017 Publication	<1 %
48	"Handbook of RAFT Polymerization", Wiley, 2008 Publication	<1 %
49	Kuruma Malkappa, Billa Narasimha Rao, Tushar Jana. "Functionalized polybutadiene diol based hydrophobic, water dispersible polyurethane nanocomposites: Role of organo-clay structure", Polymer, 2016 Publication	<1 %
50	Wenhui Zeng, Calvin O. Nyapete, Alexander H.H. Benziger, Paul A. Jelliss, Steven W. Buckner. "Encapsulation of Reactive Nanoparticles of Aluminum, Magnesium, Zinc, Titanium, or Boron within Polymers for	<1 %

Energetic Applications", Current Applied Polymer Science, 2019
Publication

51	baadalsg.inflibnet.ac.in Internet Source	<1 %
52	Submitted to Case Western Reserve University Student Paper	<1 %
53	Haibin Gu, Amalia Rapakousiou, Patricia Castel, Nicolas Guidolin, Nöel Pinaud, Jaime Ruiz, Didier Astruc. "Living Ring-Opening Metathesis–Polymerization Synthesis and Redox-Sensing Properties of Norbornene Polymers and Copolymers Containing Ferrocenyl and Tetraethylene Glycol Groups", Organometallics, 2014 Publication	<1 %
54	Kamal Bauri, Amal Narayanan, Ujjal Haldar, Priyadarsi De. "Polymerization-induced self-assembly driving chiral nanostructured materials", Polymer Chemistry, 2015 Publication	<1 %
55	Shirish H. Sonawane, Bharat A. Bhanvase, Manickam Sivakumar, Shital B. Potdar. "Current overview of encapsulation", Elsevier BV, 2020 Publication	<1 %

56	Timea Nagy-Simon, Andra-Sorina Tatar, Ana-Maria Craciun, Adriana Vulpoi et al. "Antibody Conjugated, Raman Tagged Hollow Gold–Silver Nanospheres for Specific Targeting and Multimodal Dark-Field/SERS/Two Photon-FLIM Imaging of CD19(+) B Lymphoblasts", ACS Applied Materials & Interfaces, 2017 Publication	<1 %
57	Mie Lillethorup, Kyoko Shimizu, Nicolas Plumeré, Steen U. Pedersen, Kim Daasbjerg. "Surface-Attached Poly(glycidyl methacrylate) as a Versatile Platform for Creating Dual-Functional Polymer Brushes", Macromolecules, 2014 Publication	<1 %
58	Paul Nguyen, Paloma Gómez-Elipe, Ian Manners. "Organometallic Polymers with Transition Metals in the Main Chain", Chemical Reviews, 1999 Publication	<1 %
59	Submitted to University of Bristol Student Paper	<1 %
60	patents.justia.com Internet Source	<1 %
61	www.fedoa.unina.it Internet Source	<1 %
	zaguan.unizar.es	

62	Internet Source	<1 %
63	"Organometallics in Synthesis", Wiley, 1994 Publication	<1 %
64	Pathik Sahoo, Vedavati G. Puranik, A. K. Patra, P. U. Sastry, Parthasarathi Dastidar. "Ferrocene based organometallic gelators: a supramolecular synthon approach", Soft Matter, 2011 Publication	<1 %
65	Submitted to Virginia Polytechnic Institute and State University Student Paper	<1 %
66	dergipark.ulakbim.gov.tr Internet Source	<1 %
67	Submitted to Defence Institute of Advanced Technology, Pune Student Paper	<1 %
68	Xuewei Xu, Junlian Huang. "Synthesis and characterization of amphiphilic copolymer of linear poly(ethylene oxide) linked with [poly(styrene-co-2-hydroxyethyl methacrylate)-graft-poly(□-caprolactone)] using sequential controlled polymerization", Journal of Polymer Science Part A: Polymer Chemistry, 2006 Publication	<1 %

69	rasayanjournal.co.in Internet Source	<1 %
70	www.thieme-connect.com Internet Source	<1 %
71	Kuruma Malkappa, Tushar Jana. "Hydrophobic, Water-Dispersible Polyurethane: Role of Polybutadiene Diol Structure", Industrial & Engineering Chemistry Research, 2015 Publication	<1 %
72	Tamara Winter, Xiao Su, T. Alan Hatton, Markus Gallei. "Ferrocene-Containing Inverse Opals by Melt-Shear Organization of Core/Shell Particles", Macromolecular Rapid Communications, 2018 Publication	<1 %
73	journals.tubitak.gov.tr Internet Source	<1 %
74	pericles.pericles-prod.literatumonline.com Internet Source	<1 %
75	www.freepatentsonline.com Internet Source	<1 %
76	www.ncbi.nlm.nih.gov Internet Source	<1 %
77	Billa Narasimha Rao, P. Jaya Prakash Yadav, Kuruma Malkappa, Tushar Jana, P.U. Sastry.	<1 %

	"Triazine functionalized hydroxyl terminated polybutadiene polyurethane: Influence of triazine structure", Polymer, 2015 Publication	
78	Per B. Zetterlund, Stuart C. Thickett, Sébastien Perrier, Elodie Bourgeat-Lami, Muriel Lansalot. "Controlled/Living Radical Polymerization in Dispersed Systems: An Update", Chemical Reviews, 2015 Publication	<1 %
79	eprints.whiterose.ac.uk Internet Source	<1 %
80	journals.plos.org Internet Source	<1 %
81	link.springer.com Internet Source	<1 %
82	patents.google.com Internet Source	<1 %
83	thesis.library.caltech.edu Internet Source	<1 %
84	www.tandfonline.com Internet Source	<1 %
85	Choi-Sledeski, Yong Mi, Daniel G. McGarry, Daniel M. Green, Helen J. Mason, Michael R. Becker, Roderick S. Davis, William R. Ewing, William P. Dankulich, Vincent E. Manetta,	<1 %

Robert L. Morris, Alfred P. Spada, Daniel L. Cheney, Karen D. Brown, Dennis J. Colussi, Valeria Chu, Christopher L. Heran, Suzanne R. Morgan, Ross G. Bentley, Robert J. Leadley, Sebastien Maignan, Jean-Pierre Guilloteau, Christopher T. Dunwiddie, and Henry W. Pauls. "Sulfonamidopyrrolidinone Factor Xa Inhibitors: Potency and Selectivity Enhancements via P-1 and P-4 Optimization", Journal of Medicinal Chemistry, 1999.
Publication

---

86 Raphael Barbey, Laurent Lavanant, Dusko Paripovic, Nicolas Schüwer, Caroline Sugnaux, Stefano Tugulu, Harm-Anton Klok. "Polymer Brushes via Surface-Initiated Controlled Radical Polymerization: Synthesis, Characterization, Properties, and Applications", Chemical Reviews, 2009 <1 %
Publication

---

87 pt.scribd.com <1 %
Internet Source

---

88 Krzysztof Matyjaszewski, Jianhui Xia. "Atom Transfer Radical Polymerization", Chemical Reviews, 2001 <1 %
Publication

Exclude quotes	On	Exclude matches	< 14 words
Exclude bibliography	On		